Mathematical Models of Blood Flow through Curved Arteries

By

Meriyem Hussain

PhD Thesis
SESSION 2021-2024

DEPARTMENT OF MATHEMATICS
The Islamia University of Bahawalpur
Bahawalpur, Pakistan

2024

Mathematical Models of Blood Flow through Curved Arteries

By

Meriyem Hussain

Supervised by

Dr. Muhammad Shahzad Shabbir

DEPARTMENT OF MATHEMATICS

The Islamia University of Bahawalpur

Bahawalpur, Pakistan

2024

Mathematical Models of Blood Flow through Curved Arteries

By

Meriyem Hussain

A thesis submitted to the department of Mathematics,
The Islamia University of Bahawalpur,
in the partial fulfillment for the degree of
DOCTOR OF PHILOSOPHY
IN
MATHEMATICS

Supervised by

Dr. Muhammad Shahzad Shabbir

DEPARTMENT OF MATHEMATICS
The Islamia University of Bahawalpur
Bahawalpur, Pakistan

2024

Student's Declaration

I, ***Meriyem Hussain D/O Muhammad Hussain*** PhD Scholar at the Department of Mathematics, The Islamia University of Bahawalpur, hereby declare that the research work entitled **"*Mathematical models of blood flow through curved arteries*"** is carried out by me. I also certify that nothing has been incorporated in this research work without acknowledgement and that to the best of my knowledge and belief, it does not contain any material previously published or written by any other person or any material previously submitted for a degree in any university where due reference is not made in the text.

Meriyem Hussain
D/O
Muhammad Hussain

Supervisor’s Declaration

It is hereby certified that the work presented by ***Meriyem Hussain*** in the thesis titled **“*Mathematical models of blood flow through curved arteries*”** is based on the results of a research study conducted by the candidate under my supervision. No portion of this work has been formerly offered for a higher degree in this university or any other institute of learning and to the best of the author’s knowledge, no material has been used in this dissertation which is not her work, except where due acknowledgement has been made. She has fulfilled all the requirements and is qualified to submit this dissertation in partial fulfilment for the degree of Doctor of Philosophy in Mathematics in the Faculty of Science, The Islamia University of Bahawalpur.

Dr. Muhammad Shahzad Shabbir
Supervisor
Assistant Professor
Department of Mathematics
The Islamia University of Bahawalpur

Abstract

This thesis aims to investigate blood flow in stenotic vessels under the influence of curvature. The consequences of magnetic field and periodic body acceleration have been explored. The impact of the mechanical structure of the arterial wall is highlighted by choosing w-shaped stenosis. The fundamental physical system mathematically incorporates the 2-dimensional curvilinear coordinate system. By applying the mild stenosis premise and simplifying the highly coupled momentum, energy, and mass concentration. The Herschel-Bulkley, Power law and Tangent hyperbolic fluid models are utilized to capture the Newtonian and non-Newtonian rheological behaviour of the blood in the stenosed blood vessels under diseased conditions. This study examines the dynamics of pulsating blood flow via a constricted artery using both single and two-phase flows. In two-phase flow problems, plasma and core regions are modelled using the Newtonian and Herschel-Bulkley constitutive relations, respectively. The pulsating flow of a nano-fluid (blood) through a curved artery with stenosis is analyzed numerically to determine the impacts of Thermophoresis and Brownian motion. Entropy creation in blood flow due to loss and magnetohydrodynamic processes is also investigated. The electro-osmotic effects are also taken into consideration. The non-dimensionalized governing equations associated with the boundary condition are discretized and solved using explicit finite differences methods. The research indicates that key hemodynamic flow parameters, such as velocity, wall shear stress and resistance to flow, undergo significant changes in a curved artery. The validation of the current study is ensured by comparing the numerical investigations for Newtonian fluid and straight blood vessels with the existing literature.

Contents

Preface

The fluid mechanics of blood flow is greatly aided by research on the flow of blood via arteries. It also aids in the diagnosis and treatment of several circulatory system disorders. Leukocytes, erythrocytes, and platelets are suspended in a highly concentrated solution of plasma in an aqueous solution to form blood. Blood exhibits strange behaviour. Blood has a Newtonian character in bigger arteries when the shear rate is above $100s^{-1}$, whereas a non-Newtonian character predominates in narrow arteries when the shear rate is below $100s^{-1}$. Significantly non-Newtonian blood is seen iseveralof medical disorders, including hypertension and myocardial infarction. Blood is often a non-Newtonian fluid as a result. Low-density lipoprotein in the inner walls of the blood arteries causes them to stiffen and narrow over an extended peri period cause of the increased resistance brought on by this stenotic constriction of the artery, the normal flow of blood is seriously disrupted. The non-Newtonian nature of blood cannot be adequately conveyed by a single equation that relates the stress tensor to the rate of strain tensor. It is quite difficult to solve the non-linear flow equations for blood flow in narrow channels.

In biology and medicine, magnetohydrodynamics research is crucial. Conditions including headache, travel sickness, and joint pain can be effectively treated with the application of the right magnetic field. The human body can occasionally feel the effects of an outside magnetic field. One example of an externally applied magnetic field that is highly helpful in the study of bio-flow issues is magnetic imaging resonance. The effect of externally induced entropy generation on blood flow in stenotic blood arteries is also significant. An external field on an electrolyte causes electro-osmotic movement, creating an electric double layer (EDL) as positively charged particles are attracted and negatively charged ions are repelled.

The body's temperature regulation is a remarkable feat achieved by the circulatory system. Heat transfer in the blood is of great importance in various clinical applications, including local hyperthermia and cryosurgery for tumour treatment. It is impressive that even the larger blood vessels play a significant role in convulsing the temperature distribution in the body. Meanwhile, the smaller blood vessels dynamically engage in heat exchange with the surrounding tissues. This thesis is a testament to the remarkable work of the circulatory system and the intricate processes involved in maintaining the human body's optimal temperature.

Chapter one provides a review of classical and modern literature related to the movement of narrowed arterial sections. The chapter also includes a presentation of the fundamental equations that govern the flow of blood, including continuity, momentum, energy, and mass concentration. Additionally, the chapter covers the non-Newtonian fluid model, which describes the rheology of blood, and the various methods used to solve the flow equation.

Chapter two deals with the simultaneous impacts of non-Newtonian and curvature on unstable nano-fluid flow. The pulsating flow of a nano-fluid (blood) through a curved artery with stenosis and post-stenotic dilatation in its interior is analyzed numerically to determine the impacts of Thermophoresis and Brownian motion. The basic suggested physical system mathematically incorporates the 2-dimensional curvilinear coordinate system. The Hershel-Bulkley model successfully captures the fluid's rheology. By applying the mild stenosis premise and simplifying the highly coupled momentum, energy, and mass concentration. The non-dimensionalized governing equations associated with the boundary condition can be discretized and solved using explicit finite differences methods. Graphs showing the effects of changing pertinent geometric and rheological factors on key flow characteristics, such as temperature, velocity, and mass concentration, are provided. **These findings are published in "Physica Scripta, V-98 075014 (2023)".**

Chapter three influence of Thermophoresis and Brownian motion on the pulsing flow of nano-fluid (blood) through a curved artery with stenosis and post-stenotic dilatation in its interior is investigated numerically. The Herschel-Bulkley model of fluid dynamics accurately represents the fluid's rheology. By applying the mild stenosis condition, the highly coupled momentum, energy, and mass concentration equations can be modelled and reduced. Entropy creation in blood flow due to loss and magnetohydrodynamic processes is also investigated. Graphs and discussions of the effects of changing pertinent geometric and rheological factors on key flow characteristics, such as temperature, velocity, mass concentration, wall shear stress flow rate and impedance are provided. **These findings are published in "Alexandria Engineering Journal, V-78 pages 644-656 (2023)".**

Chapter four focuses on Time-dependent blood flow via a w-shaped stenotic conduit affected by a pulsatile pressure gradient is solved numerically. The theoretical model of tangent hyperbolic fluid is utilized to formulate the problem. To represent the issue, cylindrical coordinates are used, and the electro-osmotic effects are taken into consideration. To simplify the non-dimensional governing equations of the flow problem, mild stenosis assumption is utilized. The resulting nonlinear system of differential equations is solved using an explicit finite difference method, taking into account the boundary conditions that have been stated. An examination of the numbers behind the big picture, such as axial velocity, temperature field, concentration Nusselt number, and Sherwood number, is carried out after appropriate changes have been made to the essential non-dimensional factors. **These findings are review in "Modern Physics Letters B".**

Chapter five shows the two-phase analysis of pulsatile blood flow through a stenosed, narrowed artery is presented in this work. The problem is represented using cylindrical coordinates. A modest stenosis assumption is used to simplify the non-dimensional governing equations of the flow issue. The radial coordinate transformation is utilised to reduce the effect of the blood vessel wall. An explicit finite difference approach is used to solve the resultant nonlinear system of differential equations while accounting for the provided boundary conditions. After the necessary adjustments have been made to the crucial non-dimensional parameters, an analysis of the data behind the huge image, such as axial velocity, temperature field, concentration wall shear stress, flow rate, and flow impedance, is conducted. **These findings are submitted to "Results in Physics".**

Chapter six deals with a two-phase analysis of pulsatile blood flow through a stenosed, narrowed artery is presented in this work. The Newtonian and Herschel-Bulkley constitutive relations are used to model the plasma and core regions, respectively. The problem is represented using cylindrical coordinates. A modest stenosis assumption is used to simplify the non-dimensional governing equations of the flow issue. The radial coordinate transformation is utilised to reduce the effect of the blood vessel wall. An explicit finite difference approach is used to solve the resultant nonlinear system of differential equations while accounting for the provided boundary conditions. After the necessary adjustments have been made to the crucial non-dimensional parameters, an analysis of the data behind the huge image, such as axial velocity, temperature field, concentration wall shear stress, flow rate, and flow impedance, is conducted. **These findings are submitted to "Chinese Journal of Physics".**

List of Figures

Figure 3.10: Concentration profile for various values of curvature R_c with $\Pr = 9$, $B_1 = 1.41$, $\operatorname{Re} = 1$, $Gr = 1$, $\delta = 0.1$ and $x = 0.52$.

Figure 3.11: Concentration profile for various values of Lewis number Le with $\Pr = 9$, $B_1 = 1.41$, $\operatorname{Re} = 1$, $Gr = 1$, $\delta = 0.1$ and $x = 0.52$.

Figure 3.12: Concentration profile for various values of thermophoresis N_t with $\Pr = 9$, $B_1 = 1.41$, $\operatorname{Re} = 1$, $Gr = 1$, $\delta = 0.1$ and $x = 0.52$.

Figure 3.13: Concentration profile for various values of Brownian motion N_b with $\Pr = 9$, $B_1 = 1.41$, $\operatorname{Re} = 1$, $Gr = 1$, $\delta = 0.1$ and $x = 0.52$.

Figure 3.14: Entropy generation number N_G graphs for different values of curvature R_c with $\Pr = 9$, $B_1 = 1.41$, $\operatorname{Re} = 1$, $Gr = 1$, $\delta = 0.1$ and $x = 0.52$.

Figure 3.15: Entropy generation number N_G graphs for different values of Brickmann Br with $\Pr = 9$, $B_1 = 1.41$, $\operatorname{Re} = 1$, $Gr = 1$, $\delta = 0.1$ and $x = 0.52$.

Figure 3.16: Entropy generation number N_G graph for different values of magnetic field M with $\Pr = 9$, $B_1 = 1.41$, $\operatorname{Re} = 1$, $Gr = 1$, $\delta = 0.1$ and $x = 0.52$.

Figure 3.17: Bejan number Be graph for different values of curvature R_c with $\Pr = 9$, $B_1 = 1.41$, $\operatorname{Re} = 1$, $Gr = 1$, $\delta = 0.1$ and $x = 0.52$.

Figure 3.18: Bejan number Be graph for different values of Brickmann Br with $\Pr = 9$, $B_1 = 1.41$, $\operatorname{Re} = 1$, $Gr = 1$, $\delta = 0.1$ and $x = 0.52$.

Figure 3.19: Bejan number Be graph for different values of magnetic field M with $\Pr = 9$, $B_1 = 1.41$, $\operatorname{Re} = 1$, $Gr = 1$, $\delta = 0.1$ and $x = 0.52$.

Figure 3.20: Axial distribution of wall shear stress for various values with $\Pr = 9$, $B_1 = 1.41$, $\operatorname{Re} = 1$, $Gr = 1$, $\delta = 0.1$ and $x = 0.52$.

Figure 3.21: Axial distribution of flow rate for various values with $\Pr = 9$, $B_1 = 1.41$, $\operatorname{Re} = 1$, $Gr = 1$, $\delta = 0.1$ and $x = 0.52$.

Figure 3.22: Axial distribution of impedences for various values with $\Pr = 9$, $B_1 = 1.41$, $\operatorname{Re} = 1$, $Gr = 1$, $\delta = 0.1$ and $x = 0.52$.

Figure 3.23: Validation of results with Newtonian fluid $(n=1, \tau_y=0)$ and straight blood vessels ($R_C \to \infty$).

Figure 4.1: Curved channel geometry with ω-shape overlapping stenosis and aneurysm.

Figure 4.2: Velocity profile for various values of parameter n with $\Pr=9$, $B_1=1.41$, $\mathrm{Re}=1$, $Gr=1$, $\delta=0.1$, $\mu_0=0.56$, $\mu_\infty=0.0345$, $We=0.5$, $Uhs=1$ and $x=0.9$.

Figure 4.3: Velocity profile for various values of Weissenberg numbers We with $\Pr=9$, $B_1=1.41$, $\mathrm{Re}=1$, $Gr=1$, $\delta=0.1$, $\mu_0=0.56$, $\mu_\infty=0.0345$, $Uhs=1$ and $x=0.9$.

Figure 4.4: Velocity profile for various values of electric potential k with $\Pr=9$, $B_1=1.41$, $\mathrm{Re}=1$, $Gr=1$, $\delta=0.1$, $\mu_0=0.56$, $\mu_\infty=0.0345$, $We=0.5$, $Uhs=1$ and $x=0.9$.

Figure 4.5 : Velocity profile for various values of Helmholtz-Smoulochowski parameter Uhs with $\Pr=9$, $B_1=1.41$, $\mathrm{Re}=1$, $Gr=1$, $\delta=0.1$, $\mu_0=0.56$, $\mu_\infty=0.0345$, $We=0.5$ and $x=0.9$.

Figure 4.6: Velocity profile for various values of curvature R_c with $\Pr=9$, $B_1=1.41$, $\mathrm{Re}=1$, $Gr=1$, $\delta=0.1$, $\mu_0=0.56$, $\mu_\infty=0.0345$, $We=0.5$, $Uhs=1$ and $x=0.9$.

Figure 4.7: Temperature profile for various values of curvature R_c with $\Pr=9$, $B_1=1.41$, $\mathrm{Re}=1$, $Gr=1$, $\delta=0.1$, $\mu_0=0.56$, $\mu_\infty=0.0345$, $We=0.5$, $Uhs=1$ and $x=0.9$.

.**Figure 4.8:** Temperature profile for various values of Brickmann Br with $\Pr=9$, $B_1=1.41$, $\mathrm{Re}=1$, $Gr=1$, $\delta=0.1$, $\mu_0=0.56$, $\mu_\infty=0.0345$, $We=0.5$, $Uhs=1$ and $x=0.9$.

Figure 4.9: Temperature profile for various values of Brownian motion N_b with $\Pr=9$, $B_1=1.41$, $\mathrm{Re}=1$, $Gr=1$, $\delta=0.1$, $\mu_0=0.56$, $\mu_\infty=0.0345$, $We=0.5$, $Uhs=1$ and $x=0.9$.

Figure 4.20: Temperature profile for various values of thermophoresis N_t with $\Pr = 9$, $B_1 = 1.41$, $\text{Re} = 1$, $Gr = 1$, $\delta = 0.1$, $\mu_0 = 0.56$, $\mu_\infty = 0.0345$, $We = 0.5$, $Uhs = 1$ and $x = 0.9$.

Figure 4.11: Temperature profile for various values of Helmholtz-Smoulochowski parameter Uhs with $\Pr = 9$, $B_1 = 1.41$, $\text{Re} = 1$, $Gr = 1$, $\delta = 0.1$, $\mu_0 = 0.56$, $\mu_\infty = 0.0345$, $We = 0.5$ and $x = 0.9$.

Figure 4.12: Concentration profile for various values of Lewis number Le with $\Pr = 9$, $B_1 = 1.41$, $\text{Re} = 1$, $Gr = 1$, $\delta = 0.1$, $\mu_0 = 0.56$, $\mu_\infty = 0.0345$, $We = 0.5$ and $x = 0.9$.

Figure 4.13: Concentration profile for various values of Brownian motion N_b with $\Pr = 9$, $B_1 = 1.41$, $\text{Re} = 1$, $Gr = 1$, $\delta = 0.1$, $\mu_0 = 0.56$, $\mu_\infty = 0.0345$, $We = 0.5$ and $x = 0.9$.

Figure 4.14: Concentration profile for various values of thermophoresis N_t with $\Pr = 9$, $B_1 = 1.41$, $\text{Re} = 1$, $Gr = 1$, $\delta = 0.1$, $\mu_0 = 0.56$, $\mu_\infty = 0.0345$, $We = 0.5$ and $x = 0.9$.

Figure 4.15: Variations in Nusselt number Nu for different values of Reynolds number Re with $\Pr = 9$, $B_1 = 1.41$, $\text{Re} = 1$, $Gr = 1$, $\delta = 0.1$, $\mu_0 = 0.56$, $\mu_\infty = 0.0345$, $We = 0.5$ and $x = 0.9$.

Figure 4.16: Variations in Nusselt number Nu for different values of Prandtl number $\Pr$ with $\Pr = 9$, $B_1 = 1.41$, $\text{Re} = 1$, $Gr = 1$, $\delta = 0.1$, $\mu_0 = 0.56$, $\mu_\infty = 0.0345$, $We = 0.5$ and $x = 0.9$.

Figure 4.17: Variations in Sherwood number Sh for different values of Lewis number Le with $\Pr = 9$, $B_1 = 1.41$, $\text{Re} = 1$, $Gr = 1$, $\delta = 0.1$, $\mu_0 = 0.56$, $\mu_\infty = 0.0345$, $We = 0.5$ and $x = 0.9$.

Figure 4.18: Variations in Sherwood number Sh for different values of thermophoresis N_t with $\Pr = 9$, $B_1 = 1.41$, $\text{Re} = 1$, $Gr = 1$, $\delta = 0.1$, $\mu_0 = 0.56$, $\mu_\infty = 0.0345$, $We = 0.5$ and $x = 0.9$.

Figure 4.19: Variations in Sherwood number Sh for different values of Reynolds number Re with $\Pr = 9$, $B_1 = 1.41$, $\mathrm{Re} = 1$, $Gr = 1$, $\delta = 0.1$, $\mu_0 = 0.56$, $\mu_\infty = 0.0345$, $We = 0.5$ and $x = 0.9$.

Figure 5.1: Two-phase overlapping stenosed ω-shaped in curved channel geometry.

Figure 5.2: Velocity profile for various values of curvature R_c with $\mathrm{P}e = 1.87, \mathrm{Re} = 1, B_1 = 1.41, E = 0.5, \beta = 0.1, Sc = 1, \mu_0 = 1.2, k_0 = 0.8, c_0 = 1 \; and \; \rho_0 = 1.05.$

Figure 5.3: Velocity profile for various values of Reynolds number Re with $\mathrm{P}e = 1.87, B_1 = 1.41, E = 0.5, \beta = 0.1, Sc = 1, \mu_0 = 1.2, k_0 = 0.8, c_0 = 1 \; and \; \rho_0 = 1.05.$

Figure 5.4 : Velocity profile for various values of Brickmann Br with $\mathrm{P}e = 1.87, \mathrm{Re} = 1, B_1 = 1.41, E = 0.5, \beta = 0.1, Sc = 1, \mu_0 = 1.2, k_0 = 0.8, c_0 = 1 \; and \; \rho_0 = 1.05.$

Figure 5.5 : Velocity profile for various values of Grashof number Gr, with $\mathrm{P}e = 1.87, \mathrm{Re} = 1, B_1 = 1.41, E = 0.5, \beta = 0.1, Sc = 1, \mu_0 = 1.2, k_0 = 0.8, c_0 = 1 \; and \; \rho_0 = 1.05.$

Figure 5.6: Velocity profile for various values of viscosity μ_p with $\mathrm{P}e = 1.87, \mathrm{Re} = 1, B_1 = 1.41, E = 0.5, \beta = 0.1, Sc = 1, \mu_0 = 1.2, k_0 = 0.8, c_0 = 1 \; and \; \rho_0 = 1.05.$

Figure 5.7: Temperature profile for various values of Peclet number Pe with $\mathrm{Re} = 1, B_1 = 1.41, E = 0.5, \beta = 0.1, Sc = 1, \mu_0 = 1.2, k_0 = 0.8, c_0 = 1 \; and \; \rho_0 = 1.05.$

Figure 5.8 : Temperature profile for various values of sink parameter β with $\mathrm{P}e = 1.87, \mathrm{Re} = 1, B_1 = 1.41, E = 0.5, Sc = 1, \mu_0 = 1.2, k_0 = 0.8, c_0 = 1 \; and \; \rho_0 = 1.05.$

Figure 5.9: Temperature profile for various values of ratio of specific heat c_0 with $\mathrm{P}e = 1.87, \mathrm{Re} = 1, B_1 = 1.41, E = 0.5, \beta = 0.1, Sc = 1, \mu_0 = 1.2, k_0 = 0.8, \; and \; \rho_0 = 1.05.$

Figure 5.10: Temperature profile for various values of ratio of thermal conductivity k_0 with $\mathrm{P}e = 1.87, \mathrm{Re} = 1, B_1 = 1.41, E = 0.5, Sc = 1, \mu_0 = 1.2, c_0 = 1 \; and \; \rho_0 = 1.05.$

Figure 5.11: Temperature profile for various values of ratio of density ρ_0 with $\mathrm{P}e = 1.87, \mathrm{Re} = 1, B_1 = 1.41, E = 0.5, Sc = 1, \mu_0 = 1.2, k_0 = 0.8, \; and \; c_0 = 1.$

Figure 5.12: Concentration profile for various values of Reynolds number Re with $\mathrm{P}e = 1.87, B_1 = 1.41, E = 0.5, \beta = 0.1, Sc = 1, \mu_0 = 1.2, k_0 = 0.8, c_0 = 1 \; and \; \rho_0 = 1.05.$

Figure 6.7: Temperature profile for various values of curvature R_c with $\mathrm{Re}=1, B_1=1.41, E=0.5, \beta=0.1, n=0.95, Sc=1, \mu_0=1.2, k_0=0.8, c_0=1$ *and* $\rho_0=1.05$.

Figure 6.8: Temperature profile for various values of sink parameter β with $\mathrm{P}e=1.87, \mathrm{Re}=1, B_1=1.41, E=0.5, n=0.95, Sc=1, \mu_0=1.2, k_0=0.8, c_0=1$ *and* $\rho_0=1.05$.

Figure 6.9: Temperature profile for various values of Peclet number Pe with $\mathrm{Re}=1, B_1=1.41, E=0.5, \beta=0.1, n=0.95, Sc=1, \mu_0=1.2, k_0=0.8, c_0=1$ *and* $\rho_0=1.05$.

Figure 6.10: Concentration profile for various values of Reynolds number Re with $\mathrm{P}e=1.87, B_1=1.41, E=0.5, \beta=0.1, n=0.9, Sc=1, \mu_0=1.2, k_0=0.8, c_0=1$ *and* $\rho_0=1.05$.

Figure 6.11: Concentration profile for various values of Schmidt number Sc with $\mathrm{P}e=1.87, B_1=1.41, E=0.5, \beta=0.1, \mu_0=1.2, k_0=0.8, c_0=1$ *and* $\rho_0=1.05$.

Figure 6.12: Concentration profile for various values of chemical reaction E with $\mathrm{P}e=1.87, n=0.9, B_1=1.41, \beta=0.1, Sc=1, \mu_0=1.2, k_0=0.8, c_0=1$ *and* $\rho_0=1.05$.

Figure 6.13: Wall shear stress profile for various values of curvature R_c with $n=0.95$ $\mathrm{P}e=1.87, B_1=1.41, E=0.5, \beta=0.1, Sc=1, \mu_0=1.2, k_0=0.8, c_0=1$ *and* $\rho_0=1.05$.

Figure 6.14: Flow rate for various values of sink parameter β with $\mathrm{P}e=1.87, \mathrm{Re}=1, B_1=1.41, E=0.5, n=0.95, Sc=1, \mu_0=1.2, k_0=0.8, c_0=1$ *and* $\rho_0=1.05$.

Figure 6.15: Impedences profile for various values of sink parameter β with $\mathrm{P}e=1.87, \mathrm{Re}=1, B_1=1.41, E=0.5, n=0.95, Sc=1, \mu_0=1.2, k_0=0.8, c_0=1$ *and* $\rho_0=1.05$.

Chapter 1

Introduction

This chapter provides an overview of blood flow in various shaped blood vessels, including linear and non-linear fluids.It discusses fundamental concepts, equations, and models that describe the rheology of blood. The chapter includes a presentation of constitutive equations for non-Newtonian fluid models, as well as solution techniques such as perturbation methods and explicit finite difference schemes.

1.1 Literature review

It consists of the heart, blood vessels, and blood. A major function of blood in mammals and humans alike is to carry the digested food to every portion of the body. The rhythmic pressure gradient that the heart generates when it pumps blood throughout the body. One of the great problems of the last several decades and the years to come will be the mathematical study of blood flow in the human circulatory system. To better comprehend the hemodynamical irregularities caused by stenosis, more efficient and precise numerical modelling methods should be developed.

The plasma, RBCs, WBCs, and platelets that make up human blood are suspended in a colloidal solution (Guyton & Hall, 2000). The human circulatory system, an intricate network of vascular vessels, capillaries, and arteries, functions as a closed cardiovascular system. As blood courses through larger arteries at a rapid shear rate, a dynamic process unfolds, It behavs as a Newtonian fluid in general, but as a non-Newtonian fluid in narrower arteries subjected to low shear rates. Ischemia, atherosclerosis, and angina pectoris are the most well-known forms of heart disease, which is a leading cause of death globally. Ischemia occurs when there is a momentary lack of oxygen to a specific area of the body. A narrowing (stenosis) or blockage in the blood vessel supplying that area could be the cause.

The plasma, RBCs, WBCs, and platelets that make up human blood are suspended in a colloidal solution (Guyton & Hall, 2000). The human circulatory system is a remarkable network of interconnected blood vessels, including arteries, veins, and capillaries. With its closed design, this system efficiently transports oxygen, nutrients, and hormones throughout the body, enabling us to live healthy and active lives. Understanding the importance of this system is crucial to maintaining good health and vitality. (Young and Tsai 1973) utilised these locally restricted tubes to explain certain major hydrodynamic phenomena, such as the present external field on an electrolyte causing electro-osmotic movement, creating an electric double layer (EDL) as positively charged particles are attracted and negatively charged ions are repelled. Ady flow has emerged as a hallmark of vascular stenosis experimental models (Yongchareon and Young 1979). stenosis was shown by three rigid-walled duplicates with significantly restricted passageways of varied sizes and shapes. Quantitative research on the impacts of flow viscosity through a creature's coronary blood tube casting has been reported by Cho and Kensey (1991) using a finite element technique. (Abraham, Behr et al., 2005) looked into how the liquid constitutive replica affected the results of size optimum tasks because of the optimal design issues in biomedicine and engineering. The effects of atherosclerosis on streamline contour, layer pressure drop, and increase in shear stress were quantitatively studied to alleviate the syndrome (Mandal, Manna et al. 2010). The governing equations are expressed using a finite volume approach. Research by Sharzehee, Khalafvand, et al. (2018) sought to understand how aneurysmal arteries behaved during and after buckling when exposed to pulsatile flow.

Following the work of (Chakravarty, Datta et al., 1996), which examined the impact of a single cycle of a creature's accelerations on the unstable blood flow behaviour beyond time-dependent arterial stenosis, we examine the pulsatile pressure gradient influencing the erratic flow system within the stenosis pipe. Pressure gradient and wall shear stress effects have been graphically analysed (Sanyal and Maji 1999). The creature's regular heart mechanism causes a pulsatile pressure gradient, which in turn causes the irregular motion structure in the bifurcated artery, as we can determine from the exact measurement of the body's acceleration. Examined the irregular blood flow along a curved conduit with atherosclerosis and a small amount of stenosis using a finite difference solution (Venkateswarlu and Rao 2004). Assuming a Power-law distribution for the rheology of flowing blood, overcoming the problem of blood flow through a stenosed tube is possible by (Mandal 2005).

A thorough investigation is carried out to confirm the model's feasibility by doing precise calculations of the relevant numbers from a physiological perspective and visually presenting the outcomes. According to Chakravarty and Mandal (2005), a two-dimensional model was generated from a three-dimensional model of an artery with little stenosis to study the pulsatile blood motion in an aortic section with unequal stenosis rationally utilising a precise method. Research has shown that the presence of a magnetic region can cause non-Newtonian motion of liquid through a narrow tube in atherosclerotic tubes according to (Ikbal, Chakravarty et al. 2009). The study examines pulsatile blood flow in an artery's thick media under periodic acceleration and slip conditions in the presence of a magnetic field. (Eldesoky 2012). Blood is treated as an incompressible electrically conducting liquid. A technique for studying the dynamics of an electrically conducting, thick-flowing, incompressible liquid within a cylinder that is magnetically field-enhanced and strongly inclined towards one end was proposed by Mwanthi, Mwenda et al. (2017). (Abbasian, Shams et al., 2020) presented the study's findings, the text aimed to demonstrate how different models of blood rheology affect the simulation of blood flow dynamics in atherosclerotic coronary arteries.

A study conducted by Young, Cholvin, and colleagues in 1977 titled "Pressure Drop A cross Arterial Stenosis" examines the consequences of stenosis when exposed to elevated blood flow rates caused by a vasodilator medication that is supplied locally. Researchers have shown that by using the right mathematical model, they can see how stenosis affects vascular deformability and blood flow in an artery (Chakravarty 1987). In their study, Tandon and Rana (1995) examined the flow characteristics of a blood-based suspension passing through a spherical tube that had an axial-symmetric stenosis. In particular, the hemodynamic characteristics of artery stenosis are examined (Moayeri and Zendehbudi 2003). We assume that blood is a Newtonian liquid and use the pressure and flow rate of the canine femoral tube to represent the pulsing motion. Researchers want to gain a better understanding of the properties of an external magnetic field on the velocity of Newtonian blood by creating a comprehensive model of bio-magnetic liquid dynamics (Tzirtzilakis 2005). Students were informed that their grades would be based on their capacity to analyse and explain fluid viscosity models, physiological motion circumstances, and fluid rheology, according to studies on the tapering angle (Yilmaz and Gundogdu 2008).

Findings from a study by Singh, Joshi et al. (2010) suggest that stenosis performed at regularly spaced locations can enhance their form. (Mathur and Jain 2013) examine the function of non-Newtonian fluid dynamics by mathematically modelling the movement of blood through a narrowed section of an artery, we explore the fascinating dynamics at play. The blood's unique behaviour, known as non-Newtonian, is elegantly captured by a power law function. By conducting meticulous mathematical analysis, we unravel the intricacies of non-Newtonian blood flow in minuscule arteries afflicted by stenosis (Sriyab 2014). The flow of blood through the arteries of a human being is analogous to a fluid dynamics issue (Thomas and Sumam 2016). Blood flow models in the artery network system will help us understand human physiology. (Roy Sood et al., 2018) The authors of the study report the findings of computational models that represented stenotic arteries as straight tubes and investigated the distributions of blood flow and wall shear stress. According to research (Karimipour, Mokhtari et al. 2020), a clot in half of an artery can cause a notable increase in flow. However, before clotting, the flow is very similar to the typical model of a straight artery. With this research, we hope to evaluate the flow parameters caused by stenosis by numerically simulating the cerebral arteries of a patient who has had a stroke (Rahma, Yousef et al. 2022).

The correlation between the rheological parameters of vascular diseases including atherosclerosis and thrombosis and the intricate blood flow structure through a twisted artery with an aneurysm was investigated in vitro (Niimi, Kawano et al. 1984). This proves without a reasonable doubt that when studying blood flow in arteries with a curved aneurysm, the secondary flow must be considered. There has been discussion on the nature of the abnormal blood flow in the stenosed segment (Wang and Bassingthwaighte 2003). They have shifted the emphasis from illness prevention to disease treatment. A study conducted by Nadeem and Ijaz in 2015 examined the physical characteristics of blood flow in a curved tube that was both stenosed and packed with nanoparticles. These results imply that the shear stress is exacerbated close to the outer curvature wall due to centrifugal force and that the curvature of the tube significantly affects the asymmetry of the flow (Hong, Yeom et al. 2017). The research presented in this study pertains to Navigating the effects of slide on turbulent pulsatile blood flow in a curved channel with nano-particles, considering stenosis and aneurysm (Zaman, Ali et al. 2018). The potential energy and momentum equations for nanoparticles are derived using curved coordinates. They examine the fluid-structure interaction (FSI) in a new study (Bukač, Čanić et al. 2019) that involves a stented stent in a complex coronary artery, pulsating blood flow, and the muscle contractions of the heart. (Zaman, Ali et al. 2019) looked into how nanoparticles affected the pulsatile blood flow in a curved overlapping stenosed channel. Research by Rashid, Ansar, and colleagues in 2020 examined how a curved channel's magnetic field affected the peristaltic flow of an incompressible Williamson fluid. The blood flow in a channel that has a curved shape resembling the letter "W" is pulsatile and obstructed due to stenosis. is studied to the impacts of entropy production, according to the work of Zaman, Mabood et al. (2021). Studying fluid flow and heat transfer in a curved tube with a time-varying stenosis using a two-phase blood flow model. (Kumawat, Sharma et al. 2021).

Following this, (Misra et al., 2008; Shabbir et al., 2022) hypothetically investigated blood flow with multiple stenosis. Furthermore, (Mandal 2005) used the Power law constitution equation to conduct a quantitative analysis of unstable unidirectional blood flow across stenosed arteries. The pressure gradient is a word that (Burton, 1966) first used. To further develop this notion, numerous researchers have used non-Newtonian models to simulate the pulsatile nature of the heartbeat. (Zaman & Khan, 2021) Researchers studied blood flow through a stenosed channel using a curved channel and non-Newtonian variables. Because of this, our literature review found that most research has focused on blood flow through unobstructed, stenosed arteries. Using several non-Newtonian fluid models, very few researchers have attempted to study blood flow in tortuous channels (Nadeem & Ijaz, 2016). A study was conducted by (Ram et al., 2023) that compares the migration of HIV, HBV, H1N1, and HCV through blood flow. While these studies did some work on stable blood flow, they didn't do much on unstable blood flow, which made it hard to explain artery disease.

The blood has an unusually thick consistency. Blood behaves abnormally when there are a lot of particles in the plasma. "Low shear" and "high shear" both lead to different kinds of surprises. When moving at high shear rates through arteries with bigger diameters, blood acts like a Newtonian fluid. The apparent viscosity of blood is measured by its viscosity. It decreases with decreasing blood channel diameter when measured with a capillary diameter of less than 300 m. This cannot be debated. It is well-known that viscosity and capillary radius are directly proportional. Lindqvist effect in Fahraeus. However, if the blood is pumped through tiny blood capillaries that are 20 µm or 100 µm in diameter, the blood's apparent viscosity increases, the container's diameter decreases, and the fluid shows non-Newtonian properties. This non-Newtonian feature is common in blood that flows via narrow blood arteries, such as veins. Because cells exist, this peculiar behaviour is induced. The assumption of a Newtonian fluid holds for blood when shear rates are large. It travels along a main road. Blood mimics the behaviour of Newton's fluid when subjected to tensile force, specifically shear forces greater than 100s-1. Shows properties that are not Newtonian. Knowing that blood functions similarly to a cell suspension is helpful. As a non-Newtonian fluid with a low shear rate, a tiny blood artery with a diameter of 0.020.1 mm experiences flow.

The role of blood's non-Newtonian activity in the perfused vascular bed was determined by analysing the pressure curve of an erythrocyte suspension containing 9–85% platelets in a 50–800 glass tube. The curves for each tube, independent of hematocrit, become linear with increasing flow rate and point to a "nodal point" on the negative flow axis. At loads greater than 20 dyne/cm, all of the previously obtained shear rates against wall shear stress curves were linear, but these curves have been improved using these data. All vascular layers have a shear stress higher than this, with the arterioles having a shear stress of 200 dyne/cm. It has been discovered that blood flow properties in perfusion vascular beds are essentially linear over the physiological working range, meaning that the degree of vascular breakdown largely determines the form of pressure and flow profiles in a conduit. Even though non-Newtonian blood behaviour has a significant impact on hemodynamics in cerebral vessels, most computer models still handle blood as though it were Newtonian. As part of their investigation into the influence The study investigates the impact of blood (non-Newtonian) properties on the circulation of blood in a simplified 90-degree branching model, (Frolov et al., 2018) compare Newtonian and non-Newtonian fluids as well as other flow rates between the main artery and its branches. A highly accurate representation of the change in blood viscosity is provided by the suggested local viscosity model. Where there are few returning motions, the velocity shifts are the biggest. Variable with flow rate, the typical variation is 17–22% at the systole apex and 27–60% at the diastole end. The non-Newtonian fluid model showed a viscosity 2.5 times greater after the breakpoint, and there were notable changes in the distribution of viscosity. The presence of such a viscous region significantly affects the size of the flow recirculation zone. Future studies of cerebral artery blood flow must accurately account for non-Newtonian blood behaviour, as these differences demonstrate.

The world is evolving, and cutting-edge nano-science is having a profound impact on healthcare. This study assertively showcases the impact of magnetohydrodynamics and hybrid nanoparticles on a micropolar fluid, which exhibits six distinct types of stenosis by (Ahmed & Nadeem, 2017) People are now able to get help for a wide range of illnesses because of the new nanotechnology that has revolutionised medical diagnosis and therapy. Due to the lack of pruning during surgery in developing countries, it is one of the most difficult and dangerous treatments for cancer, brain tumours, and lithotripsy. For quite some time, people have been using nanoparticles to make thermal transmission more efficient. The health sector is not the only one affected by nanotechnology. Polymer solutions, water, glycol, and blood are all examples of liquids that do not transmit heat well in comparison to solids. These fluids' thermal conductivity is enhanced by the addition of nanoparticles. The incorporation of nanoparticles with different shapes, densities, and orientations enhances heat transmission. According to (Choi & Eastman, 1995), this fluid was the first to be called a "nanofluid," and nanoparticles are widely used in biomedicine (Wagner et al., 2006). According to Ahmed and Nadeem's research (Ali et al., 2016), hybrid nanoparticles and MHD both have an impact on blood flow through narrowed arteries. They fail to take the problem of varying blood flow into account in their analysis. Stenosed with nanoparticles, Zaman studied abnormal blood flow (Zaman et al., 2018).

One of the most important systems in the human body is the cardiovascular system. The maintenance of internal homeostasis and the sustenance of life are two of its many roles. Keeping a healthy core temperature and how it relates to disease prevention. You can improve your chances of finding workable solutions by painting a realistic picture of your system. It's a normal occurrence that aids in early detection. (Berntsson et al., 2018). This has been the result of a lot of hard work. In their computational analysis of the effects of atherosclerotic circumstances on pulsatile blood flow, (Shabbir et al., 2022) take into account both heat and mass transport. This thing is designed to copy how blood moves through your veins and arteries. A straight cross-section of an arterial wall, notwithstanding the cardiovascular system's intrinsic curvature. The bending of blood vessels is similar to this. This is because different parts of the body are always moving. Thus, more precise computational models of blood flow should emerge from the ship's arc. The influence of nonlinear thermal radiation and viscous dissipation on ferrofluid flow and heat transfer through an infinitely porous spinning disc is demonstrated by (Sharma, 2022). presented a flow model that incorporates Brownian motion, viscosity changes, and thermophoresis effects.(Sharma et al., 2023).

Deformation of Herschel-Bulkley fluids, a type of non-Newtonian fluids, is induced by a limited stress known as yield stress. A theoretical investigation of Herschel-Bulkley has yielded a plethora of proposed solutions (Gudekote et al., 2018; Rajashekhar et al., 2018). With a local shear stress lower than the yield stress, these materials act as rigid bodies. The material undergoes non-linear stress-strain flow as a shear-thickening or a shear-thinning fluid after it reaches the yield point. Paints, meals, polymers, slurries, medications, polymer solutions, pulp from paper, and semi-solids are all examples of liquids that exhibit this behaviour. At even lower shear rates, the Herschel - Bulkley fluid model can be applied to extremely constricted arteries with large yield stressesInstability's impact on non - Newtonian blood flow through a stenosed vascular tube and aneurysm is demonstrated by (Shabbir et al., 2023). By comparing the blood flow in symmetrical and w-shaped stenotic areas of the arteries, (Abbas et al., 2020; Abbas et al., 2017) demonstrate one thing.

According to studies, it makes no difference whether the obstructed artery is straight or the blood possesses Newtonian characteristics; both scenarios result in the same blood flow problem. After reviewing the literature, we decided to conduct a study into how stenosed channels affect asymmetric blood flow when curvature and non-Newtonian factors are coupled. This research looks at the dynamics of blood flow through a constricted artery. Better treatments for vascular sickness in humans can be developed by medical professionals through research into this area. Here, we use Herschel-Bulkley fluid to evaluate the effects of non-Newtonian and curvature processes on unstable blood flow in curved-coordinate constrained channels. The purpose of dividing this work into sections was to give the most helpful analysis of each technique. To provide you with a comprehensive overview of each strategy, this paper is structured into sections.

Gradual constriction of the blood vessels, which is accompanied by the production of platelets. This condition is called atherosclerosis. Vascular constriction can occur as a result of growing fat deposition with time. This narrowing of blood vessels, called stenosis, stops the tissue from getting enough blood. This condition can cause stroke in some persons. A narrowing of the blood arteries, or stenosis, reduces blood flow. The initial investigator to examine blood flow in constricted arteries was (Young, 1968). The assumption of mild stenosis is crucial to his studies. We considered the theoretical and practical implications of flow in a diverging tube for the development of vascular disease, following the work of (Forrester & Young, 1970). Detailed numerical results for various Reynolds numbers (0-25) on shear stress, pressure, velocity, vortex distributions and streamlines are available by(Lee & Fung, 1970). (Chow & Soda, 1973) examined the aberrant flow caused by diseased arteries' anomalous border characteristics.

They postulated that blood would flow in a laminar fashion through a channel that was rough on the surface, with the roughness spreading at a rate far higher than the mean width of the channel. This flow would be incompressible, or isochoric. Their investigation, (Doffin & Chagneau, 1981) examined the flow over a spindle-shaped obstruction, assessing the constant flow using both theoretical and experimental approaches. The findings shed light on the potential flow conditions that can arise as a result of atherosclerosis in an artery. According to (Azuma & Fukushima, 1976), the finding of stenosis—the narrowing of blood vessels—may be an indication of cardiovascular illness. A numerical study of blood flow across small artery stenosis over time was carried out by(MacDonald, 1979). An experimental investigation of the pulsating blood flow across a model of artery stenosis, consisting of three separate virtual constricted walls, was carried out (Yongchareon & Young, 1979). To determine the axial blood flow velocity in an axisymmetric stenosis zone, (Morgan & Young, 1974) employed an integral momentum technique. They used a metal rod with diameters that varied in the axial direction to simulate oblique extension and axisymmetric stenosis. The mathematical model established by (Misra & Sahu, 1988) was used to assess the effects of a periodic acceleration field on blood flow in major arteries. For this calculation, we combine the flow equations with the formulas that describe the motion of the different walls of the vessels. Numerical calculations are used to determine the shear forces, acceleration, volume flow rate, and velocity profile of the fluid within an artery. Using Newtonian fluids, this study simulated hemorheology.

Blood exhibits several non-Newtonian behaviours, including thixotropy, viscoelasticity, and shear-thinning, as demonstrated by multiple experimental experiments. At low shear rates, the power-law fluid model showed the significance of non-Newtonian behaviour, according to the hypothetical results of (Perktold et al., 1989). This held true even though the shear rate was quite small. The model, however, disregards the behaviour that happens at very high shear rates. To help explain this discrepancy, several models can be employed, including the Sisko, Carreau, Cross, Eyring Powell, and others.

To ascertain their impacts, dimensional variables including stenosis length and stenosis severity were investigated. Researchers (Usha & Prema, 1999) investigated how acceleration was affected employing the model of particle-liquid suspension to describe pulsatile blood flow. Using Laplace and Henkel transformations, (El-Shahed, 2003) investigated the impact of Womersley blood flow on a stenotic porous channel on the acceleration of the human body. (Tu & Deville, 1996) investigated the effects of stenosis on blood flow using Galerkin's finite element approach. The two-dimensional blood flow through the narrowed artery is investigated (Mandal, 2005). He presented an alternative to Newtonian behaviour for the rheology of blood using a generic Power-law description. An important investigation of the haemorheology and biological conditions of blood flow in large vessels was conducted (Yilmaz & Gundogdu, 2008). A study by (Mekheimer and El Kot 2012) researched the effect of minor stenosis on blood flow, assuming that blood is a micropolar fluid with radial symmetry but axial non-symmetry. (Sankar & Lee 2009) developed the Womersley flow model to simulate non-Newtonian blood flow in a constricted artery. The flow assessment took blood rheology into account and was carried out using the perturbation approach in conjunction with the Herschel-Bulkley constative equation. Researchers (Ali et al., 2015) used the constitutive equation to investigate the effect of acceleration and magnetic fields on pulsing blood flow for flow through an overlapped, stenosed channel from the Carreau-Yasuda fluid model. (Zaman et al., 2016) the slip phenomenon and its effect on the time-varying movement of non-Newtonian blood through inclined overlapping constricted blood vessels were examined. The rheological behavior of the blood was represented using the power-law constitutive equation.(Roy et al., 2017) conducted a computational analysis of Carreau-Yasuda fluid flow in an artery that is 90% stenosed, showing that the patient's transient blood flow could get turbulent.

The variety in blood makes it challenging to develop a universal constitutive relationship between shear rate and stress to characterise its rheological properties. Several non-Newtonian models take rheological factors like viscoelasticity, shear-thinning and thixotropy into account in the hemodynamics literature. Since the other attributes do not significantly alter the velocity profile, shear-thinning is the only property that is crucial for blood flow models (Gijsen et al., 1999). They provide the most accurate forecasts of non-Newtonian fluid behaviour (Abbasian et al., 2020).

A power-law distribution is usually used to represent these fluids in models. It has been used to forecast the flow of the coronary arteries (Soulis et al., 2008), the thoracic aorta(Caballero & Laín, 2015; Iasiello et al., 2017), the carotid arteries (Moradicheghamahi et al., 2019), and the stenotic arteries (O'callaghan et al., 2006). On the other hand, not all non-Newtonian fluids' rheological properties can be represented by this model. Including a Power-law area, upper and lower Newtonian zones, and rheological data makes evaluation and application more challenging. Numerous studies utilised two asymptotic values for the dynamic viscosity in four-parameter models; one value was assigned to extremely high shear rates and the other to extremely low shear rates. Blood flow shear-thinning behaviour can be defined using simply the shear-rate tensor in generalised Newtonian models. Some examples of such models are those put forth by Carreau, Carreau-Yasuda, Cross, Cross-Simplified, Yeleswarapu, and Cross-

Modified in addition to others. As a result of insufficient data, four-parameter models are infamously hard to construct(Irgens, 2014).

The tangent hyperbolic model is useful for describing flow dynamics at high and moderate shear rates, despite its mathematical complexity. One advantage is that it is based on a more solid theoretical framework, such as a flow-based molecular model, rather than unstable empirical evidence. Compared to competing models, this non-Newtonian one is better. Because of its ability to anticipate the properties of shear-thinning, this particular model is particularly appropriate for ascertaining the rheological properties of beverages, meals, and even blood. It effectively simplifies the Newtonian behavior for both elevated and diminished shear stress. Readers interested in learning more about tangent hyperbolic fluid might consult references (Abbas et al., 2016; Jyothi et al., 2016; Nadeem & Ijaz, 2016).

Electrolytes with a positive charge attract positively charged particles, while electrolytes with a negative charge repel negatively charged ions. This phenomenon is called electro-osmotic movement, and it occurs when an electrolyte is exposed to an external field. The end, as a result, an electric double layer (EDL) is formed. When it comes to studying fluid dynamics using electrically charged particles, Woodson and Melcher were the trailblazers in the field of electrokinetics and electrodynamics (Melcher & Woodson, 1968). An examination of the many fluid transport mechanisms and their effects on the movement and behaviour of ionised particles is undertaken. These mechanisms include electrostatics, electro-osmosis, electrophoresis, etc. Researchers (Noreen et al., 2019) and Nooren et al. studied the effects of Joule heating and various zeta functions on the behaviour of MHD nano-fluid in a microchannel. A critical physiological process is inhibited by an increase in zeta potential, as seen here. This slowness is caused by the existence of impermeable EDL. The utilisation of a microchannel that allows for the regulation of fluid characteristics was studied by (Choudhari et al., 2022) in the investigation sought to generate electro-osmotic-modulated peristaltic flow in a non-Newtonian fluid by investigating the effect of nanoparticle size and electroosmotic forces on nanofluid flow in a narrowed and aneurysm-filled artery. (Abdelsalam et al., 2020). A more precise representation of viscosity was provided by the revised Buongiorno model, according to (Akram et al., 2022), who contrasted it with the Tiwari-Das model.

This is the result of many people's hard efforts. A computer simulation was conducted by (Shabbir et al., 2022) in an atherosclerotic scenario to determine the mass and heat transport in the pulsating blood.(Shabbir et al., 2023) shown that vascular inertia changes non-Newtonian blood flow in aneurysms and artery narrowing. By comparing blood flow in symmetrical and asymmetrical stenotic artery segments, (Abbas et al., 2017; Shabbir et al., 2022) draw some interesting conclusions. The fluid flow barrier is higher in smaller arteries compared to bigger ones, and the velocity profile is more linear in smaller arteries compared to larger ones with curves. Using stenosed, curved tubes, (Zaman et al., 2023) investigated the effects of many nanoparticles. Decreases in symmetry with increasing values of the curvature parameter were seen to affect the velocity profile. The impacts of heat transfer and body acceleration on magnetohydrodynamic (MHD) blood flow were investigated by (B. K. Sharma et al., 2022) using a curved artery. (Kumawat et al., 2021; B. Sharma et al., 2022) are two groups of researchers who have investigated the hemodynamic flow around a curved stenosis. Infected curved artery segments with pulsating nano-fluid: thermophoresis and Brownian motion effects investigated the loss and magnetohydrodynamic processes that lead to the generation of entropy in blood flow. The present study examines the fractional order dynamics of Casson tri-nanofluid flow via an angled artery with stenosis, as demonstrated by(Zaman & Ali, 2016)]. As far as the present study is concerned, (Shabbir et al., 2022)examine the Transferring mass and heat that occurs when a non-Newtonian fluid, like blood, flows through a narrowed section of an artery, such as a w-shaped one. The picture presented by (Fahim et al., 2022) depicts a pulsatile pressure gradient and non-isothermal tangent hyperbolic fluid flow within a stenosed blood artery.

Among the most common medical conditions affecting humans, arterial stenosis is primarily brought on by alterations in the mechanics of vascular fluids (Ku, 1997). It is crucial to be aware of all the factors that can affect blood flow because blood is a biological fluid. The hematocrit level is a crucial measure of blood quality since RBCs constitute a specific proportion of total blood (Medvedev & Fomin, 2011). The Fahraeus effect, which states that a decrease in arterial width results in a decrease in hematocrit levels, explains this link. Based on studies (Fahraeus & Lindqvist, 1931), erythrocytes migrate towards the centre of constricted arteries due to the Fahraeus effect, resulting in a plasma layer adjacent to the arterial wall that is depleted of cells. Flow in smaller arteries is characterised by two phases: a cell-free plasma layer along the arterial wall and a dense layer of red blood cells in the middle (Verma & Srivastava, 2014). Research on the effects of a single stenosis on blood flow through an artery has been extensive. (Manchi & Ponalagusamy, 2022) created a two-fluid model of blood flow through a constricting stenotic artery to study the two-phase blood flow behavior when these hemodynamical disturbances are present. A pair stress fluid is represented in the central part of this model, whereas a Newtonian fluid is represented by the plasma outside. If the diverging stenosis is not tapered, the wall shear stress is little; if it is tapered, the wall shear stress is large. Not only that but (Sankar, 2011) gave a mathematical description of blood flow in two phases and studied the function of a wall-bound, cell-depleted peripheral layer. Symptomatic and functional evaluation of sickle cell stenosis, both symmetric and axisymmetric. Models of two-phase blood flow via a stenosed artery that account for the additional effect of the magnetic field have been the subject of much research and development. An experimental investigation of the pulsating blood flow across a model of artery stenosis, consisting of three separate virtual constricted walls, was carried out (Yongchareon & Young, 1979). To determine the axial blood flow velocity in an axisymmetric stenosis zone, (Morgan & Young, 1974) employed an integral momentum technique. They used a metal rod with diameters that varied in the axial direction to simulate oblique extension and axisymmetric stenosis. The mathematical model established by (Misra & Sahu, 1988) was used to assess the effects of a periodic acceleration field on blood flow in major arteries. For this calculation, we combine the flow equations with the formulas that describe the motion of the different walls of the vessels. Numerical calculations are used to determine the shear forces, acceleration, volume flow rate, and velocity profile of the fluid within an artery. Using Newtonian fluids, this study simulated hemorheology.

To ascertain their impacts, dimensional variables including stenosis length and stenosis severity were investigated. To investigate how acceleration affects pulsatile blood flow, (Usha & Prema, 1999)employed the particle-liquid suspension model. A stenotic porous channel's response to Womersley blood flow was investigated by (El-Shahed, 2003)When applied to the acceleration of the human body, Laplace and Henkel's transformations provide... To model blood flow through a stenosis, (Tu & Deville, 1996) used Galerkin's finite element approach. (Mandal et al., 2007)analyses the two-dimensional blood flow through the narrowed artery. He presented an alternative to Newtonian behaviour for the rheology of blood using a generic Power-law description. On the haemorheology and biological conditions of blood flow in large vessels, (Yilmaz & Gundogdu, 2008) conducted a substantial study. Research on the effects of minor stenosis on blood flow characteristics was published by (Mekheimer & El Kot, 2012), assuming that blood is a micropolar fluid with radial symmetry but axial non-symmetry.

(Ponalagusamy & Tamil Selvi, 2015) investigated how the magnetic field affected the two-phase model of oscillatory blood flow with artery stenosis, modelling Newtonian fluids in the plasma and core areas. According to the study's authors, a stronger magnetic field causes the blood flow resistance in a stenosed artery to rise. With the assumption that the plasma region contains a Newtonian fluid and the core region a micropolar fluid, (Ponalagusamy & Priyadharshini, 2018) explored how a magnetic field may influence the flow of blood in two stages through a narrowing stenosed artery. Inside a theoretical framework, (Mirza et al., 2016) utilised a continuous approach to investigate the effects of blood flow in two phases, subjected to a transitory laminar electromagnetic-hydrodynamic field. The flow of blood in the core and plasma areas follows a Newtonian model. which (Tripathi & Sharma, 2018) analyzed while talking about how the two-phase model of blood flow through a horizontally stenosed artery is affected by heat and mass transfer.Blood is sometimes simplified to a homogeneous fluid to simplify the modelling of its complicated composition of plasma, proteins, cells, and other substances. The delicate balance of blood is maintained by many chemical interactions that aid in coagulation and dissolution. While chemical reactions were occurring, Coulson and (Hernandez, 1983)showed metabolic activities in their experimental study. Significant increases in plasma reactant concentrations following injection of some hormones, metabolites, and drugs were seen, which is an intriguing discovery. To study how blood flow affects thrombi growth, (Xu et al., 2009) built a theoretical model that considered the interaction between different blood components and chemical reactions. The interaction of chemically reactive magneto blood flow, heat transfer, and mass transport to viscosity was recently studied by (Sharma & Gaur, 2017) Including a Power-law area, upper and lower Newtonian zones, and rheological data makes evaluation and application more challenging. Numerous studies utilised two asymptotic values for the dynamic viscosity in four-parameter models; one value was assigned to extremely high shear rates and the other to extremely low shear rates. The shear-rate tensor is all that is needed to characterise the blood flow's shear-thinning behaviour in generalised Newtonian models(Irgens, 2014).

This is the result of many people's hard efforts. A computer simulation was conducted by (Shabbir et al., 2023) in an atherosclerotic scenario to determine the mass and heat transport in the pulsating blood. The vascular tube's inertia modifies the non-Newtonian blood flow in aneurysms and constricted blood vessels, according to (Abbas et al., 2017; Abbasian et al., 2020) compare blood flow in symmetrical and asymmetrical stenotic arterial segments. Research has demonstrated that smaller arteries exhibit a higher fluid flow barrier compared to bigger ones, as well as a more straight velocity profile compared to curved ones. (Zaman et al., 2023)used stenosed, curved tubes to study the effects of many nanoparticles. Decreases in symmetry with increasing values of the curvature parameter were seen to affect the velocity profile (Tripathi & Sharma, 2018) studied how a curved artery affected MHD blood flow about heat transfer and body acceleration. In two separate studies (B. Sharma et al., 2022) and (Kumawat et al., 2021) examined the hemodynamic flow around a curved stenosis. This study examines the heat and mass transfer that occurs when a non-Newtonian fluid, such as blood, flows through a stenotic arterial segment, as described by (Tu & Deville, 1996). B. Tripathi and B. K. Sharma have published the results of their two-part study on the chemical effects of radiation on pulsatile blood flow via a stenosed, narrowed artery(Tripathi & Sharma, 2018).

1.2 Basic definitions

1.2.1 Cardiovascular system

This system is made up of a heart and peripheral blood channels (arteries, capillaries and veins). Its primary task is to supply the oxygen, carbon dioxide and nutrients carried by the blood to and from several parts of the body. Additionally, it controls body temperature by transferring heat from the center to the periphery, where it can evaporate into the surrounding environment.

The cardiovascular system consists of two separate parts connected by the heart.

i) Systemtic circulation

ii) Pulmonary circulation

The systematic blood is circulated to every area of the body, with the exception of the lungs. The pulmonary circulation, which performs gas exchange, supplies the lungs. While the pulmonary circulation operates as a low pressure system, the systemic circulation operates as a high pressure system.

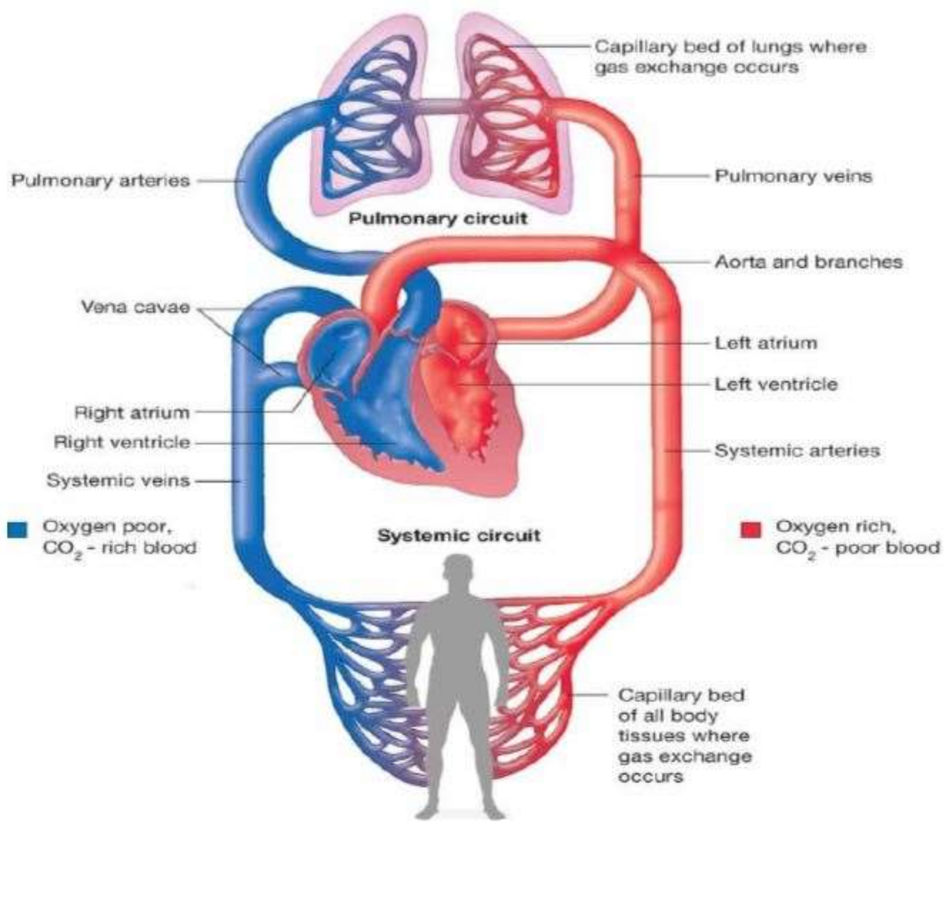

Figure. 1.1

1.2.2 Cardiac cycle

It is the description of volume, pressure and flow phenomenon in terms of times when the heart beats. It is composed of diastole, during which ventricles are filling with blood and the systole, during which blood is pumped out of the heart.

1.2.3 Arteries

Arteries are blood vessels that responsible for supplying the blood from heat to the entire body. They have thick elastic walls. These vessels' flexibility enables them to expand during cardiac systole and contract during diastole.

1.2.5 Capillaries

Capillaries are microscopic thin-walled blood vessels. They link the circulatory system's venous and arterial portions. They have thin permeable walls that allow the exchange of nutrients gases and waste materials.

1.2.6 Arterial Stenosis

The abnormal narrowing of blood vessels at several locations of the cardiovascular system due to the sedimentation of saturated fatty acid is identified as stenosis. The presence of stenosis in the blood vessel disturbs the normal flow of blood. If a stenosis is present in the heart artery, the patient may have symptoms of a heart attack. If the stenosis is present in the arteries leading towards the brain, the patient may have a danger of brain stroke.

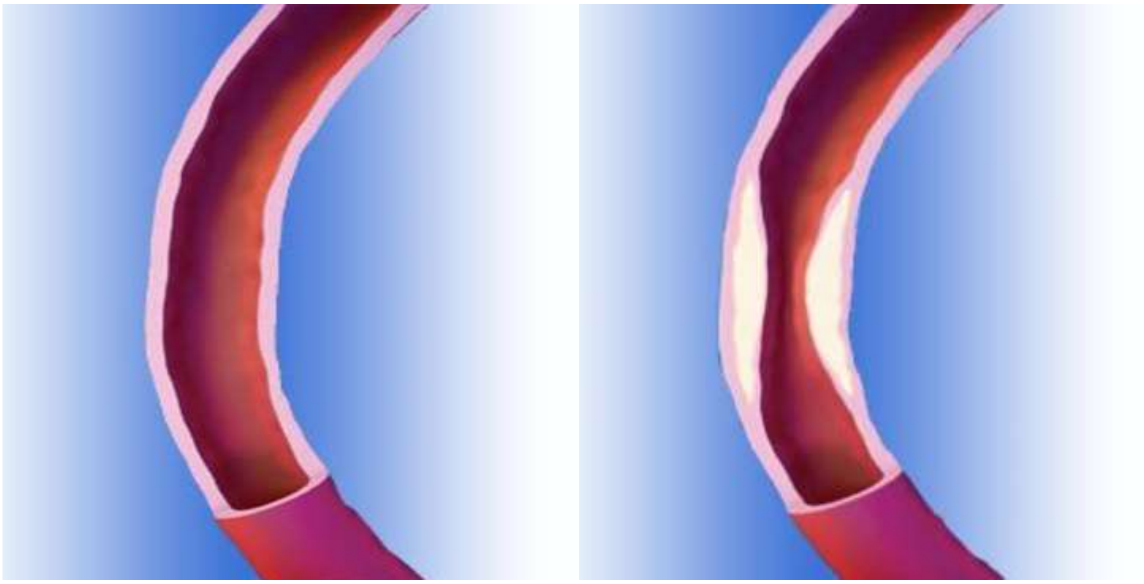

Figure. 1.2

1.2.4 Veins

Veins are the blood vessels that are responsible for collecting the blood from the entire body and returning it to the heart. They have thin walls. They have a semilunar valve to stop the blood flowing backwards.

1.2.7 Pulsatile flow

An unsteady flow due to periodic time dependency is referred to as a pulsatile flow.

1.3 Basic Equation in Curvilinear Coordinates

The Cartesian coordinates $\left(\hat{x},\ \hat{y},\ \hat{z}\right)$ of a point in space. Let $\left(\hat{v}_1,\ \hat{v}_2,\ \hat{v}_3\right)$ are a point of three scalar functions such that,

$$\left.\begin{aligned} \hat{v}_1 &= \hat{v}_1\left(\hat{x},\ \hat{y},\ \hat{z}\right), \\ \hat{v}_2 &= \hat{v}_2\left(\hat{x},\ \hat{y},\ \hat{z}\right), \\ \hat{v}_3 &= \hat{v}_3\left(\hat{x},\ \hat{y},\ \hat{z}\right), \end{aligned}\right\} \tag{1.1}$$

If the functions work well and their partial derivatives are continuous for all values $(\hat{x}, \hat{y}, \hat{z})$, including the Jacobian (J) of the transformation defined by,

$$J = \frac{\partial(\hat{v}_1, \hat{v}_2, \hat{v}_3)}{\partial(\hat{x}, \hat{y}, \hat{z})} = \begin{vmatrix} \frac{\partial \hat{v}_1}{\partial \hat{x}} & \frac{\partial \hat{v}_1}{\partial \hat{y}} & \frac{\partial \hat{v}_1}{\partial \hat{z}} \\ \frac{\partial \hat{v}_2}{\partial \hat{x}} & \frac{\partial \hat{v}_2}{\partial \hat{y}} & \frac{\partial \hat{v}_2}{\partial \hat{z}} \\ \frac{\partial \hat{v}_3}{\partial \hat{x}} & \frac{\partial \hat{v}_3}{\partial \hat{y}} & \frac{\partial \hat{v}_3}{\partial \hat{z}} \end{vmatrix}, \tag{1.2}$$

If the value does not disappear, then Equation (1.1) establishes a unique relationship between two things $(\hat{x}, \hat{y}, \hat{z})$ and $(\hat{v}_1, \hat{v}_2, \hat{v}_3)$.

In this case, the point P is also uniquely defined by the triads $(\hat{v}_1, \hat{v}_2, \hat{v}_3)$. We called $(\hat{v}_1, \hat{v}_2, \hat{v}_3)$ the curvilinear coordinates of the point P.
Let us consider the curvilinear orthogonal coordinates $\hat{w}_1, \hat{w}_2$ and $\hat{w}_3$ which can be calculated from the Cartesian coordinates $\hat{x}_1, \hat{x}_2$ and $\hat{x}_3$.

.

$$\hat{w}_1 = \hat{w}_1 \left(\hat{x}_1, \hat{x}_2, \hat{x}_3\right), \quad \hat{w}_2 = \hat{w}_2 \left(\hat{x}_1, \hat{x}_2, \hat{x}_3\right), \quad \hat{w}_3 = \hat{w}_3 \left(\hat{x}_1, \hat{x}_2, \hat{x}_3\right),$$

or in short

$$\hat{w}_i = \hat{w}_i\left(\hat{x}_i\right) . \tag{1.3}$$

We assume that (1.3) has a unique inverse

$$\hat{x}_i = \hat{x}_i\left(\hat{w}_j\right) .$$

If $\hat{w}_2$ and $\hat{w}_3$ are kept constant, the vector $\hat{x} = \hat{x}\left(\hat{w}_1\right)$ describes a curve in space which is the coordinate curve $\hat{w}_1\left(\partial\hat{x}/\partial\hat{w}_1\right)$ is the tangent vector to this curve. The corresponding unit vector in the direction of increasing $\hat{w}_1$ is

$$\hat{e}_1 = \frac{\partial\hat{x}/\partial\hat{w}_1}{\left|\partial\hat{x}/\partial\hat{w}_1\right|}. \tag{1.4}$$

Let $\left|\partial\hat{x}/\partial\hat{w}_1\right| = \hat{h}$, then

$$\frac{\partial\hat{x}}{\partial\hat{w}_1} = \hat{e}_1 \hat{h}_1, \tag{1.5}$$

and in the same way

$$\frac{\partial \hat{x}}{\partial \hat{w}_2} = \hat{e}_2\, \hat{h}_2, \tag{1.6}$$

$$\frac{\partial \hat{x}}{\partial \hat{w}_3} = \hat{e}_3\, \hat{h}_3, \tag{1.7}$$

with $\left|\partial \hat{x}/\partial \hat{w}_2\right| = \hat{h}_2$ and $\left|\partial \hat{x}/\partial \hat{w}_3\right| = \hat{h}_3$, where $\hat{h}_1$, $\hat{h}_2$ and $\hat{h}_3$ are called scale factors.

Because of $\hat{x} = \hat{x}\left(\hat{w}_j\right)$ it follow that

$$d\hat{x} = \frac{\partial \hat{x}}{\partial \hat{w}_1} d\hat{w}_1 + \frac{\partial \hat{x}}{\partial \hat{w}_2} d\hat{w}_2 + \frac{\partial \hat{x}}{\partial \hat{w}_3} d\hat{w}_3 = \hat{h}_1 d\hat{w}_1 \hat{e}_1 + \hat{h}_2 d\hat{w}_2 \hat{e}_2 + \hat{h}_3 d\hat{w}_3 \hat{e}_3. \tag{1.8}$$

If $\hat{v}_1$, $\hat{v}_2$ and $\hat{v}_3$ are the components of the vector $\boldsymbol{V}$ in the direction of increasing $\hat{w}_1$, $\hat{w}_2$ and $\hat{w}_3$ then $\nabla \cdot \boldsymbol{V}$, $\nabla \times \boldsymbol{V}$, ∇^2 and $\nabla^2 \varphi$ are given in curvilinear coordinates as

$$\nabla \cdot V = \frac{1}{\hat{h}_1 \hat{h}_2 \hat{h}_3} \left[\frac{\partial}{\partial \hat{w}_1} \left(\hat{h}_2 \hat{h}_3 \hat{v}_1 \right) + \frac{\partial}{\partial \hat{w}_2} \left(\hat{h}_3 \hat{h}_1 \hat{v}_2 \right) + \frac{\partial}{\partial \hat{w}_3} \left(\hat{h}_1 \hat{h}_2 \hat{v}_3 \right) \right], \tag{1.9}$$

$$\left.\begin{aligned}
\left(\nabla \times V\right)_1 &= \frac{1}{\hat{h}_2 \hat{h}_3} \left[\frac{\partial}{\partial \hat{w}_2} \left(\hat{h}_3 \hat{v}_3 \right) - \frac{\partial}{\partial \hat{w}_3} \left(\hat{h}_2 \hat{v}_2 \right) \right], \\
\left(\nabla \times V\right)_2 &= \frac{1}{\hat{h}_3 \hat{h}_1} \left[\frac{\partial}{\partial \hat{w}_3} \left(\hat{h}_1 \hat{v}_1 \right) - \frac{\partial}{\partial \hat{w}_1} \left(\hat{h}_3 \hat{v}_3 \right) \right], \\
\left(\nabla \times V\right)_3 &= \frac{1}{\hat{h}_1 \hat{h}_2} \left[\frac{\partial}{\partial \hat{w}_1} \left(\hat{h}_2 \hat{v}_2 \right) - \frac{\partial}{\partial \hat{w}_2} \left(\hat{h}_1 \hat{v}_1 \right) \right],
\end{aligned}\right\} \tag{1.10}$$

$$\nabla^2 = \frac{1}{\hat{h}_1 \hat{h}_2 \hat{h}_3} \left\{ \frac{\partial}{\partial \hat{w}_1} \left(\frac{\hat{h}_2 \hat{h}_3}{\hat{h}_1} \frac{\partial}{\partial \hat{w}_1} \right) + \frac{\partial}{\partial \hat{w}_2} \left(\frac{\hat{h}_3 \hat{h}_1}{\hat{h}_2} \frac{\partial}{\partial \hat{w}_2} \right) + \frac{\partial}{\partial \hat{w}_3} \left(\frac{\hat{h}_1 \hat{h}_2}{\hat{h}_3} \frac{\partial}{\partial \hat{w}_3} \right) \right\}, \tag{1.11}$$

$$\nabla \varphi = \frac{1}{\hat{h}_1} \frac{\partial \varphi}{\partial \hat{w}_1} + \frac{1}{\hat{h}_2} \frac{\partial \varphi}{\partial \hat{w}_2} + \frac{1}{\hat{h}_3} \frac{\partial \varphi}{\partial \hat{w}_3}. \tag{1.12}$$

1.3.1 Continuity equation

The mathematical principle of mass conservation for a fluid is expressed by the continuity equation.

$$\frac{\partial \rho}{\partial t} + \nabla \cdot \left(\rho V \right).$$

Using Eq. (1.9) we get

$$\frac{\partial \rho}{\partial t}+\frac{1}{\widehat{h}_1\widehat{h}_2\widehat{h}_3}\left[\frac{\partial}{\partial \widehat{w}_1}\left(\widehat{h}_2\widehat{h}_3\rho\widehat{v}_1\right)+\frac{\partial}{\partial \widehat{w}_2}\left(\widehat{h}_3\widehat{h}_1\rho\widehat{v}_2\right)+\frac{\partial}{\partial \widehat{w}_3}\left(\widehat{h}_1\widehat{h}_2\rho\widehat{v}_3\right)\right]=0. \tag{1.13}$$

where $\widehat{V}$ is the velocity and ρ is the mass density of the fluid. For incompressible fluid $\nabla.\left(\widehat{V}\right)=0.$

1.3.2 Momentum equation

The momentum equation is defined as

$$\rho\left[\frac{\partial \widehat{V}}{\partial t}-\widehat{V}\times\left(\nabla\times\widehat{V}\right)+\nabla\left(\frac{V^2}{2}\right)\right]=-\nabla\vec{p}+\nabla\cdot\widehat{\tau} \tag{1.14}$$

So using Eq. (10) components of $\widehat{V}\times\left(\nabla\times\widehat{V}\right)$ will be

$$\left[\widehat{V}\times\left(\nabla\times\widehat{V}\right)\right]_1=\frac{\widehat{v}_2}{\widehat{h}_1\widehat{h}_2}\left[\frac{\partial}{\partial \widehat{w}_1}\left(\widehat{h}_2\widehat{v}_2\right)-\frac{\partial}{\partial \widehat{w}_2}\left(\widehat{h}_1\widehat{v}_1\right)\right]-\frac{\widehat{v}_3}{\widehat{h}_3\widehat{h}_1}\left[\frac{\partial}{\partial \widehat{w}_3}\left(\widehat{h}_1\widehat{v}_1\right)-\frac{\partial}{\partial \widehat{w}_1}\left(\widehat{h}_3\widehat{v}_3\right)\right], \tag{1.15}$$

$$\left[\widehat{V}\times\left(\nabla\times\widehat{V}\right)\right]_2=\frac{\widehat{v}_3}{\widehat{h}_2\widehat{h}_3}\left[\frac{\partial}{\partial \widehat{w}_2}\left(\widehat{h}_3\widehat{v}_3\right)-\frac{\partial}{\partial \widehat{w}_3}\left(\widehat{h}_2\widehat{v}_2\right)\right]-\frac{\widehat{v}_1}{\widehat{h}_1\widehat{h}_2}\left[\frac{\partial}{\partial \widehat{w}_1}\left(\widehat{h}_2\widehat{v}_2\right)-\frac{\partial}{\partial \widehat{w}_2}\left(\widehat{h}_1\widehat{v}_1\right)\right], \tag{1.16}$$

$$\left[\widehat{V}\times\left(\nabla\times\widehat{V}\right)\right]_3=\frac{\widehat{v}_1}{\widehat{h}_3\widehat{h}_1}\left[\frac{\partial}{\partial \widehat{w}_3}\left(\widehat{h}_1\widehat{v}_1\right)-\frac{\partial}{\partial \widehat{w}_1}\left(\widehat{h}_3\widehat{v}_3\right)\right]-\frac{\widehat{v}_2}{\widehat{h}_2\widehat{h}_3}\left[\frac{\partial}{\partial \widehat{w}_2}\left(\widehat{h}_3\widehat{v}_3\right)-\frac{\partial}{\partial \widehat{w}_3}\left(\widehat{h}_2\widehat{v}_2\right)\right], \tag{1.17}$$

The components of the stress tensor's divergence are:

$$\begin{aligned}\left(\nabla\cdot\widehat{\tau}\right)_1&=\frac{1}{\widehat{h}_1\widehat{h}_2\widehat{h}_3}\left[\frac{\partial}{\partial \widehat{w}_1}\left(\widehat{h}_2\widehat{h}_3\widehat{\tau}_{11}\right)+\frac{\partial}{\partial \widehat{w}_2}\left(\widehat{h}_3\widehat{h}_1\widehat{\tau}_{21}\right)+\frac{\partial}{\partial \widehat{w}_3}\left(\widehat{h}_1\widehat{h}_2\widehat{\tau}_{31}\right)\right]\\&+\frac{\widehat{\tau}_{21}}{\widehat{h}_1\widehat{h}_2}\frac{\partial \widehat{h}_1}{\partial \widehat{w}_2}+\frac{\widehat{\tau}_{31}}{\widehat{h}_1\widehat{h}_3}\frac{\partial \widehat{h}_1}{\partial \widehat{w}_3}-\frac{\widehat{\tau}_{22}}{\widehat{h}_1\widehat{h}_2}\frac{\partial \widehat{h}_2}{\partial \widehat{w}_2}-\frac{\widehat{\tau}_{33}}{\widehat{h}_1\widehat{h}_3}\frac{\partial \widehat{h}_3}{\partial \widehat{w}_1},\end{aligned} \tag{1.18}$$

$$\begin{aligned}\left(\nabla\cdot\widehat{\tau}\right)_2&=\frac{1}{\widehat{h}_1\widehat{h}_2\widehat{h}_3}\left[\frac{\partial}{\partial \widehat{w}_1}\left(\widehat{h}_2\widehat{h}_3\widehat{\tau}_{12}\right)+\frac{\partial}{\partial \widehat{w}_2}\left(\widehat{h}_3\widehat{h}_1\widehat{\tau}_{22}\right)+\frac{\partial}{\partial \widehat{w}_3}\left(\widehat{h}_1\widehat{h}_2\widehat{\tau}_{32}\right)\right]\\&+\frac{\widehat{\tau}_{32}}{\widehat{h}_2\widehat{h}_3}\frac{\partial \widehat{h}_2}{\partial \widehat{w}_3}+\frac{\widehat{\tau}_{12}}{\widehat{h}_2\widehat{h}_1}\frac{\partial \widehat{h}_2}{\partial \widehat{w}_1}-\frac{\widehat{\tau}_{33}}{\widehat{h}_2\widehat{h}_3}\frac{\partial \widehat{h}_3}{\partial \widehat{w}_2}-\frac{\widehat{\tau}_{11}}{\widehat{h}_2\widehat{h}_1}\frac{\partial \widehat{h}_1}{\partial \widehat{w}_2},\end{aligned} \tag{1.19}$$

$$
\begin{aligned}
\left(\nabla\cdot\hat{\tau}\right)_3 &= \frac{1}{\hat{h}_1\hat{h}_2\hat{h}_3}\left[\frac{\partial}{\partial\hat{w}_1}\left(\hat{h}_2\hat{h}_3\hat{\tau}_{13}\right)+\frac{\partial}{\partial\hat{w}_2}\left(\hat{h}_3\hat{h}_1\hat{\tau}_{23}\right)+\frac{\partial}{\partial\hat{w}_3}\left(\hat{h}_1\hat{h}_2\hat{\tau}_{33}\right)\right]\\
&+\frac{\hat{\tau}_{13}}{\hat{h}_3\hat{h}_1}\frac{\partial\hat{h}_3}{\partial\hat{w}_1}+\frac{\hat{\tau}_{23}}{\hat{h}_3\hat{h}_2}\frac{\partial\hat{h}_3}{\partial\hat{w}_2}-\frac{\hat{\tau}_{11}}{\hat{h}_3\hat{h}_1}\frac{\partial\hat{h}_1}{\partial\hat{w}_3}-\frac{\hat{\tau}_{22}}{\hat{h}_3\hat{h}_2}\frac{\partial\hat{h}_2}{\partial\hat{w}_3},
\end{aligned}
\tag{1.20}
$$

The symbolic form of the Cauchy-Poisson law applies to the stress components.

$$
\hat{e}_{11}=\frac{1}{\hat{h}_1}\frac{\partial\hat{v}_1}{\partial\hat{w}_1}+\frac{\hat{v}_2}{\hat{h}_1\hat{h}_2}\frac{\partial\hat{h}_1}{\partial\hat{w}_2}+\frac{h\hat{v}_3}{\hat{h}_3\hat{h}_1}\frac{\partial\hat{h}_1}{\partial\hat{w}_3},\qquad
\hat{e}_{22}=\frac{1}{\hat{h}_2}\frac{\partial\hat{v}_2}{\partial\hat{w}_2}+\frac{\hat{v}_3}{\hat{h}_2\hat{h}_3}\frac{\partial\hat{h}_2}{\partial\hat{w}_3}+\frac{\hat{v}_1}{\hat{h}_1\hat{h}_2}\frac{\partial\hat{h}_2}{\partial\hat{w}_1},
$$

$$
\hat{e}_{33}=\frac{1}{\hat{h}_3}\frac{\partial\hat{v}_3}{\partial\hat{w}_3}+\frac{\hat{v}_1}{\hat{h}_3\hat{h}_1}\frac{\partial\hat{h}_3}{\partial\hat{w}_1}+\frac{\hat{v}_2}{\hat{h}_2\hat{h}_3}\frac{\partial\hat{h}_3}{\partial\hat{w}_2},\qquad
2\hat{e}_{32}=\frac{\hat{h}_3}{\hat{h}_2}\frac{\partial\left(\hat{v}_3/\hat{h}_3\right)}{\partial\hat{w}_2}+\frac{\hat{h}_2}{\hat{h}_3}\frac{\partial\left(\hat{v}_2/\hat{h}_2\right)}{\partial\hat{w}_3}=2\hat{e}_{23},
$$

$$
2\hat{e}_{13}=\frac{\hat{h}_1}{\hat{h}_3}\frac{\partial\left(\hat{v}_1/\hat{h}_1\right)}{\partial\hat{w}_3}+\frac{\hat{h}_3}{\hat{h}_1}\frac{\partial\left(\hat{v}_3/\hat{h}_3\right)}{\partial\hat{w}_1}=2\hat{e}_{31},\qquad
2\hat{e}_{21}=\frac{\hat{h}_2}{\hat{h}_1}\frac{\partial\left(\hat{v}_2/\hat{h}_2\right)}{\partial\hat{w}_1}+\frac{\hat{h}_1}{\hat{h}_2}\frac{\partial\left(\hat{v}_1/\hat{h}_1\right)}{\partial\hat{w}_2}=2\hat{e}_{12}.
$$

So momentum equation in components form is

$$
\begin{aligned}
&\rho\left[\frac{\partial\hat{v}_1}{\partial t}-\frac{\hat{v}_2}{\hat{h}_1\hat{h}_2}\left\{\frac{\partial}{\partial\hat{w}_1}\left(\hat{h}_2\hat{v}_2\right)-\frac{\partial}{\partial\hat{w}_2}\left(\hat{h}_1\hat{v}_1\right)\right\}+\frac{\hat{v}_3}{\hat{h}_3\hat{h}_1}\left\{\frac{\partial}{\partial\hat{w}_3}\left(\hat{h}_1\hat{v}_1\right)-\frac{\partial}{\partial\hat{w}_1}\left(\hat{h}_3\hat{v}_3\right)\right\}+\frac{1}{2}\frac{\partial\left(\hat{v}_1^2+\hat{v}_2^2+\hat{v}_3^2\right)}{\partial\hat{w}_1}\right]=\\
&-\frac{1}{\hat{h}_1}\frac{\partial\hat{p}}{\partial\hat{w}_1}+\frac{1}{\hat{h}_1\hat{h}_2\hat{h}_3}\left[\frac{\partial}{\partial\hat{w}_1}\left(\hat{h}_2\hat{h}_3\hat{\tau}_{11}\right)+\frac{\partial}{\partial\hat{w}_2}\left(\hat{h}_3\hat{h}_1\hat{\tau}_{21}\right)+\frac{\partial}{\partial\hat{w}_3}\left(\hat{h}_1\hat{h}_2\hat{\tau}_{31}\right)\right]\\
&+\frac{\hat{\tau}_{21}}{\hat{h}_1\hat{h}_2}\frac{\partial\hat{h}_1}{\partial\hat{w}_2}+\frac{\hat{\tau}_{31}}{\hat{h}_1\hat{h}_3}\frac{\partial\hat{h}_1}{\partial\hat{w}_3}-\frac{\hat{\tau}_{22}}{\hat{h}_1\hat{h}_2}\frac{\partial\hat{h}_2}{\partial\hat{w}_2}-\frac{\hat{\tau}_{33}}{\hat{h}_1\hat{h}_3}\frac{\partial\hat{h}_3}{\partial\hat{w}_1},
\end{aligned}
\tag{1.21}
$$

$$
\begin{aligned}
&\rho\left[\frac{\partial\hat{v}_2}{\partial t}-\frac{\hat{v}_3}{\hat{h}_2\hat{h}_3}\left\{\frac{\partial}{\partial\hat{w}_2}\left(\hat{h}_3\hat{v}_3\right)-\frac{\partial}{\partial\hat{w}_3}\left(\hat{h}_2\hat{v}_2\right)\right\}+\frac{\hat{v}_1}{\hat{h}_1\hat{h}_2}\left\{\frac{\partial}{\partial\hat{w}_1}\left(\hat{h}_2\hat{v}_2\right)-\frac{\partial}{\partial\hat{w}_2}\left(\hat{h}_1\hat{v}_1\right)\right\}+\frac{1}{2}\frac{\partial\left(\hat{v}_1^2+\hat{v}_2^2+\hat{v}_3^2\right)}{\partial\hat{w}_2}\right]=\\
&-\frac{1}{\hat{h}_2}\frac{\partial\hat{p}}{\partial\hat{w}_2}+\frac{1}{\hat{h}_1\hat{h}_2\hat{h}_3}\left[\frac{\partial}{\partial\hat{w}_1}\left(\hat{h}_2\hat{h}_3\hat{\tau}_{12}\right)+\frac{\partial}{\partial\hat{w}_2}\left(\hat{h}_3\hat{h}_1\hat{\tau}_{22}\right)+\frac{\partial}{\partial\hat{w}_3}\left(\hat{h}_1\hat{h}_2\hat{\tau}_{32}\right)\right]\\
&+\frac{\hat{\tau}_{32}}{\hat{h}_2\hat{h}_3}\frac{\partial\hat{h}_2}{\partial\hat{w}_3}+\frac{\hat{\tau}_{12}}{\hat{h}_2\hat{h}_1}\frac{\partial\hat{h}_2}{\partial q_1}-\frac{\hat{\tau}_{33}}{\hat{h}_2\hat{h}_3}\frac{\partial\hat{h}_3}{\partial\hat{w}_2}-\frac{\hat{\tau}_{11}}{\hat{h}_2\hat{h}_1}\frac{\partial\hat{h}_1}{\partial\hat{w}_2},
\end{aligned}
\tag{1.22}
$$

$$\rho\left[\frac{\partial \widehat{v}_3}{\partial t}-\frac{\widehat{v}_1}{\widehat{h}_3\widehat{h}_1}\left\{\frac{\partial}{\partial \widehat{w}_3}\left(\widehat{h}_1\widehat{v}_1\right)-\frac{\partial}{\partial \widehat{w}_1}\left(\widehat{h}_3\widehat{v}_3\right)\right\}+\frac{\widehat{v}_2}{\widehat{h}_2\widehat{h}_3}\left\{\frac{\partial}{\partial \widehat{w}_2}\left(\widehat{h}_3\widehat{v}_3\right)-\frac{\partial}{\partial \widehat{w}_3}\left(\widehat{h}_2\widehat{v}_2\right)\right\}+\frac{1}{2}\frac{\partial\left(\widehat{v}_1^2+\widehat{v}_2^2+\widehat{v}_3^2\right)}{\partial \widehat{w}_3}\right]=$$
$$-\frac{1}{\widehat{h}_3}\frac{\partial \widehat{p}}{\partial \widehat{w}_3}+\frac{1}{\widehat{h}_1\widehat{h}_2\widehat{h}_3}\left[\frac{\partial}{\partial \widehat{w}_1}\left(\widehat{h}_2\widehat{h}_3\widehat{\tau}_{13}\right)+\frac{\partial}{\partial \widehat{w}_2}\left(\widehat{h}_3\widehat{h}_1\widehat{\tau}_{23}\right)+\frac{\partial}{\partial \widehat{w}_3}\left(\widehat{h}_1\widehat{h}_2\widehat{\tau}_{33}\right)\right]$$
$$+\frac{\widehat{\tau}_{13}}{\widehat{h}_3\widehat{h}_1}\frac{\partial \widehat{h}_3}{\partial \widehat{w}_1}+\frac{\widehat{\tau}_{23}}{\widehat{h}_3\widehat{h}_2}\frac{\partial \widehat{h}_3}{\partial \widehat{w}_2}-\frac{\widehat{\tau}_{11}}{\widehat{h}_3\widehat{h}_1}\frac{\partial \widehat{h}_1}{\partial \widehat{w}_3}-\frac{\widehat{\tau}_{22}}{\widehat{h}_3\widehat{h}_2}\frac{\partial \widehat{h}_2}{\partial \widehat{w}_3},$$
(1.23)

1.3.3 Energy equation

Coordinates of the Energy equation are defined as

$$\rho c_p\left[\frac{\partial T}{\partial t}+\left(\widehat{V}\cdot\nabla\right)T\right]=k\nabla^2T+\tau\cdot\widehat{L}. \tag{1.24}$$

Using Eqs. (1.11) and (1.12), we get

$$\rho c_p\left[\frac{\partial T}{\partial t}+\frac{\widehat{v}_1}{\widehat{h}_1}\frac{\partial T}{\partial \widehat{w}_1}+\frac{\widehat{v}_2}{\widehat{h}_2}\frac{\partial T}{\partial \widehat{w}_2}+\frac{\widehat{v}_3}{\widehat{h}_3}\frac{\partial T}{\partial \widehat{w}_3}\right]=\frac{k}{\widehat{h}_1\widehat{h}_2\widehat{h}_3}\left\{\frac{\partial}{\partial \widehat{w}_1}\left(\frac{\widehat{h}_2\widehat{h}_3}{\widehat{h}_1}\frac{\partial T}{\partial \widehat{w}_1}\right)+\frac{\partial}{\partial \widehat{w}_2}\left(\frac{\widehat{h}_3\widehat{h}_1}{\widehat{h}_2}\frac{\partial T}{\partial \widehat{w}_2}\right)+\frac{\partial}{\partial \widehat{w}_3}\left(\frac{\widehat{h}_1\widehat{h}_2}{\widehat{h}_3}\frac{\partial T}{\partial \widehat{w}_3}\right)\right\}$$
$$+\eta\left[2\left(\widehat{e}_{11}^2+\widehat{e}_{22}^2+\widehat{e}_{33}^2\right)+\widehat{e}_{23}^2+\widehat{e}_{13}^2+\widehat{e}_{12}^2\right],$$
(1.25)

Where k is the thermal conductivity.

1.3.4 Concentration equation

Concentration equation in coordinates is defined as

$$\frac{\partial T}{\partial t}+\left(\widehat{V}\cdot\nabla\right)C=D\nabla^2C, \tag{1.26}$$

Using Eqs. (1.11) and (1.12), we get

$$\frac{\partial C}{\partial t}+\frac{\widehat{v}_1}{\widehat{h}_1}\frac{\partial C}{\partial \widehat{w}_1}+\frac{\widehat{v}_2}{\widehat{h}_2}\frac{\partial C}{\partial \widehat{w}_2}+\frac{\widehat{v}_3}{\widehat{h}_3}\frac{\partial C}{\partial \widehat{w}_3}=\frac{D}{\widehat{h}_1\widehat{h}_2\widehat{h}_3}\left\{\frac{\partial}{\partial \widehat{w}_1}\left(\frac{\widehat{h}_2\widehat{h}_3}{\widehat{h}_1}\frac{\partial C}{\partial \widehat{w}_1}\right)+\frac{\partial}{\partial \widehat{w}_2}\left(\frac{\widehat{h}_3\widehat{h}_1}{\widehat{h}_2}\frac{\partial C}{\partial \widehat{w}_2}\right)+\frac{\partial}{\partial \widehat{w}_3}\left(\frac{\widehat{h}_1\widehat{h}_2}{\widehat{h}_3}\frac{\partial C}{\partial \widehat{w}_3}\right)\right\},$$
(1.27)

where C is the concentration and D is the diffusion of the fluid.

1.4 Mathematical models of blood flow

1.4.1 Newtonian fluid

The rate of strain, stress and relationship for Newtonian fluid is

$$\mathbf{T} = -p\mathbf{I} + 2\mu\mathbf{A_1} \tag{1.28}$$

where p , $\mathbf{I}$, μ and $\mathbf{A_1}, p, \mathbf{I}$ and μ are first Rivilin Erickson tensor, pressure, identity tensor, and dynamic viscosity respectively. And

$$\mathbf{A_1} = grad(\mathbf{V}) + (grad(\mathbf{V}))^t \tag{1.29}$$

1.4.2 Power law fluid model

The constitutive equation for the power law fluid model is:

$$\mathbf{T} = -p\mathbf{I} + \mathbf{S} \tag{1.30}$$

where extra stress tensor is $\mathbf{S}$, such that

$$\mathbf{S} = \mu\dot{\gamma}^{n-1}\mathbf{A_1} \tag{1.31}$$

in which power law index is n and

$$\dot{\gamma} = \sqrt{\frac{1}{2}trace(\mathbf{A_1}^{\mathbf{2}})} \tag{1.32}$$

where $n<1$ and $n>1$ corresponds to pseudoplastic power law model and dilatant fluid power law fluid model and if $n=1$ this reduces to Newtonian fluid model.

1.4.3 Tangent Hyperbolic fluid model

The extra stress tensor of Tangent hyperbolic fluid model is

$$\boldsymbol{S} = \left\{\mu_\infty + \left(\mu_0 - \mu_\infty\right)\tanh\left(\Gamma\,|\overset{*}{\gamma}|^n\right)\right\}, \tag{1.33}$$

1.4.4 Herschel-Bulkley fluid model

The mathematical model for Herschel-Bulkley fluid is

$$\mathbf{S} = \left(\mu \dot{\gamma}^{n-1} + \frac{\tau_y}{\dot{\gamma}} \right) \mathbf{A_1} \tag{1.34}$$

where τ is represents the yield stress.

$\boldsymbol{\tau} = \boldsymbol{S} - p\boldsymbol{I}$,

1.4.5 Buongiorno's model

Buongiono's model is a highly accurate mathematical model that predicts the thermal conductivity of nanofluids, in which nanoparticles are suspended inside a base fluid. The model considers the impact of Brownian motion, nanoparticle size, and the volume fraction of the nanofluid. Introduced in 2006, this model is based on the concept of effective thermal conductivity, which considers how nanoparticles affect the thermal conductivity of a fluid. The model assumes that the nanoparticles are uniformly distributed in the fluid and confidently predicts that the thermal conductivity of the nanofluid will be significantly greater than that of the base fluid alone.

1.4.6 Tiwari-Das's model

Tiwari-Das's model is a theoretical model for using the effective medium approximation to forecast the boiling point of nanofluids (EMA). This model considers the effects of nanoparticle size, concentration, and shape on the thermal conductivity of the nanofluid. Tiwari-Das's model, introduced in 2009, is a modification of Buongiorno's model and considers the non-uniform distribution of nanoparticles in the fluid. This model predicts that the thermal conductivity of the nanofluid will depend on the size and concentration of the nanoparticles, as well as the fluid velocity and temperature.

1.5 Solution methods

Non-Newtonian blood flow modelling results in complex non-linear partial differential equations. Solving these equations is a challenge due to strong nonlinearity, but analytical and numerical techniques are available. Numerical methods are preferred due to the complexity of the equations.

1.5.1 Finite difference method

The oldest and simplest way of solving differential equations is by using finite difference methods. This technique involves solving for the derivatives of the given equation. by using finite differences. The idea of using finite differences for numerical analysis was first introduced in the early 1950s. The advancement of this method was driven by the rise of the computer era, which provided the appropriate tools to deal with the complexity of problems in technology and science. The differential equation's derivatives are swapped out for the appropriate finite differences in the finite difference approach. Consequently, It is possible to simplify the differential equation by reducing it to an algebraic system. When it comes to handling non-linear partial differential equations, central difference approximations are used to replace the space derivatives of the partial differential equation, whereas forward difference approximations are used to replace the time derivatives. Consider the differential equation

Hoffman's book details different numerical schemes for different classes of PDEs. According to the book theme mentioned, the most appropriate method for solving parabolic PDEs is an explicit finite difference scheme. In this scheme, time variables are applied forward diffs and spatial components are applied central diffs. The book also provides stability conditions that depend on the step size of the defined variables. For example, the size of the spatiotemporal variable is chosen $\Delta x = 0.025, \Delta t = 0.0001$ so that the stability condition is finally met. Hoffman's work defines the forward/central partial derivative's algebraic formulation.

$$\frac{\partial W}{\partial r} \cong \frac{W_{i+1}^{k} - W_{i-1}^{k}}{2\Delta r} = W_{r,} \tag{1.35}$$

$$\frac{\partial^2 W}{\partial r^2} \cong \frac{W_{i+1}^{k} - 2W_{i}^{k} + W_{i-1}^{k}}{\left(\Delta r\right)^2} = W_{rr,} \tag{1.36}$$

and

$$\frac{\partial W}{\partial t} \cong \frac{W_{i}^{k+1} - W_{i}^{k}}{\Delta t}. \tag{1.37}$$

Chapter 2

Impact of Brownian Motion and Thermophoresis on Pulsating Nanofluid in a Curved Atherosclerotic Artery Segment

In this chapter nano-fluid flow that is unstable due to both non-Newtonian and curvature effects. Thermophoresis and the effects of Brownian motion are assessed statistically on the pulsing flow of a nano-fluid (blood) via a curved artery with stenosis and post-stenotic dilatation in its interior. The 2-dimensional curvilinear coordinate system is mathematically incorporated into the basic recommended physical system. The rheology of the fluid is satisfactorily represented by the Hershel-Bulkley model. Using the mild stenosis assumption and simplifying the concentration of mass, energy, and momentum that are highly linked. It is possible to discretize and solve the non-dimensionalized governing equations related to the boundary condition using explicit finite differences techniques. There are graphs that demonstrate how altering relevant geometric and rheological parameters affects important flow parameters including temperature, velocity, and mass concentration.

2.1 Flow Equation

The blood's characteristic equation considers incompressible laminar flow. Furthermore, it is assumed that the geometry of the cross-section is that of a radially curved channel. A curvilinear coordinate system has been developed as part of the process of developing curved stenosed channels. The curved stenosed channel has a mathematical equation.

$$R(z)=\begin{cases}\left(\tau' z+e_0\right)\left(1-\frac{64}{10}\eta\left(\frac{11}{32}l_0^3\left(z-d\right)-\frac{47}{48}l_0^2\left(z-d\right)^2+l_0\left(z-d\right)^3-\frac{1}{3}\left(z-d\right)^4\right)\right), & d\le z\le d+\frac{3}{2}l_0,\\ \left(\tau' z+e_0\right), & otherwise\end{cases},$$

$$Outer\ wall,$$

$$-R(z)=\begin{cases}\left(\tau' z-e_0\right)\left(1-\frac{64}{10}\eta\left(\frac{11}{32}l_0^3\left(z-d\right)-\frac{47}{48}l_0^2\left(z-d\right)^2+l_0\left(z-d\right)^3-\frac{1}{3}\left(z-d\right)^4\right)\right), & d\le z\le d+\frac{3}{2}l_0,\\ \left(\tau' z-e_0\right), & otherwise\end{cases},$$

$$Inner\ wall. \tag{2.1}$$

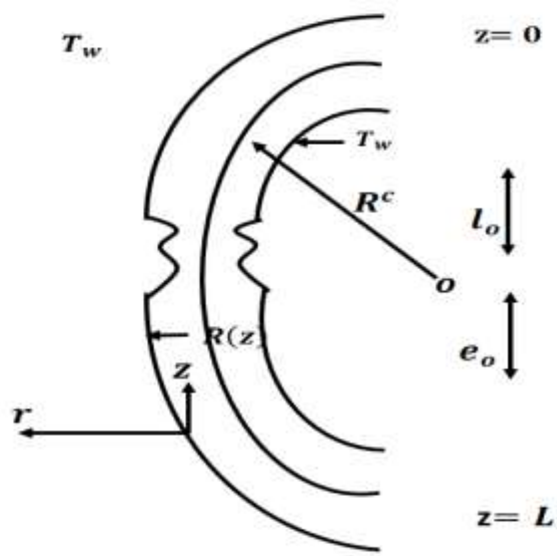

Figure 2.1

The study of the mechanics of blood flow in arteries is a major aspect of vascular research since it has a significant influence on healthThe geometry depicted in (Fig. 2.1), R^c shows that denotes the radius on the bent channel. The curved stenosed channel's mathematical equation is expressed as where, $R(z)$ s the radius of the curved channel segment within the stenotic area. In the above equations, e_0 stands in for the non-tapered channel's radius., l_0 represents the stenotic region length, T_w represent the wall temperature, r is radial coordinate, z axial coordinate and the non-stenotic region length is d . The parameter η is constant defined as:

$$\eta = \frac{4\delta^*}{a{l_0}^4}, \tag{2.2}$$

in this, δ^* displays the stenotic zone's essential height appearing in two locations i.e.,

$$z = d + \frac{8l_0}{25}, \text{ and } z = d + \frac{61l_0}{50}. \tag{2.3}$$

The governing equation of the flow field is defined as:

$$\begin{aligned} \bar{V} &= U(t,r,z),0,W(t,r,z), \\ T^* &= T^*(t,r,z), \\ C^1 &= C^1(t,r,z). \end{aligned} \tag{2.4}$$

In Eq. (2.4), U and W Both stand for the tangential and vertical components of the total velocity, T^* is temperature component and C^1 is nanoparitcles concentration component. Equations for continuity, momentum, energy absorption, and mass absorption are

$$\frac{\partial}{\partial r}\left(r+R^c\right)U + R^c\frac{\partial W}{\partial z} = 0, \tag{2.5}$$

$$\rho\left(\frac{\partial U}{\partial t} + U\frac{\partial U}{\partial r} + \frac{R^c}{r+R^c}W\frac{\partial U}{\partial z} - \frac{U^2}{r+R^c}\right) = -\frac{\partial p}{\partial r} + \frac{1}{\left(r+R^c\right)^2}\frac{\partial}{\partial r}\left(\left(r+R^c\right)S^{rr}\right) + \frac{R^c}{r+R^c}\frac{\partial S^{rz}}{\partial z} - \frac{S^{zz}}{r+R^c}, \tag{2.6}$$

$$\rho\left(\frac{\partial W}{\partial t} + U\frac{\partial W}{\partial r} + \frac{R^c}{r+R^c}W\frac{\partial W}{\partial z} + \frac{UW}{r+R^c}\right) = -\left(\frac{R^c}{r+R^c}\right)\frac{\partial p}{\partial z} + \frac{1}{\left(r+R^c\right)^2}\frac{\partial}{\partial r}\left(\left(r+R^c\right)S^{rz}\right) + \frac{R^c}{r+R^c}\frac{\partial S^{zz}}{\partial z} + \rho g\alpha_T\left(T^* - T_w\right) + \rho g\alpha_{C^1}\left(C^1 - C_1\right), \tag{2.7}$$

$$\left(\rho c_p\right)_f\left(\frac{\partial T^*}{\partial t} + U\frac{\partial T^*}{\partial r} + \frac{R^c}{r+R^c}W\frac{\partial T^*}{\partial z}\right) = k_f\left(\frac{\partial^2 T^*}{\partial r^2} + \frac{1}{r+R^c}\frac{\partial T^*}{\partial r} + \left(\frac{R^c}{r+R^c}\right)^2\frac{\partial^2 T^*}{\partial z^2}\right) + \left(\rho c\right)_p\left[\left(D_\beta\left(\frac{\partial C^1}{\partial r}\frac{\partial T^*}{\partial r} + \left(\frac{R^c}{r+R^c}\right)^2\frac{\partial C^1}{\partial z}\frac{\partial T^*}{\partial z}\right) + \frac{D_{T^*}}{T_w - T_1}\left(\left(\frac{\partial T^*}{\partial r}\right)^2 + \left(\frac{R^c}{r+R^c}\right)^2\left(\frac{\partial T^*}{\partial z}\right)^2\right)\right)\right], \tag{2.8}$$

$$\frac{\partial C^1}{\partial t}+U\frac{\partial C^1}{\partial r}+W\frac{\partial C^1}{\partial z}=D_\beta\left(\frac{\partial^2 C^1}{\partial r^2}+\frac{1}{r+R^c}\frac{\partial C^1}{\partial r}+\left(\frac{R^c}{r+R^c}\right)^2\frac{\partial^2 C^1}{\partial z^2}\right)$$
$$+\frac{D_{T^*}}{T_w-T_1}\left(\frac{\partial^2 T^*}{\partial r^2}+\frac{1}{r+R^c}\frac{\partial T^*}{\partial r}+\left(\frac{R^c}{r+R^c}\right)^2\frac{\partial^2 T^*}{\partial z^2}\right). \tag{2.9}$$

The term S^{rr}, S^{rz} *and* S^{zz} are the extra stress tensor component which is seeming in Eqs. (2.6) and (2.7). The relation of the Herschel-Bulkley model is

$$S=\left(\mu\Pi^{n-1}+\frac{\tau_y}{\Pi}\right)\boldsymbol{A}^1. \tag{2.10}$$

In (2.10), μ is the consistency index, n is the power law index, τ_y is the yield stress and A^1 is the Rivlin-Ericksen tensor defined by:

$$\boldsymbol{A}^1=\nabla\boldsymbol{V}+\nabla\boldsymbol{V}^T. \tag{2.11}$$

Where the first Rivlin-Ericksen tensor of the second invariant (Π) is defined as:

$$\Pi=\sqrt{\frac{1}{2}tra\left(A^{1^2}\right)}. \tag{2.12}$$

The constitutive relation (2.10) for the case of curved channel yields is shown in Eq (2.4).

$$S^{rr}=2\left(\mu\Pi^{n-1}+\frac{\tau_y}{\Pi}\right)\left(\frac{\partial U}{\partial r}\right), \tag{2.13}$$

$$S^{zz}=2\left(\mu\Pi^{n-1}+\frac{\tau_y}{\Pi}\right)\left(\frac{R^c}{r+R^c}\frac{\partial W}{\partial z}+\frac{U}{r+R^c}\right), \tag{2.14}$$

$$S^{rz}=\left(\mu\Pi^{n-1}+\frac{\tau_y}{\Pi}\right)\left(\frac{\partial W}{\partial r}+\frac{R^c}{r+R^c}\frac{\partial U}{\partial z}-\frac{W}{r+R^c}\right), \tag{2.15}$$

$$\Pi=\left\|\left[\frac{1}{2}\left(\left(2\frac{\partial U}{\partial r}\right)^2+2\left(\frac{\partial W}{\partial r}+\frac{R^c}{r+R^c}\frac{\partial U}{\partial z}-\frac{W}{r+R^c}\right)^2+\left(\frac{R^c}{r+R^c}\frac{\partial W}{\partial z}+\frac{U}{r+R^c}\right)^2\right)\right]\right\|. \tag{2.16}$$

Introducing the dimensionless variables

By using the following variables Eqs. (2.5)-(2.9) are made dimensionless from:

$$\bar{r}=\frac{r}{e_0},\quad \bar{W}=\frac{W}{U_0},\quad \bar{U}=\frac{l_0 U}{\delta^* U_0},\quad \bar{t}=\frac{U_0}{e_0}t,\quad \bar{z}=\frac{z}{l_0},\quad R_c=\frac{R^c}{e_0},\quad \bar{p}=\frac{e_0^2 p}{U_0 l_0 \mu_0},\quad \theta=\frac{T^*-T_w}{T_1-T_w},$$

$$P_r=\frac{\left(c_p\right)_f \mu_f}{k_f},\ Gr_T=\frac{\rho g \alpha_T e_0^2}{U_0\mu_0}\left(T_1-T_w\right),\quad Br=\frac{\rho g e_0^2}{U_0\mu_0}\alpha_C C_1,\ Le=\frac{\mu_0}{\rho D_\beta},\ N_t=\frac{\tau D_{T^*}}{k_f},$$

$$\mathrm{Re}=\frac{\rho_f U_0 e_0}{\mu_0},\ \ \bar{S}^{rz}=\frac{e_0}{U_0\mu_0}S^{rz},\ \bar{S}^{rr}=\frac{l_0}{U_0\mu_0}S^{rr},\quad \bar{S}^{zz}=\frac{l_0}{U_0\mu_0}S^{zz},\ \sigma=\frac{C^1-C_1}{C_1},N_b=\frac{\tau D_\beta C_1}{k_f}. \tag{2.17}$$

In the above definitions, $\bar{W}$ is axial velocity, $\bar{r}$ is radial coordinate, $\bar{z}$ axial directional co-ordinate, $\bar{t}$ is time, $\bar{R}$ is the radius, $\bar{p}$ is the pressure, Br the Brinkman number, Re is the Reynolds number, Gr is the local thermal Grashof number, Pr is the Prandtl number, U_0 is the average velocity of the blood and T_w represent the wall temperature.

After removing the bars the Simplified Eqs. (2.5)-(2.9) are:

$$\delta\left(\frac{\partial}{\partial r}\left(r+R_c\right)U\right)+R_c\frac{\partial W}{\partial z}=0, \tag{2.18}$$

$$\mathrm{Re}\,\delta\varepsilon^2\left(\frac{\partial U}{\partial t}+\delta\varepsilon U\frac{\partial U}{\partial r}+\varepsilon\frac{R_c}{r+R_c}W\frac{\partial U}{\partial z}-\frac{\varepsilon}{\delta}\frac{U^2}{r+R_c}\right)=-\frac{\partial p}{\partial r}+\varepsilon^2\left(\frac{1}{\left(r+R_c\right)^2}\frac{\partial}{\partial r}\left(\left(r+R_c\right)S^{rr}\right)\right)$$
$$+\varepsilon^2\left(\frac{R_c}{r+R_c}\right)\frac{\partial S^{rz}}{\partial z}-\frac{\varepsilon^2 S^{zz}}{r+R_c}, \tag{2.19}$$

$$\mathrm{Re}\frac{\partial W}{\partial t}+\mathrm{Re}\left(\delta\varepsilon\frac{\partial W}{\partial r}+\varepsilon\frac{R_c}{r+R_c}W\frac{\partial W}{\partial z}+\delta\varepsilon\frac{UW}{r+R^c}\right)=-\left(\frac{R_c}{r+R_c}\right)\frac{\partial p}{\partial z}+\frac{1}{\left(r+R_c\right)^2}\frac{\partial}{\partial r}\left(\left(r+R_c\right)^2 S^{rz}\right)$$
$$+\varepsilon^2\left(\frac{R_c}{r+R_c}\right)\frac{\partial S^{zz}}{\partial z}+Gr_T\theta+Br\sigma, \tag{2.20}$$

$$\Pr\mathrm{Re}\left(\frac{\partial\theta}{\partial t}+\delta\varepsilon\frac{\partial\theta}{\partial r}+\varepsilon\frac{R_c}{r+R_c}W\frac{\partial\theta}{\partial z}\right)=\frac{\partial^2\theta}{\partial r^2}+\frac{1}{r+R_c}\frac{\partial\theta}{\partial r}+\varepsilon^2\left(\frac{R_c}{r+R_c}\right)^2\frac{\partial^2\theta}{\partial z^2}$$
$$+N_b\left(\frac{\partial\sigma}{\partial r}\frac{\partial\theta}{\partial r}+\varepsilon^2\left(\frac{R_c}{r+R_c}\right)^2\frac{\partial\sigma}{\partial z}\frac{\partial\theta}{\partial z}\right)+N_t\left(\left(\frac{\partial\theta}{\partial r}\right)^2+\varepsilon^2\left(\frac{R_c}{r+R_c}\right)^2\left(\frac{\partial\theta}{\partial z}\right)^2\right), \tag{2.21}$$

$$\operatorname{Re} Le\left(\frac{\partial \sigma}{\partial t}+\delta\varepsilon\frac{\partial \sigma}{\partial r}+\varepsilon W\frac{\partial \sigma}{\partial z}\right)=\frac{\partial^2 \sigma}{\partial r^2}+\frac{1}{r+R_c}\frac{\partial \sigma}{\partial r}+\varepsilon^2\left(\frac{R_c}{r+R_c}\right)^2\frac{\partial^2 \sigma}{\partial z^2}$$
$$+\frac{N_t}{N_b}\left(\frac{\partial^2 \theta}{\partial r^2}+\frac{1}{r+R_c}\frac{\partial \theta}{\partial r}+\varepsilon^2\left(\frac{R_c}{r+R_c}\right)^2\frac{\partial^2 \theta}{\partial z^2}\right). \tag{2.22}$$

Two assumptions to which we subsequently subject the mild stenotic suppositions: $\varepsilon\left(=\frac{e_0}{l_0}\right)=O(1)$ and $\delta\left(=\frac{\delta^*}{e_0}\right)\ll 1$ i.e. The first need is that the stenotic area and the channel's radius have lengths that are similar.. The second condition depends on height of the track length being less than the radius of channel. Equation (2.11) to (2.13) is reduced as follows:

$$\frac{\partial p}{\partial r}=0, \tag{2.23}$$

$$\operatorname{Re}\frac{\partial W}{\partial t}=-\left(\frac{R_c}{r+R_c}\right)\frac{\partial p}{\partial z}+Gr_T\theta+Br\sigma$$
$$+\frac{1}{(r+R_c)^2}\frac{\partial}{\partial r}\left((r+R_c)^2\left(\mu\left(\frac{\partial W}{\partial r}-\frac{W}{r+R^c}\right)^{n-1}+\tau\left(\frac{\partial W}{\partial r}-\frac{W}{r+R^c}\right)^{-\frac{1}{2}}\right)\left(\frac{\partial W}{\partial r}-\frac{W}{r+R^c}\right)\right), \tag{2.24}$$

$$\Pr\operatorname{Re}\frac{\partial \theta}{\partial t}=\frac{\partial^2 \theta}{\partial r^2}+\frac{1}{r+R_c}\frac{\partial \theta}{\partial r}+N_b\left(\frac{\partial \sigma}{\partial r}\frac{\partial \theta}{\partial r}\right)+N_t\left(\frac{\partial \theta}{\partial r}\right)^2, \tag{2.25}$$

$$\operatorname{Re} Le\frac{\partial \sigma}{\partial t}=\frac{\partial^2 \sigma}{\partial r^2}+\frac{1}{r+R_c}\frac{\partial \sigma}{\partial r}+\frac{N_t}{N_b}\left(\frac{\partial^2 \theta}{\partial r^2}+\frac{1}{r+R_c}\frac{\partial \theta}{\partial r}\right). \tag{2.26}$$

Introduced the equation of Pulsatile Pressure gradient:

$$-\frac{\partial p}{\partial z}=A_0+A_1\cos\left(2\pi\omega_p t\right),\qquad t>0. \tag{2.27}$$

In Eq. (2.27), A_0 designates the mean pressure gradient and A_1 represent the amplitude of the pulsatile component. By using Eq. (2.9) in Eq. (2.18) we get:

$$-\frac{\partial p}{\partial z}=B_1\left(1+c\cos\left(c_1 t\right)\right), \tag{2.28}$$

Where

$$c_1 = \frac{2\pi\omega_p e_0}{U_0}, \quad c = \frac{A_1}{A_0}, \quad B_1 = \frac{A_0 e_0^2}{\mu_0 U_0}. \tag{2.29}$$

Using the term $-\partial p / \partial z$ in Eq. (2.24)

$$\mathrm{Re}\frac{\partial W}{\partial t} = \left(\frac{R_c}{r+R_c}\right) B_1\left(1 + c\cos\left(c_1 t\right)\right) + Gr_T\theta + Br\sigma$$
$$+\frac{1}{\left(r+R_c\right)^2}\frac{\partial}{\partial r}\left(\left(r+R_c\right)^2\left(\mu\left(\frac{\partial W}{\partial r} - \frac{W}{r+R^c}\right)^{n-1} + \tau\left(\frac{\partial W}{\partial r} - \frac{W}{r+R^c}\right)^{-\frac{1}{2}}\right)\left(\frac{\partial W}{\partial r} - \frac{W}{r+R^c}\right)\right), \tag{2.30}$$

Eqs. (2.25)-(2.26) and (2.30) are subjected to the following boundary and initial condition:

$$W\left(t,r\right)\Big|_{r=R} = 0, \quad W\left(t,r\right)\Big|_{r=-R} = 0, \quad W\left(0,r\right) = 0.0, \tag{2.31}$$

$$\sigma\left(t,r\right)\Big|_{r=R} = 0, \quad \sigma\left(t,r\right)\Big|_{r=-R} = 0, \quad \sigma\left(0,r\right) = 0.0, \tag{2.32}$$

$$\theta\left(t,r\right)\Big|_{r=R} = 1, \quad \theta\left(t,r\right)\Big|_{r=-R} = 1, \quad \theta\left(0,r\right) = 0.0, \tag{2.33}$$

The formula for volumetric flow rate $\left(Q\right)$, resistance impedance $\left(\Lambda\right)$ and wall shear stress $\left(\tau_S\right)$ in the new variable becomes:

$$Q = \int_{-R}^{R} W dr, \tag{2.34}$$

$$\tau_S = \left(\mu\left(\frac{\partial W}{\partial r} - \frac{W}{r+R^c}\right)^{n-1} + \tau\left(\frac{\partial W}{\partial r} - \frac{W}{r+R^c}\right)^{-\frac{1}{2}}\right)\left(\frac{\partial W}{\partial r} - \frac{W}{r+R^c}\right)_{r=R}, \tag{2.35}$$

$$\Lambda = \frac{\left(\frac{\partial p}{\partial z}\right)}{Q}. \tag{2.36}$$

The dimensionalized geometry equation for the arterial segment can be easily defined as follows:

$$R\left(z\right) = \left(1+\tau z\right)\left[1 - \frac{64}{10}\eta_1\left(\frac{11}{32}\left(z-\sigma\right) - \frac{47}{48}\left(z-\sigma\right)^2 + \left(z-\sigma\right)^3 - \frac{1}{3}\left(z-\sigma\right)^4\right)\right],$$

$$\sigma \le z \le \sigma + \frac{3}{2}, \ \ Outer\ wall,$$

$$-R(z)=(-1+\tau z)\left[1+\frac{64}{10}\eta_1\left(\frac{11}{32}(z-\sigma)-\frac{47}{48}(z-\sigma)^2+(z-\sigma)^3-\frac{1}{3}(z-\sigma)^4\right)\right],\tag{2.37}$$

$$\sigma \le z \le \sigma+\frac{3}{2},\ \textit{Inner wall},$$

Where $\eta_1=4\delta,\ \delta=\dfrac{\delta^*}{e_0},\ \sigma=\dfrac{d}{l_0},\ \tau=\dfrac{\tau' l_0}{e_0}.$

2.2 Solution Methodlogy

In the numerical approach, we use the explicit finite difference technique.

Using the above algebraic transformation in Eqs. (2.17) and (2.21):

$$W_i^{k+1}=W_i^k+\left(\frac{R_c}{r+R_c}\right)\frac{\Delta t}{\mathrm{Re}}B_1\left(1+c\cos(c_1 t)\right)+Gr_T\theta_i^k+Br\sigma_i^k$$
$$+\frac{1}{(r+R_c)^2}\frac{\partial}{\partial r}\left((r+R_c)^2\left(\mu\left(W_r-\frac{W_i^k}{r+R^c}\right)^{n-1}+\tau\left(W_r-\frac{W_i^k}{r+R^c}\right)^{-\frac{1}{2}}\right)\left(W_r-\frac{W_i^k}{r+R^c}\right)\right),\tag{2.38}$$

$$\theta_i^{k+1}=\theta_i^k+\frac{\Delta t}{\mathrm{Re}\,\mathrm{Pr}}\left\{\left(\theta_{rr}+\frac{1}{r+R_c}\theta_r\right)+N_b\theta_r\sigma_r+N_t\left(\theta_r\right)^2\right\},\tag{2.39}$$

$$\sigma_i^{j+1}=\sigma_i^j+\frac{\Delta t}{\mathrm{Re}\,Le}\left\{\left(\sigma_{rr}+\frac{1}{r+R_c}\sigma_r\right)+\frac{N_t}{N_b}\left(\theta_{rr}+\frac{1}{r+R_c}\theta_r\right)\right\}.\tag{2.40}$$

The numerical boundary as well as the initial condition is defined as:

$$\begin{aligned}
&W_i^1=0=\theta_i^1\ ,\ \sigma_i^1=0 && at\ t=0,\\
&W_1^k=\theta_1^k=1\ ,\ \sigma_i^1=0 && at\ r=-R(x),\\
&W_{N+1}^k=\theta_{N+1}^k=1\ ,\ \sigma_i^1=0 && at\ r=R(x).
\end{aligned}\tag{2.41}$$

2.3 Discussion of Results

The subsequent sections meticulously scrutinize the acquired numerical results. Velocity graphs are employed to assess the impact of varying factors of interest. The partial differential equation is resolved by selecting several preordained values (PDE) $\Pr = 9,\ B_1 = 1.41,$

$\mathrm{Re} = 1,\ x = 0.9.$ Moreover, it is illustrated that the aforementioned data showcases a strong correlation with conditions within the actual bloodstream, serving as a tangible reflection of reality. Viscous and inertial forces exhibit comparable magnitudes in the low Reynolds number approximation, where Re is defined as a unit, and rheological currents in microscopic capillaries align with the norm. Within the body's circulatory system, both heat and nanoparticles disseminate at identical rates due to diffusivity being the determining factor and the Lewis number serving as a gauge of the heat/species ratio (quantity of nanoparticles).

Velocity curves are computed at multiple points across the cross-section of the artery and at various exits. Speed profiles at different locations are depicted as the curvature parameter $\left(R_c\right)$ varies, as illustrated in Figure (2.2). Indicates the speed at which the curvature parameter's value is increasing. The level of $\left(R_c\right)$ is growing Fig. (2.2). The effect of temperature is illustrated in Fig. (2.3), where we can see that as the temperature increases, the graph of velocity decreases. The impact of shear/thickening factors may be seen in the graph below Fig. (2.4). The amount of the shear thickening effect is increased by increasing the value of (n). As the Brownian motion parameter $\left(N_b\right)$, is increased, the behaviour of velocity decreases as seen in Fig. (2.5). The graph of thermophoresis parameter $\left(N_t\right)$ is shown in Fig. (2.6), by increasing $\left(N_{t's}\right)$ amplitude the velocity profile is also increasing

Temperature plots for various Lewis number $\left(Le\right)$ values, thermophoresis parameter $\left(N_t\right)$, and curvature $\left(R_c\right)$.Figure (2.7) depicts the parameter $\left(R_c\right)$ with the transition from $\left(Le\right)$ to $\left(N_t\right)$, the temperature distribution changed little. Fig. (2.8) and Fig. (2.9) show a small shift in temperature distribution. Fig. (2.9) shows how curvature $\left(R_c\right)$ effects are transformed to a temperature distribution profile.

Fig. (2.10) show Lewis number (Le) and Fig. (2.11) shows thermophoresis $\left(N_t\right)$. An inverse trend has been noted, with researchers attributing it to the increased volatility of these components. The concentration profile is enhanced by increasing $N_{t's}$ amplitude, whereas increasing $Le's$ size has the opposite effect. Also fluctuations in the concentration profile as a function of Fig. (2.12) shows the graph of Brownian motion $\left(N_b\right)$ and Fig. (2.13) shows the effects of curvature $\left(R_c\right)$. As the Brownian motion parameter$\left(N_b\right)$, is increased, the behavior seen in Fig. (2.12). Due to the fact that an increase in $\left(N_b\right)$ causes a greater degree of random motion among the suspended nanoparticles, resulting in a lower concentration in the flow system, nanofluids behave more like two-phase liquids in nature. The concentration profiles inherit the curvature effect, as shown in Fig. (2.1). This graph illustrates the solute's journey along the curved channel. The surgeon may find this analysis useful when administering drugs to a patient during surgery.

Figure (2.14) depicts the fluctuation of the wall shear stress over time for a given set of parameters $\left(R_c\right)$, (n), $\left(N_t\right)$, and $\left(N_b\right)$. Each parameter's transformed wall shear profile is named for easy comparison. Because of this, the effects of freely adjustable parameters can be studied. Each alternative layout is evaluated in relation to the gold standard, which is a simple line drawing. As the values of $\left(R_c\right)$, (n), and $\left(N_t\right)$ increased, the profile model showed that stress on the wall rose as a result of when inappropriate behaviour was revealed for $\left(N_b\right)$. For a new set of inputs, Figure (2.15) displays the computed rate of change through time. Analyze the impact of different throughput parameters by comparing the patterns shown in Fig. (2.15). To round out the proposal scenario, a standard curve is computed, and the remainder of the profiles are built using altered versions of a given set of parameters. Simulation of the premeditatedly computed arrangement where a larger flow is achieved by increasing $\left(R_c\right)$ or $\left(N_t\right)$. Increasing the values of $\left(N_b\right)$ and n have the opposite consequences. Streams it is evident from the scale profiles that blood rheology displays a solid blood pattern when the shear value thickness parameter is increased. What this means is that n will be utilised as a parameter to control the rheology of human blood. The resulting impedance is displayed in Fig. (2.16).The mathematical expression for impedance is given by Eq. (2.36), and it is proportional to the flow rate in the opposite direction. As can be seen in Figure (2.16), the impedance profiles are carried over from this formulation.

2.4 Concluding Remarks

This chapter explores the potential impact of curvature on non-Newtonian blood flow. The phenomenon of unstable nanofluid (blood) flow through curved channels under non-Newtonian conditions remains unexplored. Therefore, this study represents a novel contribution to the existing literature. The Herschel-Bulkley fluid model is employed to predict the non-Newtonian behavior of blood in narrow arteries. The primary conclusions drawn from the present investigation are as follows:

- The curvature of the channel exerts a notable influence on the rheological properties of the blood; nevertheless, these effects can be mitigated by adjusting the tuning parameter. (n).
- The variation in Lewis number exerts a substantial influence on the size of the concentration(Le).
- Increasing the value of (n) enhances the magnitude of the shear thickening effect.
- In flow systems with lower concentrations, nanofluids exhibit behavior more akin to that of two-phase liquids in nature.
- Simulation of the intentionally calculated configuration results in a greater flow rate achieved by increasing $\left(R_c\right)$ or $\left(N_t\right)$.
- The effects of the curved channel parameter are more pronounced in the middle section of the artery.

- When a stenosed channel straightens, the shape of the trapping bolus in the upper and lower areas undergoes a change. This design illustrates the axisymmetric flow in this manner.

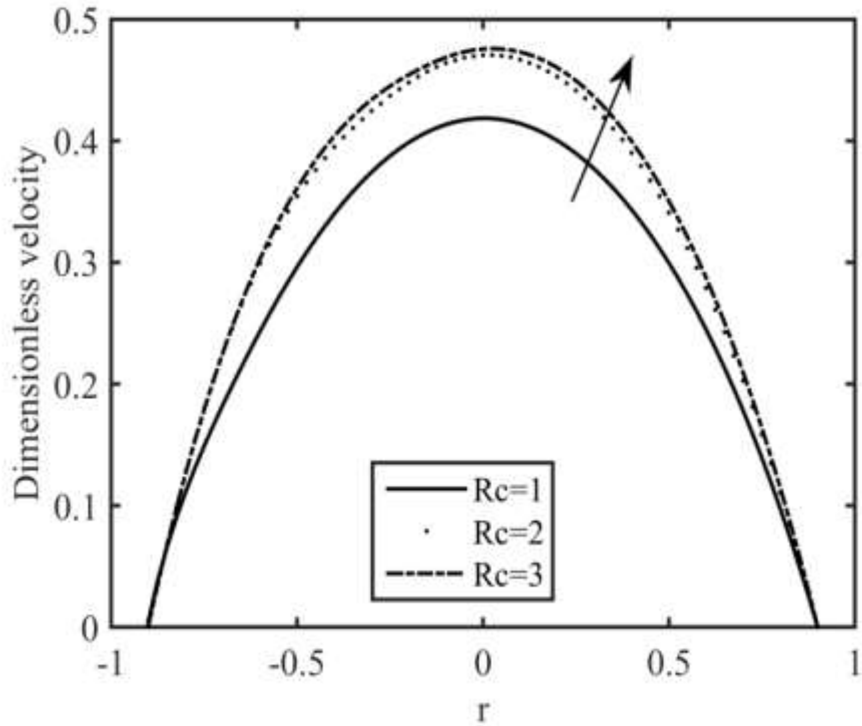

Figure 2.2

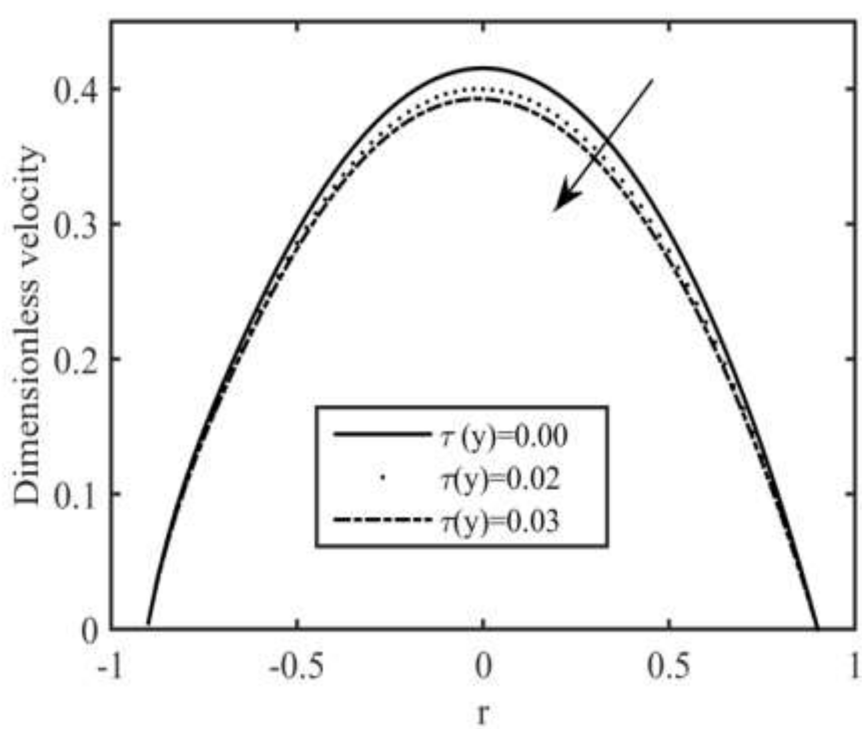

Figure 2.3

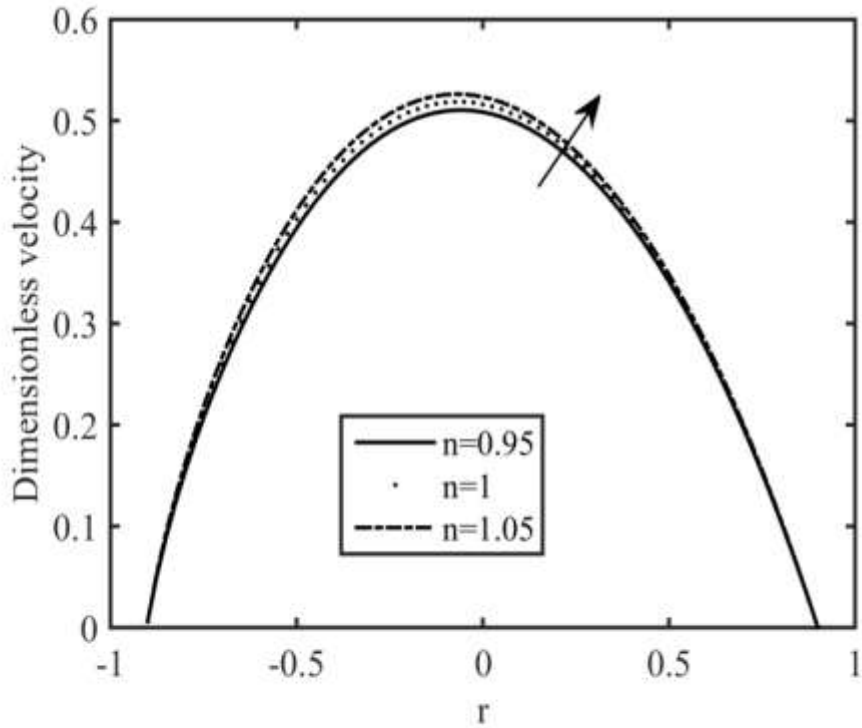

Figure 2.4

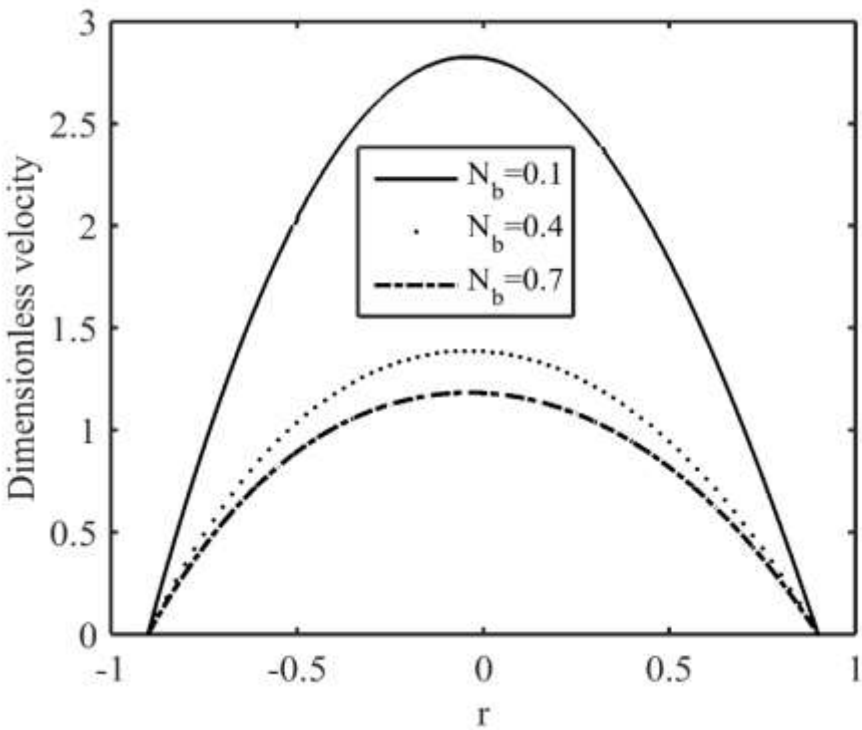

Figure 2.5

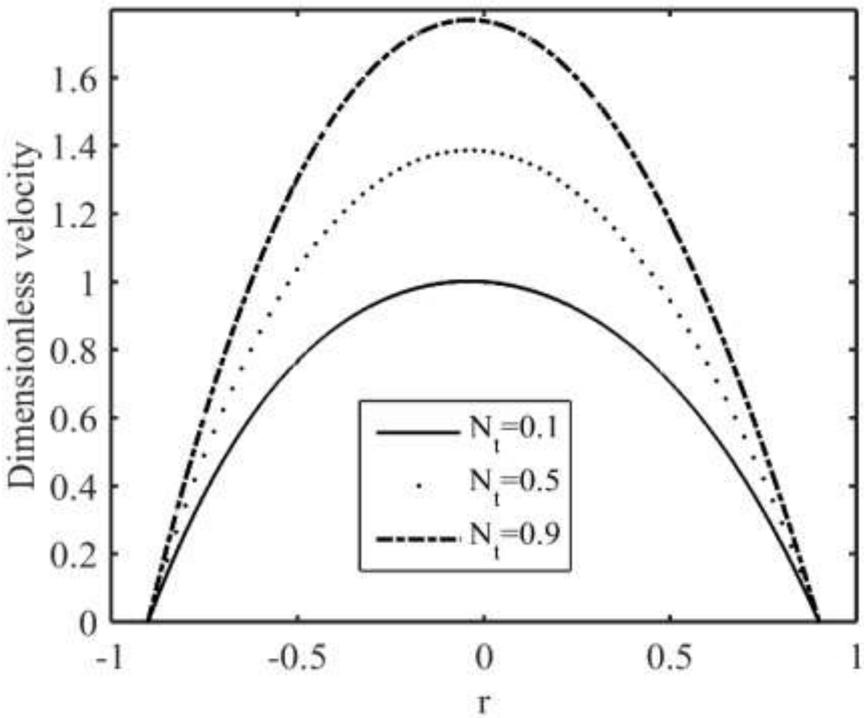

Figure 2.6

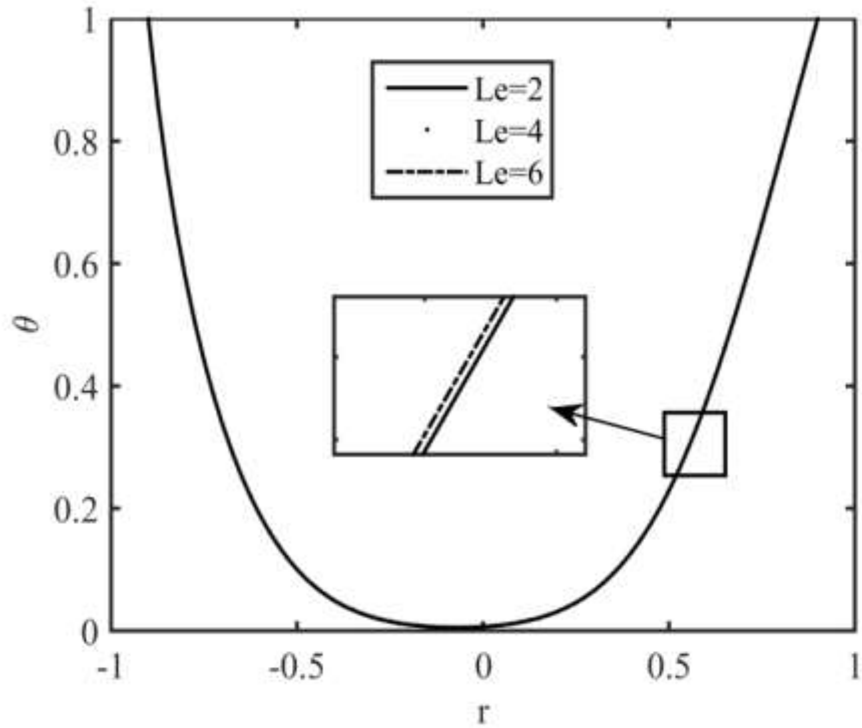

Figure 2.7

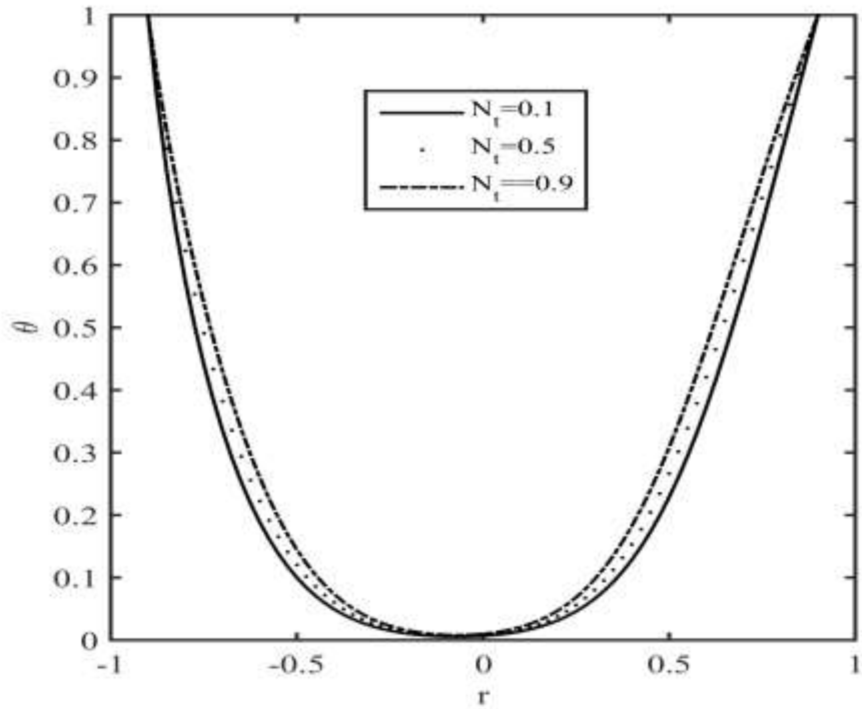

Figure 2.8

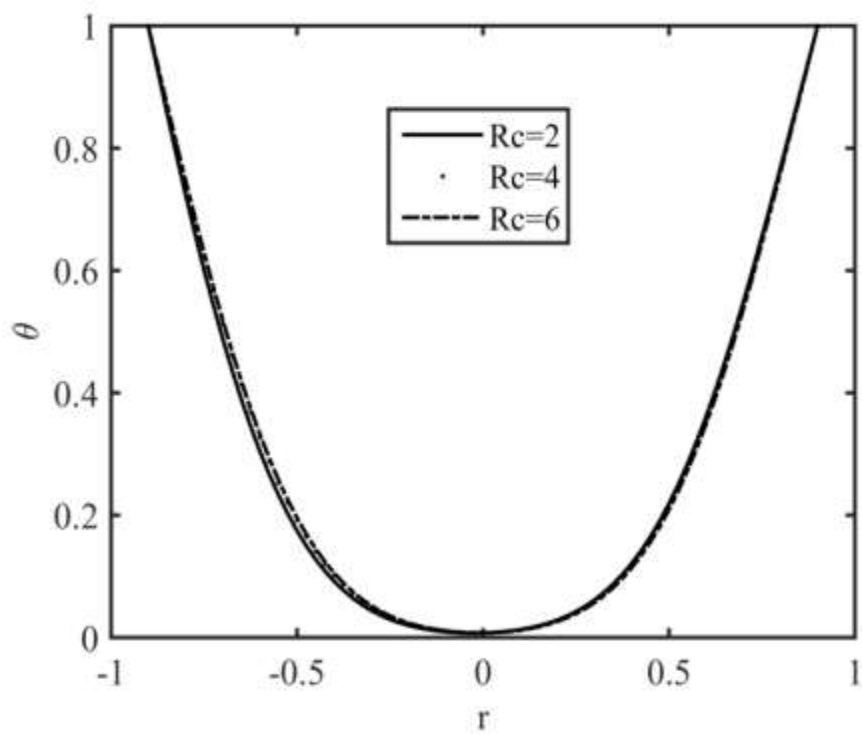

Figure 2.9

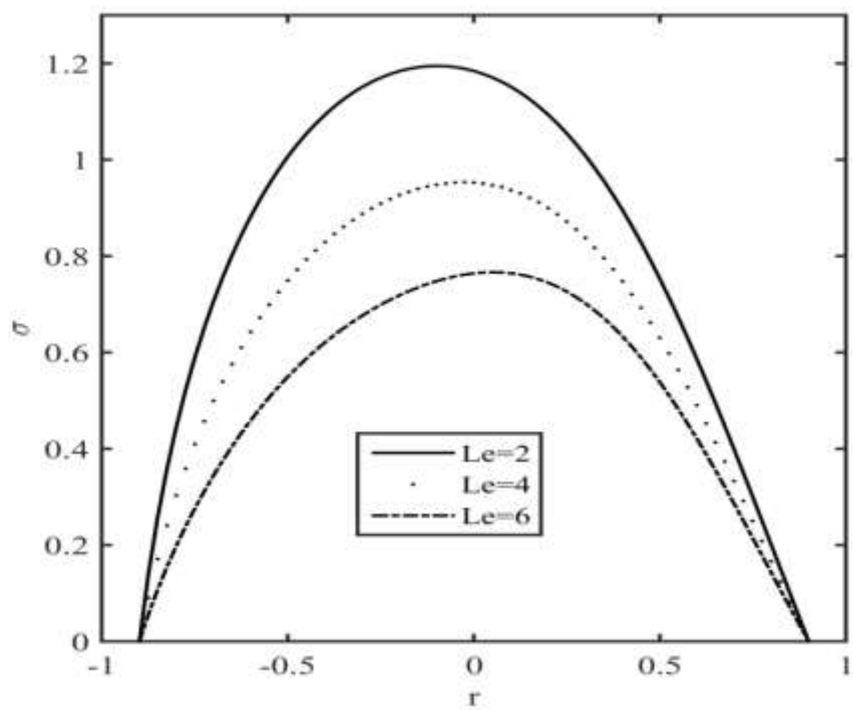

Figure 2.10

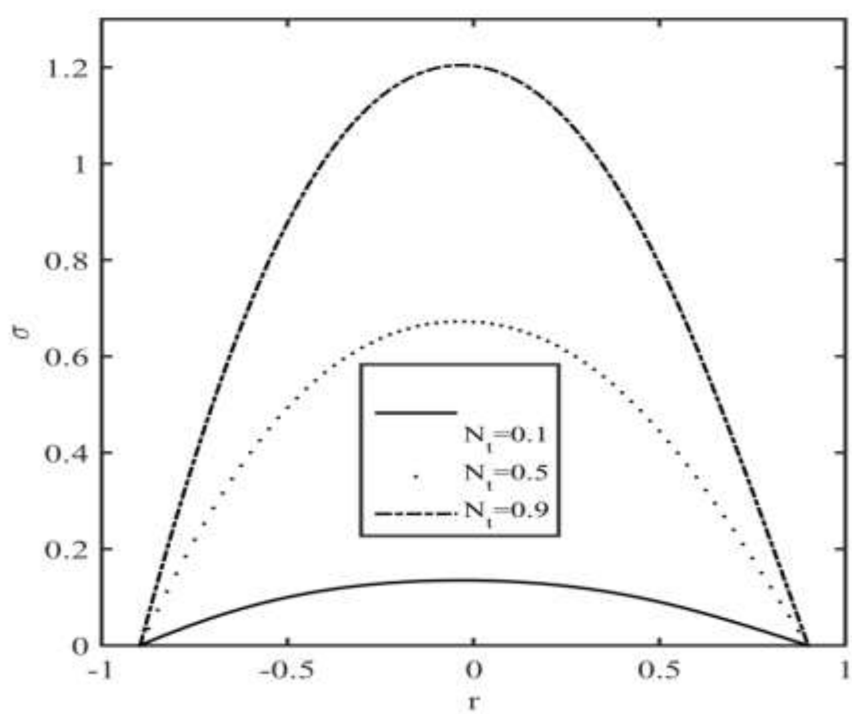

Figure 2.11

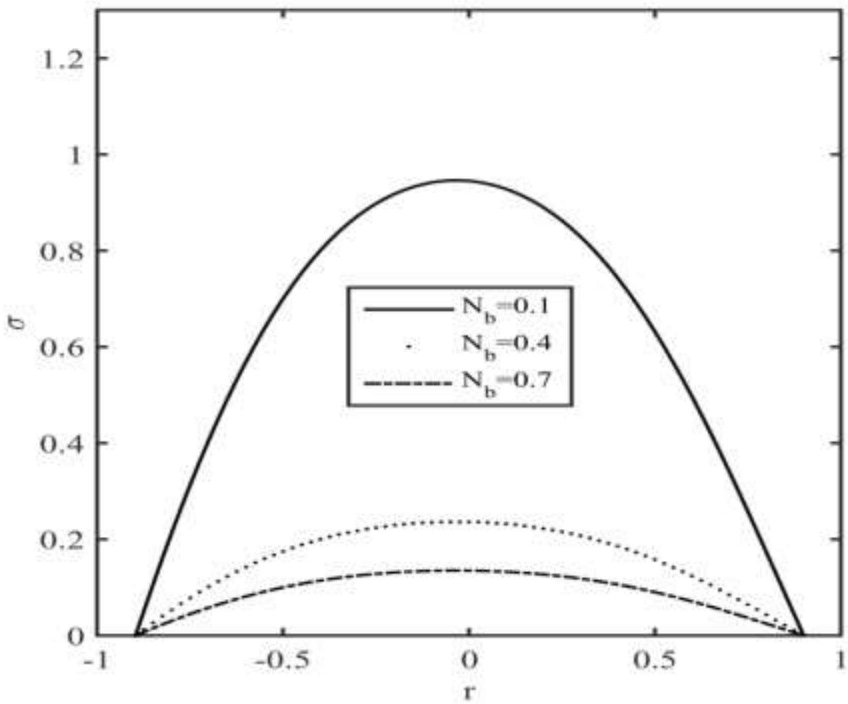

Figure 2.12

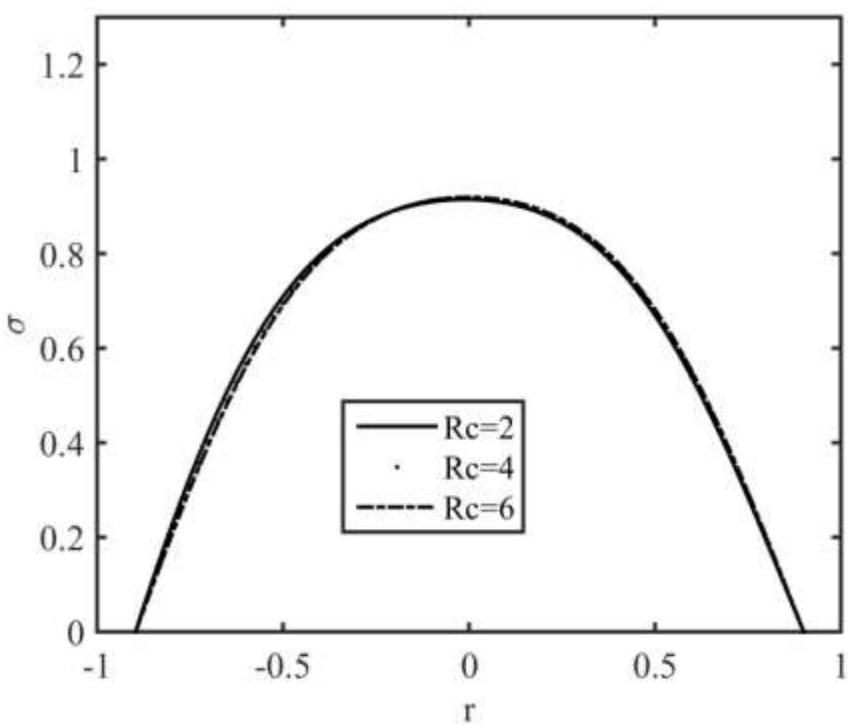

Figure 2.13

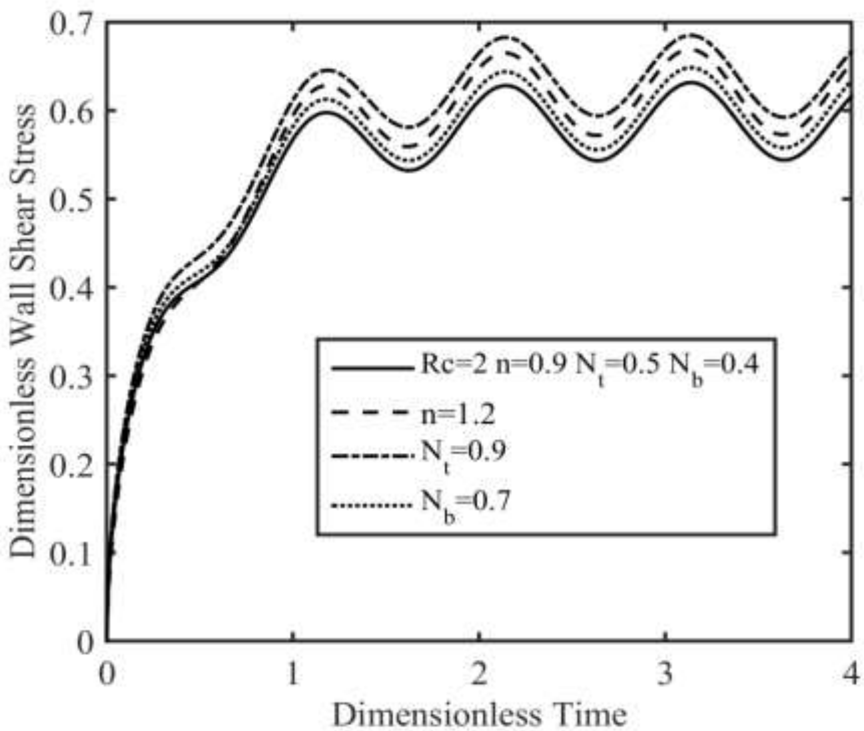

Figure 2.14

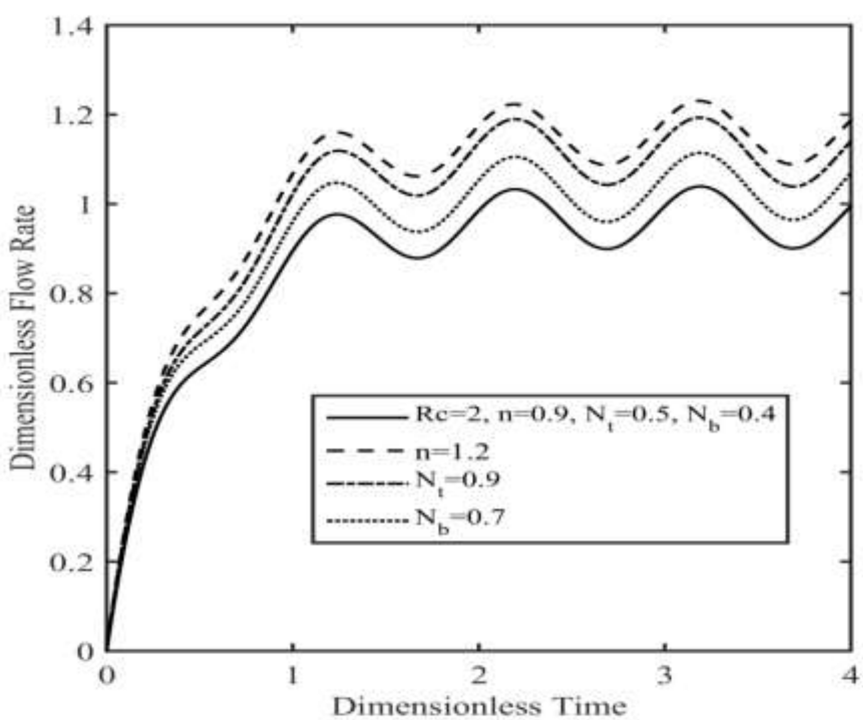

Figure 2.15

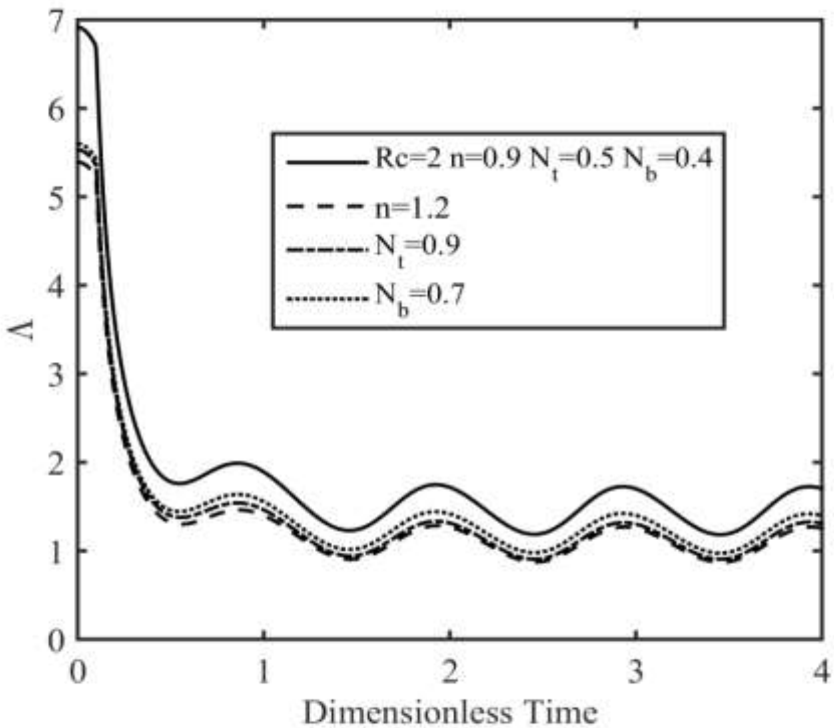

Figure 2.16

Chapter 3

A Study of Brownian Motion and Entropy Generation in the Pulsatile Flow of Herschel-Bulkley Fluid in a Mutilated Curved Artery

This chapter examines the influence of Thermophoresis and Brownian motion on the pulsatile flow of nanofluid (blood) through a curved artery with stenosis and post-stenotic dilatation internally, utilizing numerical investigations. The Herschel-Bulkley model of fluid dynamics accurately represents the fluid's rheology. By applying the mild stenosis condition, the highly coupled momentum, energy, and mass concentration equations can be modeled and reduced. The study also delves into entropy creation in blood flow resulting from loss and magnetohydrodynamic processes. Graphs and discussions on the effects of changing relevant geometric and rheological factors on key flow characteristics such as temperature, velocity, mass concentration, wall shear stress, flow rate, and impedances are provided.

3.1 Flow Equation

This analysis considers the unsteady, laminar, fully developed flow of blood through a curved blood vessel, featuring overlapping stenosis in its lumen. Additionally, it is assumed that the cross-sectional geometry resembles that of a radially curved channel. A curvilinear coordinate system has been developed as part of the process of constructing curved stenosed channels. The curved stenosed channel is described by a mathematical equation.

$$R(z)=\begin{Bmatrix}\left(\tau' z+e_0\right)\left(1-\frac{64}{10}\eta\left(\frac{11}{32}l_0^3\left(z-d\right)-\frac{47}{48}l_0^2\left(z-d\right)^2+l_0\left(z-d\right)^3-\frac{1}{3}\left(z-d\right)^4\right)\right), & d\le z\le d+\frac{3}{2}l_0,\\ \left(\tau' z+e_0\right), & otherwise\end{Bmatrix},$$

Outer wall,

$$-R(z)=\begin{Bmatrix}\left(\tau' z-e_0\right)\left(1-\frac{64}{10}\eta\left(\frac{11}{32}l_0^3\left(z-d\right)-\frac{47}{48}l_0^2\left(z-d\right)^2+l_0\left(z-d\right)^3-\frac{1}{3}\left(z-d\right)^4\right)\right), & d\le z\le d+\frac{3}{2}l_0,\\ \left(\tau' z-e_0\right), & otherwise\end{Bmatrix},$$

Inner wall.

(3.1)

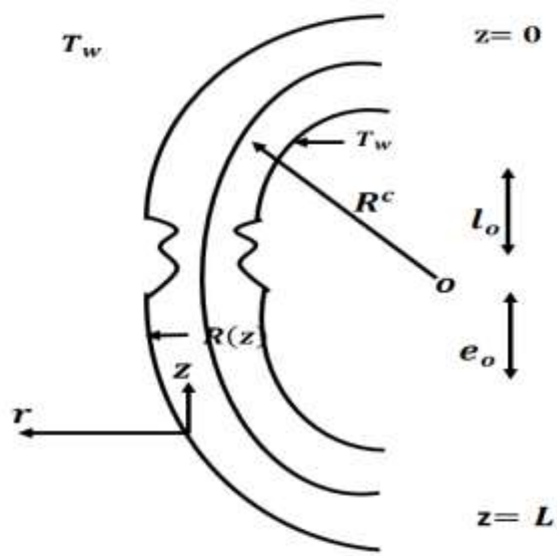

Figure 3.1

Studying the mechanics of blood flow in arteries is a crucial aspect of vascular research due to its significant impact on health. In the depicted geometry (Fig. 3.1), R^c stands for the curvature of the canal. The following equation describes the curved stenosed channel mathematically.: where represents $R(z)$ the stenotic region's curved channel segment radius. In the above equations, e_0 is used to denote the radius of the non-tapered channel l_0, represents the length of the stenotic region, T_w represents the wall temperature, r represents the radial coordinate, z represents the axial coordinate, and the length of the non-stenotic region d is denoted by . The parameter η is a constant defined as:

$$\eta = \frac{4\delta^*}{a l_0^{\;4}}, \tag{3.2}$$

in this, δ^* displays the stenotic zone's essential height appearing in two locations i.e.,

$$z = d + \frac{8l_0}{25}, \text{ and } z = d + \frac{61l_0}{50}. \tag{3.3}$$

The governing equation of the flow field is defined as:

$$\begin{aligned} &\bar{V} = U(t,r,z), 0, W(t,r,z),\\ &T^* = T^*(t,r,z),\\ &C^1 = C^1(t,r,z). \end{aligned} \tag{3.4}$$

In Eq. (3.4), U and W Both stand for the tangential and vertical components of the total velocity, T^* is temperature component and C^1 is nanoparitcles concentration component. Equations for continuity, momentum, energy absorption, and mass absorption are

$$\frac{\partial}{\partial r}\left(r + R^c\right)U + R^c \frac{\partial W}{\partial z} = 0, \tag{3.5}$$

$$\begin{aligned} \rho\left(\frac{\partial U}{\partial t} + U\frac{\partial U}{\partial r} + \frac{R^c}{r+R^c}W\frac{\partial U}{\partial z} - \frac{U^2}{r+R^c}\right) = -\frac{\partial p}{\partial r} + \frac{1}{\left(r+R^c\right)^2}\frac{\partial}{\partial r}\left(\left(r+R^c\right)S^{rr}\right)\\ + \frac{R^c}{r+R^c}\frac{\partial S^{rz}}{\partial z} - \frac{S^{zz}}{r+R^c}, \end{aligned} \tag{3.6}$$

$$\begin{aligned} &\rho\left(\frac{\partial W}{\partial t} + U\frac{\partial W}{\partial r} + \frac{R^c}{r+R^c}W\frac{\partial W}{\partial z} + \frac{UW}{r+R^c}\right) = -\left(\frac{R^c}{r+R^c}\right)\frac{\partial p}{\partial z} + \frac{1}{\left(r+R^c\right)^2}\frac{\partial}{\partial r}\left(\left(r+R^c\right)S^{rz}\right)\\ &+ \frac{R^c}{r+R^c}\frac{\partial S^{zz}}{\partial z} + \rho g \alpha_T\left(T^* - T_w\right) + \rho g \alpha_{C^1}\left(C^1 - C_1\right) - \left(\frac{R^c}{r+R^c}\right)^2 \alpha\beta_o^2 W, \end{aligned} \tag{3.7}$$

$$\begin{aligned} &\left(\rho c_p\right)_f\left(\frac{\partial T^*}{\partial t} + U\frac{\partial T^*}{\partial r} + \frac{R^c}{r+R^c}W\frac{\partial T^*}{\partial z}\right) = k_f\left(\frac{\partial^2 T^*}{\partial r^2} + \frac{1}{r+R^c}\frac{\partial T^*}{\partial r} + \left(\frac{R^c}{r+R^c}\right)^2\frac{\partial^2 T^*}{\partial z^2}\right)\\ &+ \left(\rho c\right)_p\left[\left(D_\beta\left(\frac{\partial C^1}{\partial r}\frac{\partial T^*}{\partial r} + \left(\frac{R^c}{r+R^c}\right)^2\frac{\partial C^1}{\partial z}\frac{\partial T^*}{\partial z}\right) + \frac{D_{T^*}}{T_w - T_1}\left(\left(\frac{\partial T^*}{\partial r}\right)^2 + \left(\frac{R^c}{r+R^c}\right)^2\left(\frac{\partial T^*}{\partial z}\right)^2\right)\right)\right]\\ &+ \left(\frac{R^c}{r+R^c}\right)^2 \alpha\beta_o^2 W^2, \end{aligned} \tag{3.8}$$

$$\frac{\partial C^1}{\partial t}+U\frac{\partial C^1}{\partial r}+W\frac{\partial C^1}{\partial z}=D_\beta\left(\frac{\partial^2 C^1}{\partial r^2}+\frac{1}{r+R^c}\frac{\partial C^1}{\partial r}+\left(\frac{R^c}{r+R^c}\right)^2\frac{\partial^2 C^1}{\partial z^2}\right)$$
$$+\frac{D_{T^*}}{T_w-T_1}\left(\frac{\partial^2 T^*}{\partial r^2}+\frac{1}{r+R^c}\frac{\partial T^*}{\partial r}+\left(\frac{R^c}{r+R^c}\right)^2\frac{\partial^2 T^*}{\partial z^2}\right). \tag{3.9}$$

The term $S^{rr}, S^{rz}\ and\ S^{zz}$ are the extra stress tensor component which is seeming in Eqs. (3.6) and (3.7). The relation of the Herschel-Bulkley model is

$$S=\left(\mu\prod^{n-1}+\frac{\tau_y}{\prod}\right)\boldsymbol{A}^1. \tag{3.10}$$

In (3.10), μ is the consistency index, n is the power law index, τ_y is the yield stress and A^1 is the Rivlin-Ericksen tensor defined by:

$$\boldsymbol{A}^1=\nabla\boldsymbol{V}+\nabla\boldsymbol{V}^T. \tag{3.11}$$

Where the first Rivlin-Ericksen tensor of the second invariant ($\prod$) is defined as:

$$\prod=\sqrt{\frac{1}{2}tra\left(A^{1^2}\right)}. \tag{3.12}$$

The constitutive relation (3.10) when dealing with curved channels, the yield is shown in Eq (3.4).

$$S^{rr}=2\left(\mu\prod^{n-1}+\frac{\tau_y}{\prod}\right)\left(\frac{\partial U}{\partial r}\right), \tag{3.13}$$

$$S^{zz}=2\left(\mu\prod^{n-1}+\frac{\tau_y}{\prod}\right)\left(\frac{R^c}{r+R^c}\frac{\partial W}{\partial z}+\frac{U}{r+R^c}\right), \tag{3.14}$$

$$S^{rz}=\left(\mu\prod^{n-1}+\frac{\tau_y}{\prod}\right)\left(\frac{\partial W}{\partial r}+\frac{R^c}{r+R^c}\frac{\partial U}{\partial z}-\frac{W}{r+R^c}\right), \tag{3.15}$$

$$\prod=\left\|\left[\frac{1}{2}\left(\left(2\frac{\partial U}{\partial r}\right)^2+2\left(\frac{\partial W}{\partial r}+\frac{R^c}{r+R^c}\frac{\partial U}{\partial z}-\frac{W}{r+R^c}\right)^2+\left(\frac{R^c}{r+R^c}\frac{\partial W}{\partial z}+\frac{U}{r+R^c}\right)^2\right)\right]\right\|. \tag{3.16}$$

The mathematical formulation of the entropy generation is as:

$$E=\frac{K}{T_m^2}\left(\left(\frac{R^c}{r+R^c}\frac{\partial T^*}{\partial z}\right)^2+\left(\frac{\partial T^*}{\partial r}\right)^2\right)+\frac{1}{T_m}S_{rz}\left(\frac{\partial W}{\partial r}+\frac{R^c}{r+R^c}\frac{\partial U}{\partial z}-\frac{W}{r+R^c}\right)+\left(S_{rr}-S_{rz}\right)\frac{\partial U}{\partial r}$$
$$+\left(\frac{R^c}{r+R^c}\right)^2\alpha\beta_o^2W^2+\frac{RD_\beta}{C_m}\left(\frac{\partial C^1}{\partial r}+\frac{R^c}{r+R^c}\frac{\partial C^1}{\partial z}\right)^2+\frac{RD_\beta}{C_m}\left(\frac{\partial C^1}{\partial r}\frac{\partial T^*}{\partial r}+\left(\frac{R^c}{r+R^c}\right)^2\frac{\partial C^1}{\partial z}\frac{\partial T^*}{\partial z}\right). \tag{3.17}$$

Introducing the dimensionless variables

By using the following variables Eqs. (3.5)-(3.9) are made dimensionless from:

$$\bar{r}=\frac{r}{e_0},\ \ \overline{W}=\frac{W}{U_0},\ \ \overline{U}=\frac{l_0U}{\delta^*U_0},\ \ \bar{t}=\frac{U_0}{e_0}t,\ \ \bar{z}=\frac{z}{l_0},\ \ R_c=\frac{R^c}{e_0},\ \ \bar{p}=\frac{e_0^2p}{U_0l_0\mu_0},\ \ \theta=\frac{T^*-T_w}{T_1-T_w},$$
$$P_r=\frac{\left(c_p\right)_f\mu_f}{k_f},\ Gr_T=\frac{\rho g\alpha_Te_0^2}{U_0\mu_0}\left(T_1-T_w\right),\ \ Br=\frac{\rho ge_0^2}{U_0\mu_0}\alpha_CC_1,\ Le=\frac{\mu_0}{\rho D_\beta},\ N_t=\frac{\tau D_{T^*}}{k_f},$$
$$\mathrm{Re}=\frac{\rho_fU_0e_0}{\mu_0},\ \ \overline{S}^{rz}=\frac{e_0}{U_0\mu_0}S^{rz},\ \ \overline{S}^{rr}=\frac{l_0}{U_0\mu_0}S^{rr},\ \ \overline{S}^{zz}=\frac{l_0}{U_0\mu_0}S^{zz},\ \sigma=\frac{C^1-C_1}{C_1},$$
$$N_b=\frac{\tau D_\beta C_1}{k_f},\ \Lambda=\frac{T^*-T_w}{T_m},\ M^2=\frac{\alpha\beta_o^2e_0}{\mu_0}. \tag{3.18}$$

In the above definitions, $\overline{W}$ is axial velocity, $\bar{r}$ is radial coordinate, $\bar{z}$ axial directional co-ordinate, $\bar{t}$ is time, $\overline{R}$ is the radius, $\bar{p}$ is the pressure, Br the Brinkman number, Re is the Reynolds number, Gr is the local thermal Grashof number, Pr is the Prandtl number, U_0 is the average velocity of the blood, T_w represent the wall temperature and T_m represent the thermodynamic temperature.

After removing the bars the Simplified Eqs. (3.5)-(3.9) and Eqs. (3.17) are:

$$\delta\left(\frac{\partial}{\partial r}\left(r+R_c\right)U\right)+R_c\frac{\partial W}{\partial z}=0, \tag{3.19}$$

$$\operatorname{Re}\delta\varepsilon^2\left(\frac{\partial U}{\partial t}+\delta\varepsilon U\frac{\partial U}{\partial r}+\varepsilon\frac{R_c}{r+R_c}W\frac{\partial U}{\partial z}-\frac{\varepsilon}{\delta}\frac{U^2}{r+R_c}\right)=-\frac{\partial p}{\partial r}+\varepsilon^2\left(\frac{1}{\left(r+R_c\right)^2}\frac{\partial}{\partial r}\left(\left(r+R_c\right)S^{rr}\right)\right)$$
$$+\varepsilon^2\left(\frac{R_c}{r+R_c}\right)\frac{\partial S^{rz}}{\partial z}-\frac{\varepsilon^2 S^{zz}}{r+R_c}, \tag{3.20}$$

$$\operatorname{Re}\frac{\partial W}{\partial t}+\operatorname{Re}\left(\delta\varepsilon\frac{\partial W}{\partial r}+\varepsilon\frac{R_c}{r+R_c}W\frac{\partial W}{\partial z}+\delta\varepsilon\frac{UW}{r+R^c}\right)=-\left(\frac{R_c}{r+R_c}\right)\frac{\partial p}{\partial z}+\frac{1}{\left(r+R_c\right)^2}\frac{\partial}{\partial r}\left(\left(r+R_c\right)^2S^{rz}\right)$$
$$+\varepsilon^2\left(\frac{R_c}{r+R_c}\right)\frac{\partial S^{zz}}{\partial z}+Gr_T\theta+Br\sigma-\left(\frac{R_c}{r+R_c}\right)^2M^2W, \tag{3.21}$$

$$\Pr\operatorname{Re}\left(\frac{\partial\theta}{\partial t}+\delta\varepsilon\frac{\partial\theta}{\partial r}+\varepsilon\frac{R_c}{r+R_c}W\frac{\partial\theta}{\partial z}\right)=\frac{\partial^2\theta}{\partial r^2}+\frac{1}{r+R_c}\frac{\partial\theta}{\partial r}+\varepsilon^2\left(\frac{R_c}{r+R_c}\right)^2\frac{\partial^2\theta}{\partial z^2}$$
$$+N_b\left(\frac{\partial\sigma}{\partial r}\frac{\partial\theta}{\partial r}+\varepsilon^2\left(\frac{R_c}{r+R_c}\right)^2\frac{\partial\sigma}{\partial z}\frac{\partial\theta}{\partial z}\right)+N_t\left(\left(\frac{\partial\theta}{\partial r}\right)^2+\varepsilon^2\left(\frac{R_c}{r+R_c}\right)^2\left(\frac{\partial\theta}{\partial z}\right)^2\right) \tag{3.22}$$
$$+\left(\frac{R_c}{r+R_c}\right)^2BrM^2W^2,$$

$$\operatorname{Re}Le\left(\frac{\partial\sigma}{\partial t}+\delta\varepsilon\frac{\partial\sigma}{\partial r}+\varepsilon W\frac{\partial\sigma}{\partial z}\right)=\frac{\partial^2\sigma}{\partial r^2}+\frac{1}{r+R_c}\frac{\partial\sigma}{\partial r}+\varepsilon^2\left(\frac{R_c}{r+R_c}\right)^2\frac{\partial^2\sigma}{\partial z^2}$$
$$+\frac{N_t}{N_b}\left(\frac{\partial^2\theta}{\partial r^2}+\frac{1}{r+R_c}\frac{\partial\theta}{\partial r}+\varepsilon^2\left(\frac{R_c}{r+R_c}\right)^2\frac{\partial^2\theta}{\partial z^2}\right). \tag{3.23}$$

$$E=\frac{K}{T_m^2}\left(\left(\varepsilon^2\frac{R_c}{r+R_c}\frac{\partial\theta}{\partial z}\right)^2+\left(\frac{\partial\theta}{\partial r}\right)^2\right)+\frac{1}{T_m}S_{rz}\left(\frac{\partial W}{\partial r}+\frac{\varepsilon R_c}{r+R_c}\frac{\partial U}{\partial z}-\frac{W}{r+R_c}\right)+\delta^2\varepsilon^2\left(S_{rr}-S_{rz}\right)\frac{\partial U}{\partial r}$$
$$+\left(\frac{R_c}{r+R_c}\right)^2\alpha\beta_o^2W^2+\frac{L\xi}{\Lambda^2}\left(\frac{\partial\sigma}{\partial r}+\frac{\varepsilon R_c}{r+R_c}\frac{\partial\sigma}{\partial z}\right)^2+\frac{L}{\Lambda}\left(\frac{\partial\sigma}{\partial r}\frac{\partial\theta}{\partial r}+\varepsilon^2\left(\frac{R_c}{r+R_c}\right)^2\frac{\partial\sigma}{\partial z}\frac{\partial\theta}{\partial z}\right) \tag{3.24}$$

The following study is based on two assumptions: moderate stenotic suppositions: $\varepsilon\left(=\frac{e_0}{l_0}\right)=O(1)$ and $\delta\left(=\frac{\delta^*}{e_0}\right)\ll 1$ i.e. The first need is that the stenotic area and the channel's radius have lengths that are similar. The second condition depends on the height of the track length being less than the radius of a channel. Equation (3.19) to (3.24) is reduced as follows:

$$\frac{\partial p}{\partial r}=0, \tag{3.25}$$

$$\operatorname{Re}\frac{\partial W}{\partial t}=-\left(\frac{R_c}{r+R_c}\right)\frac{\partial p}{\partial z}+Gr_T\theta+Br\sigma-\left(\frac{R_c}{r+R_c}\right)^2 M^2W$$
$$+\frac{1}{\left(r+R_c\right)^2}\frac{\partial}{\partial r}\left(\left(r+R_c\right)^2\left(\mu\left(\frac{\partial W}{\partial r}-\frac{W}{r+R^c}\right)^{n-1}+\tau\left(\frac{\partial W}{\partial r}-\frac{W}{r+R^c}\right)^{-\frac{1}{2}}\right)\left(\frac{\partial W}{\partial r}-\frac{W}{r+R^c}\right)\right), \tag{3.26}$$

$$\Pr\operatorname{Re}\frac{\partial\theta}{\partial t}=\frac{\partial^2\theta}{\partial r^2}+\frac{1}{r+R_c}\frac{\partial\theta}{\partial r}+N_b\left(\frac{\partial\sigma}{\partial r}\frac{\partial\theta}{\partial r}\right)+N_t\left(\frac{\partial\theta}{\partial r}\right)^2+\left(\frac{R_c}{r+R_c}\right)^2 M^2BrW^2, \tag{3.27}$$

$$\operatorname{Re}Le\frac{\partial\sigma}{\partial t}=\frac{\partial^2\sigma}{\partial r^2}+\frac{1}{r+R_c}\frac{\partial\sigma}{\partial r}+\frac{N_t}{N_b}\left(\frac{\partial^2\theta}{\partial r^2}+\frac{1}{r+R_c}\frac{\partial\theta}{\partial r}\right). \tag{3.28}$$

Where

$$E=\frac{K}{T_m^2}\left(\left(\frac{\partial\theta}{\partial r}\right)^2\right)+\frac{Br}{\Lambda}\left(\mu\left(\frac{\partial W}{\partial r}-\frac{W}{r+R^c}\right)^{n-1}+\tau\left(\frac{\partial W}{\partial r}-\frac{W}{r+R^c}\right)^{-\frac{1}{2}}\right)\left(\frac{\partial W}{\partial r}-\frac{W}{r+R_c}\right)$$
$$+\left(\frac{R_c}{r+R_c}\right)^2\frac{BrM^2}{\Lambda}W^2+\frac{L\xi}{\Lambda^2}\left(\frac{\partial\sigma}{\partial r}\right)^2+\frac{L}{\Lambda}\left(\frac{\partial\sigma}{\partial r}\frac{\partial\theta}{\partial r}\right). \tag{3.29}$$

The equation of Pulsatile Pressure gradient:

$$-\frac{\partial p}{\partial z}=A_0+A_1\cos\left(2\pi\omega_p t\right),\qquad t>0. \tag{3.30}$$

In Eq.(3.27), A_0 designates the mean pressure gradient and A_1 represent the amplitude of the pulsatile component. By using Eq.(3.9) in Eq.(3.18) we get :

$$-\frac{\partial p}{\partial z}=B_1\left(1+c\cos\left(c_1 t\right)\right), \tag{3.31}$$

Where

$$c_1=\frac{2\pi\omega_p e_0}{U_0},\quad c=\frac{A_1}{A_0},\quad B_1=\frac{A_0e_0^2}{\mu_0U_0}. \tag{3.32}$$

Using the term $-\partial p/\partial z$ in Equation (3.31)

$$\mathrm{Re}\frac{\partial W}{\partial t}=\left(\frac{R_c}{r+R_c}\right)B_1\left(1+c\cos\left(c_1 t\right)\right)-\left(\frac{R_c}{r+R_c}\right)^2 M^2 W+Gr_T\theta+Br\sigma$$
$$+\frac{1}{\left(r+R_c\right)^2}\frac{\partial}{\partial r}\left(\left(r+R_c\right)^2\left(\mu\left(\frac{\partial W}{\partial r}-\frac{W}{r+R^c}\right)^{n-1}+\tau\left(\frac{\partial W}{\partial r}-\frac{W}{r+R^c}\right)^{-\frac{1}{2}}\right)\left(\frac{\partial W}{\partial r}-\frac{W}{r+R^c}\right)\right),$$

(3.33)

Eqs. (3.27)-(3.28) and (3.33) are subjected to the following boundary and initial condition:

$$W\left(t,r\right)\big|_{r=R}=0,\quad W\left(t,r\right)\big|_{r=-R}=0,\quad W\left(0,r\right)=0.0, \tag{3.34}$$

$$\sigma\left(t,r\right)\big|_{r=R}=0,\quad \sigma\left(t,r\right)\big|_{r=-R}=0,\quad \sigma\left(0,r\right)=0.0, \tag{3.35}$$

$$\theta\left(t,r\right)\big|_{r=R}=1,\quad \theta\left(t,r\right)\big|_{r=-R}=1,\quad \theta\left(0,r\right)=0.0, \tag{3.36}$$

The formula for volumetric flow rate $\left(Q\right)$, resistance impedance $\left(\Lambda\right)$ and wall shear stress $\left(\tau_S\right)$ in the new variable becomes:

$$Q=\int_{-R}^{R}Wdr, \tag{3.37}$$

$$\tau_S=\left(\mu\left(\frac{\partial W}{\partial r}-\frac{W}{r+R^c}\right)^{n-1}+\tau\left(\frac{\partial W}{\partial r}-\frac{W}{r+R^c}\right)^{-\frac{1}{2}}\right)\left(\frac{\partial W}{\partial r}-\frac{W}{r+R^c}\right)_{r=R}, \tag{3.38}$$

$$\Lambda=\frac{\left(\frac{\partial p}{\partial z}\right)}{Q}. \tag{3.39}$$

The dimensionalized geometry equation for the arterial segment can be easily defined as follows:

$$R\left(z\right)=\left(1+\tau z\right)\left[1-\frac{64}{10}\eta_1\left(\frac{11}{32}\left(z-\sigma\right)-\frac{47}{48}\left(z-\sigma\right)^2+\left(z-\sigma\right)^3-\frac{1}{3}\left(z-\sigma\right)^4\right)\right],$$
$$\sigma\le z\le\sigma+\frac{3}{2},\ \ Outer\ wall,$$

(3.40)

$$-R(z) = (-1+\tau z)\left[1+\frac{64}{10}\eta_1\left(\frac{11}{32}(z-\sigma)-\frac{47}{48}(z-\sigma)^2+(z-\sigma)^3-\frac{1}{3}(z-\sigma)^4\right)\right],$$

$\sigma \le z \le \sigma + \frac{3}{2},$ *Inner wall*,

Where $\eta_1 = 4\delta,\ \delta = \frac{\delta^*}{e_0},\ \sigma = \frac{d}{l_0},\ \tau = \frac{\tau' l_0}{e_0}.$

3.2 Entropy Generation

The Entropy generation (N_G) is defined as:

$N_G = \frac{E}{S_G}$, where $S_G = \frac{k\left(T^* - T_W\right)^2}{T_m^2 e_o^2}$, using S_G in N_G, we get

$$N_G = \frac{T_m^2 e_o^2}{k\left(T^* - T_W\right)^2}(E), \tag{3.41}$$

Use of E in Eq. (3.41):

$$N_G = \left(\frac{\partial\theta}{\partial r}\right)^2 + \frac{Br}{\Lambda}\left(\mu\left(\frac{\partial W}{\partial r} - \frac{W}{r+R^c}\right)^{n-1} + \tau\left(\frac{\partial W}{\partial r} - \frac{W}{r+R^c}\right)^{-\frac{1}{2}}\right)\left(\frac{\partial W}{\partial r} - \frac{W}{r+R_c}\right) + \left(\frac{R_c}{r+R_c}\right)^2 \frac{BrM^2}{\Lambda} W^2$$
$$+\frac{L\xi}{\Lambda^2}\left(\frac{\partial\sigma}{\partial r}\right)^2 + \frac{L}{\Lambda}\left(\frac{\partial\sigma}{\partial r}\frac{\partial\theta}{\partial r}\right). \tag{3.42}$$

The mathematical formulation of the Bejan number (Be) is:

$Be = \frac{(\partial\theta/\partial r)^2}{N_G}$, after incorporating the entropy generation (N_G), it takes the following form:

$$Be = \frac{1}{1+\psi}, \tag{3.43}$$

$$Where\ \psi=\frac{\left(\begin{array}{l}\frac{Br}{\Lambda}\left(\mu\left(\frac{\partial W}{\partial r}-\frac{W}{r+R^{c}}\right)^{n-1}+\tau\left(\frac{\partial W}{\partial r}-\frac{W}{r+R^{c}}\right)^{-\frac{1}{2}}\right)\left(\frac{\partial W}{\partial r}-\frac{W}{r+R_{c}}\right)+\left(\frac{R_{c}}{r+R_{c}}\right)^{2}\frac{BrM^{2}}{\Lambda}W^{2}\\+\frac{L\xi}{\Lambda^{2}}\left(\frac{\partial\sigma}{\partial r}\right)^{2}+\frac{L}{\Lambda}\left(\frac{\partial\sigma}{\partial r}\frac{\partial\theta}{\partial r}\right)\end{array}\right)}{\left(\partial\theta/\partial r\right)^{2}}.$$

3.3 Solution Methodology

In the numerical approach, we use the explicit finite difference technique.

Using the above algebraic transformation in Eqs.(3.26) and (3.29):

$$\begin{aligned}W_{i}^{k+1}&=W_{i}^{k}+\left(\frac{R_{c}}{r+R_{c}}\right)\frac{\Delta t}{\mathrm{Re}}B_{1}\left(1+c\cos\left(c_{1}t\right)\right)-\left(\frac{R_{c}}{r+R_{c}}\right)^{2}M^{2}W_{i}^{k}\\&+\frac{1}{\left(r+R_{c}\right)^{2}}\frac{\partial}{\partial r}\left(\left(r+R_{c}\right)^{2}\left(\mu\left(W_{r}-\frac{W_{i}^{k}}{r+R^{c}}\right)^{n-1}+\tau\left(W_{r}-\frac{W_{i}^{k}}{r+R^{c}}\right)^{-\frac{1}{2}}\right)\left(W_{r}-\frac{W_{i}^{k}}{r+R^{c}}\right)\right)\\&+Gr_{T}\theta_{i}^{k}+Br\sigma_{i}^{k},\end{aligned}\tag{3.44}$$

$$\theta_{i}^{k+1}=\theta_{i}^{k}+\frac{\Delta t}{\mathrm{Re}\,\mathrm{Pr}}\left\{\left(\theta_{rr}+\frac{1}{r+R_{c}}\theta_{r}\right)+N_{b}\theta_{r}\sigma_{r}+N_{t}\left(\theta_{r}\right)^{2}+\left(\frac{R_{c}}{r+R_{c}}\right)^{2}M^{2}Br\left(W^{2}\right)_{i}^{k}\right\},\tag{3.45}$$

$$\sigma_{i}^{k+1}=\sigma_{i}^{k}+\frac{\Delta t}{\mathrm{Re}\,Le}\left\{\left(\sigma_{rr}+\frac{1}{r+R_{c}}\sigma_{r}\right)+\frac{N_{t}}{N_{b}}\left(\theta_{rr}+\frac{1}{r+R_{c}}\theta_{r}\right)\right\}.\tag{3.46}$$

$$Be_{i}^{k}=\frac{\left(\theta_{r}^{2}\right)_{i}^{k}}{\left(N_{G}\right)_{i}^{k}},$$

$$\begin{aligned}\left(N_{G}\right)_{i}^{k}&=\left(\theta_{r}\right)^{2}+\frac{Br}{\Lambda}\left(\mu\left(W_{r}-\frac{W_{i}^{k}}{r+R^{c}}\right)^{n-1}+\tau\left(W_{r}-\frac{W_{i}^{k}}{r+R^{c}}\right)^{-\frac{1}{2}}\right)\left(W_{r}-\frac{W_{i}^{k}}{r+R^{c}}\right)\\&+\left(\frac{R_{c}}{r+R_{c}}\right)^{2}\frac{BrM^{2}}{\Lambda}W_{i}^{2k}+\frac{L\xi}{\Lambda^{2}}\left(\sigma_{r}\right)^{2}+\frac{L}{\Lambda}\left(\sigma_{r}\right)\left(\theta_{r}\right).\end{aligned}\tag{3.47}$$

Here we define both the numerical border and the initial condition as:

$$\begin{aligned}
&W_i^1 = 0 = \theta_i^1\ ,\ \sigma_i^1 = 0 && at\ t = 0, \\
&W_1^k = \theta_1^k = 1\ ,\ \sigma_i^1 = 0 && at\ r = -R(x), \\
&W_{N+1}^k = \theta_{N+1}^k = 1\ ,\ \sigma_i^1 = 0 && at\ r = R(x).
\end{aligned} \tag{3.48}$$

3.4 Discussion of Results

This section discusses the generation of entropy, which consequently impacts heat energy and, ultimately, blood flow rate. It also explores the presence and nature of a magnetic field within a curved, multiple-stenosed channel. Various profiles are generated to isolate the effects of new factors on velocity, temperature, and Bejan values. The outlines of the flow field, in particular, illustrate how the curvature parameter influences the motion of blood. These parameter settings allow for more precise estimations.

$\sigma_1 = 0.2,\ \sigma_2 = 1.5,\ \delta = 0.1,\ \mathrm{Re} = 1,\ B1 = 1.41,\ Gr = 1,\ n = 0.95,\ x = 0.52,\ R_c = 3,\ M = 0.1,\ Le = 2,$
$\mathrm{Pr} = 9$

At various points in the artery cross-section and at various exits, velocity curves are calculated. Speed profiles at different positions are depicted as the curvature parameter (R_c) varies, as shown in Figure (3.2). The curve indicates the speed at which the curvature parameter's value is increasing. (R_c) the value of curvature is raised in Fig. (3.2), the vessel's structure becomes more linear, and the velocity field takes on a more symmetrical appearance. In Fig. (3.3), the value of the Reynolds number is shown with the velocity profile. Fig. (3.4) illustrates how the amplitude and shape of the velocity are significantly affected by the blood stress tuning parameter magnetic field (M). With a higher (M) value of the tuning parameter (M), the velocity becomes more pronounced. According to the results of this study, the blood's velocity can be adjusted by altering two parameters: the tuning parameter and the curvature parameter. According to the results of this study, the blood's velocity can be adjusted by adjusting two parameters: the tuning parameter (M) and the curvature parameter (R_c). The effect of temperature is illustrated in Fig. (3.5), where we can see that as the temperature increases, the graph of velocity decreases.

Drawings illustrating the special effects of curvature $\left(R_c\right)$ and magnetic field $\left(M\right)$ on the temperature profile are presented in Figures (3.6) and (3.7). It appears from examining Fig. (3.6) that the curvature parameter $\left(R_c\right)$ has a minor impact on the temperature distribution. Curvature has a vanishingly small impact on temperature. The influence of a magnetic field on a temperature profile is seen in Fig. (3.7). The data show that when the magnetic parameter increases, so does the temperature $\left(M\right)$. However, magnetic fields can have a minor impact on temperature. Temperature plots for various Le (Lewis number) values, thermophoretic parameter $\left(N_t\right)$, and curvature Figure (3.8) and (3.9) depicts the parameter $\left(R_c\right)$. With the transition from Le to N_t, the temperature distribution changed little.

Figures (3.10)-(3.11) display concentration profiles computed with varying curvature parameter $\left(R_c\right)$ and Lewis number$\left(Le\right)$. As seen in Fig. (3.10), the artery's geometry shifts somewhat, resulting in a more vertical concentration profile. Fig. (3.11) shows, however, how the Lewis number $\left(Le\right)$ impacts the concentration field. It has a significant impact on the size of the concentration profile and exhibits a negative correlation. As Lewis number increases, concentrations decrease in magnitude

Figure (3.12) and (3.13) depicts the difference in amplitude of the concentration profiles owing to variations $\left(N_t\right)$. The concentration profile is enhanced by increasing $N_{t's}$ amplitudeand the Brownian motion parameter $\left(N_b\right)$, is increased, the behavior seen. Due to the fact that an increase in $\left(N_b\right)$ causes a greater degree of random motion among the suspended nanoparticles, resulting in a lower concentration in the flow system, nanofluids behave more like two-phase liquids in nature. The concentration profiles inherit the curvature effect, as shown in Fig. (3.1). This graph illustrates the solute's journey along the curved channel. The surgeon may find this analysis useful when administering drugs to a patient during surgery.

The N_G (Entropy generation number) graphs for different values of curvature$\left(R_c\right)$, brickman number $\left(Br\right)$, and magnetic parameter $\left(M\right)$ are shown in Figure (3.14),(3.15), and (3.16), respectively (c). Heat transmission plus heat lost through contact is what adds up to entropy, according to the mathematical definition. Modulations in entropy as a function of curve measure $\left(R_c\right)$ are displayed in Fig. (3.14). As the curvature parameter $\left(R_c\right)$ is increased, or as the shape of the vessel straightens, a more symmetrical collection of profiles is displayed. In Figure (3.15) and (3.16), we can see that the distributions of the Brickmann $\left(Br\right)$ and Magnetic field parameter $\left(M\right)$ contributions to the change in the entropy number $\left(N_G\right)$ are roughly comparable. By increasing the Brickmann $\left(Br\right)$ and Magnetic field components, entropy can be increased$\left(M\right)$. The barrier to heat absorption increases as the magnetic field's influence grows$\left(M\right)$.

The Bejan number $\left(Be\right)$ and entropy $\left(N_G\right)$ plots as a function of various factors are displayed in Figures (3.17), (3.18), and (3.19), respectively (R_c, Br and M). As can be seen in Fig. (3.17), the Bejan number $\left(Be\right)$ impacts are more localized in a curved conduit than in an unbend one. The results of adjusting the Brickman $\left(Br\right)$value are shown in Figure (3.18). Results show that with a higher$\left(Br\right)$, the influence of the Bejan number is mitigated. The impacts of magnetic field on the Bejan number $\left(Be\right)$ are shown in Fig. (3.19) below and are quite striking. Bejan numbers $\left(Be\right)$ rise in significance as magnetic field strength decreases.

Figure (3.20) depicts the fluctuation of the wall shear stress over time for a given set of parameters $\left(R_c\right)$, $\left(n\right)$, $\left(N_t\right)$, and $\left(N_b\right)$. Each parameter's transformed wall shear profile is named for easy comparison. Because of this, the effects of freely adjustable parameters can be studied. Each alternative layout is evaluated in relation to the gold standard, which is a simple line drawing. As the values of $\left(R_c\right)$, $\left(n\right)$, and $\left(N_t\right)$ increased, the profile model showed that the stress on the wall increased when inappropriate behavior was revealed for $\left(N_b\right)$. For a new set of inputs, Figure (3.21) displays the computed flow rate of change through time. Analyze the impact of different throughput parameters by comparing the patterns shown in Fig. (3.21). To round out the proposal scenario, a standard curve is computed, and the remainder of the profiles are built using altered versions of a given set of parameters. Simulation of the premeditatedly computed arrangement where a larger flow is achieved by increasing $\left(R_c\right)$ or $\left(N_t\right)$ .Increasing the values of and $\left(n\right)$ have the opposite consequences. Streams it is evident from the scale profiles that blood rheology displays a solid blood pattern when the Shear value Thickness parameter is increased. What this means is that n will be utilized as a parameter to control the rheology of human blood. The resulting impedance is displayed in Fig. (3.22). The mathematical expression for impedance is given by Eq. (3.39), and it is proportional to the flow rate in the opposite direction. As can be seen in Figure (3.22), the impedance profiles are carried over from this formulation. For validation purpose, our results for Newtonian fluid $(n=1, \tau_y=0)$ and straight blood vessels ($R_C \to \infty$) are compared with the existing study in Figure (3.23). It is evident from Figure (3.23) The numerical results we obtained align well with the analytical results that were reported by previous reports. This surely authenticates our model and findings.

3.5 Concluding Remarks

This investigation combines the production of entropy and the transmission of heat during blood flow through a stenotic, multi-curved conduit. The resulting differential equations are solved using the explicit finite difference method to obtain numerical findings. The true bodily challenge is simulated by the time-dependent pressure gradient expression. We emphasize the most notable features of blood flow and gain a comprehensive understanding of the heat irreversibility it causes by calculating the Bejan number and entropy generation. Here are some of the most significant results from the study:

- The Bejan number is directly related to the Brickmann number (Br), and the entropy generation number is inversely related to the Brickmann generation number (Br).
- The magnetic field significantly influences the velocity profile and entropy.
- Symmetry in the velocity and Bejan number (Be) profiles can be restored by increasing the values of the curvature parameter or by straightening the curved arrangement.
- Curvature has a negligible impact on temperature, while magnetic fields exhibit a minor effect on temperature.

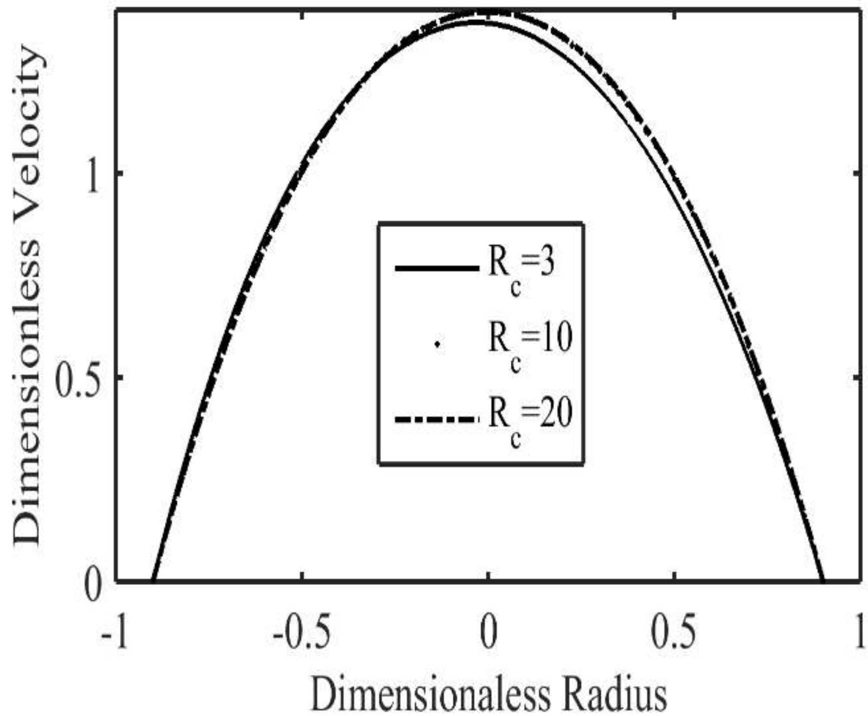

Figure 3.2

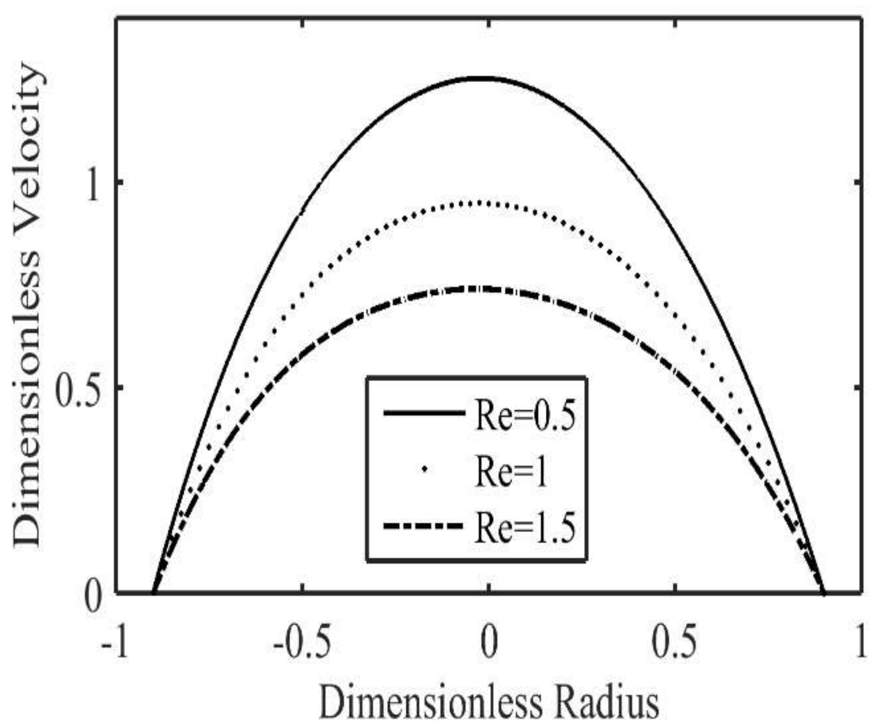

Figure 3.3

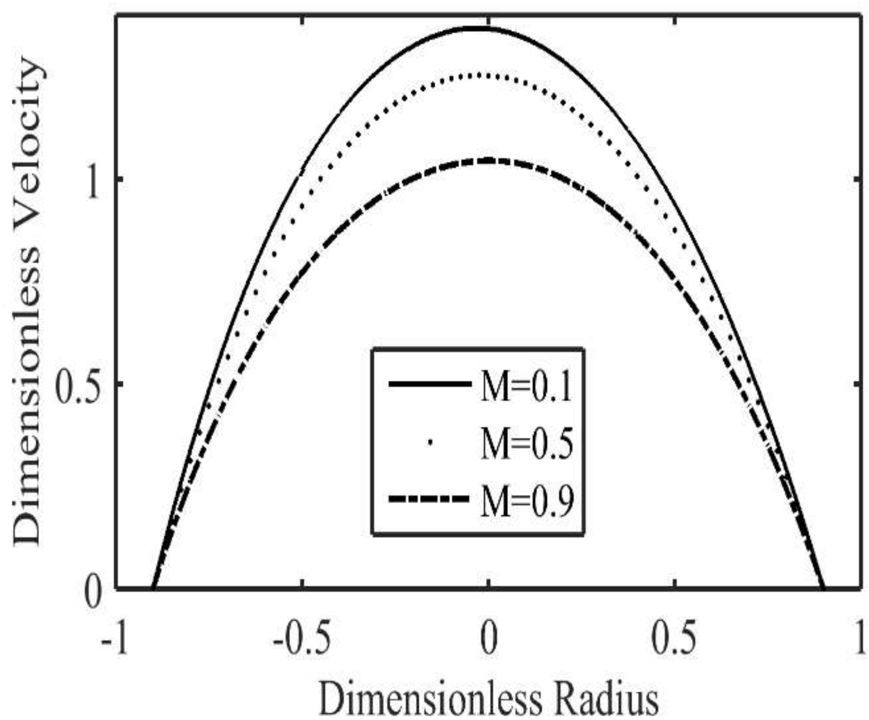

Figure 3.4

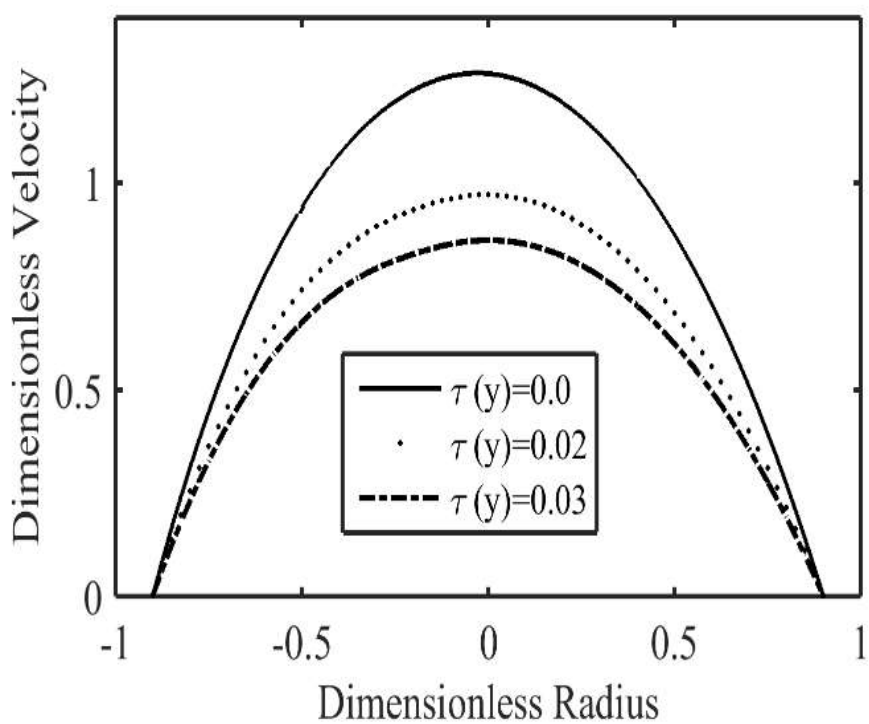

Figure 3.5

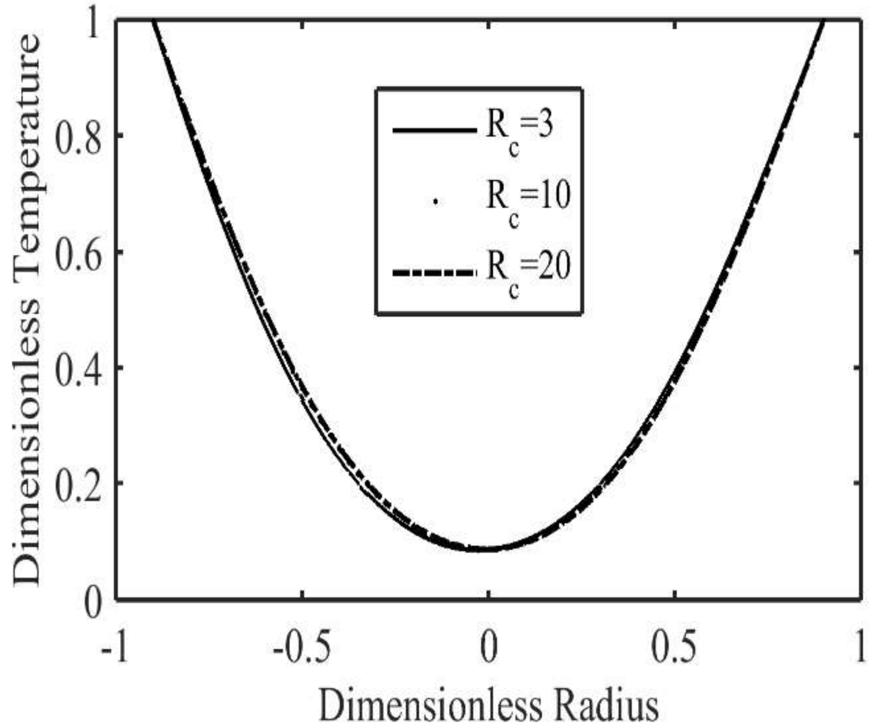

Figure 3.6

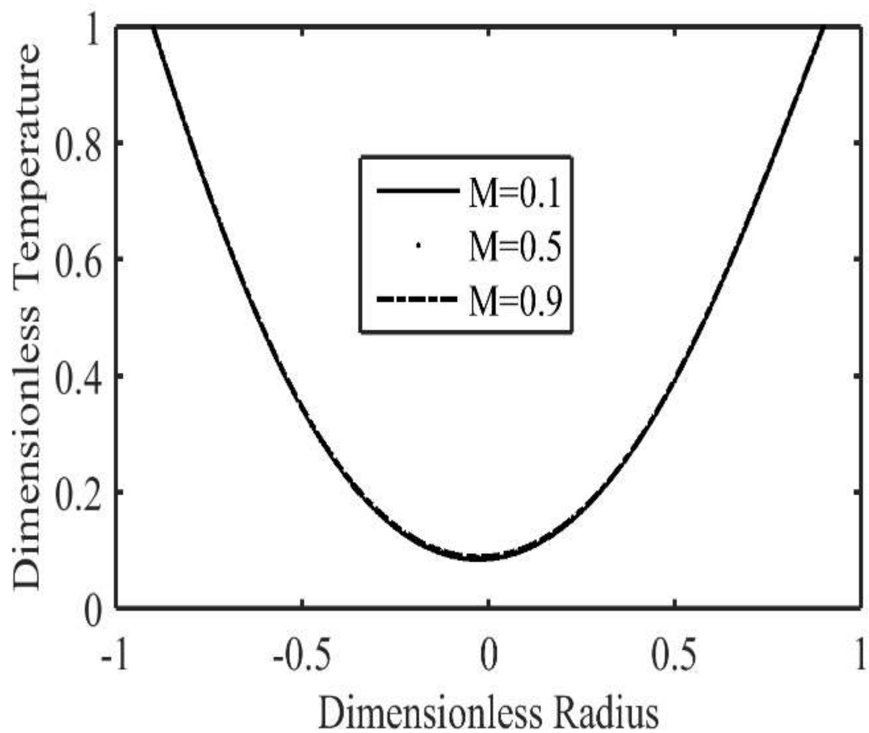

Figure 3.7

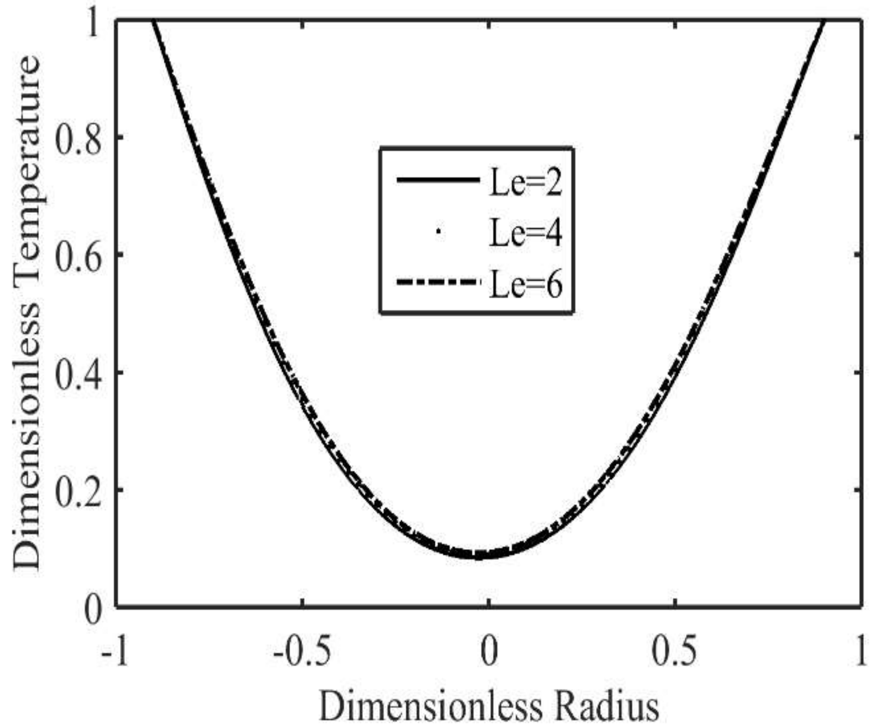

Figure 3.8

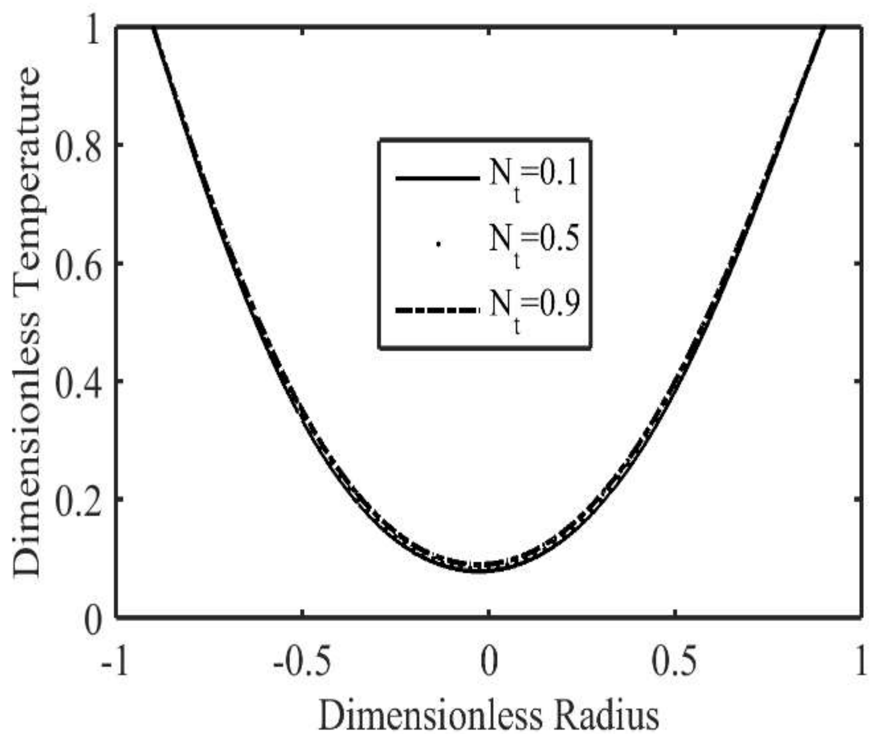

Figure 3.9

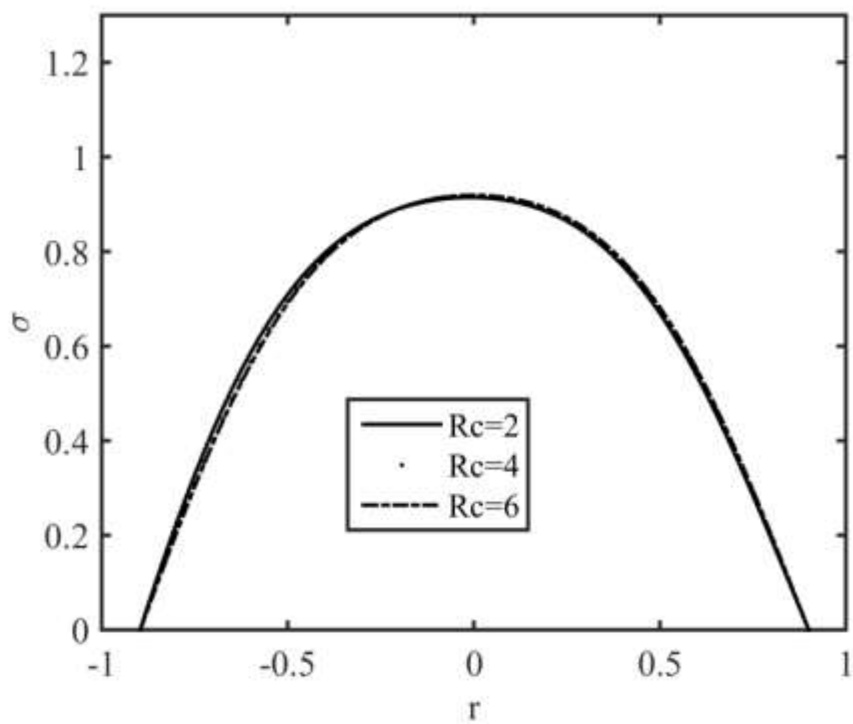

Figure 3.10

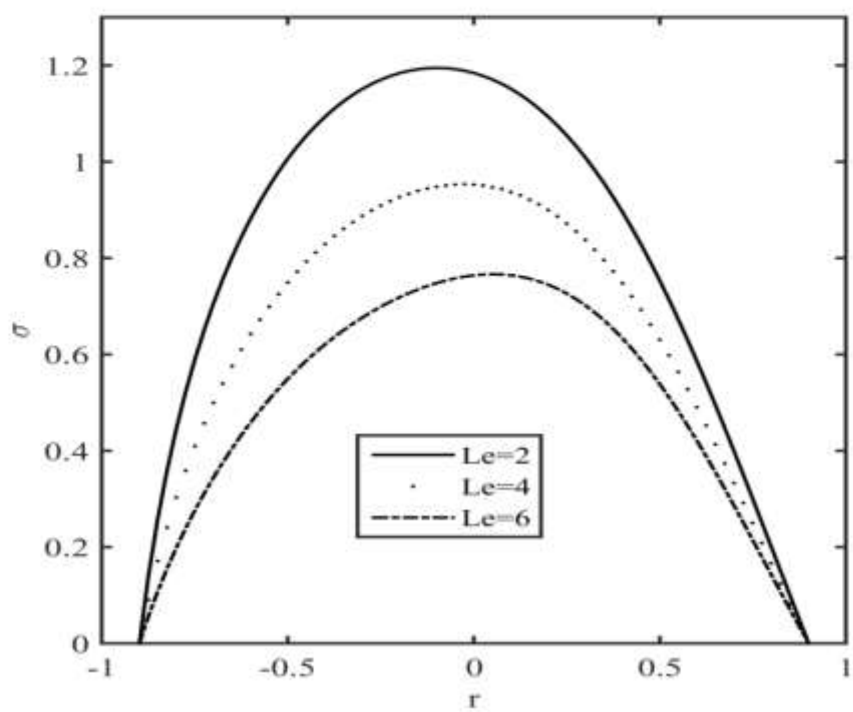

Figure 3.11

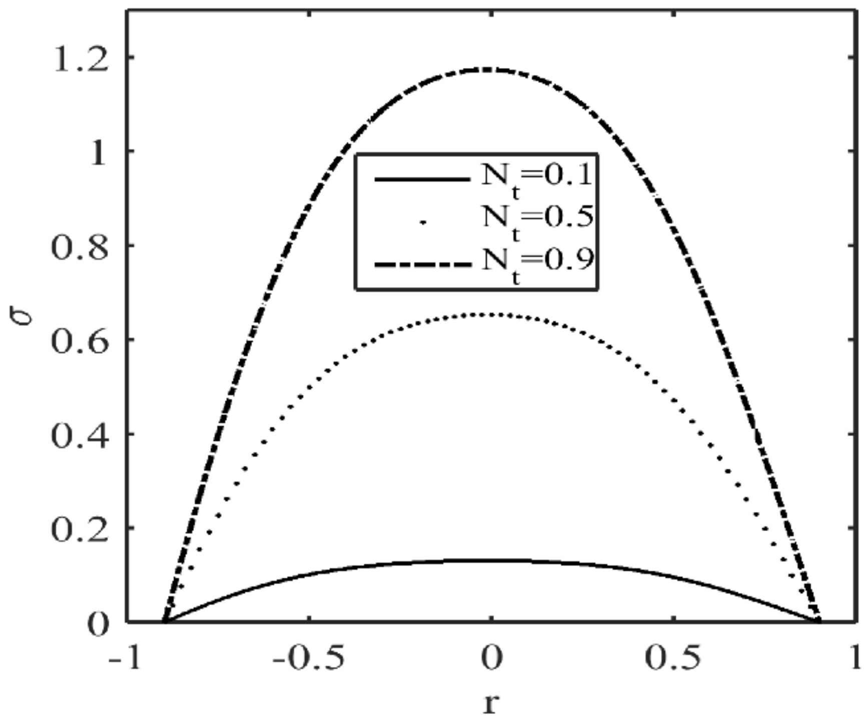

Figure 3.12

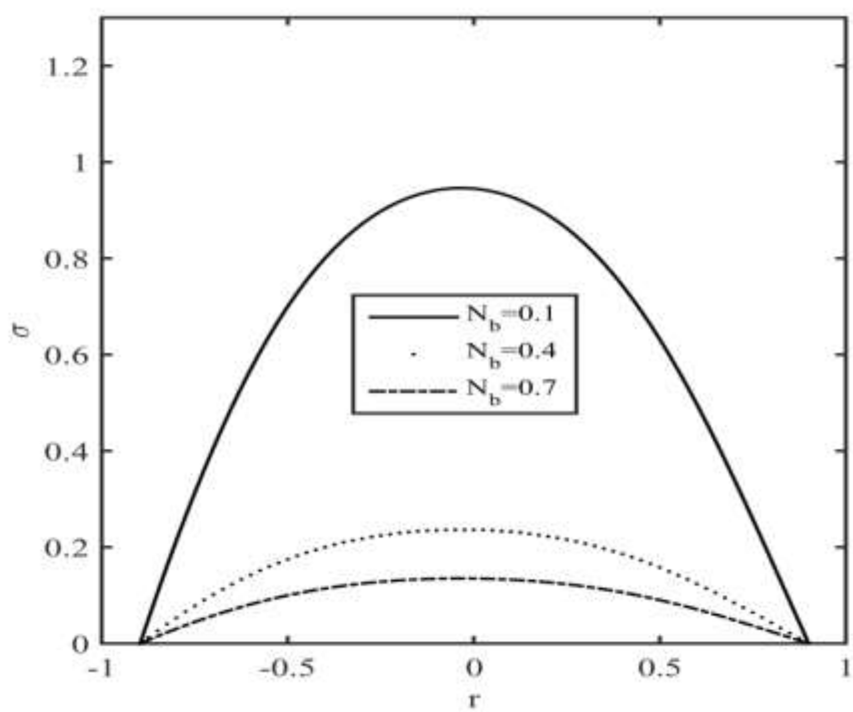

Figure 3.13

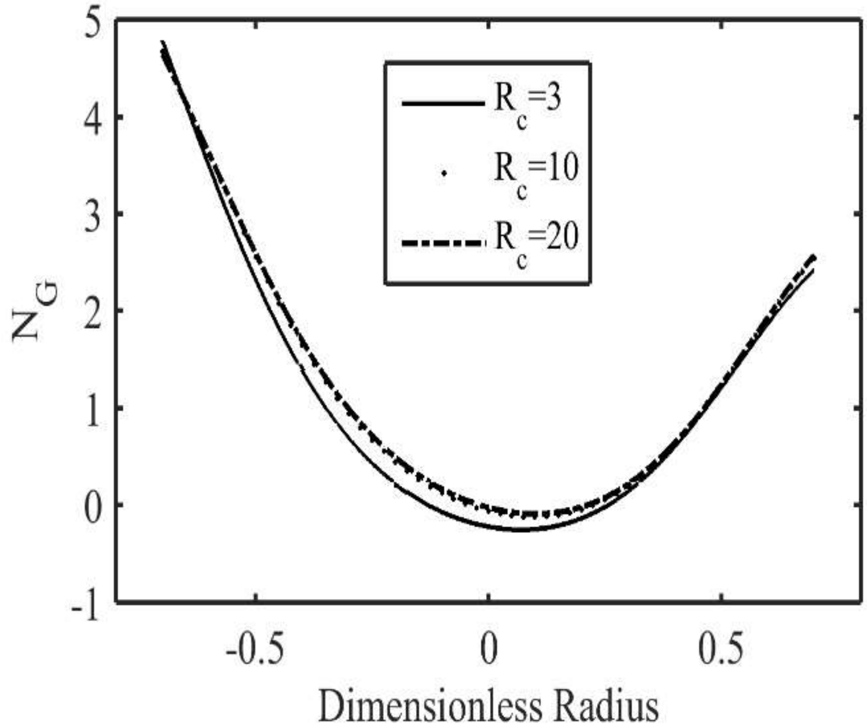

Figure 3.14

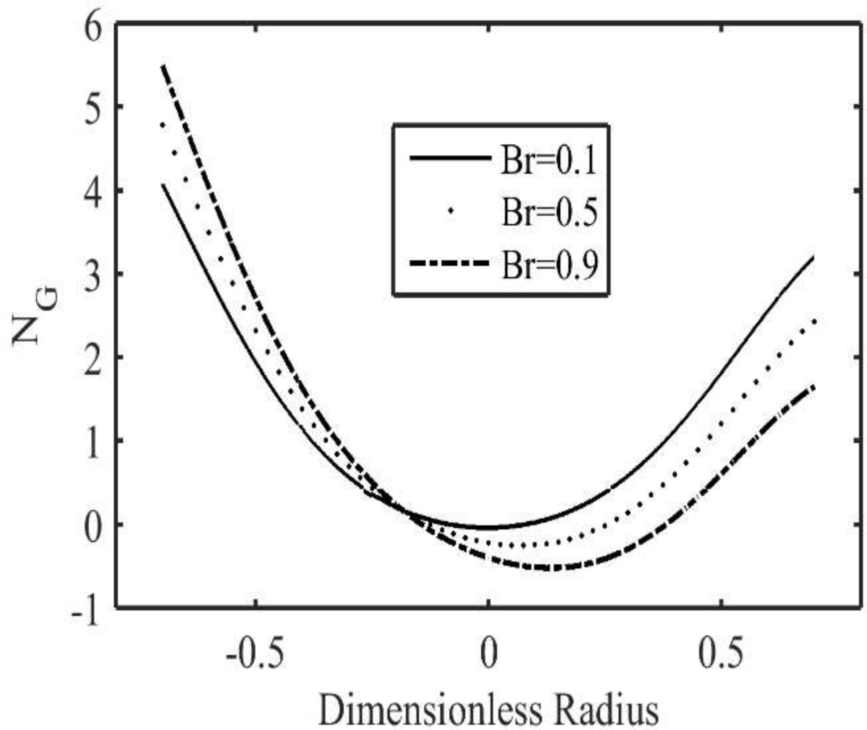

Figure 3.15

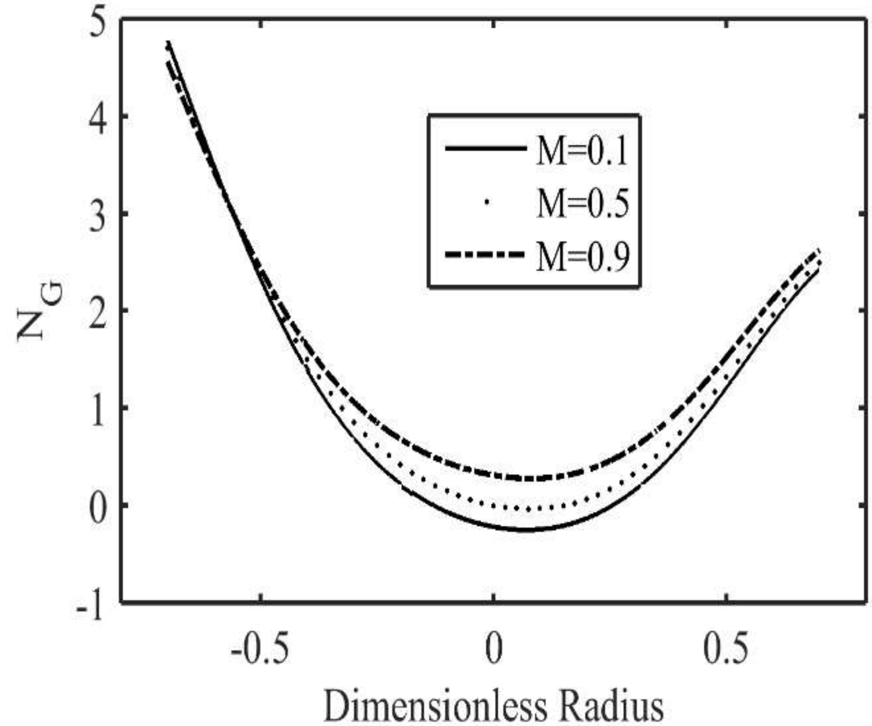

Figure 3.16

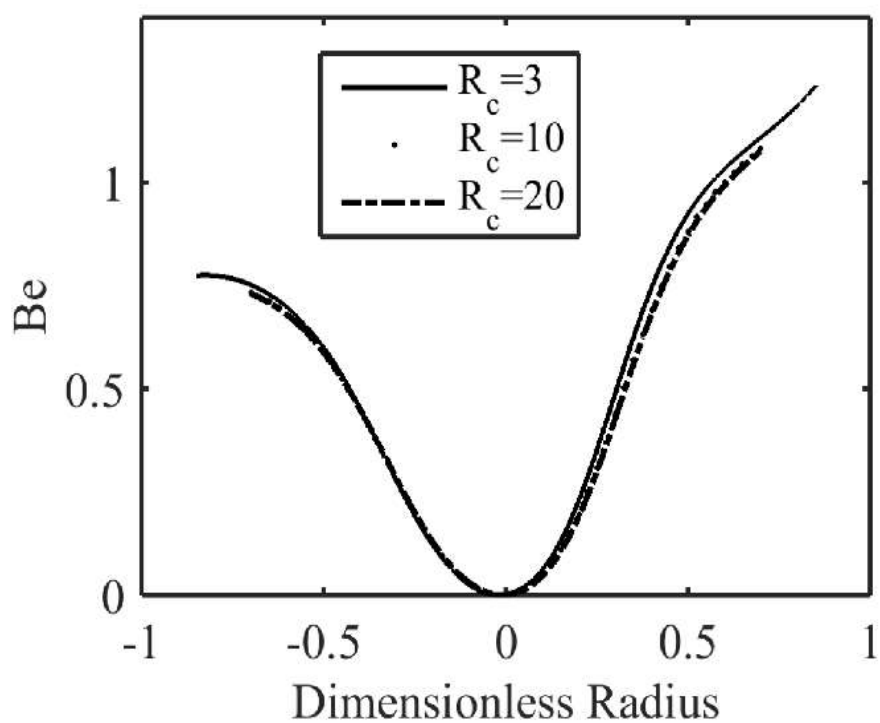

Figure 3.17

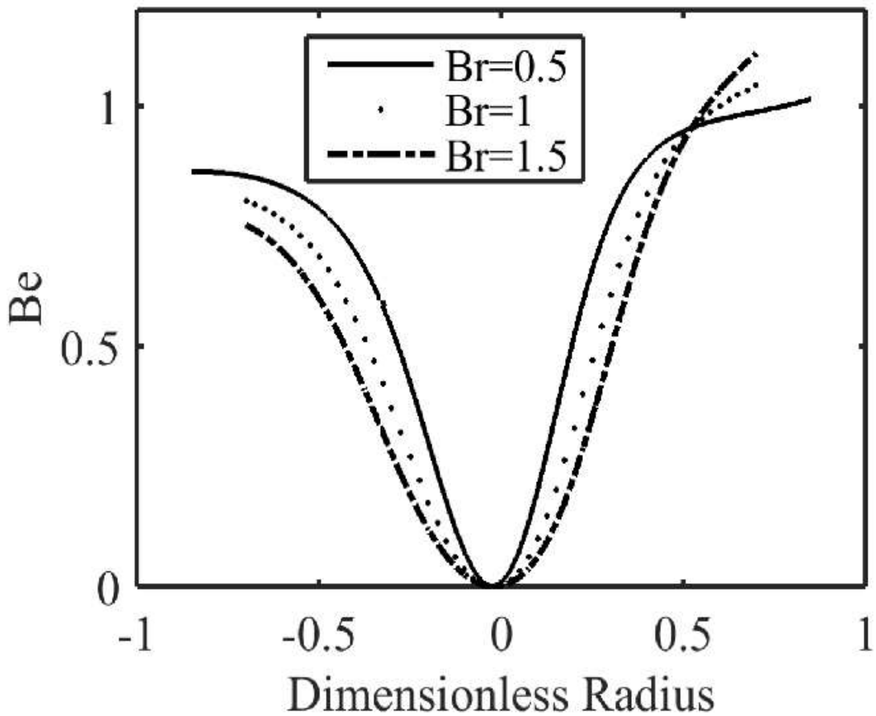

Figure 3.18

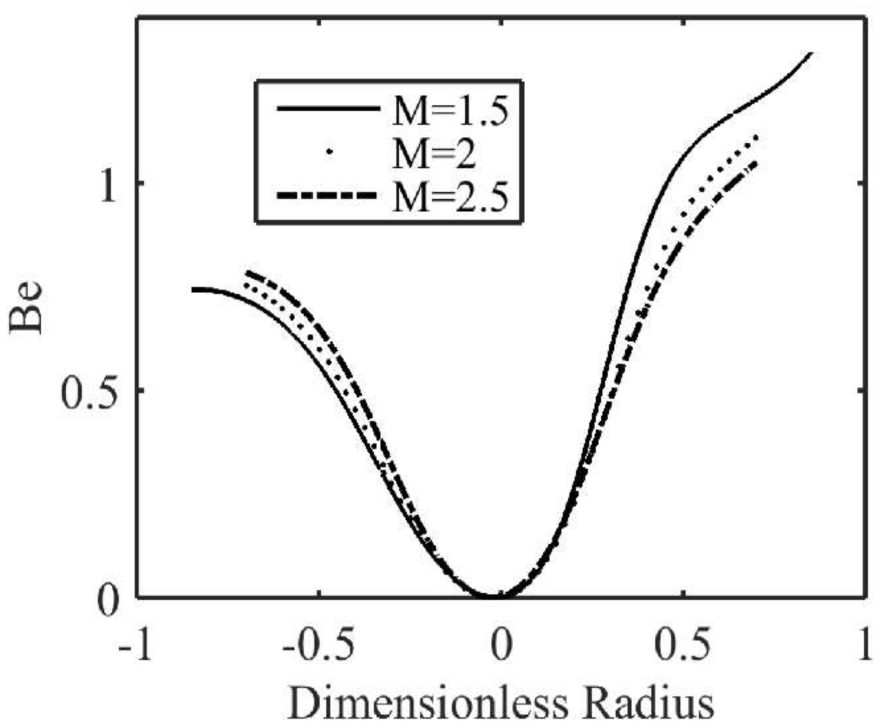

Figure 3.19

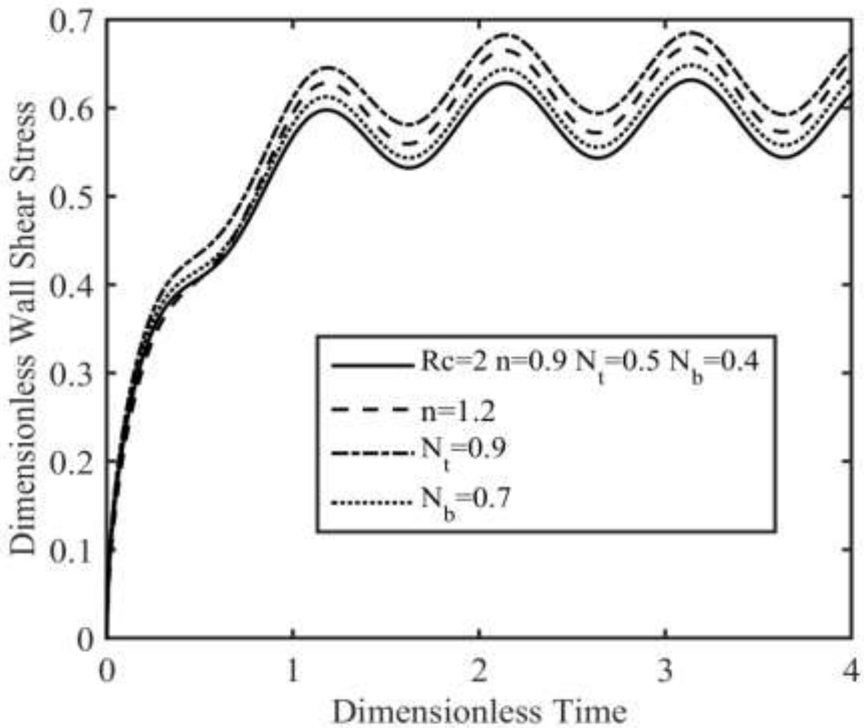

Figure 3.20

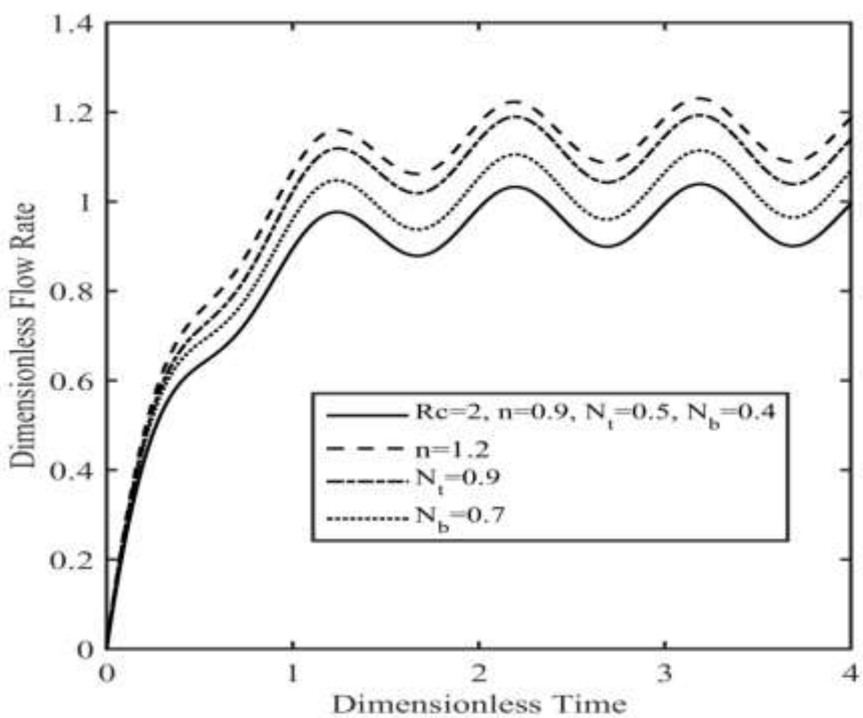

Figure 3.21

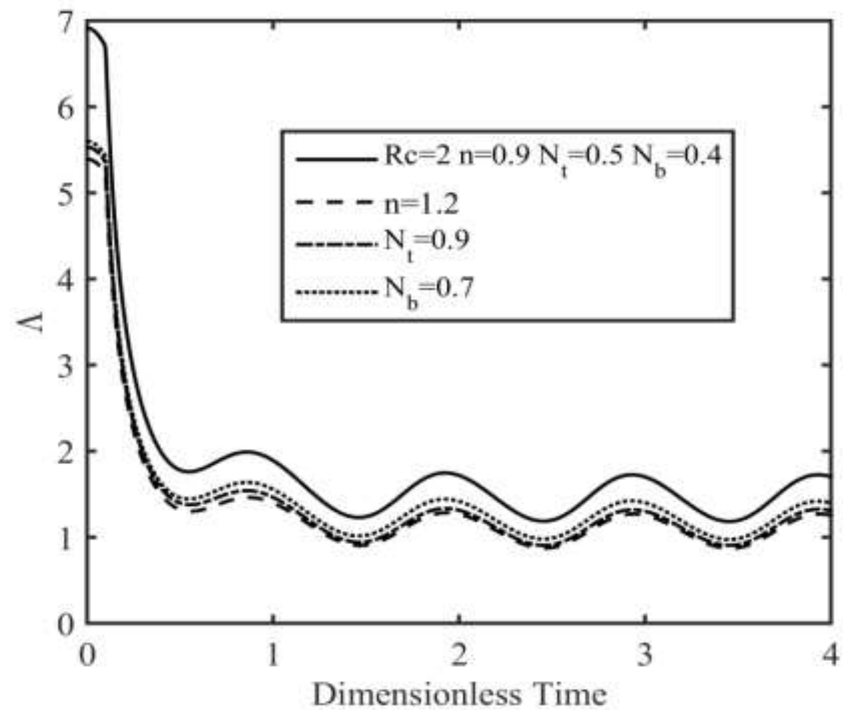

Figure 3.22

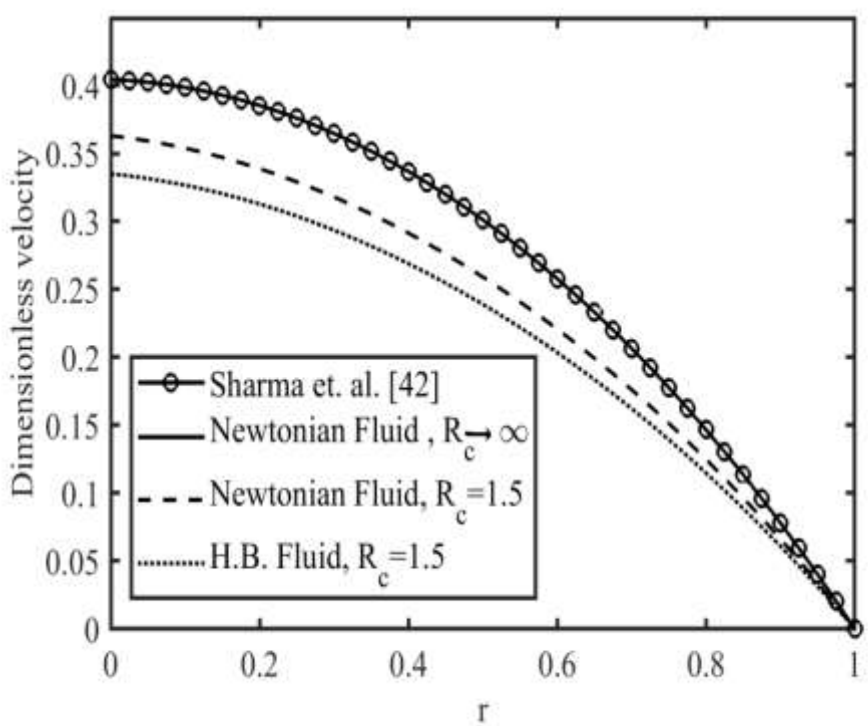

Figure 3.23

Chapter 4

Numerical Simulation of Pulsatile Flow of Tangent Hyperbolic Fluid in a Diseased Curved Artery with Electro-Osmotic Effects

In this chapter Time-dependent blood flow via a w-shaped stenotic conduit affected by a pulsatile pressure gradient is solved numerically. The theoretical model of tangent hyperbolic fluid is utilized to formulate the problem. To represent the issue, cylindrical coordinates are used, and the electro-osmotic effects are taken into consideration. To simplify the non-dimensional governing equations of the flow problem, mild stenosis assumption is utilized. The impact of the wall of the blood vessel is mitigated by employing the radial coordinate transformation. To resolve the consequent nonlinear set of differential equations, an explicit finite difference approach is employed, taking into account the boundary conditions that have been stated. An examination of the numbers behind the big picture, such as axial velocity, temperature field, concentration Nusselt number, and Sherwood number, is carried out after appropriate changes have been made to the essential non-dimensional factors. These results are presented in a graphical format, and a concise explanation of them is provided below.

4.1 Flow Equation

The unsteady, laminar, fully developed flow of blood through a curved blood vessel, having overlapping stenosis in its limen is taken into account. The artery of length "L" is spiraled in a circle of radius R^c. The mathematical expression for the geometry of the curved blood vessel is defined as:

$$R(z)=\left\{\begin{array}{ll}\left(\tau' z+e_0\right)\left(1-\frac{64}{10}\eta\left(\frac{11}{32}l_0^3\left(z-d\right)-\frac{47}{48}l_0^2\left(z-d\right)^2+l_0\left(z-d\right)^3-\frac{1}{3}\left(z-d\right)^4\right)\right), & d\le z\le d+\frac{3}{2}l_0, \\ \left(\tau' z+e_0\right), & otherwise\end{array}\right\}, Outer\ wall,$$

$$-R(z)=\left\{\begin{array}{ll}\left(\tau' z-e_0\right)\left(1-\frac{64}{10}\eta\left(\frac{11}{32}l_0^3\left(z-d\right)-\frac{47}{48}l_0^2\left(z-d\right)^2+l_0\left(z-d\right)^3-\frac{1}{3}\left(z-d\right)^4\right)\right), & d\le z\le d+\frac{3}{2}l_0, \\ \left(\tau' z-e_0\right), & otherwise\end{array}\right\}, Inner\ wall.$$

(4.1)

Here, the outer and inner walls of the curved blood vessel are designated by $R(z)$ and $-R(z)$ respectively. In the Eq. (4.1) e_0 is the radius of the normal blood vessel, $\tau'=\tan\varphi$ is the tapering parameter and φ is the tapering angle, d symbolized the location of the abnormality present in the lumen of the blood vessel, l_0 is the length of the stenosis. The radial and axial coordinates are represented by r and z respectively. This η parameter is declared as a constant, and it is used as:

$$\eta=\frac{4\delta^*}{a{l_0}^4}, \tag{4.2}$$

The value of δ^* is negative post stenotic dilatation and positive for stenosis this, δ^* shows the critical height of the stenotic zone in two places (i.e).

$$z=d+\frac{8l_0}{25},\ \text{and}\ z=d+\frac{61l_0}{50}. \tag{4.3}$$

The schematic diagram of the diseased curved blood vessel is shown in Fig. (4.1)

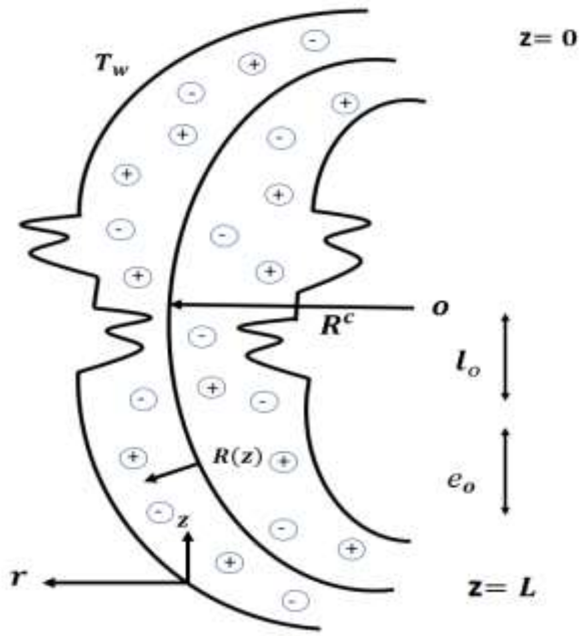

Figure 4.1

The flow field's governing equation is given by:

$$\bar{V} = u(t,r,z), 0, w(t,r,z)\ , \quad T^* = T^*(t,r,z), \quad C^* = C^*(t,r,z). \tag{4.4}$$

The u is radial component w is the axial component of velocity in Eq. (4.4), whereas is the temperature component denoted by T^* and the concentration component of nanoparticles denoted by C^*.

The following are the continuity equation, momentum equation, energy equation, and mass absorption equation are:

$$\frac{\partial}{\partial r}\left(r+R^c\right)u + R^c\frac{\partial w}{\partial z} = 0, \tag{4.5}$$

$$\begin{aligned}\rho_f\left(\frac{\partial u}{\partial t} + u\frac{\partial u}{\partial r} + \frac{R^c}{r+R^c}w\frac{\partial u}{\partial z} - \frac{u^2}{r+R^c}\right) = -\frac{\partial p}{\partial r} + \frac{1}{\left(r+R^c\right)^2}\frac{\partial}{\partial r}\left(\left(r+R^c\right)S^{rr}\right) \\ + \frac{R^c}{r+R^c}\frac{\partial S^{rz}}{\partial z} - \frac{S^{zz}}{r+R^c},\end{aligned} \tag{4.6}$$

$$\rho_f\left(\frac{\partial w}{\partial t}+u\frac{\partial w}{\partial r}+\frac{R^c}{r+R^c}w\frac{\partial w}{\partial z}+\frac{uw}{r+R^c}\right)=+\rho g\alpha_{C^1}\left(C^*-C_1\right)-\left(\frac{R^c}{r+R^c}\right)^2\alpha\beta_o^2w+\rho_eE_z$$
$$-\left(\frac{R^c}{r+R^c}\right)\frac{\partial p}{\partial z}+\frac{R^c}{r+R^c}\frac{\partial S^{zz}}{\partial z}+\frac{1}{\left(r+R^c\right)^2}\frac{\partial}{\partial r}\left(\left(r+R^c\right)S^{rz}\right)+\rho g\alpha_T\left(T^*-T_w\right), \tag{4.7}$$

$$\left(\rho c_p\right)_f\left(\frac{\partial T^*}{\partial t}+u\frac{\partial T^*}{\partial r}+\frac{R^c}{r+R^c}w\frac{\partial T^*}{\partial z}\right)=k_f\left(\frac{\partial^2T^*}{\partial r^2}+\frac{1}{r+R^c}\frac{\partial T^*}{\partial r}+\left(\frac{R^c}{r+R^c}\right)^2\frac{\partial^2T^*}{\partial z^2}\right)$$
$$+\left(\rho c\right)_p\left[\left(D_\beta\left(\frac{\partial C^*}{\partial r}\frac{\partial T^*}{\partial r}+\left(\frac{R^c}{r+R^c}\right)^2\frac{\partial C^*}{\partial z}\frac{\partial T^*}{\partial z}\right)+\frac{D_{T^*}}{T_w-T_1}\left(\left(\frac{\partial T^*}{\partial r}\right)^2+\left(\frac{R^c}{r+R^c}\right)^2\left(\frac{\partial T^*}{\partial z}\right)^2\right)\right)\right]$$
$$+\left(\frac{R^c}{r+R^c}\right)^2\alpha\beta_o^2w^2, \tag{4.8}$$

$$\frac{\partial C^*}{\partial t}+u\frac{\partial C^*}{\partial r}+w\frac{\partial C^*}{\partial z}=D_\beta\left(\frac{\partial^2C^*}{\partial r^2}+\left(\frac{R^c}{r+R^c}\right)^2\frac{\partial^2C^*}{\partial z^2}+\frac{1}{r+R^c}\frac{\partial C^*}{\partial r}\right)$$
$$+\frac{D_{T^*}}{T_w-T_1}\left(\frac{\partial^2T^*}{\partial r^2}+\left(\frac{R^c}{r+R^c}\right)^2\frac{\partial^2T^*}{\partial z^2}+\frac{1}{r+R^c}\frac{\partial T^*}{\partial r}\right). \tag{4.9}$$

The terms S^{rr}, S^{rz} and S^{zz} are the supplementary part of the stress tensor represented by Eqs. (6) and (7). In the tangent hyperbolic model, the connection is expressed as: $\boldsymbol{\tau}=\boldsymbol{S}-p\boldsymbol{I}, \boldsymbol{S}=\left\{\mu_\infty+\left(\mu_0-\mu_\infty\right)\tanh\left(\Gamma\,|\overset{*}{\gamma}|^n\right)\right\},$ (4.10)

In (4.10) p is signifies pressure, $\boldsymbol{I}$ is identity tensor and the $\boldsymbol{S}$ is noninotropic component. The shear viscosity of a fluid changes from Newtonian to infinitely shear thinning at the transition from 0 to 1 in the power-law index n .Several factors, such as Molecular weight distribution, solvent, polymer type and concentration, etc., The shear rates that mark the beginning and end of the upper and lower viscosity limits can be influenced. Consequently, it might be difficult to draw reliable generalizations. The viscosity limit μ_0, which is challenging to estimate with current experimental approaches, is around 10 times greater than μ_∞ in stable states. There have been various generalized Newtonian models proposed for blood viscosities $\mu_0=0.56$ and $\mu_\infty=0.0345$.

The first Rivlin-Ericksen tensor can be constructed $\overset{*}{\gamma}$ as

$$\overset{*}{\gamma}=\sqrt{\frac{1}{2}\pi}. \tag{4.11}$$

Definition of the first Rivlin-Ericksen tensor for the second invariant

$$\pi=trac\left(\nabla\boldsymbol{V}+\nabla\boldsymbol{V}^{T}\right). \tag{4.12}$$

For a curved channel, we get the same result as in Eq. (4.4) from the constitutive relation (4.10).

$$S^{rr}=2\left\{\mu_{\infty}+\left(\mu_{0}-\mu_{\infty}\right)\tanh\left(\Gamma\,|\overset{*}{\gamma}|^{n}\right)\right\}\left(\frac{\partial u}{\partial r}\right), \tag{4.13}$$

$$S^{zz}=2\left\{\mu_{\infty}+\left(\mu_{0}-\mu_{\infty}\right)\tanh\left(\Gamma\,|\overset{*}{\gamma}|^{n}\right)\right\}\left(\frac{R^{c}}{r+R^{c}}\frac{\partial w}{\partial z}+\frac{u}{r+R^{c}}\right), \tag{4.14}$$

$$S^{rz}=\left\{\mu_{\infty}+\left(\mu_{0}-\mu_{\infty}\right)\tanh\left(\Gamma\,|\overset{*}{\gamma}|^{n}\right)\right\}\left(\frac{\partial w}{\partial r}+\frac{R^{c}}{r+R^{c}}\frac{\partial u}{\partial z}-\frac{w}{r+R^{c}}\right), \tag{4.15}$$

$$\pi=\left\|\left[\frac{1}{2}\left(\left(2\frac{\partial u}{\partial r}\right)^{2}+2\left(\frac{\partial w}{\partial r}+\frac{R^{c}}{r+R^{c}}\frac{\partial u}{\partial z}-\frac{w}{r+R^{c}}\right)^{2}+\left(\frac{R^{c}}{r+R^{c}}\frac{\partial w}{\partial z}+\frac{u}{r+R^{c}}\right)^{2}\right)\right]\right\|. \tag{4.16}$$

The dimensions of the following equations are removed when utilizing variables (4.5)-(4.9):

$$\bar{r}=\frac{r}{e_{0}},\;\; \bar{w}=\frac{w}{U_{0}},\;\; \bar{u}=\frac{l_{0}u}{\delta^{*}U_{0}},\;\; \bar{t}=\frac{U_{0}}{e_{0}}t,\;\; \bar{z}=\frac{z}{l_{0}},\;\; R_{c}=\frac{R^{c}}{e_{0}},\;\; \bar{p}=\frac{e_{0}^{2}p}{U_{0}l_{0}\mu_{0}},\;\; \theta=\frac{T^{*}-T_{w}}{T_{1}-T_{w}},$$
$$P_{r}=\frac{\left(c_{p}\right)_{f}\mu_{f}}{k_{f}},\;\; Gr_{T}=\frac{\rho g\alpha_{T}e_{0}^{2}}{U_{0}\mu_{0}}\left(T_{1}-T_{w}\right),\;\rho_{e}=-\nabla^{2}\varphi E,\;\; Br=\frac{\rho ge_{0}^{2}}{U_{0}\mu_{0}}\alpha_{C}C_{1},\;\; \varphi=\frac{\bar{\varphi}}{\varphi_{m}},$$
$$Le=\frac{\mu_{0}}{\rho D_{\beta}},\;\; N_{t}=\frac{\tau D_{T^{*}}}{k_{f}},\;\mathrm{Re}=\frac{\rho_{f}U_{0}e_{0}}{\mu_{0}},m=\frac{\mu_{\infty}}{\mu_{0}},\bar{S}^{rz}=\frac{e_{0}}{U_{0}\mu_{0}}S^{rz},\;\; \bar{S}^{rr}=\frac{l_{0}}{U_{0}\mu_{0}}S^{rr},$$
$$\bar{S}^{zz}=\frac{l_{0}}{U_{0}\mu_{0}}S^{zz},We=\frac{\Gamma U_{0}}{e_{0}},\;\sigma=\frac{C^{*}-C_{1}}{C_{1}},\;\; M^{2}=\frac{\alpha\beta_{o}^{2}e_{0}}{\mu_{0}},\;N_{b}=\frac{\tau D_{\beta}C_{1}}{k_{f}}. \tag{4.17}$$

In the above definitions, $\bar{w}$ is axial velocity, $\bar{r}$ is radial coordinate, $\bar{z}$ axial directional co-ordinate, $\bar{t}$ is time, $\bar{R}$ is the radius, $\bar{p}$ is the pressure, Br the Brinkman number, Re is the Reynolds number, Gr is the local thermal Grashof number, Pr is the Prandtl number, U_0 is the average velocity of the blood, T_w represent the wall temperature, σ is nanoparticles concentration function and T_m represent the thermodynamic temperature. When the constraints were lifted, the Simplified Eqs. (4.5)-(4.9) are:

$$\delta\left(\frac{\partial}{\partial r}(r+R_c)u\right)+R_c\frac{\partial w}{\partial z}=0, \tag{4.18}$$

$$\operatorname{Re}\delta\varepsilon^2\left(\frac{\partial u}{\partial t}+\delta\varepsilon u\frac{\partial u}{\partial r}+\varepsilon\frac{R_c}{r+R_c}w\frac{\partial u}{\partial z}-\frac{\varepsilon}{\delta}\frac{u^2}{r+R_c}\right)=-\frac{\partial p}{\partial r}+\varepsilon^2\left(\frac{1}{(r+R_c)^2}\frac{\partial}{\partial r}\left((r+R_c)S^{rr}\right)\right)$$
$$+\varepsilon^2\left(\frac{R_c}{r+R_c}\right)\frac{\partial S^{rz}}{\partial z}-\frac{\varepsilon^2 S^{zz}}{r+R_c}, \tag{4.19}$$

$$\operatorname{Re}\frac{\partial w}{\partial t}+\operatorname{Re}\left(\delta\varepsilon\frac{\partial w}{\partial r}+\varepsilon\frac{R_c}{r+R_c}w\frac{\partial w}{\partial z}+\delta\varepsilon\frac{uw}{r+R^c}\right)=-\left(\frac{R_c}{r+R_c}\right)\frac{\partial p}{\partial z}+\frac{1}{(r+R_c)^2}\frac{\partial}{\partial r}\left((r+R_c)^2S^{rz}\right)$$
$$+\varepsilon^2\left(\frac{R_c}{r+R_c}\right)\frac{\partial S^{zz}}{\partial z}+Gr_T\theta+Br\sigma-\left(\frac{R_c}{r+R_c}\right)^2M^2w+Uhs\left(\frac{\partial^2\varphi}{\partial r^2}+\frac{1}{r+R_c}\frac{\partial\varphi}{\partial r}+\delta^2\left(\frac{R_c}{r+R_c}\right)^2\frac{\partial^2\varphi}{\partial r^2}\right), \tag{4.20}$$

$$\Pr\operatorname{Re}\left(\frac{\partial\theta}{\partial t}+\delta\varepsilon\frac{\partial\theta}{\partial r}+\varepsilon\frac{R_c}{r+R_c}w\frac{\partial\theta}{\partial z}\right)=\frac{\partial^2\theta}{\partial r^2}+\frac{1}{r+R_c}\frac{\partial\theta}{\partial r}+\varepsilon^2\left(\frac{R_c}{r+R_c}\right)^2\frac{\partial^2\theta}{\partial z^2}$$
$$+N_b\left(\frac{\partial\sigma}{\partial r}\frac{\partial\theta}{\partial r}+\varepsilon^2\left(\frac{R_c}{r+R_c}\right)^2\frac{\partial\sigma}{\partial z}\frac{\partial\theta}{\partial z}\right)+N_t\left(\left(\frac{\partial\theta}{\partial r}\right)^2+\varepsilon^2\left(\frac{R_c}{r+R_c}\right)^2\left(\frac{\partial\theta}{\partial z}\right)^2\right) \tag{4.21}$$
$$+\left(\frac{R_c}{r+R_c}\right)^2BrM^2w^2,$$

$$\operatorname{Re}Le\left(\frac{\partial\sigma}{\partial t}+\delta\varepsilon\frac{\partial\sigma}{\partial r}+\varepsilon w\frac{\partial\sigma}{\partial z}\right)=\frac{\partial^2\sigma}{\partial r^2}+\frac{1}{r+R_c}\frac{\partial\sigma}{\partial r}+\varepsilon^2\left(\frac{R_c}{r+R_c}\right)^2\frac{\partial^2\sigma}{\partial z^2}$$
$$+\frac{N_t}{N_b}\left(\frac{\partial^2\theta}{\partial r^2}+\frac{1}{r+R_c}\frac{\partial\theta}{\partial r}+\varepsilon^2\left(\frac{R_c}{r+R_c}\right)^2\frac{\partial^2\theta}{\partial z^2}\right). \tag{4.22}$$

We utilize two assumptions based on mild stenosis in the accompanying analysis: $\varepsilon\left(=\frac{e_0}{l_0}\right)=O(1)$ and $\delta\left(=\frac{\delta^*}{e_0}\right)\ll 1$ i.e. The first requirement is that the stenotic region be no longer than the channel's radius. The second requirement is that the track length's elevation be smaller than the channel radius.

4.2 Electroosmotic Effects

A mass fluid is displaced across a dense area by particles in an electrical double layer (EDL) under the influence of a strong external electric field. The term for this phenomenon is electroosmotic flow (EOF). Using the Poisson-Boltzmann equation, we can show how the electric-osmotic potential is distributed:

$$\nabla^2 \overline{\varphi} = \frac{\overline{\varphi}}{k^2}, \tag{4.23}$$

Where

$$\nabla^2 = \frac{\partial^2}{\partial r^2} + \frac{1}{r+R^c}\frac{\partial}{\partial r} + \left(\frac{R^c}{r+R^c}\right)^2 \frac{\partial^2}{\partial z^2}.$$

When an electrolyte solution (blood) and solid conduct (arterial walls) come into touch, a phenomenon known as electroosmotic happens. A layer called the electrical double layer (EDL) forms near the surface due to ion concentration differences.

$$\nabla^2 \overline{\varphi} = -\frac{\rho_e}{E}, \tag{4.24}$$

ρ_e is total net charge density per unit volume of liquid (blood) is defined, where φ is the electro-osmotic function, E is the dielectric constant, and defined as

$$\rho_e = e\overline{z}\left(n^+ - n^-\right). \tag{4.25}$$

The numerical density of caution and anion, as given by the Boltzmann distribution, is:

$$n^{\pm} = n_0 exp\left(\pm \frac{e\overline{z\varphi}}{k_B \overline{T}}\right), \tag{4.26}$$

Determine the n_0 bulk ion concentration, the electric constant, and k_B the Boltzmann constant from where $\overline{z}$ and e is the charge balance and the electric constant respectively. We can combine Eqs. (4.25) and (4.26) By utilizing the property of $\sinh = \frac{e^x - e^{-x}}{2}$, we get:

$$\rho_e = -2n_0 e\overline{z}\sinh\left(\frac{e\overline{z\varphi}}{k_B\overline{T}}\right). \tag{4.27}$$

In accordance with the Debye-Huckel linearization principle, Equation (4.27) can be written as

$$\rho_e = -\frac{2n_0 e^2\overline{z}^2}{k_B\overline{T}}\overline{\varphi}. \tag{4.28}$$

The Specific arrangement of conditions is gotten with these circumstances

$$\varphi(t,r)\big|_{r=R} = 1, \qquad \varphi(0,r) = 0.0, \qquad \varphi(t,r)\big|_{r=-R} = 1 \ . \tag{4.29}$$

Combine the Eqs. (4.24) and (4.29), to get the Poisson-Boltzmann equation as:

$$\frac{\partial^2\varphi}{\partial r^2} + \frac{1}{r+R_c}\frac{\partial\varphi}{\partial r} = k^2\varphi. \tag{4.30}$$

The equation (4.30) provides a boundary value problem, and an analytical solution to this problem can be derived as

$$\varphi(r,z) = \frac{\begin{array}{c} I_o\left(k\left(R-R_c\right)\right)K_0\left(-k\left(r+R_c\right)\right) - I_o\left(k\left(R+R_c\right)\right)K_0\left(-k\left(r+R_c\right)\right) + \\ I_o\left(k\left(r+R_c\right)\right)K_0\left(-k\left(R+R_c\right)\right) - I_o\left(k\left(r+R_c\right)\right)K_0\left(k\left(R-R_c\right)\right) \end{array}}{I_o\left(k\left(R-R_c\right)\right)K_0\left(-k\left(R+R_c\right)\right) - I_o\left(k\left(R+R_c\right)\right)K_0\left(k\left(R-R_c\right)\right)}. \tag{4.31}$$

Here I_0 and K_0 are Bessel functions with modifications of the first and second kinds.

Equation (4.18) to (4.22) is here's a reduction of the following:

$$\frac{\partial p}{\partial r} = 0, \tag{4.32}$$

$$\operatorname{Re}\frac{\partial w}{\partial t}=-\left(\frac{R_c}{r+R_c}\right)\frac{\partial p}{\partial z}+Gr_T\theta+Br\sigma-\left(\frac{R_c}{r+R_c}\right)^2 M^2 w+U_{HS}k^2\varphi(r,z)+$$
$$\frac{1}{(r+R_c)^2}\frac{\partial}{\partial r}\left((r+R_c)^2\left(m+(1-m)\tanh\left(We\left(\frac{\partial w}{\partial r}-\frac{w}{r+R^c}\right)\right)^n\right)\left(\frac{\partial w}{\partial r}-\frac{w}{r+R^c}\right)\right), \tag{4.33}$$

$$\Pr\operatorname{Re}\frac{\partial\theta}{\partial t}=\frac{\partial^2\theta}{\partial r^2}+\frac{1}{r+R_c}\frac{\partial\theta}{\partial r}+N_b\left(\frac{\partial\sigma}{\partial r}\frac{\partial\theta}{\partial r}\right)+N_t\left(\frac{\partial\theta}{\partial r}\right)^2+\left(\frac{R_c}{r+R_c}\right)^2 M^2 Brw^2, \tag{4.34}$$

$$\operatorname{Re}Le\frac{\partial\sigma}{\partial t}=\frac{\partial^2\sigma}{\partial r^2}+\frac{1}{r+R_c}\frac{\partial\sigma}{\partial r}+\frac{N_t}{N_b}\left(\frac{\partial^2\theta}{\partial r^2}+\frac{1}{r+R_c}\frac{\partial\theta}{\partial r}\right). \tag{4.35}$$

The equation for the Pulsatile Pressure gradient is:

$$-\frac{\partial p}{\partial z}=A_0+A_1\cos(2\pi\omega_p t),\qquad t>0. \tag{4.36}$$

Equation (36), A_0 denotes the mean pressure gradient, and A_1 which represents the amplitude of the pulsatile component, which may be found by solving for it.

$$-\frac{\partial p}{\partial z}=B_1(1+c\cos(c_1 t)), \tag{4.37}$$

Where

$$c_1=\frac{2\pi\omega_p e_0}{U_0},\quad c=\frac{A_1}{A_0},\quad B_1=\frac{A_0e_0^2}{\mu_0U_0}. \tag{4.38}$$

In Equation (4.37) using the term $-\partial p/\partial z$ we get:

$$\operatorname{Re}\frac{\partial w}{\partial t}=\left(\frac{R_c}{r+R_c}\right)B_1(1+c\cos(c_1t))-\left(\frac{R_c}{r+R_c}\right)^2 M^2 w+U_{HS}k^2\varphi(r,z)+$$
$$\frac{1}{(r+R_c)^2}\frac{\partial}{\partial r}\left((r+R_c)^2\left(m+(1-m)\tanh\left(We\left(\frac{\partial w}{\partial r}-\frac{w}{r+R^c}\right)\right)^n\right)\left(\frac{\partial w}{\partial r}-\frac{w}{r+R^c}\right)\right)+Gr_T\theta+Br\sigma, \tag{4.39}$$

Eqs. (4.33)-(4.34) and (4.35) have the following set of constraints and beginning conditions imposed on them::

$$w(t,r)\big|_{r=R}=0,\qquad w(0,r)=0.0,\qquad w(t,r)\big|_{r=-R}=0. \tag{4.40}$$

$$\sigma(t,r)\big|_{r=R}=0, \qquad \sigma(0,r)=0.0, \qquad \sigma(t,r)\big|_{r=-R}=0. \tag{4.41}$$

$$\theta(t,r)\big|_{r=R}=1, \qquad \theta(0,r)=0.0, \qquad \theta(t,r)\big|_{r=-R}=1. \tag{4.42}$$

The rate of heat transfer (as measured by the Nusselt number) and the rate of mass transfer (as measured by the Sherwood number) are two essential criteria for evaluating blood flow.

$$Nu=\frac{R_c q_w}{k(T_1-T_w)}=-\left[\frac{\partial\theta}{\partial r}\right]_{r=1} \qquad \text{where} \quad q_w=-k\left[\frac{\partial T^*}{\partial r}\right]_{r=R} \tag{4.43}$$

$$Sh=\frac{R_c J_w}{D_\beta C_1}=-\left[\frac{\partial\sigma}{\partial r}\right]_{r=1} \qquad \text{where} \quad J_w=-D_\beta\left[\frac{\partial C^*}{\partial r}\right]_{r=R} \tag{4.44}$$

The simple equation for the dimensionlized geometry of an arterial segment is as follows:

$$\begin{aligned}
&R(z)=(1+\tau z)\left[1-\frac{64}{10}\eta_1\left(\frac{11}{32}(z-\sigma)-\frac{47}{48}(z-\sigma)^2+(z-\sigma)^3-\frac{1}{3}(z-\sigma)^4\right)\right],\\
&\sigma\le z\le\sigma+\frac{3}{2},\ \textit{Outer wall},\\
&-R(z)=(-1+\tau z)\left[1+\frac{64}{10}\eta_1\left(\frac{11}{32}(z-\sigma)-\frac{47}{48}(z-\sigma)^2+(z-\sigma)^3-\frac{1}{3}(z-\sigma)^4\right)\right],\\
&\sigma\le z\le\sigma+\frac{3}{2},\ \textit{Inner wall},
\end{aligned} \tag{4.45}$$

Where $\eta_1=4\delta,\ \delta=\dfrac{\delta^*}{e_0},\ \sigma=\dfrac{d}{l_0},\ \tau=\dfrac{\tau' l_0}{e_0}.$

4.3 Solution Methodology

We utilize the explicit finite difference approach in the numerical method.

By utilizing the algebraic transformation provided above in Eqs. (4.39), (4.34) and (4.35):

$$w_i^{k+1} = w_i^k + \left(\frac{R_c}{r+R_c}\right)\frac{\Delta t}{\mathrm{Re}}B_1\left(1+c\cos\left(c_1 t\right)\right) - \left(\frac{R_c}{r+R_c}\right)^2 M^2 w_i^k + U_{HS}k^2\varphi\left(r,z\right) +$$
$$\frac{1}{\left(r+R_c\right)^2}\frac{\partial}{\partial r}\left(\left(r+R_c\right)^2\left(m+\left(1-m\right)\tanh\left(We\left(w_r - \frac{w_i^k}{r+R^c}\right)\right)^n\right)\left(w_r - \frac{w_i^k}{r+R^c}\right)\right) \tag{4.46}$$
$$+Gr_T\theta_i^k + Br\sigma_i^k,$$

$$\theta_i^{k+1} = \theta_i^k + \frac{\Delta t}{\mathrm{Re}\,\mathrm{Pr}}\left\{\left(\theta_{rr} + \frac{1}{r+R_c}\theta_r\right) + N_b\theta_r\sigma_r + N_t\left(\theta_r\right)^2 + \left(\frac{R_c}{r+R_c}\right)^2 M^2 Br\left(W^2\right)_i^k\right\}, \tag{4.47}$$

$$\sigma_i^{j+1} = \sigma_i^j + \frac{\Delta t}{\mathrm{Re}\,Le}\left\{\left(\sigma_{rr} + \frac{1}{r+R_c}\sigma_r\right) + \frac{N_t}{N_b}\left(\theta_{rr} + \frac{1}{r+R_c}\theta_r\right)\right\}. \tag{4.48}$$

The numerical boundary and initial condition have been defined as follows:

$$\begin{aligned} &w_i^1 = 0 = \theta_i^1,\ \sigma_i^1 = 0 && at\ t = 0,\\ &w_1^k = \theta_1^k = 1,\ \sigma_i^1 = 0 && at\ r = -R\left(x\right),\\ &w_{N+1}^k = \theta_{N+1}^k = 1,\ \sigma_i^1 = 0 && at\ r = R\left(x\right). \end{aligned} \tag{4.49}$$

4.4 Discussion of Results

The sections that follow analyses the outcomes of the numerical results in considerable depth. The programming code is developed in MATLAB. To solve the partial differential equation, a set of preset integers is chosen. $\mathrm{Pr} = 9,\ \mathrm{Re} = 1,\ B_1 = 1.41,$ $x = 0.9, \mu_0 = 0.56, \mu_\infty = 0.0345, We = 0.5, Uhs = 1.$ It has been demonstrated that the mentioned data is strongly linked to conditions in the bloodstream, which is a real-world manifestation. Small blood artery rheological currents are consistent with the mode and are of proportionally the same size according to the low estimate of the Reynolds number (Re). Both heat and nanoparticles diffuse through a substance at since the diffusivity and the Lewis number are equivalent measures of rate quantifies the heat to species ratio. The next part is divided into two subsections. We place importance on the velocity profile because of the huge amount of information it provides about the fluid dynamics at play.

Fig. (4.2), we can pay attention to how the power-law exponent influences the axial velocity distribution. Increases in the exponent of the power law, the blood velocity decreases near the arterial wall and increases closer to the artery's core. According to Fig. (4.3), blood velocity decreases linearly with increasing (We). The fluid's viscoelastic properties are described by the dimensionless parameter (We), which establishes a relationship between elastic and viscous forces. Therefore, slower velocities are observed with greater viscoelastic blood is likely the case due to the fact that the shear thinning feature of blood is increased at higher Weissenberg numbers (We), this ultimately leads to a decrease in the apparent viscosity of the blood. As a result of this reduction in viscosity, there is a gradual slowing down in the axial velocity of the blood. Calculating the amount of work required to transport a unit charge from one site to another within the electroosmotic flow of aqueous solutions is an extremely important step in the process. Examining the distribution of electric potential (k) in the radial direction is the focus of this particular investigation. It is possible to demonstrate, using the data presented in Fig. (4.4) that the electric potential (k) grows exponentially as the size of the electric potential ratio increases. Within the context of curved channel flow, the degree to which the channel is curved has a substantial bearing on the flow of fluid. Fig. (4.5) shows the impact of curvature on electric potential Helmholtz-Smoulochowski parameter (Uhs). It should be observed that when the curvature parameter in the microchannel increases, the Helmholtz-Smoulochowski parameter (Uhs) also rises. This implies that while one moves, their electric potential rises microchannels can be straight or curved. At larger curvatures $\left(R_c\right)$ the velocity profile increases because the artery becomes straight, as shown in Fig. (4.6).

All signs point to the blood temperature being highest close to the arterial surface and lowest along the arterial centerline, as depicted by these figures. Examining Fig. (4.7) leads one to the conclusion that the curvature parameter $\left(R_c\right)$ has a relatively insignificant effect on the temperature distribution. The influence of curvature on temperature is negligibly insignificant. The temperature distribution in a stenotic blood artery for different Brinkman number $\left(Br\right)$ levels is shown in Fig. (4.8) the hypothesis that increasing (Br) levels raises blood temperature along the arterial axis is tested. Temperature plots for various Brownian motion parameter (N_b) and thermophoretic parameter (N_t) Fig. (4.9) and Fig. (4.10) with the change from (N_b) to (N_t), There was minimal change in the distribution of temperature.Fig (4.11) shows the effect of electric potential Helmholtz-Smoulochowski parameter (Uhs) on temperature profile which shows that (Uhs) is increasing. Figure (4.12) illustrates how the concentration field is affected by the Lewis number (Le). The size of the concentration profile and this component have a significant inverse connection. Concentrations decrease in magnitude as Lewis number (Le) rises. Concentration plots for various Brownian motion parameters (N_b) and thermophoretic parameters (N_t). Fig.(4.13) and Fig.(4.14) with the change from (N_b) to (N_t), both are showing opposite effects on concentration. By raising the amplitude and the Brownian motion parameter (N_b), the behaviour seen is improved in the concentration profile. Nanofluids behave more like two-phase liquids in nature because a rise in results in a larger degree of random motion among the suspended nanoparticles, which in turn creates a lower concentration in the flow system.

In Figure (4.15) and (4.16) we can see the variations in Nusselt number over time for a specific combination of parameters, such as (Re) and (Pr). This allows us to investigate the effect of fully modifiable settings. We compare each potential design to gold standard, depicted here with a single line. Under the low Reynolds number (Re) in Fig. (4.15) approximation, which is a consistent decrease in computational blood flow in small artery, is fixed at 1, meaning that viscous and inertial forces are roughly equivalent. The effect of Prandtl number (Pr) on blood temperature is shown in Fig. (4.16) According to the literature on hemodynamics, Prandtl number (Pr) values greater than 10 are preferable for blood flow. Consequently, intra-arterial temperature graphs are constructed for 10, 15, 20, and 25 Prandtl number (Pr). As may be seen, as the Prandtl number $(\Pr)$ increases, the transfer of heat from the vessel wall to the blood decreases, causing the blood's temperature to decline.

The fluctuations in Sherwood number over time for a distinct set of parameters, such as $(Le),(N_t)$ and (Re). Fig. (4.17) demonstrates the effect the Lewis number has on the temporal field. The magnitude of the temperature profile is inversely related to this variable. The scale of the graph diminishes as Lewis's number (Le) rises. Fig. (4.18) and (4.19) illustrate that when the Reynolds number (Re) and the thermophoretic parameter (N_t) grow, the graph flattens out.

4.5 Concluding Remarks

The tangent hyperbolic fluid model's pulsating blood flow is investigated in a segment of a constricted artery with overlapping stenosis. These investigations take into consideration the effects of electroosmotic and periodic pressure gradient. The finite difference method was used to assess the numerical solution. The major objectives of the study were to locate regions of low blood velocity and high flow resistance, and to learn how non-Newtonian behaviour, electroosmotic, and stenosis affect arterial blood flow. The study shows that modifying the Weissenberg number (We) and power-law index (n) values can mitigate these negative stenosis consequences.

- The Brinkman number (Br) can calculate the amount of viscous dissipation. It heats up the fluid from the channel walls and may cause the maximum temperature to occur away from the wall.

- The value of the Electro-osmotic parameter (k) and Helmholtz-Smoulochowski parameter (Uhs) the velocity of blood increases.

  The current study's findings suggest that the electroosmosis process can be used to regulate blood flow.

- It's also important to remember that the divergent tapering artery is both the hottest and the most resistant to flow of all the arteries, tapering or not. all of which are equally significant. This demonstrates how the taper angle plays a significant role in establishing the relevant flow parameters. Therefore, the taper angle needs to be factored in at all times process.

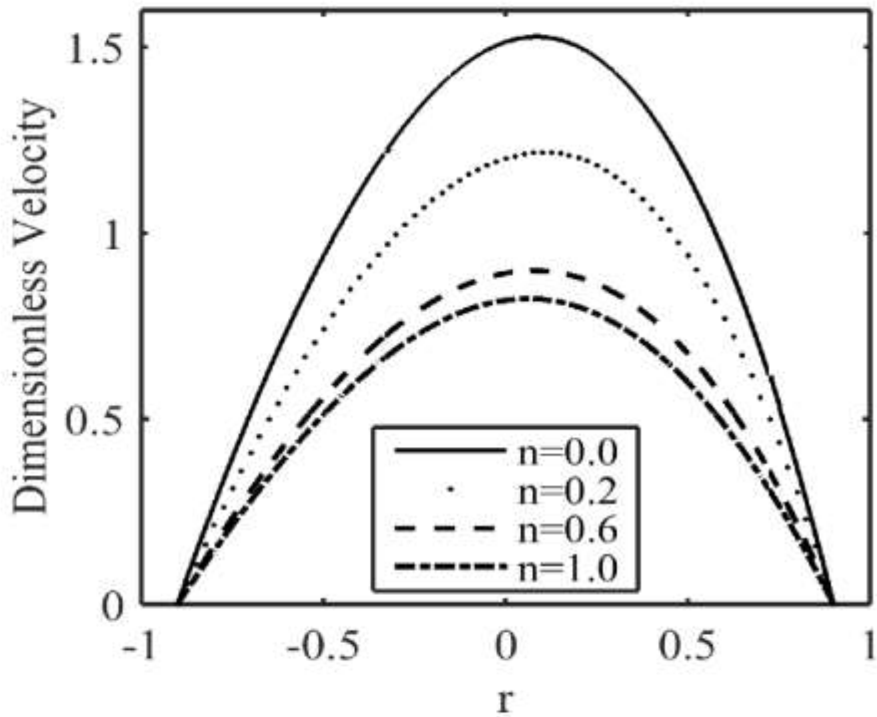

Figure 4.2

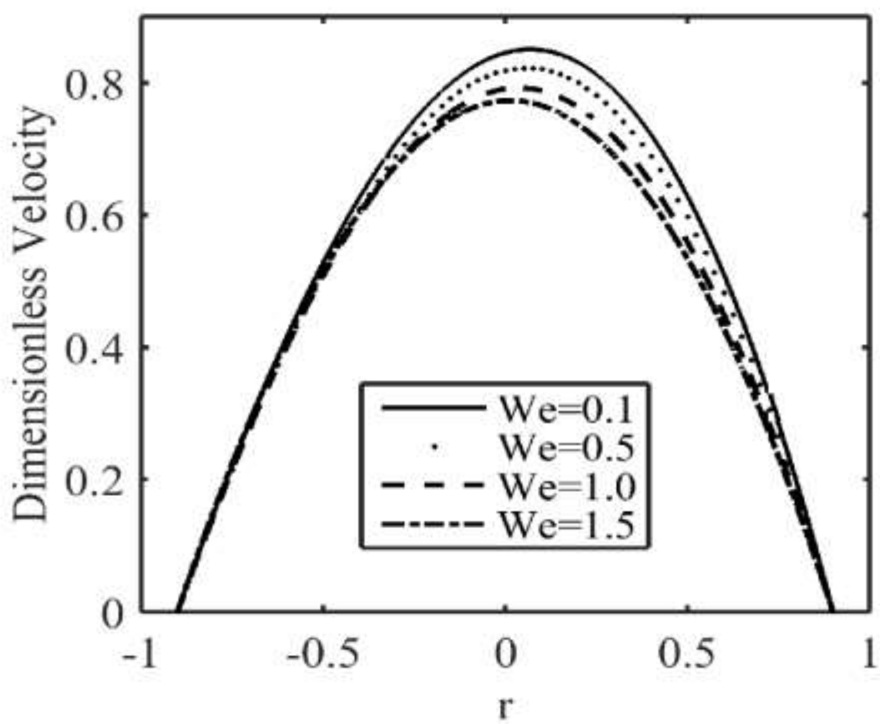

Figure 4.3

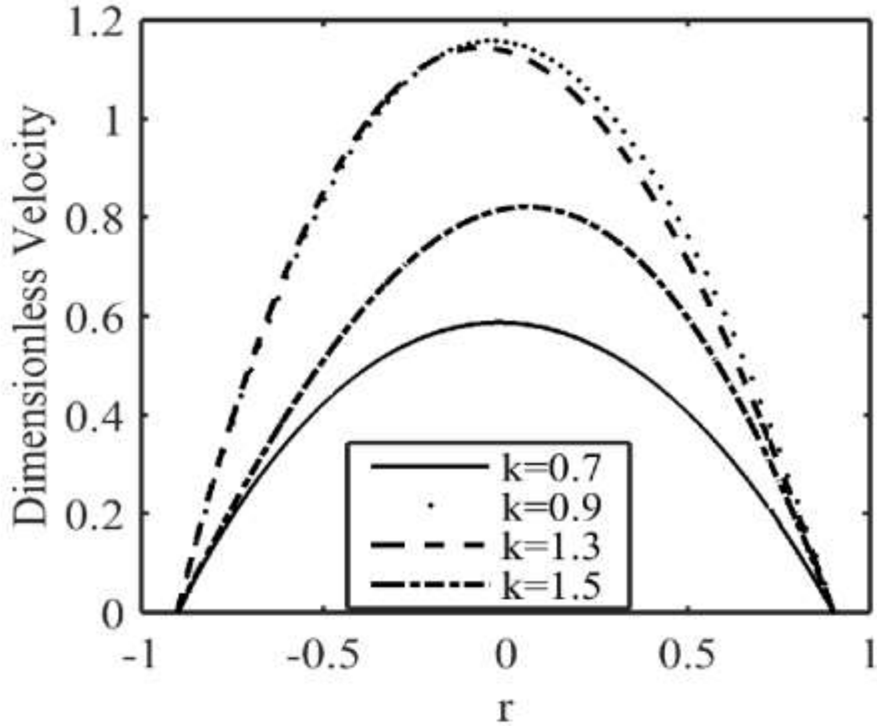

Figure 4.4

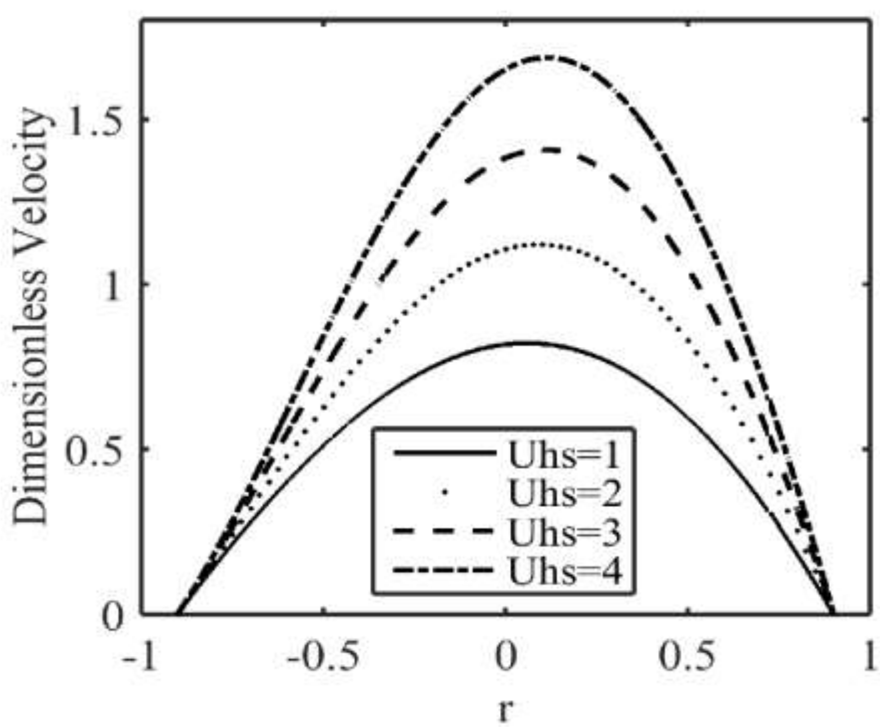

Figure 4.5

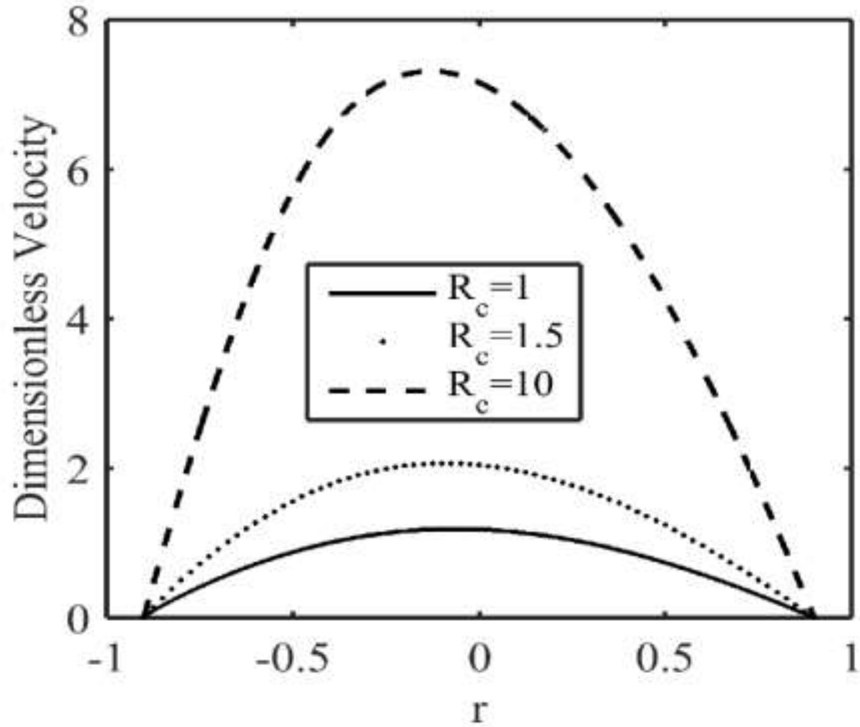

Figure 4.6

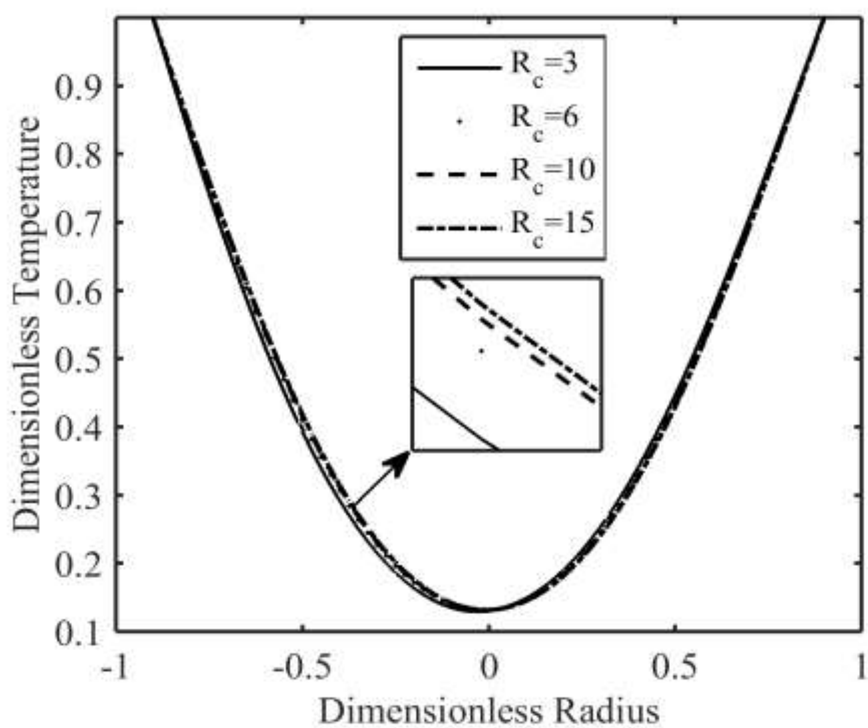

Figure 4.7

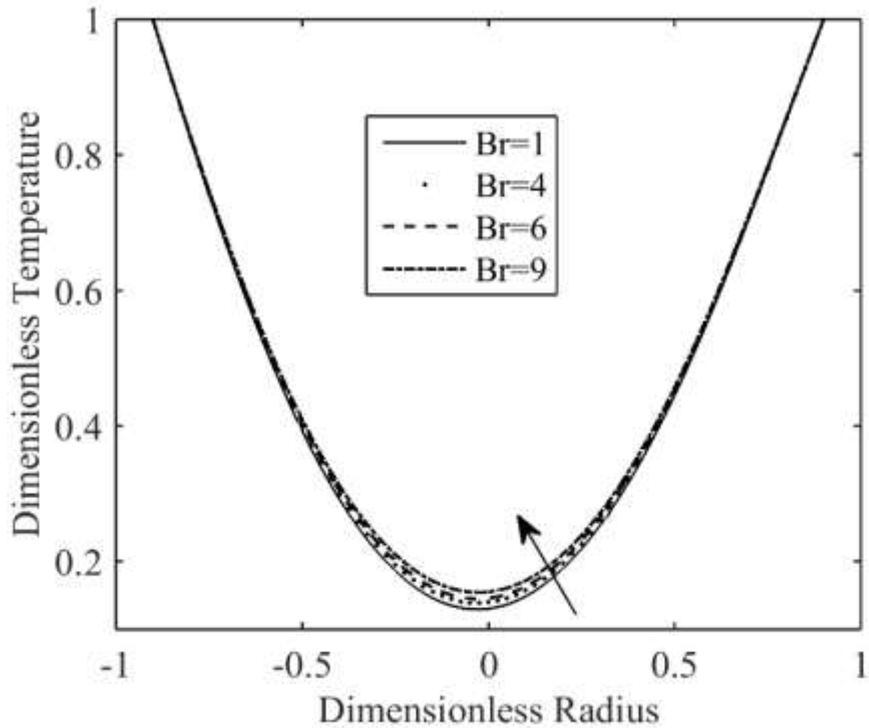

Figure 4.8

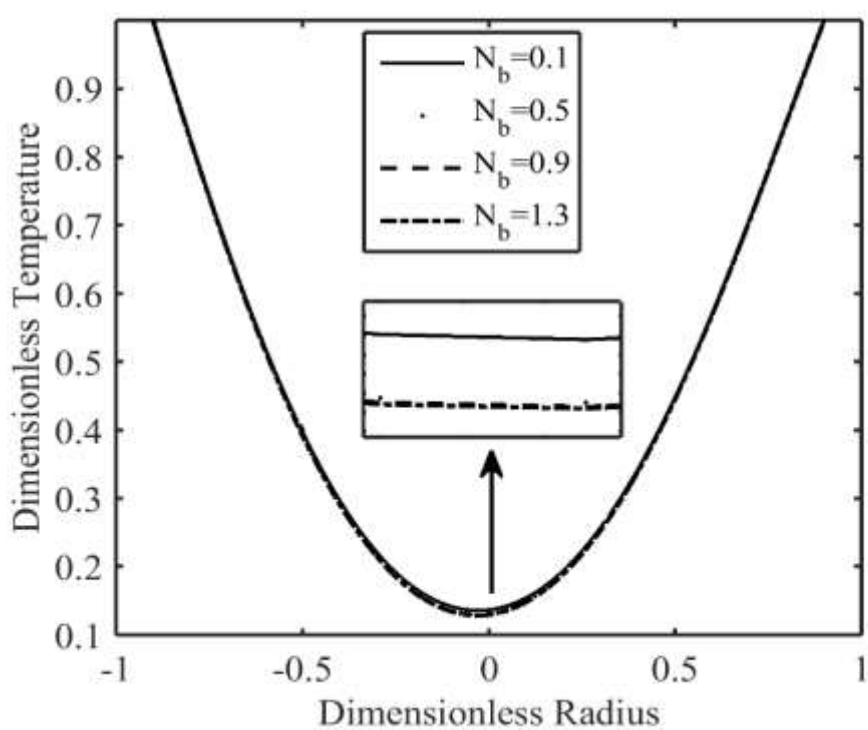

Figure 4.9

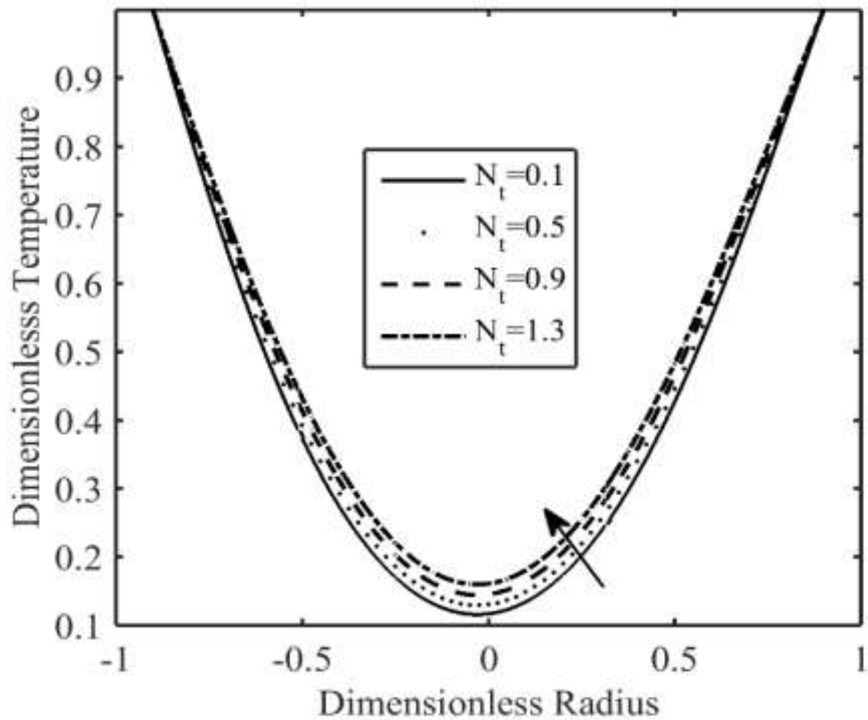

Figure 4.10

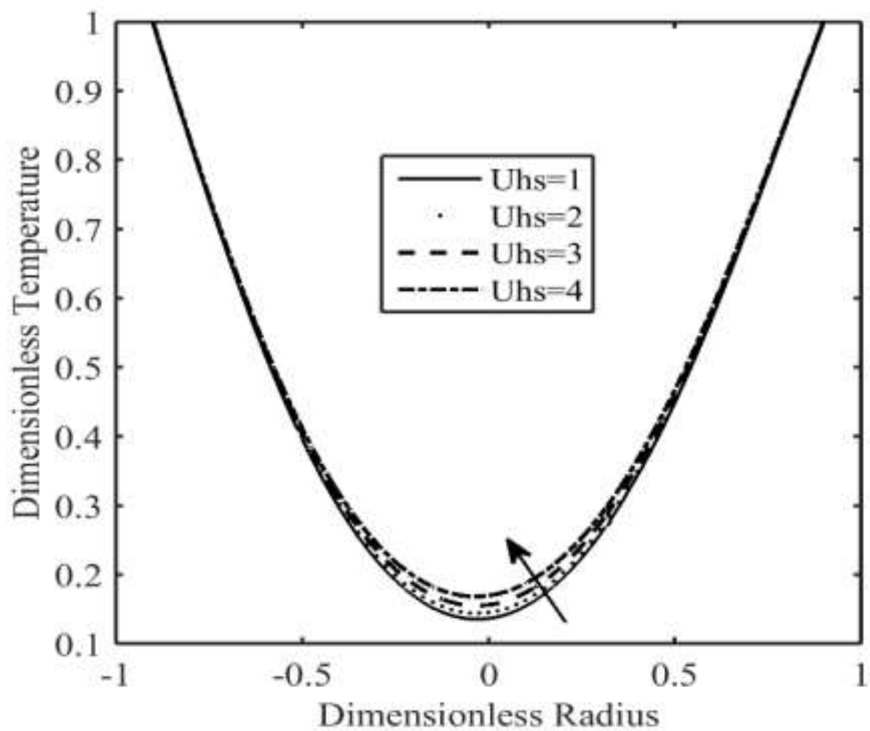

Figure 4.11

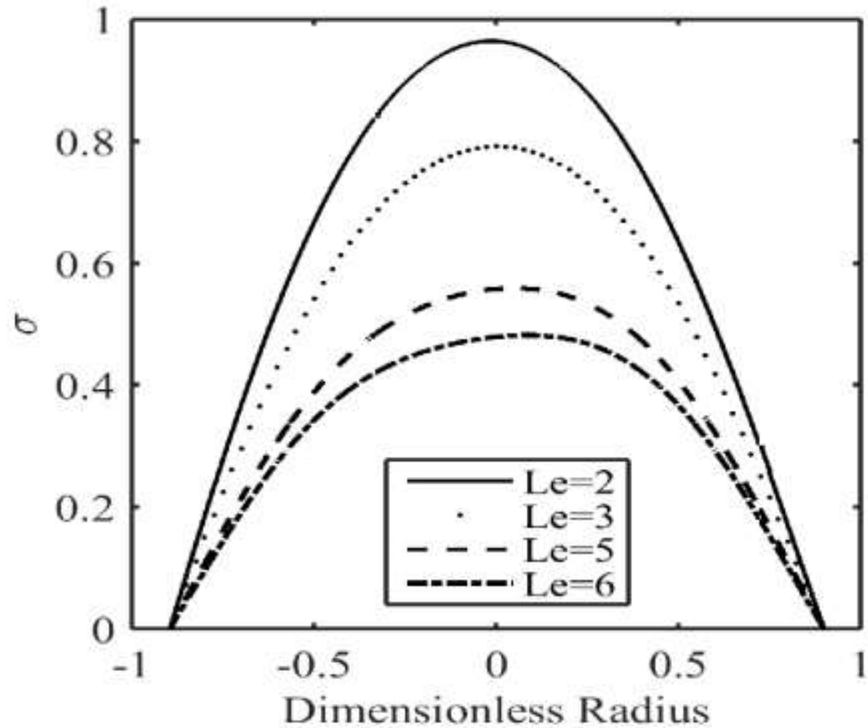

Figure 4.12

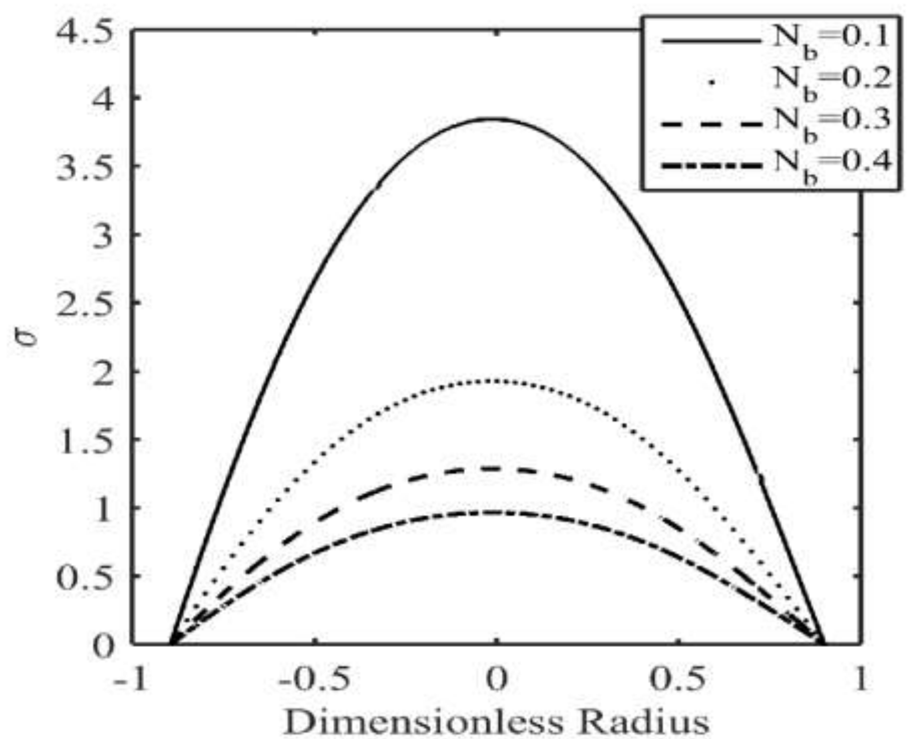

Figure 4.13

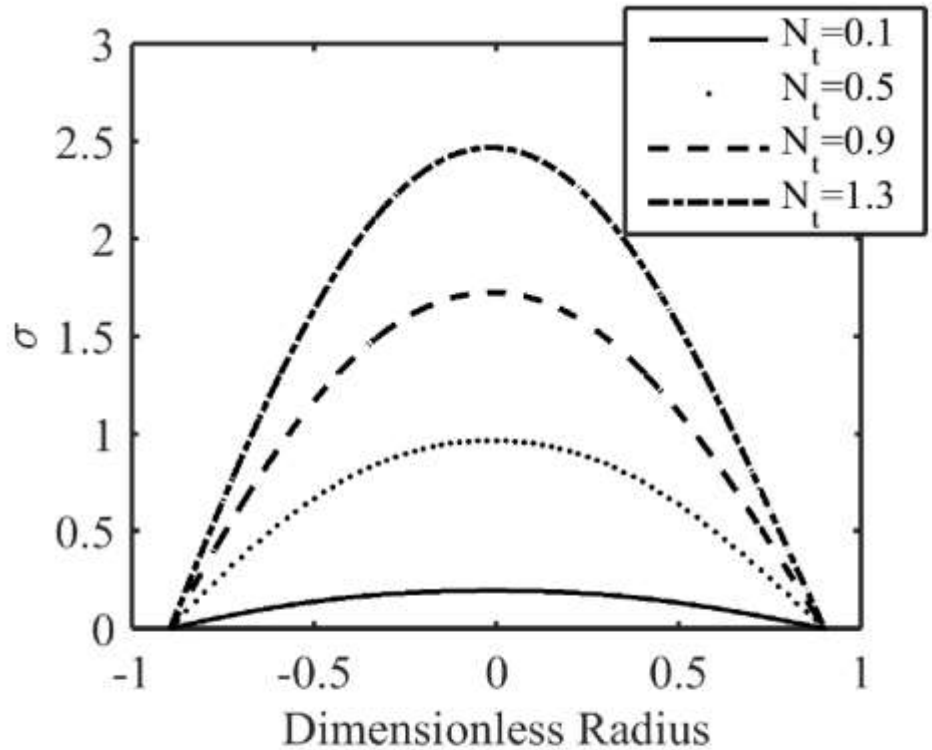

Figure 4.14

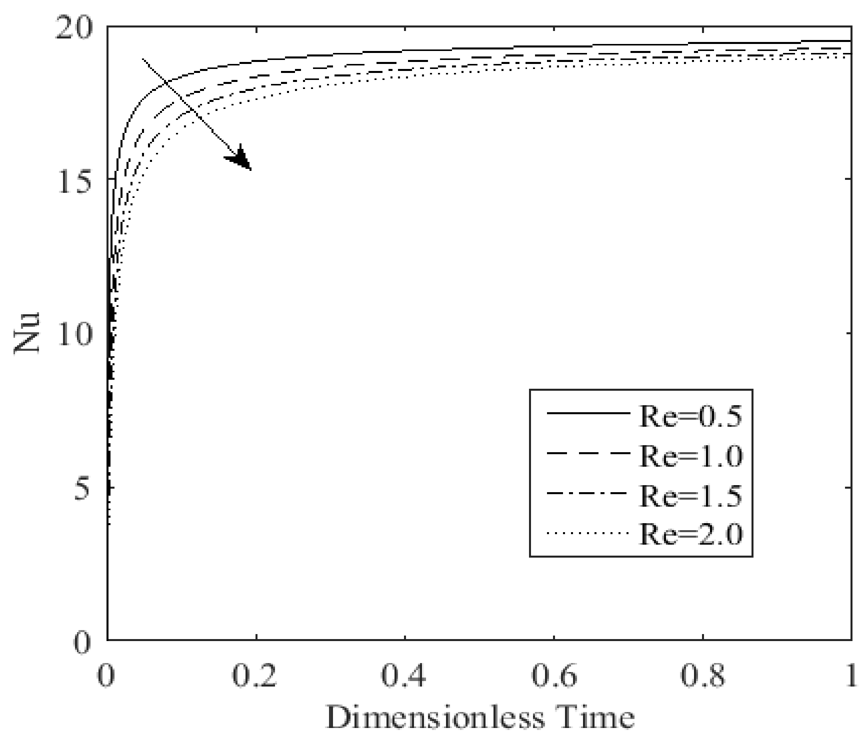

Figure 4.15

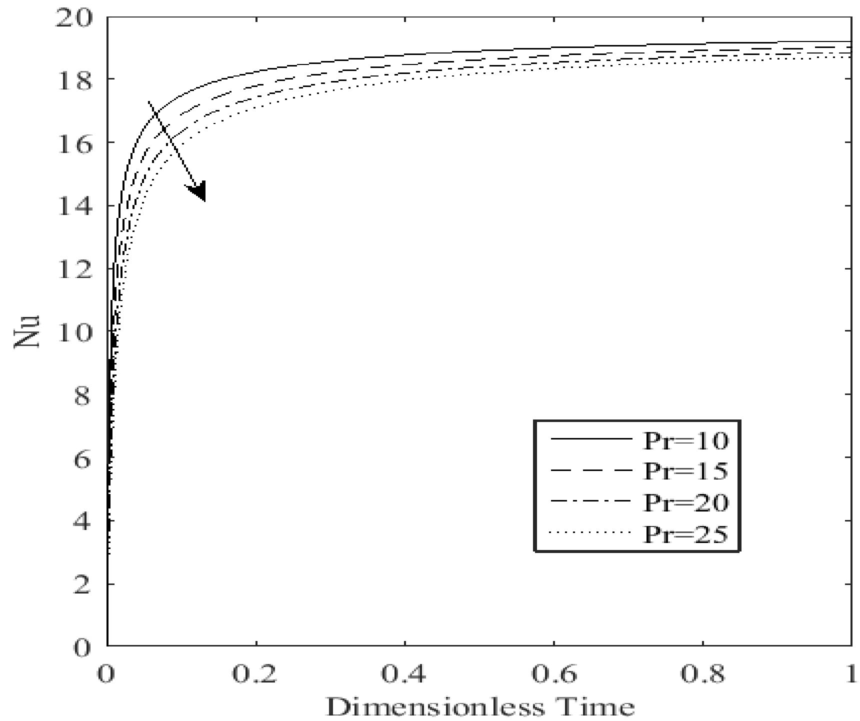

Figure 4.16

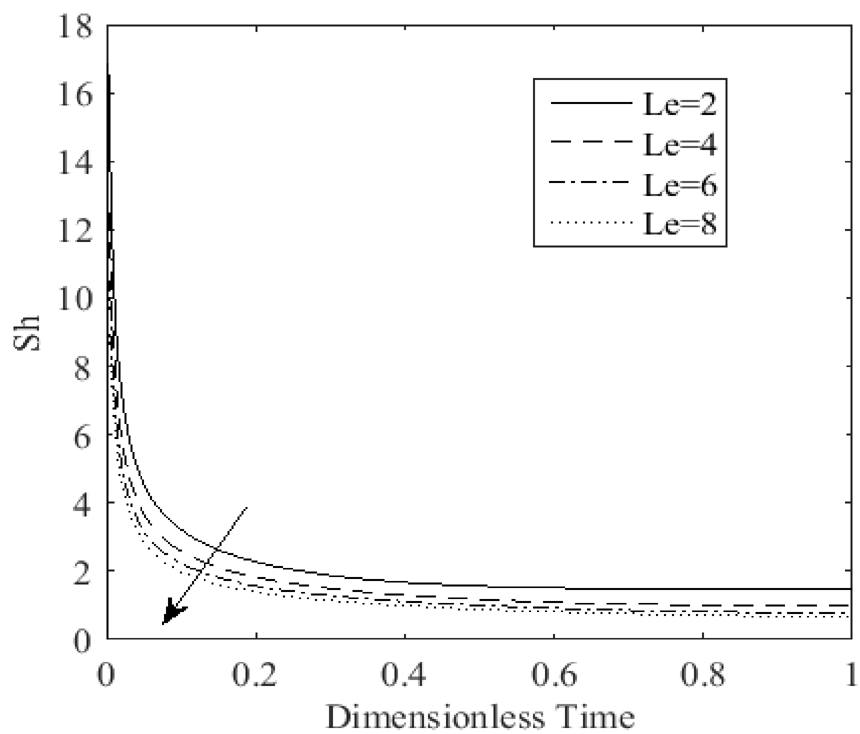

Figure 4.17

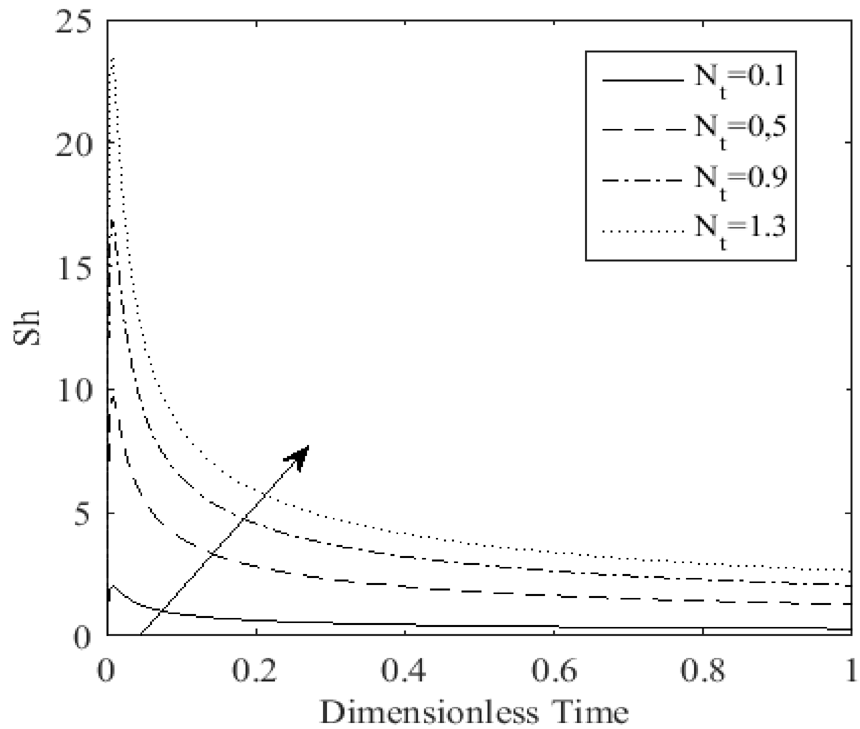

Figure 4.18

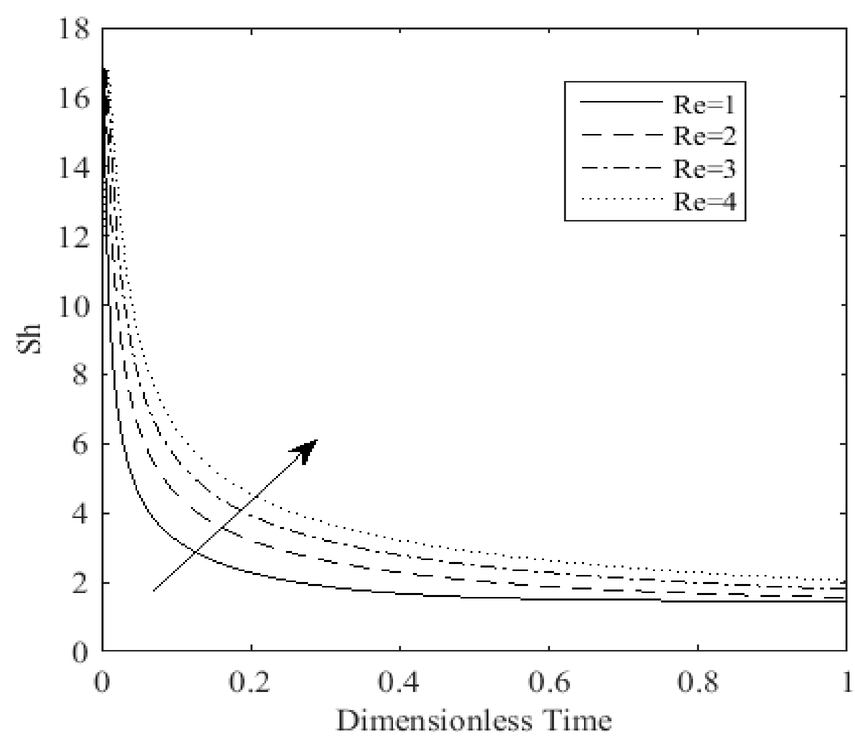

Figure 4.19

Chapter 5

Flow of Blood through a Diseased Curved Aetery: A Two-Phase Analysis

This chapter deal with a two-stage model of pulsatile blood flow in a constricted artery. The problem is represented using cylindrical coordinates. A modest stenosis assumption is used to simplify the non-dimensional governing equations of the flow issue. The radial coordinate transformation is utilised to reduce the effect of the blood vessel wall. An explicit finite difference approach is used to solve the resultant nonlinear system of differential equations while accounting for the provided boundary conditions. After the necessary adjustments have been made to the crucial non-dimensional parameters, an analysis of the data behind the huge image, such as axial velocity, temperature field, concentration wall shear stress, flow rate, and flow impedance, is conducted.

5.1 Flow Equations

The unsteady, laminar, fully developed two-phase flow of blood through a curved blood vessel, having overlapping stenosis in its limen is taken into account. The artery of length "L" is spiraled in a circle of radius R^c. The mathematical expression for the geometry of the curved blood vessel is defined as:

$$R_i(z)=\left.\begin{cases}\left(\tau' z+e_0\right)\left(\beta-\frac{64}{10}\eta\left(\frac{11}{32}l_0^3(z-d)-\frac{47}{48}l_0^2(z-d)^2+l_0(z-d)^3-\frac{1}{3}(z-d)^4\right)\right), & d\le z\le d+\frac{3}{2}l_0,\\ \left(\tau' z+e_0\right), & otherwise\end{cases}\right\},Outer\ wall,$$

$$-R_{1i}(z)=\left.\begin{cases}\left(\tau' z-e_0\right)\left(\beta-\frac{64}{10}\eta\left(\frac{11}{32}l_0^3(z-d)-\frac{47}{48}l_0^2(z-d)^2+l_0(z-d)^3-\frac{1}{3}(z-d)^4\right)\right), & d\le z\le d+\frac{3}{2}l_0,\\ \left(\tau' z-e_0\right), & otherwise\end{cases}\right\},Inner\ wall. \tag{5.1}$$

Here, the outer and inner walls of the curved blood vessel are designated by $R_i(z)$ and $-R_{1i}(z)$, where $i=1$ is for core region and $i\le 2$ is for plasma region, respectively. $\beta<1$ shows for core region and $\beta=1$ shows plasma region in the Eq. (5.1) e_0 is the radius of the normal blood vessel, $\tau'=\tan\varphi$ is the tapering parameter and φ is the tapering angle, d symbolized the location of the abnormality present in the lumen of the blood vessel, l_0 is the length of the stenosis. The radial and axial coordinates are represented by r and z respectively. This η parameter is declared as a constant, and it is used as:

$$\eta=\frac{4\delta^*}{al_0^{\,4}}, \tag{5.2}$$

In this, δ^* shows the critical height of the stenotic zone in two places (i.e).

$$z=d+\frac{8l_0}{25},\ \text{and}\ z=d+\frac{61l_0}{50}. \tag{5.3}$$

The schematic diagram of the diseased curved blood vessel is shown in Fig. (5.1).

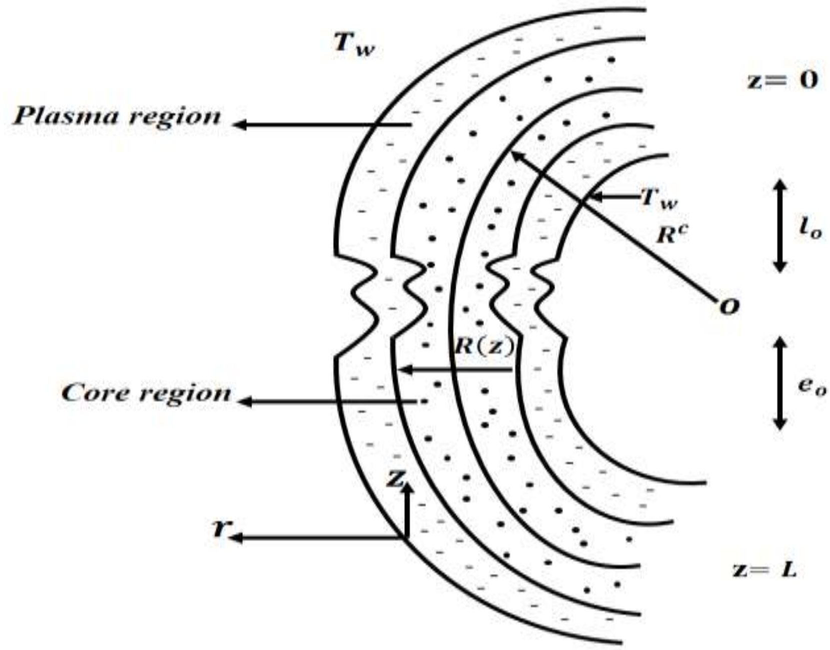

Figure 5.1

The flow field's governing equation is given by:

Core Region

$$\bar{V}_C = U_C(t,r,z),0,W_C(t,r,z)\ , \quad T_C^* = T_C^*(t,r,z), \quad C_C^1 = C_C^1(t,r,z). \tag{5.4}$$

Plasma Region

$$\bar{V}_P = U_P(t,r,z),0,W_P(t,r,z)\ , \quad T_P^* = T_P^*(t,r,z), \quad C_P^1 = C_P^1(t,r,z). \tag{5.5}$$

The lower subscript C and P shows the core and plasma region in this article. The U is radial component W is the axial component of velocity in Eq. (6.4)-(6.5), where the temperature component denoted by T^* and the concentration component of nanoparticles denoted by C^1.

The following are the continuity equation, momentum equation, energy equation, and mass absorption equation for core region using the previously established flow variables.

$$\frac{\partial}{\partial r}\left(r+R^c\right)U_C+R^c\frac{\partial W_C}{\partial z}=0, \tag{5.6}$$

$$\rho_C\left(\frac{\partial U_C}{\partial t}+U_C\frac{\partial U_C}{\partial r}+\frac{R^c}{r+R^c}W_C\frac{\partial U_C}{\partial z}-\frac{U_C^2}{r+R^c}\right)=-\frac{\partial p}{\partial r}+\frac{1}{\left(r+R^c\right)}\frac{\partial}{\partial r}\left(\mu_C\left(r+R^c\right)\frac{\partial U_C}{\partial r}\right)$$
$$+\left(\frac{R^c}{r+R^c}\right)^2\frac{\partial^2 W_C}{\partial z^2}-\frac{W_C}{\left(r+R^c\right)^2}-\frac{2R^c}{\left(r+R^c\right)^2}\frac{\partial U_C}{\partial z}, \tag{5.7}$$

$$\rho_C\left(\frac{\partial W_C}{\partial t}+U_C\frac{\partial W_C}{\partial r}+\frac{R^c}{r+R^c}W_C\frac{\partial W_C}{\partial z}+\frac{U_C W_C}{r+R^c}\right)=-\left(\frac{R^c}{r+R^c}\right)\frac{\partial p}{\partial z}+\left(\frac{1}{\left(r+R^c\right)}\frac{\partial}{\partial r}\left(\mu_C\left(r+R^c\right)\frac{\partial W_C}{\partial r}\right)\right)$$
$$+\left(\frac{R^c}{r+R^c}\right)^2\frac{\partial^2 W_C}{\partial z^2}-\frac{W_C}{\left(r+R^c\right)^2}+\frac{2R^c}{\left(r+R^c\right)^2}\frac{\partial W_C}{\partial z}+\rho_C g\alpha_T\left(T_C^*-T_w\right)+\rho_C g\alpha_{C^1}\left(C_C^1-C_1\right), \tag{5.8}$$

$$\left(\rho c_p\right)_{Cf}\left(\frac{\partial T_C^*}{\partial t}+U_C\frac{\partial T_C^*}{\partial r}+\frac{R^c}{r+R^c}W_C\frac{\partial T_C^*}{\partial z}\right)=k_{Cf}\left(\frac{\partial^2 T_C^*}{\partial r^2}+\frac{1}{r+R^c}\frac{\partial T_C^*}{\partial r}+\left(\frac{R^c}{r+R^c}\right)^2\frac{\partial^2 T_C^*}{\partial z^2}\right)+\theta_0, \tag{5.9}$$

$$\frac{\partial C_C^1}{\partial t}+U_C\frac{\partial C_C^1}{\partial r}+W_C\frac{\partial C_C^1}{\partial z}=D_C\left(\frac{\partial^2 C_C^1}{\partial r^2}+\frac{1}{r+R^c}\frac{\partial C_C^1}{\partial r}+\left(\frac{R^c}{r+R^c}\right)^2\frac{\partial^2 C_C^1}{\partial z^2}\right)+E_C^{'}\left(C_C^1-C_1\right), \tag{5.10}$$

Similarly for the plasma region,

$$\frac{\partial}{\partial r}\left(r+R^c\right)U_P+R^c\frac{\partial W_P}{\partial z}=0, \tag{5.11}$$

$$\rho_P\left(\frac{\partial U_P}{\partial t}+U_P\frac{\partial U_P}{\partial r}+\frac{R^c}{r+R^c}W_P\frac{\partial U_P}{\partial z}-\frac{U_P^2}{r+R^c}\right)=-\frac{\partial p}{\partial r}+\frac{1}{\left(r+R^c\right)}\frac{\partial}{\partial r}\left(\mu_P\left(r+R^c\right)\frac{\partial U_P}{\partial r}\right)$$
$$+\left(\frac{R^c}{r+R^c}\right)^2\frac{\partial^2 W_P}{\partial z^2}-\frac{W_P}{\left(r+R^c\right)^2}-\frac{2R^c}{\left(r+R^c\right)^2}\frac{\partial U_P}{\partial z}, \tag{5.12}$$

$$\rho_P\left(\frac{\partial W_P}{\partial t}+U_P\frac{\partial W_P}{\partial r}+\frac{R^c}{r+R^c}W_P\frac{\partial W_P}{\partial z}+\frac{U_PW_P}{r+R^c}\right)=-\left(\frac{R^c}{r+R^c}\right)\frac{\partial p}{\partial z}+\left(\frac{1}{\left(r+R^c\right)}\frac{\partial}{\partial r}\left(\mu_P\left(r+R^c\right)\frac{\partial W_P}{\partial r}\right)\right)$$

$$+\left(\frac{R^c}{r+R^c}\right)^2\frac{\partial^2W_P}{\partial z^2}-\frac{W_P}{\left(r+R^c\right)^2}+\frac{2R^c}{\left(r+R^c\right)^2}\frac{\partial W_P}{\partial z}+\rho_Pg\alpha_T\left(T_P^*-T_w\right)+\rho_Pg\alpha_{C^1}\left(C_P^1-C_1\right),$$

(5.13)

$$\left(\rho c_p\right)_{Pf}\left(\frac{\partial T_P^*}{\partial t}+U_P\frac{\partial T_P^*}{\partial r}+\frac{R^c}{r+R^c}W_P\frac{\partial T_P^*}{\partial z}\right)=k_{Pf}\left(\frac{\partial^2T_P^*}{\partial r^2}+\frac{1}{r+R^c}\frac{\partial T_P^*}{\partial r}+\left(\frac{R^c}{r+R^c}\right)^2\frac{\partial^2T_P^*}{\partial z^2}\right)+\theta_0,$$

(5.14)

$$\frac{\partial C_P^1}{\partial t}+U_P\frac{\partial C_P^1}{\partial r}+W_P\frac{\partial C_P^1}{\partial z}=D_P\left(\frac{\partial^2C_P^1}{\partial r^2}+\frac{1}{r+R^c}\frac{\partial C_P^1}{\partial r}+\left(\frac{R^c}{r+R^c}\right)^2\frac{\partial^2C_P^1}{\partial z^2}\right)+E_P^{'}\left(C_P^1-C_1\right).$$

(5.15)

The two-phase blood flow model's momentum, energy, and concentration equations are resolved in relation to the artery wall's no-slip boundary conditions. At the point where the velocity, temperature, and concentration functions meet, the core and plasma regions' values are considered to be equal because it is assumed that these functions are continuous. Their gradient disappears with the axis due to symmetry.. The following boundary conditions are appropriate for the given model:

$$\begin{cases} W_P=0,\ T_P^*=T_W^*,\ C_P^1=C_W^1 \quad at\ r=R(z) \\ W_C=W_P,\ T_P^*=T_C^*,\ C_P^1=C_C^1 \ \ at\ r=R_1(z) \\ \dfrac{\partial W_C}{\partial r}=0,\ \dfrac{\partial T_C^*}{\partial r}=0,\ \dfrac{\partial C_C^1}{\partial r}=0\ at\ r=0 \\ \dfrac{\partial T_C^*}{\partial r}=\dfrac{\partial T_P^*}{\partial r},\ \dfrac{\partial C_C^1}{\partial r}=\dfrac{\partial C_P^1}{\partial r}\ at\ r=R_1(z) \end{cases} \tag{5.16}$$

The dimensions of the following equations are removed when utilizing variables (5)-(16):

$$r=\bar{r}e_0,\ W_C=\overline{W_C}U_0,\ U_C=\frac{\overline{U_C}\delta^* U_0}{l_0},\quad t=\frac{\bar{t}e_0}{U_0},\quad z=\bar{z}l_0,\ R^c=R_c e_0,\quad p=\frac{\bar{p}U_0 l_0\mu_0}{e_0^2},$$

$$T_C^*-T_w=\theta\left(T_1-T_w\right),\ \mathrm{Re}=\frac{\rho_f U_0 e_0}{\mu_0},\quad C_C^1-C_1=\sigma_C C_1,\ Br=\frac{\rho_P g e_0^2}{U_0\mu_0}\alpha_C C_1,$$

$$\mathrm{Re}=\frac{\rho_f U_0 e_0}{\mu_0}, P_e=\frac{\overline{c_{pf}}\,\overline{\rho_P}e_0^2 U_0}{\overline{\overline{k_{Pf}}}}, Sc=\frac{\overline{\mu_P}}{\overline{\overline{D_p}}\,\overline{\overline{\rho_P}}}, \beta=\frac{\theta_0 e_0^2}{k_{Pf}\left(T_1-T_w\right)}, \overline{E_P^{'}}=\frac{E\overline{\mu_P}}{\overline{\overline{\rho_P}}e_0^2}, W_P=\overline{W_P}U_0,$$

$$U_P=\frac{\overline{U_P}\delta^* U_0}{l_0}, T_P^*-T_w=\theta_P\left(T_1-T_w\right), C_P^1-C_1=\sigma_P C_1,\ Gr_T=\frac{\rho_P g\alpha_T e_0^2}{U_0\mu_0}\left(T_1-T_w\right),$$

$$\mu_0=\frac{\overline{\mu_P}}{\overline{\overline{\mu_C}}},\ E_0=\frac{\overline{E_P^{'}}}{\overline{\overline{E_C^{'}}}},\ D_0=\frac{\overline{D_P}}{\overline{\overline{D_C}}},\quad \rho_0=\frac{\overline{\rho_P}}{\overline{\overline{\rho_C}}},\ c_0=\frac{\overline{c_P}}{\overline{\overline{c_C}}}. \tag{5.17}$$

In the above definitions, $\overline{W}$ is axial velocity, $\bar{r}$ is radial coordinate, $\bar{z}$ axial directional co-ordinate, $\bar{t}$ is time, $\overline{R}$ is the radius, $\bar{p}$ is the pressure, Br the Brinkman number, Pe is Peclet number, Re is the Reynolds number, Gr is the local thermal Grashof number, Pr is the Prandtl number, U_0 is the average velocity of the blood, T_w represent the wall temperature, σ is nanoparticles concentration function, T_m represent the thermodynamic temperature, μ_0 is ratio of viscosities in core and plasma regions, ρ_0 is ratio of density in core and plasma regions, E is chemical reaction parameter, k_0 is ratio of thermal conductivity in core and plasma regions, Sc is Schmidt parameter and β is heat source or sink parameter.

When the constraints were lifted, the Simplified Eqs. (5.5)-(5.16) are:

Core region:

$$\delta\left(\frac{\partial}{\partial r}\left(r+R_c\right)U_C\right)+R_c\frac{\partial W_C}{\partial z}=0, \tag{5.18}$$

$$\mathrm{Re}\,\delta\varepsilon^2\frac{1}{\rho_0}\left(\frac{\partial U_C}{\partial t}+\delta\varepsilon U_C\frac{\partial U_C}{\partial r}+\varepsilon\frac{R_c}{r+R_c}W_C\frac{\partial U_C}{\partial z}-\delta\varepsilon\frac{U_C^2}{r+R_c}\right)=-\frac{\partial p}{\partial r}$$

$$+\frac{\mu_P}{\mu_0^2 l_0^2}\delta\frac{1}{\left(r+R_c\right)}\frac{\partial}{\partial r}\left(\left(r+R_c\right)\frac{\partial U_C}{\partial r}\right)+\left(\frac{R_c}{\overline{r}+R_c}\right)^2\frac{1}{\mu_0}\varepsilon^3\frac{\partial^2 W_C}{\partial z^2}-\frac{1}{\mu_0}\varepsilon\frac{W_C}{\left(r+R_c\right)^2}-\frac{2R_c}{\left(r+R_c\right)^2}\delta\varepsilon\frac{\partial U_C}{\partial z}, \tag{5.19}$$

$$\frac{1}{\rho_0}\operatorname{Re}\frac{\partial W_C}{\partial t}+\frac{1}{\rho_0}\operatorname{Re}\left(\delta\varepsilon\frac{\partial W_C}{\partial r}+\varepsilon\frac{R_c}{r+R_c}W_C\frac{\partial W_C}{\partial z}+\delta\varepsilon\frac{U_C W_C}{r+R^c}\right)=-\left(\frac{R_c}{r+R_c}\right)\frac{\partial p}{\partial z}$$

$$+\frac{\mu_P}{{\mu_0}^2}\frac{1}{(r+R_c)}\frac{\partial}{\partial r}\left((r+R_c)\frac{\partial W_C}{\partial r}\right)+\left(\frac{R_c}{r+R_c}\right)^2\frac{1}{\mu_0}\varepsilon^2\frac{\partial^2 W_C}{\partial z^2}-\frac{1}{\mu_0}\frac{W_C}{(r+R_c)^2} \tag{5.20}$$

$$-\frac{2R_c}{(r+R_c)^2}\frac{1}{\mu_0}\varepsilon\frac{\partial W_C}{\partial z}+\frac{1}{\rho_0}Gr_T\theta_C+\frac{1}{\rho_0}Br\sigma_C,$$

$$\frac{Pe}{\rho_0 c_0}\left(\frac{\partial\theta_C}{\partial t}+\delta\varepsilon\frac{\partial\theta_C}{\partial r}+\varepsilon\frac{R_c}{r+R_c}W_C\frac{\partial\theta_C}{\partial z}\right)=\frac{\partial^2\theta_C}{\partial r^2}+\frac{1}{r+R_c}\frac{\partial\theta_C}{\partial r}+\varepsilon^2\left(\frac{R_c}{r+R_c}\right)^2\frac{\partial^2\theta_C}{\partial z^2}+\frac{\theta_0(e_0)^2}{(T_1-T_w)}\frac{k_{0f}}{k_{Pf}}, \tag{5.21}$$

$$\operatorname{Re}\left(\frac{\partial\sigma_C}{\partial t}+\delta\varepsilon\frac{\partial\sigma_C}{\partial r}+\varepsilon W\frac{\partial\sigma_C}{\partial z}\right)=\frac{1}{D_0}\frac{1}{Sc}\left(\frac{\partial^2\sigma_C}{\partial r^2}+\frac{1}{r+R_c}\frac{\partial\sigma_C}{\partial r}+\varepsilon^2\left(\frac{R_c}{r+R_c}\right)^2\frac{\partial^2\sigma_C}{\partial z^2}\right)+\frac{E}{E_0}\sigma_C. \tag{5.22}$$

Plasma region:

$$\delta\left(\frac{\partial}{\partial r}(r+R_c)U_P\right)+R_c\frac{\partial W_P}{\partial z}=0, \tag{5.23}$$

$$\operatorname{Re}\delta\varepsilon^2\left(\frac{\partial U_P}{\partial t}+\delta\varepsilon U_P\frac{\partial U_P}{\partial r}+\varepsilon\frac{R_c}{r+R_c}W_P\frac{\partial U_P}{\partial z}-\delta\varepsilon\frac{U_P^2}{r+R_c}\right)=-\frac{\partial p}{\partial r}$$

$$+\frac{\mu_P}{\mu_0 {l_0}^2}\delta\frac{1}{(r+R_c)}\frac{\partial}{\partial r}\left((r+R_c)\frac{\partial U_P}{\partial r}\right)+\left(\frac{R_c}{r+R_c}\right)^2\frac{1}{\mu_0}\varepsilon^3\frac{\partial^2 W_P}{\partial z^2}-\frac{1}{\mu_0}\varepsilon\frac{W_P}{(r+R_c)^2}-\frac{2R_c}{(r+R_c)^2}\delta\varepsilon\frac{\partial U_P}{\partial z} \tag{5.24}$$

$$\operatorname{Re}\frac{\partial W_P}{\partial t}+\operatorname{Re}\left(\delta\varepsilon\frac{\partial W_P}{\partial r}+\varepsilon\frac{R_c}{r+R_c}W_P\frac{\partial W_P}{\partial z}+\delta\varepsilon\frac{U_P W_P}{r+R^c}\right)=-\left(\frac{R_c}{r+R_c}\right)\frac{\partial p}{\partial z}$$

$$+\frac{1}{(r+R_c)}\frac{\partial}{\partial r}\left((r+R_c)\frac{\partial W_P}{\partial r}\right)+\left(\frac{R_c}{r+R_c}\right)^2\varepsilon^2\frac{\partial^2 W_P}{\partial z^2}-\frac{W_P}{(r+R_c)^2} \tag{5.25}$$

$$-\frac{2R_c}{(r+R_c)^2}\varepsilon\frac{\partial W_P}{\partial z}+Gr_T\theta_P+Br\sigma_P,$$

$$\mathrm{P}e\left(\frac{\partial\theta_P}{\partial t}+\delta\varepsilon\frac{\partial\theta_P}{\partial r}+\varepsilon\frac{R_c}{r+R_c}W_P\frac{\partial\theta_P}{\partial z}\right)=\frac{\partial^2\theta_P}{\partial r^2}+\frac{1}{r+R_c}\frac{\partial\theta_P}{\partial r}+\varepsilon^2\left(\frac{R_c}{r+R_c}\right)^2\frac{\partial^2\theta_P}{\partial z^2}+\frac{\theta_0(e_0)^2}{(T_1-T_w)k_{Pf}}, \tag{5.26}$$

$$\mathrm{Re}\left(\frac{\partial\sigma_P}{\partial t}+\delta\varepsilon\frac{\partial\sigma_P}{\partial r}+\varepsilon W\frac{\partial\sigma_P}{\partial z}\right)=\frac{1}{Sc}\left(\frac{\partial^2\sigma_P}{\partial r^2}+\frac{1}{r+R_c}\frac{\partial\sigma_P}{\partial r}+\varepsilon^2\left(\frac{R_c}{r+R_c}\right)^2\frac{\partial^2\sigma_P}{\partial z^2}\right)+E\sigma_P. \tag{5.27}$$

We utilize two assumptions based on mild stenosis in the accompanying analysis: $\varepsilon\left(=\frac{e_0}{l_0}\right)=O(1)$ and $\delta\left(=\frac{\delta^*}{e_0}\right)\ll 1$ i.e. The first requirement is that the stenotic region be no longer than the channel's radius. The second requirement is that the track length's elevation be smaller than the channel radius.

Equation (5.18) to (5.27) is here's a reduction of the following:

Core region:

$$\frac{\partial p}{\partial r}=0, \tag{5.28}$$

$$\frac{1}{\rho_0}\mathrm{Re}\frac{\partial W_C}{\partial t}=-\left(\frac{R_c}{r+R_c}\right)\frac{\partial p}{\partial z}+\frac{\mu_P}{\mu_0^{\,2}}\frac{1}{(r+R_c)}\frac{\partial}{\partial r}\left((r+R_c)\frac{\partial W_C}{\partial r}\right)-\frac{1}{\mu_0}\frac{W_C}{(r+R_c)^2}+\frac{1}{\rho_0}Gr_T\theta_C+\frac{1}{\rho_0}Br\sigma_C, \tag{5.29}$$

$$\frac{\mathrm{P}ek_0}{\rho_0 c_0}\frac{\partial\theta_C}{\partial t}=\frac{\partial^2\theta_C}{\partial r^2}+\frac{1}{r+R_c}\frac{\partial\theta_C}{\partial r}+k_0\beta, \tag{5.30}$$

$$\mathrm{Re}\frac{\partial\sigma_C}{\partial t}=\frac{1}{D_0}\frac{1}{Sc}\left(\frac{\partial^2\sigma_C}{\partial r^2}+\frac{1}{r+R_c}\frac{\partial\sigma_C}{\partial r}\right)+\frac{E}{E_0}\sigma_C. \tag{5.31}$$

Plasma region:

$$\frac{\partial p}{\partial r}=0, \tag{5.32}$$

$$\mathrm{Re}\frac{\partial W_P}{\partial t}=-\left(\frac{R_c}{r+R_c}\right)\frac{\partial p}{\partial z}+\frac{1}{(r+R_c)}\frac{\partial}{\partial r}\left((r+R_c)\frac{\partial W_P}{\partial r}\right)-\frac{W_P}{(r+R_c)^2}+Gr_T\theta_P+Br\sigma_P, \tag{5.33}$$

$$\mathrm{P}e\frac{\partial\theta_P}{\partial t}=\frac{\partial^2\theta_P}{\partial r^2}+\frac{1}{r+R_c}\frac{\partial\theta_P}{\partial r}+\beta, \tag{5.34}$$

$$\mathrm{Re}\frac{\partial\sigma_P}{\partial t}=\frac{1}{Sc}\left(\frac{\partial^2\sigma_P}{\partial r^2}+\frac{1}{r+R_c}\frac{\partial\sigma_P}{\partial r}\right)+E\sigma_P. \tag{5.35}$$

The equation for the Pulsatile Pressure gradient:

$$-\frac{\partial p}{\partial z} = A_0 + A_1 \cos\left(2\pi\omega_p t\right), \qquad t > 0. \tag{5.36}$$

Equation (5.36), A_0 denotes the mean pressure gradient, and A_1 which represents the amplitude of the pulsatile component, which may be found by solving for it.

$$-\frac{\partial p}{\partial z} = B_1\left(1 + c\cos\left(c_1 t\right)\right), \tag{5.37}$$

Where

$$c_1 = \frac{2\pi\omega_p e_0}{U_0}, \quad c = \frac{A_1}{A_0}, \quad B_1 = \frac{A_0 e_0^2}{\mu_0 U_0}. \tag{5.38}$$

In Equation (5.29) and (5.33) using the term $-\partial p / \partial z$ we get:

$$\begin{aligned}\frac{1}{\rho_0}\mathrm{Re}\frac{\partial W_C}{\partial t} = {} & \left(\frac{R_c}{r + R_c}\right) B_1\left(1 + c\cos\left(c_1 t\right)\right) + \frac{\mu_P}{\mu_0^{\,2}}\frac{1}{\left(r + R_c\right)}\frac{\partial}{\partial r}\left(\left(r + R_c\right)\frac{\partial W_C}{\partial r}\right) \\ & - \frac{1}{\mu_0}\frac{W_C}{\left(r + R_c\right)^2} + \frac{1}{\rho_0} Gr_T \theta_C + \frac{1}{\rho_0} Br\sigma_C,\end{aligned} \tag{5.39}$$

$$\mathrm{Re}\frac{\partial W_P}{\partial t} = \left(\frac{R_c}{r + R_c}\right) B_1\left(1 + c\cos\left(c_1 t\right)\right) + \frac{1}{\left(r + R_c\right)}\frac{\partial}{\partial r}\left(\left(r + R_c\right)\frac{\partial W_P}{\partial r}\right) - \frac{W_P}{\left(r + R_c\right)^2} + Gr_T\theta_P + Br\sigma_P, \tag{5.40}$$

Eqs. (5.16) have the following set of constraints and beginning conditions imposed on them:

$$\begin{cases} W_P = 0,\ \theta_P = 1,\ \sigma_P = 1 & at \quad r = R(z), \\ W_P = W_C,\ \theta_P = \theta_C,\ \sigma_P = \sigma_C & at \quad r = R_1(z), \\ \dfrac{\partial \theta_C}{\partial r} = \dfrac{\partial \theta_P}{\partial r},\ \dfrac{\partial \sigma_C}{\partial r} = \dfrac{\partial \sigma_P}{\partial r} & at \quad r = R_1(z), \\ \dfrac{\partial W_C}{\partial r} = 0,\ \dfrac{\partial \theta_C}{\partial r} = 0,\ \dfrac{\partial \sigma_C}{\partial r} = 0 & at \quad r = 0. \end{cases} \tag{5.41}$$

Wall shear stress is a crucial flow component to assess in the study of stenosed arterial blood flow, since physical stress causes vascular tissue in the artery to change histologically and morphologically. The shear stress at the core-plasma contact wall is determined as

$$\tau = \left(\frac{\partial W_C}{\partial r}\right)_{R_1}, \tag{5.42}$$

Shear stress at the arteries outside the wall is calculated as

$$\tau' = \frac{1}{\mu_0}\left(\frac{\partial W_P}{\partial r}\right)_{R_0}, \tag{5.43}$$

where the ratio of viscosity between the core and plasma regions is denoted by μ_0.

The blood flow in the artery's total volumetric flow rate is computed as

$$Q = \int_{-R}^{R} W dr. \tag{5.44}$$

The continuous impedance in pulsed flow is defined as the modulation of the pressure gradient with respect to the flow rate. Blood flow can be understood as a result of the forces acting on it in response to the local pressure gradient, and this impedance provides a link between the two.

$$\Lambda = \frac{\left(\frac{\partial p}{\partial z}\right)}{Q}. \tag{5.45}$$

The simple equation for the dimensionalized geometry of an arterial segment is as follows:

$$\begin{aligned}
&R(z) = (1+\tau z)\left[\beta - \frac{64}{10}\eta_1\left(\frac{11}{32}(z-\sigma) - \frac{47}{48}(z-\sigma)^2 + (z-\sigma)^3 - \frac{1}{3}(z-\sigma)^4\right)\right],\\
&\sigma \le z \le \sigma + \frac{3}{2},\ \textit{Outer wall},\\
&R_1(z) = (-1+\tau z)\left[\beta - \frac{64}{10}\eta_1\left(\frac{11}{32}(z-\sigma) - \frac{47}{48}(z-\sigma)^2 + (z-\sigma)^3 - \frac{1}{3}(z-\sigma)^4\right)\right],\\
&\sigma \le z \le \sigma + \frac{3}{2},\ \textit{Inner wall},
\end{aligned} \tag{5.46}$$

Where $\eta_1 = 4\delta,\ \delta = \frac{\delta^*}{e_0},\ \sigma = \frac{d}{l_0},\ \tau = \frac{\tau' l_0}{e_0}.$

5.2 Solution Methodology

To apply the numerical method, we need to use the explicit finite difference approach. By utilizing the algebraic transformation provided above in Eqs. (5.39) & (5.40) for core and plasma region respectively:

$$W_{Ci}^{k+1}=W_{Ci}^{k}+\frac{\Delta t\rho_0}{\mathrm{Re}}\left\{\begin{array}{c}\left(\frac{R_c}{r+R_c}\right)B_1\left(1+c\cos\left(c_1t\right)\right)+\frac{\mu_P}{\mu_0{}^2}\frac{1}{\left(r+R_c\right)}\frac{\partial}{\partial r}\left(\left(r+R_c\right)\left(W_C\right)_r\right)\\ -\frac{1}{\mu_0}\frac{W_{Ci}^{k}}{\left(r+R_c\right)^2}+\frac{1}{\rho_0}Gr_T\theta_{Ci}^{k}+\frac{1}{\rho_0}Br\sigma_{Ci}^{k},\end{array}\right\}, \tag{5.47}$$

$$W_{Pi}^{k+1}=W_{Pi}^{k}+\frac{\Delta t}{\mathrm{Re}}\left\{\begin{array}{l}\left(\frac{R_c}{r+R_c}\right)B_1\left(1+c\cos\left(c_1t\right)\right)+\frac{1}{\left(r+R_c\right)}\frac{\partial}{\partial r}\left(\left(r+R_c\right)\left(W_P\right)_r\right)\\ -\frac{W_{Pi}^{k}}{\left(r+R_c\right)^2}+Gr_T\theta_{pi}^{k}+Br\sigma_{pi}^{k}\end{array}\right\}, \tag{5.48}$$

Eqs. (5.30) & (5.34) becomes,

$$\theta_{Ci}^{k+1}=\theta_{Ci}^{k}+\frac{\Delta t\,\rho_0c_0}{\mathrm{Pe}\,k_0}\left\{\left(\theta_C\right)_{rr}+\frac{1}{r+R_c}\left(\theta_C\right)_r+k_0\beta\right\}, \tag{5.49}$$

$$\theta_{Pi}^{k+1}=\theta_{Pi}^{k}+\frac{\Delta t}{\mathrm{Pe}}\left\{\left(\theta_P\right)_{rr}+\frac{1}{r+R_c}\left(\theta_P\right)_r+\beta\right\}, \tag{5.50}$$

Eqs. (5.31) & (5.35) becomes

$$\sigma_{Ci}^{j+1}=\sigma_{Ci}^{j}+\frac{\Delta t}{\mathrm{Re}}\left\{\frac{1}{D_0}\frac{1}{Sc}\left(\left(\sigma_C\right)_{rr}+\frac{1}{r+R_c}\left(\sigma_C\right)_r\right)+\frac{E}{E_0}\sigma_{Ci}^{j}\right\}, \tag{5.51}$$

$$\sigma_{Pi}^{j+1}=\sigma_{Pi}^{j}+\frac{\Delta t}{\mathrm{Re}}\left\{\frac{1}{Sc}\left(\left(\sigma_P\right)_{rr}+\frac{1}{r+R_c}\left(\sigma_P\right)_r\right)+E\sigma_{Pi}^{j}\right\}. \tag{5.52}$$

The numerical boundary and initial condition have been defined as follows:

$$\begin{cases} W_{Pi}^{1}=0,\ \theta_{Pi}^{1}=1,\ \sigma_{Pi}^{1}=1 & at\quad r=R(z),\\ W_{P1}^{\ k}=W_{C1}^{\ k},\ \theta_{P1}^{\ k}=\theta_{C1}^{\ k},\ \sigma_{P1}^{\ j}=\sigma_{C1}^{\ j} & at\quad r=R_1(z),\\ \left(\theta_C\right)_r=\left(\theta_P\right)_r,\ \left(\sigma_C\right)_r=\left(\sigma_P\right)_r & at\quad r=R_1(z),\\ \left(W_C\right)_r=0,\ \left(\theta_C\right)_r=0,\ \left(\sigma_C\right)_r=0 & at\quad r=0. \end{cases} \tag{5.53}$$

5.3 Discussion of Results

The sections that follow analyse the outcomes of the numerical results in considerable depth. The programming code is developed in MATLAB. Velocity, temperature and concentration graphs are used to assess the impact of altering elements of interest. To solve the partial differential equation, a set of preset integers is chosen. $\mathrm{P}e = 1.87,\ \mathrm{Re} = 1,\ B_1 = 1.41,\ E = 0.5,\ \beta = 0.1,\ Sc = 1,\ \mu_0 = 1.2,\ k_0 = 0.8,\ c_0 = 1,\ \rho_0 = 1.05.$

It has been demonstrated that the mentioned data is strongly linked to conditions in the bloodstream, which is a real-world manifestation. The next part is divided into two subsections. The analysis examines velocity, temperature, and concentration profiles resulting from pulsing activity, and establishes the relationship between wall shear stress, flow rate, and concentration.

Assuming pulsatile, This two-phase flow behaviour of blood via a stenosed artery segment can be understood with the use of accurate attribute estimations made possible by Newtonian central nervous system and plasma venous blood flow. The impact on blood flow of a plasma layer devoid of cells as a function of several quantities of interest have been demonstrated in a computational study. Figures provides the default values of the parameters that are used to visually examine the model's efficiency.

Fig. (5.2) shows the graph of curvature $\left(R_c\right)$. At larger curvatures $\left(R_c\right)$ the velocity profile increases because the artery becomes straight, as shown in Fig. (5.2). Fig. (5.3) shows the graph of Reynold number (Re) is decreasing in the core region and plasma region the effects are clearer in the core region. The velocity distribution in a stenotic blood artery for different Brinkman number (Br) levels is shown in Fig. (5.4) the hypothesis that increasing (Br) levels raise blood temperature along the arterial axis is tested. The Grashof number (Gr), The ratio of the buoyancy to the viscous force acting on the plasma and core areas grows as a dimensionless parameter.. By increasing the Grashof number (Gr), viscous forces become weaker as a result, the velocity profile shows that the shear thinning forces are amplified. Fig. (5.5). Fig. (5.6) shows the velocity profile with parameter plasma layer with viscosity (μ_p). Also, since the flow at the interface is continuous according to the boundary condition, the angular velocity of the plasma fluid is directly affected by the reduced red blood cell velocity. The viscous torque, which causes the plasma region's velocity to decrease, is created by the difference in angular velocities of the plasma and red blood cells.

Various variations of the Peclet number result in varied blood flow temperature profiles. (Pe), as seen in Fig. (5.7). As the Peclet number increases, the graphic shows that the temperature profile in the core and plasma regions decreases. Fig. (5.8) illustrates that the heat source or sink parameter has a positive and growing effect on the temperature profile (β). The specific heat ratio between the plasma and core regions (c_0) are increasing in temperature profile shown in Fig. (5.9). Fig. (5.10) shows the temperature profile decreases with comparison between the plasma and core regions' thermal conductivity (k_0). Fig. (5.11) shows the ratio of density in core and plasma regions (ρ_0). The density increases in blood flow temperature profile.

The ratio of particular heat across the core and plasma areas show a reduction when the Reynold number (Re) and Schmidt number (Sc) decrease, respectively, as shown in Figures (5.12) and (5.13), which are part of the current computational work. For certain values of the Reynold number and Schmidt number, the concentration profile fall from the arterial wall and the interface region towards the middle of the artery and beyond. The graphs of different parameter like (D_0) and (E_0) are shown that concentration profile decreases in Fig. (5.14) and (5.15) respectively. For Fig. (5.16) certain values of the chemical reaction parameter (E) the concentration profile rises from the arterial wall and the interface region towards the middle of the artery and beyond. This tendency is depicted in the concentration profile because, as the chemical reaction parameter (E) values increase, the molecular diffusivity decreases, hence reducing the species concentration.

Assuming pulsatile, Newtonian blood flow for both the core and plasma areas has allowed for accurate estimation of flow wall shear stress, total flow rate, and resistance, which are necessary for comprehending how blood moves in two phases via a narrowed section of an artery. The modulation of blood flow by the plasma layer in relation to several quantities of interest have been demonstrated in a computational study. Fig (5.17), (5.18) & (5.19) provides the parameters' initial values that are used to visually examine the model's efficiency.

Figure (5.17) displays the wall shear stress graph as a function of the viscosity ratio (μ_p) in the core and plasma regions. The graph increases as the viscosity ratio increases. The graph in Fig. (5.18) shows how the blood flow rate decreases as the density ratio (ρ_0) between the core and plasma region decreases. Fig (5.19) shows the graph of curvature Figure (5.19) displays the resistance profile's curvature (R_c) graph, which decreases as the curvature increases. in the resistance profile which decreases with curvature (R_c) increases.

5.4 Concluding Remarks

In order to achieve pulsatile blood flow through a w-shaped stenosed artery, where the core and plasma portions experience Newtonian blood flow, a two-layer mathematical model has been constructed.. The finite difference method was used to assess the numerical solution.

- As the peripheral plasma layer becomes thicker, the blood flow's velocity, temperature, and concentration profile all drop.
- Raising the chemical reaction parameter (E) causes a decline in the concentration profile. Rising molecule diffusivity directly dampens the flow's concentration profile, causing this to occur.
- The study reveals that Peclet number (Pe) and Schmidt's number (Sc) both function to lower blood flow concentration and temperature, respectively.
- It's also important to remember that the divergent tapering artery is both the hottest and the most resistant to the flow of all the arteries, tapering or not all of which are equally significant.

- This demonstrates how the taper angle plays a significant role in establishing the relevant flow parameters. Therefore, the taper angle needs to be factored in at all times process.

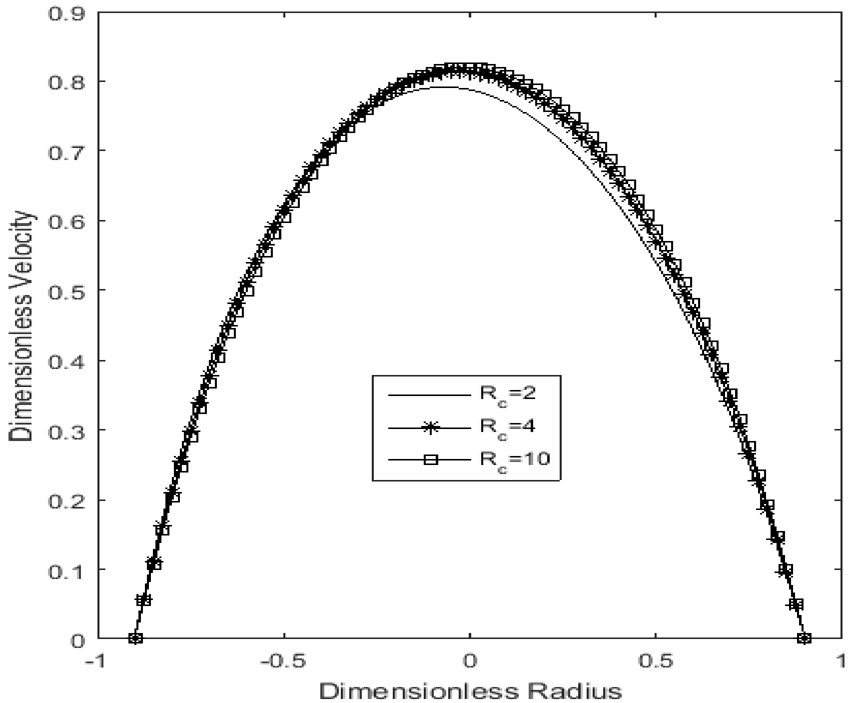

Figure 5.2

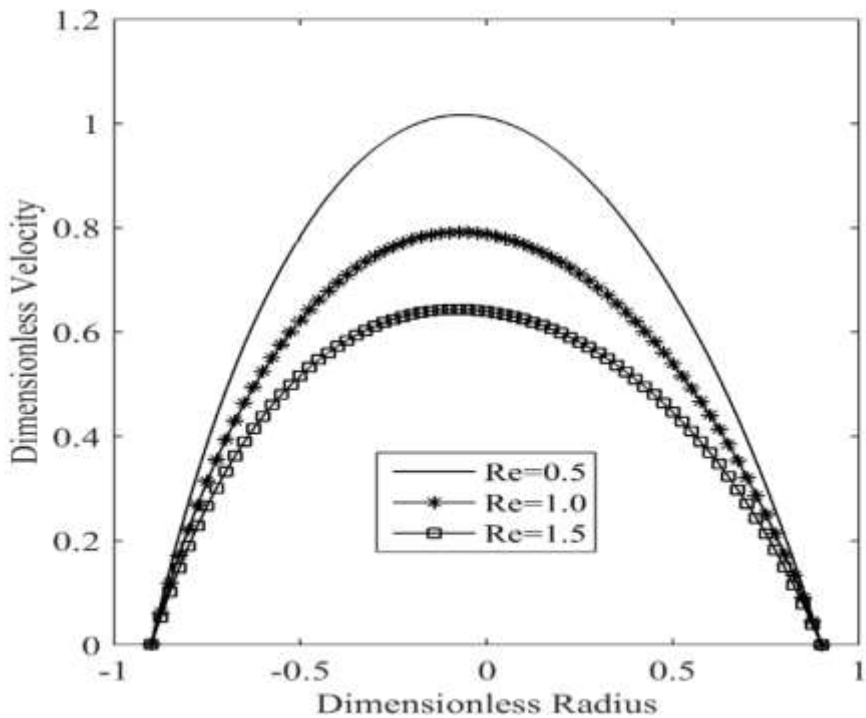

Figure 5.3

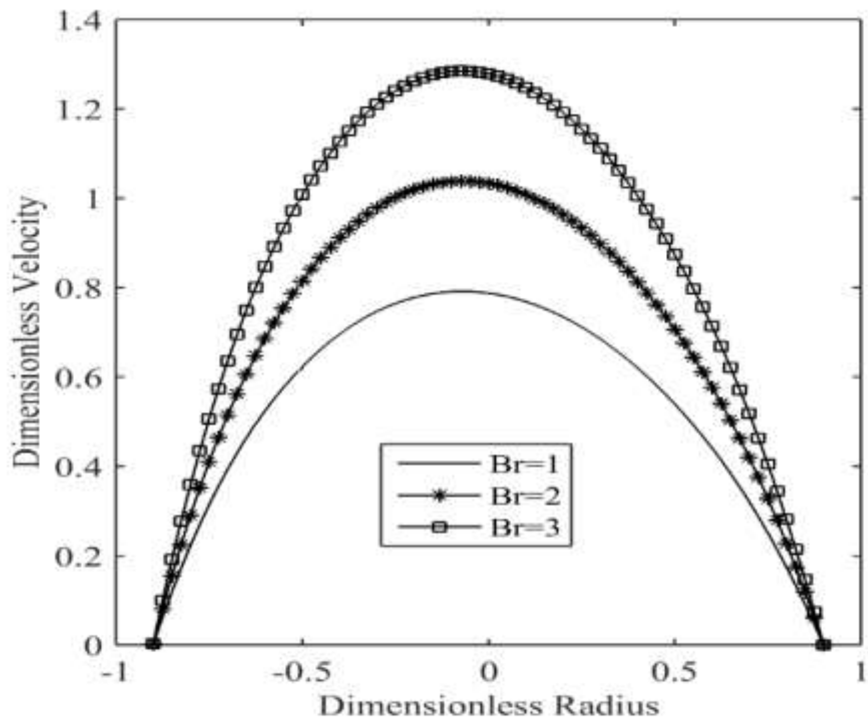

Figure 5.4

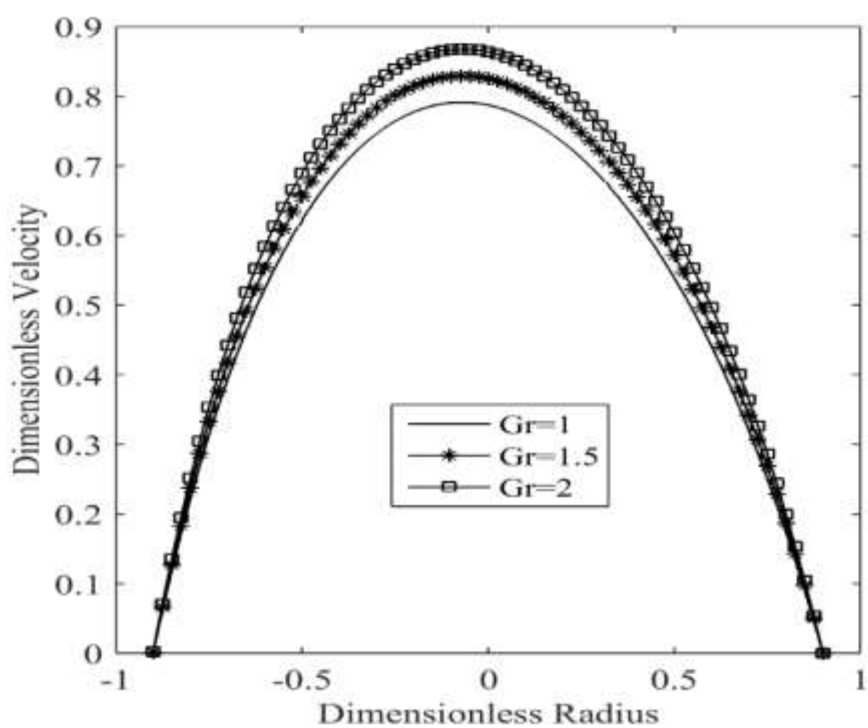

Figure 5.5

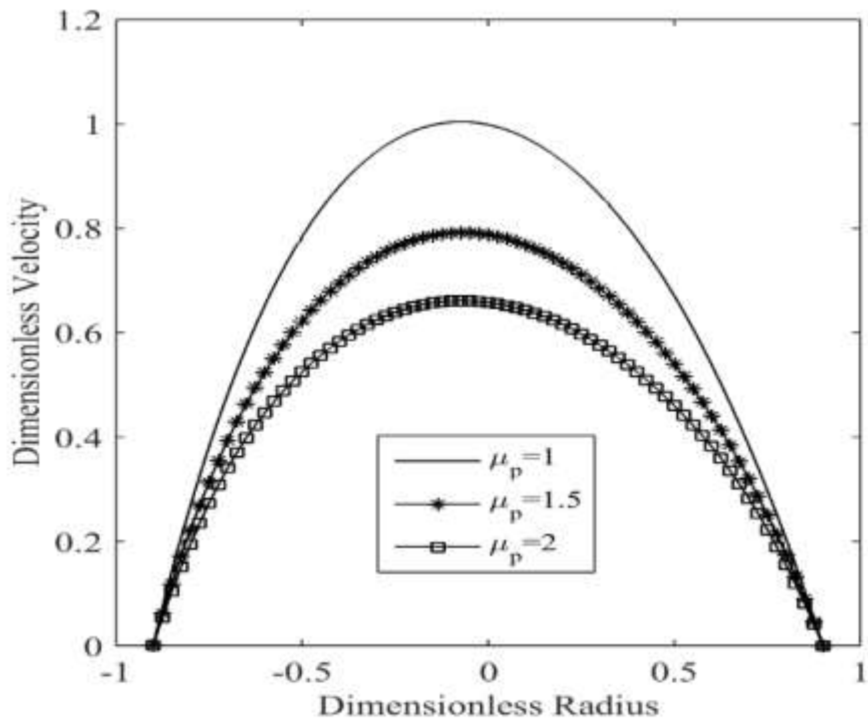

Figure 5.6

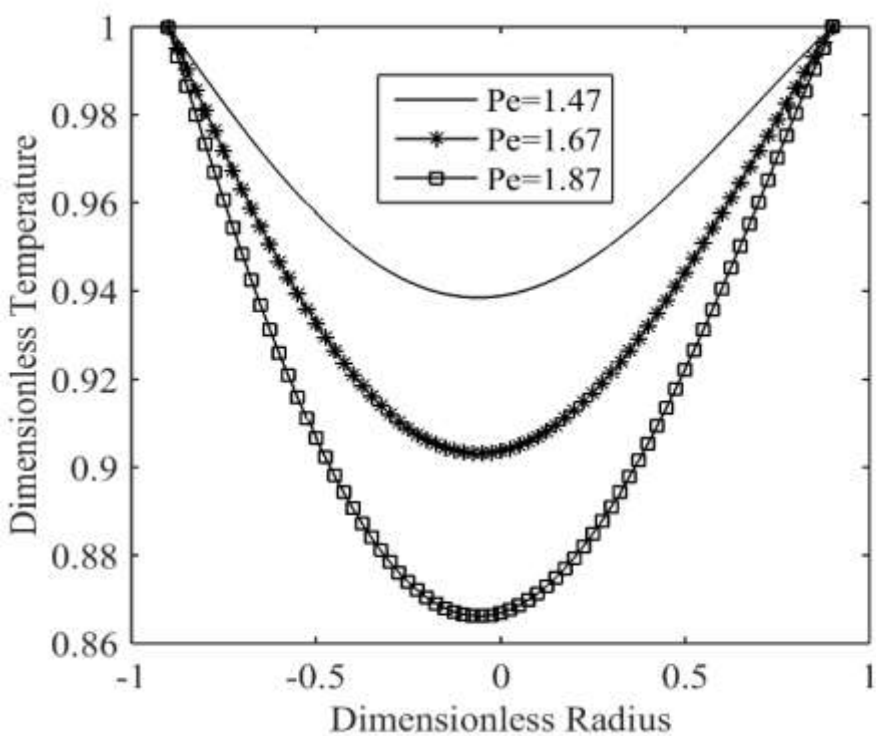

Figure 5.7

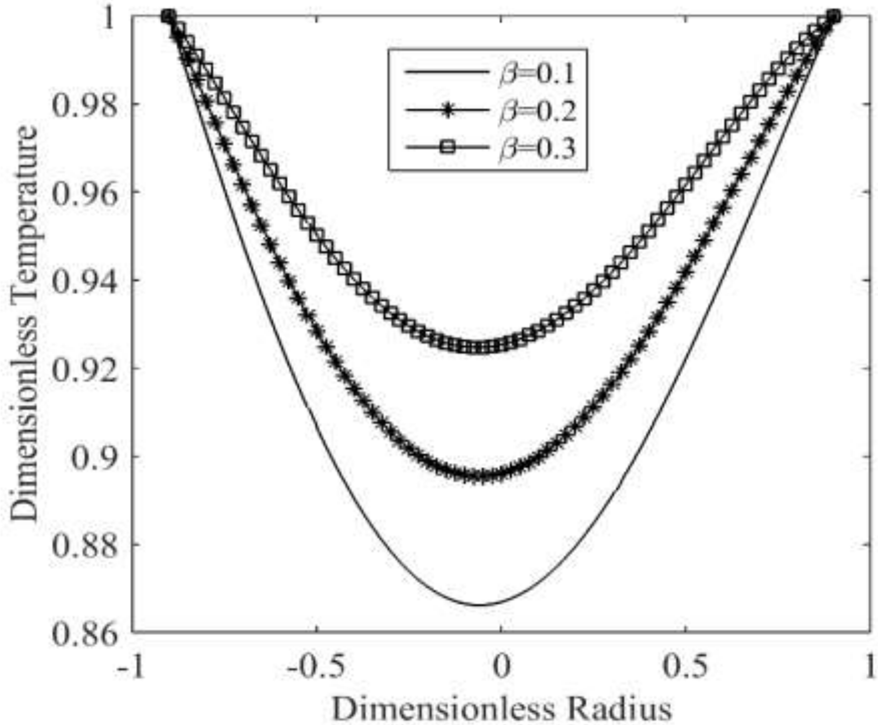

Figure 5.8

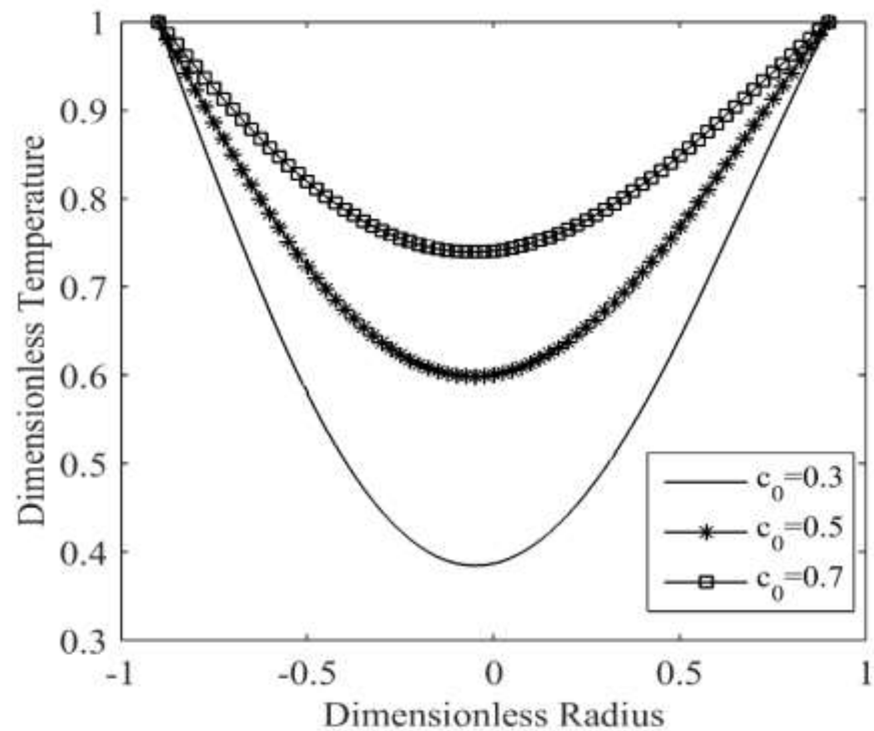

Figure 5.9

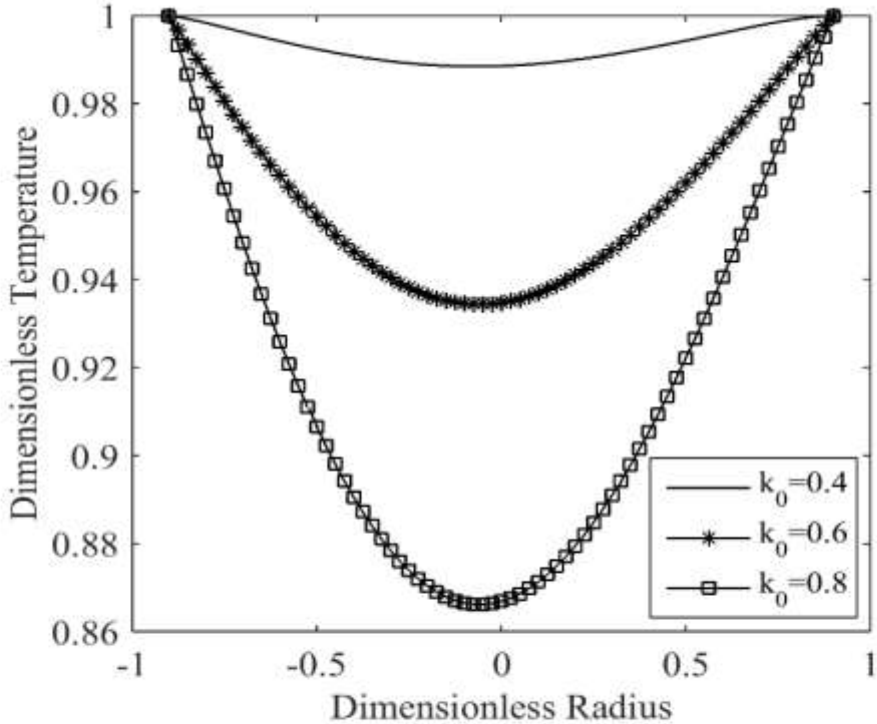

Figure 5.10

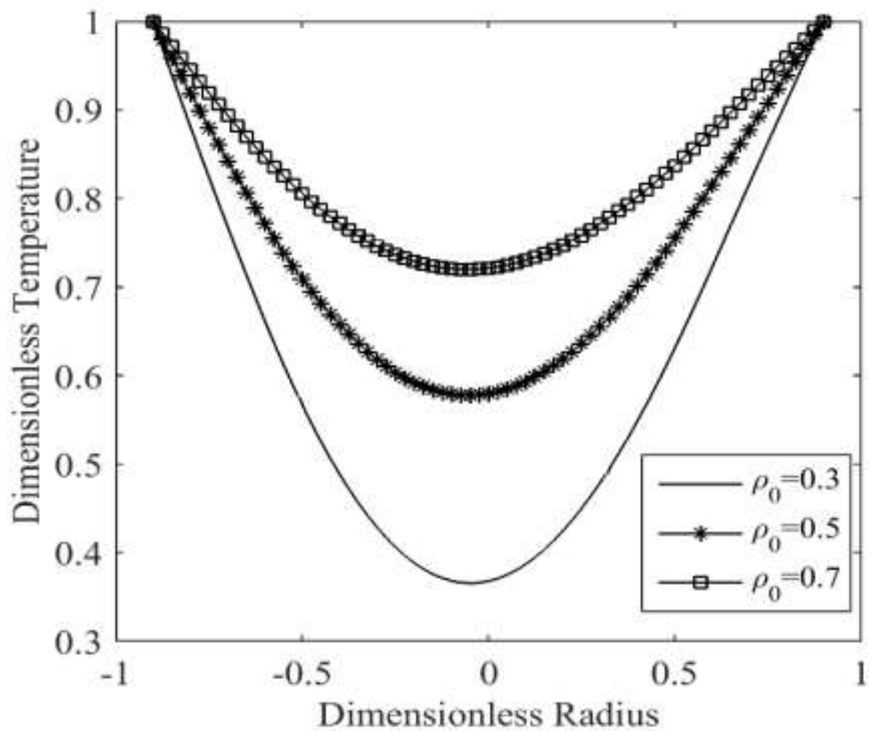

Figure 5.1

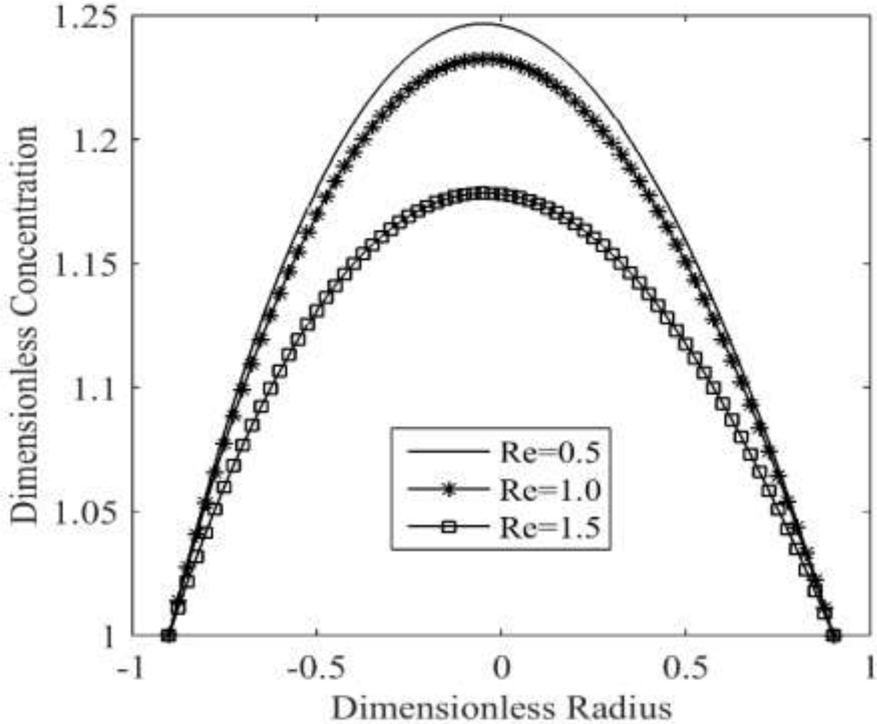

Figure 5.12

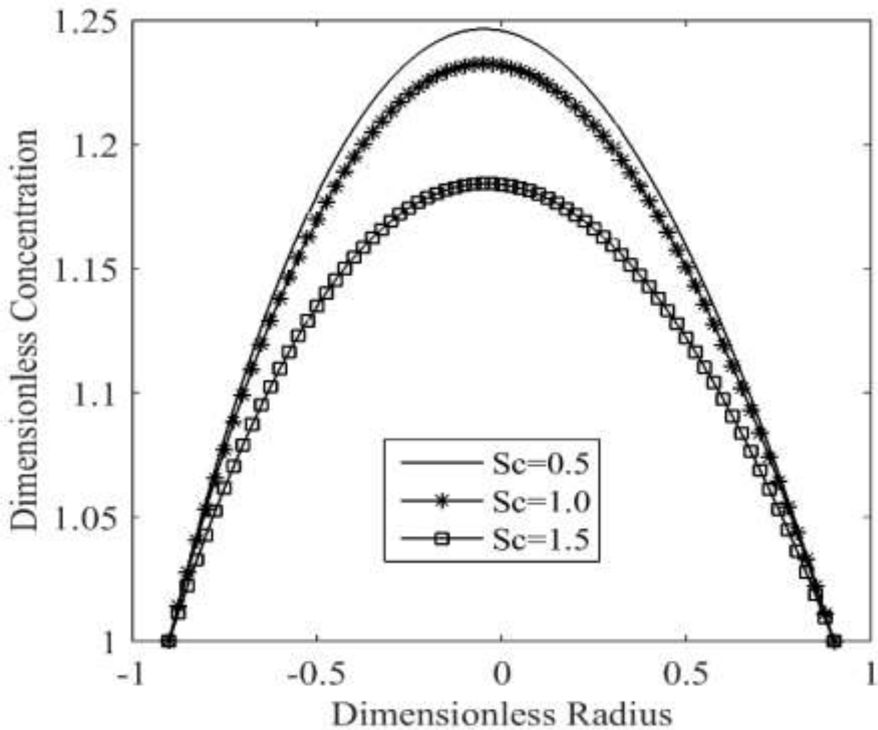

Figure 5.13

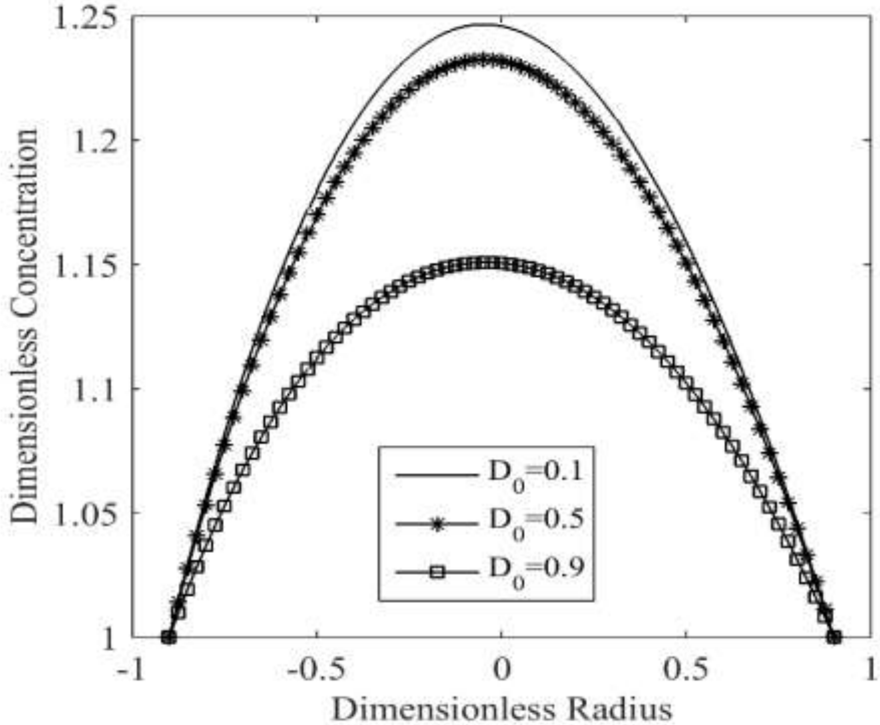

Figure 5.14

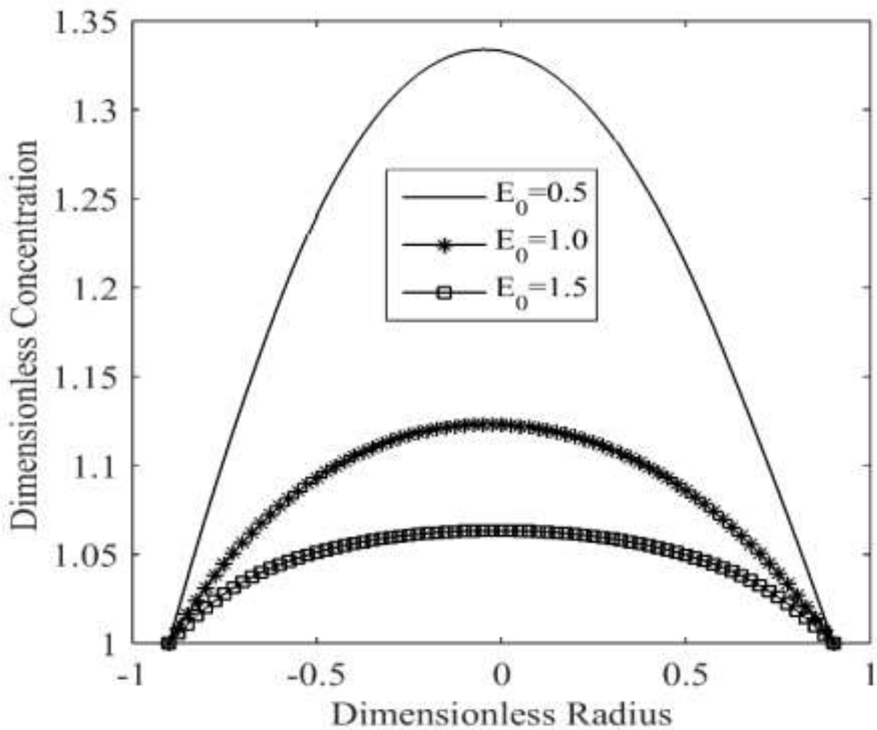

Figure 5.15

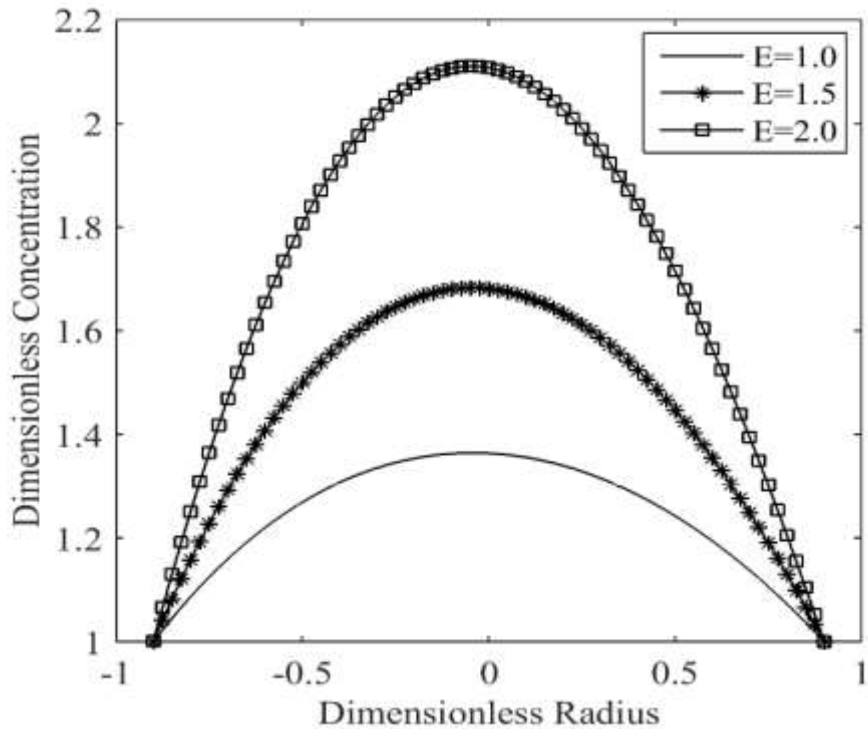

Figure 5.16

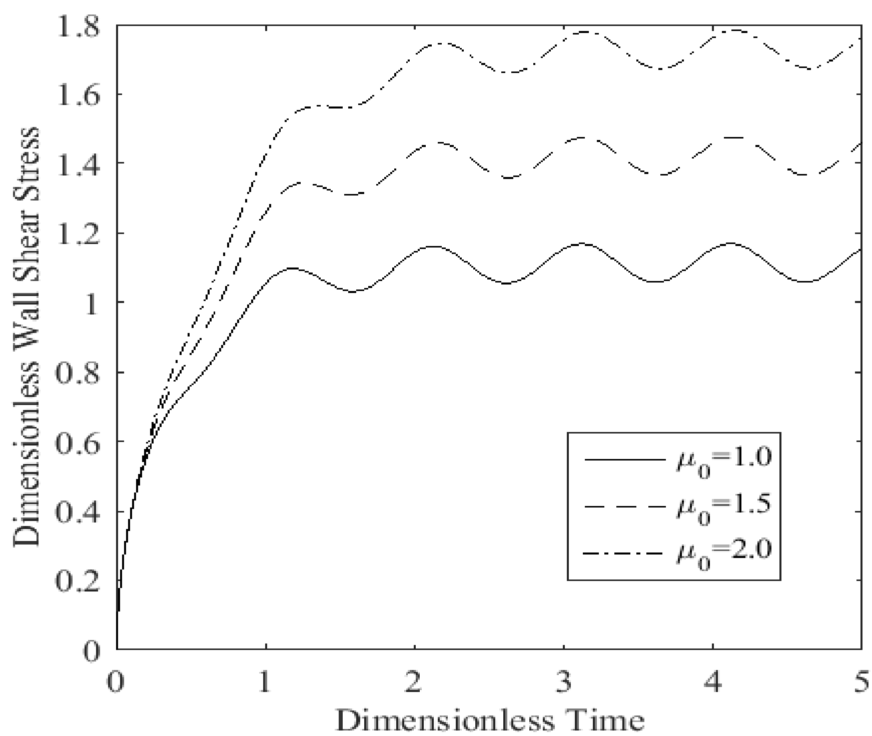

Figure 5.17

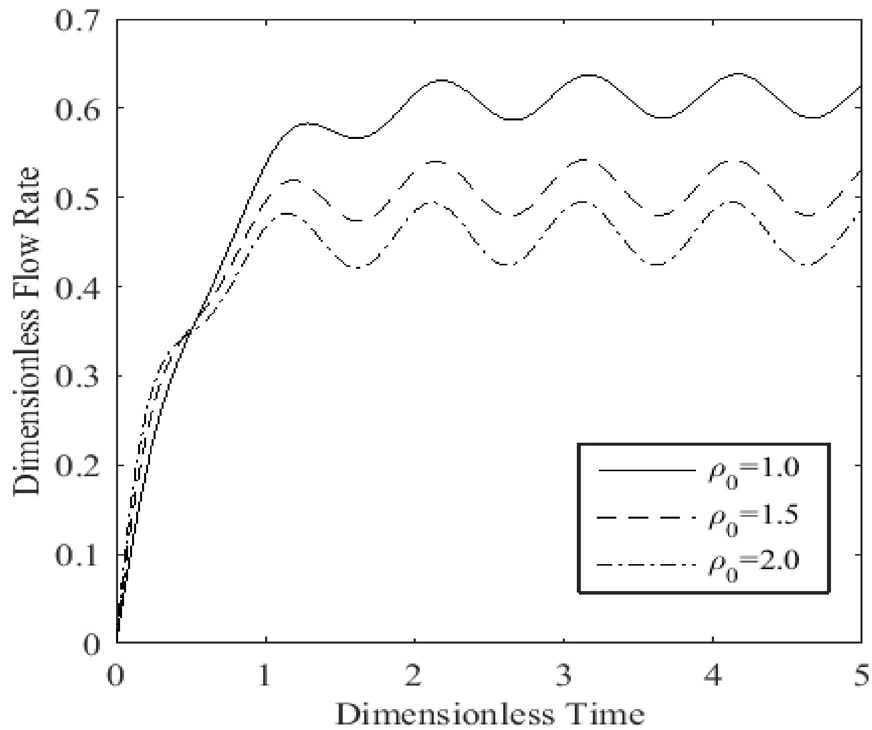

Figure 5.18

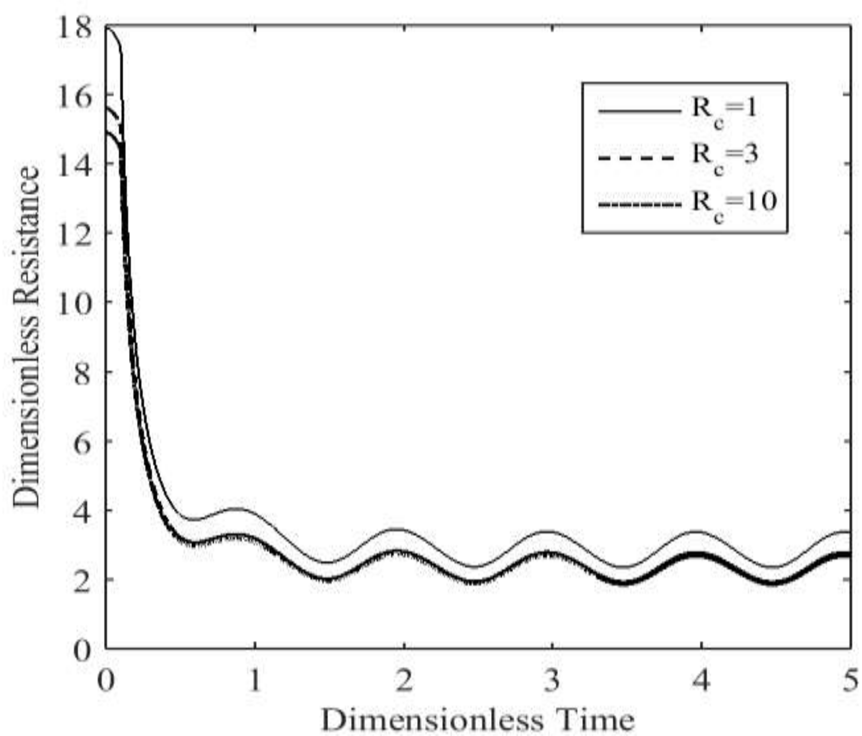

Figure 5.19

Chapter 6

Two Fluid Flow of Blood in a Curved Stenotic Artery under Pulsating Condition

The present chapter deal with a two-phase examination of pulsatile blood flow via a stenosed, restricted artery. The plasma and core areas are modeled using the Herschel-Bulkley constitutive relation and the Newtonian constitutive relation, respectively.The problem is represented using cylindrical coordinates. A modest stenosis assumption is used to simplify the non-dimensional governing equations of the flow issue. The radial coordinate transformation is utilised to reduce the effect of the blood vessel wall. An explicit finite difference approach is used to solve the resultant nonlinear system of differential equations while accounting for the provided boundary conditions. After the necessary adjustments have been made to the crucial non-dimensional parameters, an analysis of the data behind the huge image, such as axial velocity, temperature field, concentration wall shear stress, flow rate, and flow impedance, is conducted.

6.1 Flow Equation

The unsteady, laminar, fully developed circulation of blood in two phases through a curved blood vessel, having overlapping stenosis in its limen is taken into account. The artery of length "L" is spiraled in a circle of radius R^c. The mathematical expression for the geometry of the curved blood vessel is defined as:

$$\left.\begin{array}{l} R_i(z)=\left\{\begin{array}{ll}\left(\tau' z+e_0\right)\left(\beta-\frac{64}{10}\eta\left(\frac{11}{32}l_0^3(z-d)-\frac{47}{48}l_0^2(z-d)^2+l_0(z-d)^3-\frac{1}{3}(z-d)^4\right)\right), & d\le z\le d+\frac{3}{2}l_0, \\ \left(\tau' z+e_0\right), & otherwise\end{array}\right\}, Outer\ wall, \\ -R_{1i}(z)=\left\{\begin{array}{ll}\left(\tau' z-e_0\right)\left(\beta-\frac{64}{10}\eta\left(\frac{11}{32}l_0^3(z-d)-\frac{47}{48}l_0^2(z-d)^2+l_0(z-d)^3-\frac{1}{3}(z-d)^4\right)\right), & d\le z\le d+\frac{3}{2}l_0, \\ \left(\tau' z-e_0\right), & otherwise\end{array}\right\}, Inner\ wall. \end{array}\right\} \tag{6.1}$$

Here, the outer and inner walls of the curved blood vessel are designated by $R_i(z)$ and $-R_{1i}(z)$, where $i=1$ is for core region and $i\le 2$ is for plasma region, respectively. $\beta<1$ shows for core region and $\beta=1$ shows plasma region in the Eq. (5.1) e_0 is the radius of the normal blood vessel, $\tau'=\tan\varphi$ is the tapering parameter and φ is the tapering angle, d symbolized the location of the abnormality present in the lumen of the blood vessel, l_0 is the length of the stenosis. The radial and axial coordinates are represented by r and z respectively. This η parameter is declared as a constant, and it is used as:

$$\eta=\frac{4\delta^*}{a l_0^{\,4}}, \tag{6.2}$$

In this, δ^* shows the critical height of the stenotic zone in two places (i.e).

$$z=d+\frac{8l_0}{25}, \text{ and } z=d+\frac{61l_0}{50}. \tag{6.3}$$

The schematic diagram of the diseased curved blood vessel is shown in Fig. (6.1).

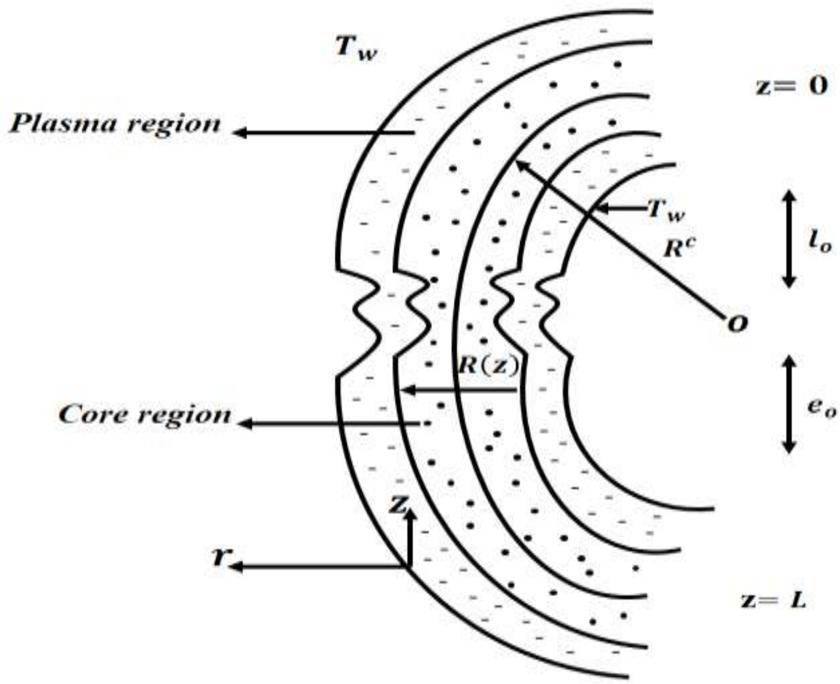

Figure 6.1

The flow field's governing equation is given by:

Core Region

$$\bar{V}_C = U_C(t,r,z), 0, W_C(t,r,z), \quad T_C^* = T_C^*(t,r,z), \quad C_C^1 = C_C^1(t,r,z). \tag{6.4}$$

Plasma Region

$$\bar{V}_P = U_P(t,r,z), 0, W_P(t,r,z), \quad T_P^* = T_P^*(t,r,z), \quad C_P^1 = C_P^1(t,r,z). \tag{6.5}$$

The lower subscript C and P shows the core and plasma region in this article. The U is radial component W is the axial component of velocity in Eq. (6.4)-(6.5), whereas is the temperature component denoted by T^* and the concentration component of nanoparticles denoted by C^1.

The following are the continuity equation, momentum equation, energy equation, and mass absorption equation for core region using the previously established flow variables.

$$\frac{\partial}{\partial r}\left(r + R^c\right)U_C + R^c \frac{\partial W_C}{\partial z} = 0, \tag{6.6}$$

$$\rho_C\left(\frac{\partial U_C}{\partial t}+U_C\frac{\partial U_C}{\partial r}+\frac{R^c}{r+R^c}W_C\frac{\partial U_C}{\partial z}-\frac{U_C^2}{r+R^c}\right)=-\frac{\partial p}{\partial r}+\frac{1}{\left(r+R^c\right)^2}\frac{\partial}{\partial r}\left(\left(r+R^c\right)S^{rr}\right)+\frac{R^c}{r+R^c}\frac{\partial S^{rz}}{\partial z}-\frac{S^{zz}}{r+R^c},\tag{6.7}$$

$$\rho_C\left(\frac{\partial W_C}{\partial t}+U_C\frac{\partial W_C}{\partial r}+\frac{R^c}{r+R^c}W_C\frac{\partial W_C}{\partial z}+\frac{U_C W_C}{r+R^c}\right)=-\left(\frac{R^c}{r+R^c}\right)\frac{\partial p}{\partial z}+\frac{1}{\left(r+R^c\right)^2}\frac{\partial}{\partial r}\left(\left(r+R^c\right)S^{rz}\right)$$
$$+\frac{R^c}{r+R^c}\frac{\partial S^{zz}}{\partial z}+\rho_C g\alpha_T\left(T_C^*-T_w\right)+\rho_C g\alpha_{C^1}\left(C_C^1-C_1\right),\tag{6.8}$$

$$\left(\rho c_p\right)_{Cf}\left(\frac{\partial T_C^*}{\partial t}+U_C\frac{\partial T_C^*}{\partial r}+\frac{R^c}{r+R^c}W_C\frac{\partial T_C^*}{\partial z}\right)=k_{Cf}\left(\frac{\partial^2 T_C^*}{\partial r^2}+\frac{1}{r+R^c}\frac{\partial T_C^*}{\partial r}+\left(\frac{R^c}{r+R^c}\right)^2\frac{\partial^2 T_C^*}{\partial z^2}\right)+\theta_0,\tag{6.9}$$

$$\frac{\partial C_C^1}{\partial t}+U_C\frac{\partial C_C^1}{\partial r}+W_C\frac{\partial C_C^1}{\partial z}=D_C\left(\frac{\partial^2 C_C^1}{\partial r^2}+\frac{1}{r+R^c}\frac{\partial C_C^1}{\partial r}+\left(\frac{R^c}{r+R^c}\right)^2\frac{\partial^2 C_C^1}{\partial z^2}\right)+E_C^{'}\left(C_C^1-C_1\right),\tag{6.10}$$

Similarly for the plasma region,

$$\frac{\partial}{\partial r}\left(r+R^c\right)U_P+R^c\frac{\partial W_P}{\partial z}=0,\tag{6.11}$$

$$\rho_P\left(\frac{\partial U_P}{\partial t}+U_P\frac{\partial U_P}{\partial r}+\frac{R^c}{r+R^c}W_P\frac{\partial U_P}{\partial z}-\frac{U_P^2}{r+R^c}\right)=-\frac{\partial p}{\partial r}+\frac{1}{\left(r+R^c\right)}\frac{\partial}{\partial r}\left(\mu_P\left(r+R^c\right)\frac{\partial U_P}{\partial r}\right)$$
$$+\left(\frac{R^c}{r+R^c}\right)^2\frac{\partial^2 W_P}{\partial z^2}-\frac{W_P}{\left(r+R^c\right)^2}-\frac{2R^c}{\left(r+R^c\right)^2}\frac{\partial U_P}{\partial z},\tag{6.12}$$

$$\rho_P\left(\frac{\partial W_P}{\partial t}+U_P\frac{\partial W_P}{\partial r}+\frac{R^c}{r+R^c}W_P\frac{\partial W_P}{\partial z}+\frac{U_P W_P}{r+R^c}\right)=-\left(\frac{R^c}{r+R^c}\right)\frac{\partial p}{\partial z}+\left(\frac{1}{\left(r+R^c\right)}\frac{\partial}{\partial r}\left(\mu_P\left(r+R^c\right)\frac{\partial W_P}{\partial r}\right)\right)$$
$$+\left(\frac{R^c}{r+R^c}\right)^2\frac{\partial^2 W_P}{\partial z^2}-\frac{W_P}{\left(r+R^c\right)^2}+\frac{2R^c}{\left(r+R^c\right)^2}\frac{\partial W_P}{\partial z}+\rho_P g\alpha_T\left(T_P^*-T_w\right)+\rho_P g\alpha_{C^1}\left(C_P^1-C_1\right),\tag{6.13}$$

$$\left(\rho c_p\right)_{Pf}\left(\frac{\partial T_P^*}{\partial t}+U_P\frac{\partial T_P^*}{\partial r}+\frac{R^c}{r+R^c}W_P\frac{\partial T_P^*}{\partial z}\right)=k_{Pf}\left(\frac{\partial^2 T_P^*}{\partial r^2}+\frac{1}{r+R^c}\frac{\partial T_P^*}{\partial r}+\left(\frac{R^c}{r+R^c}\right)^2\frac{\partial^2 T_P^*}{\partial z^2}\right)+\theta_0, \tag{6.14}$$

$$\frac{\partial C_P^1}{\partial t}+U_P\frac{\partial C_P^1}{\partial r}+W_P\frac{\partial C_P^1}{\partial z}=D_P\left(\frac{\partial^2 C_P^1}{\partial r^2}+\frac{1}{r+R^c}\frac{\partial C_P^1}{\partial r}+\left(\frac{R^c}{r+R^c}\right)^2\frac{\partial^2 C_P^1}{\partial z^2}\right)+E_P^{'}\left(C_P^1-C_1\right). \tag{6.15}$$

The term S^{rr}, S^{rz} *and* S^{zz} are the extra stress tensor component which is seeming in Eqs. (6.7) and (6.8). The relation of the Herschel-Bulkley model is:

$$S=\left(\mu\Pi^{n-1}+\frac{\tau_y}{\Pi}\right)\boldsymbol{A}^1. \tag{6.16}$$

In (6.16), μ is the consistency index, n is the power law index, τ_y is the yield stress and A^1 is the Rivlin-Ericksen tensor defined by:

$$\boldsymbol{A}^1=\nabla\boldsymbol{V}+\nabla\boldsymbol{V}^T. \tag{6.17}$$

Where the first Rivlin-Ericksen tensor of the second invariant (Π) is defined as:

$$\Pi=\sqrt{\frac{1}{2}tra\left(A^{1^2}\right)}. \tag{6.18}$$

The constitutive relation (6.16) for the case of curved channel yields is shown in Eq (6.4).

$$S^{rr}=2\left(\mu\Pi^{n-1}+\frac{\tau_y}{\Pi}\right)\left(\frac{\partial U_C}{\partial r}\right), \tag{6.19}$$

$$S^{zz}=2\left(\mu\Pi^{n-1}+\frac{\tau_y}{\Pi}\right)\left(\frac{R^c}{r+R^c}\frac{\partial W_C}{\partial z}+\frac{U_C}{r+R^c}\right), \tag{6.20}$$

$$S^{rz}=\left(\mu\Pi^{n-1}+\frac{\tau_y}{\Pi}\right)\left(\frac{\partial W_C}{\partial r}+\frac{R^c}{r+R^c}\frac{\partial U_C}{\partial z}-\frac{W_C}{r+R^c}\right), \tag{6.21}$$

$$\Pi=\left\|\left[\frac{1}{2}\left(\left(2\frac{\partial U_C}{\partial r}\right)^2+2\left(\frac{\partial W_C}{\partial r}+\frac{R^c}{r+R^c}\frac{\partial U_C}{\partial z}-\frac{W_C}{r+R^c}\right)^2+\left(\frac{R^c}{r+R^c}\frac{\partial W_C}{\partial z}+\frac{U_C}{r+R^c}\right)^2\right)\right]\right\|. \tag{6.22}$$

The following boundary conditions are appropriate for the given model:

$$
\begin{cases}
W_P = 0,\ T_P^* = T_W^*,\ C_P^1 = C_W^1 \quad at\ r = R(z), \\
W_C = W_P,\ T_P^* = T_C^*,\ C_P^1 = C_C^1\ \ at\ r = R_1(z), \\
\dfrac{\partial W_C}{\partial r} = 0,\ \dfrac{\partial T_C^*}{\partial r} = 0,\ \dfrac{\partial C_C^1}{\partial r} = 0\ at\ r = 0, \\
\dfrac{\partial T_C^*}{\partial r} = \dfrac{\partial T_P^*}{\partial r},\ \dfrac{\partial C_C^1}{\partial r} = \dfrac{\partial C_P^1}{\partial r}\ at\ r = R_1(z).
\end{cases}
\tag{6.23}
$$

The dimensions of the following equations are removed when utilizing variables (6)-(15):

$$
\begin{gathered}
r = \bar{r}e_0,\ W_C = \overline{W_C}U_0,\ U_C = \frac{\overline{U_C}\delta^* U_0}{l_0},\ \ t = \frac{\bar{t}e_0}{U_0},\ \ z = \bar{z}l_0,\ R^c = R_c e_0,\ \ p = \frac{\bar{p}U_0 l_0 \mu_0}{e_0^2}, \\
T_C^* - T_w = \theta\left(T_1 - T_w\right),\ \mathrm{Re} = \frac{\rho_f U_0 e_0}{\mu_0},\ \ C_C^1 - C_1 = \sigma_C C_1,\ Br = \frac{\rho_P g e_0^2}{U_0 \mu_0}\alpha_C C_1,\ \bar{S}^{zz} = \frac{l_0}{U_0\mu_0}S^{zz}, \\
\mathrm{Re} = \frac{\rho_f U_0 e_0}{\mu_0}, P_e = \frac{\overline{c_{pf}}\,\overline{\rho_P} e_0^2 U_0}{\overline{k_{Pf}}},\ Sc = \frac{\overline{\mu_P}}{\overline{D_p}\,\overline{\rho_P}},\ \beta = \frac{\theta_0 e_0^2}{k_{Pf}\left(T_1 - T_w\right)}, \overline{E_P^{'}} = \frac{E\overline{\mu_P}}{\overline{\rho_P} e_0^2}, W_P = \overline{W_P}U_0, \\
U_P = \frac{\overline{U_P}\delta^* U_0}{l_0}, T_P^* - T_w = \theta_P\left(T_1 - T_w\right), C_P^1 - C_1 = \sigma_P C_1,\ Gr_T = \frac{\rho_P g \alpha_T e_0^2}{U_0\mu_0}\left(T_1 - T_w\right), \\
\bar{S}^{rz} = \frac{e_0}{U_0\mu_0}S^{rz},\ \ \bar{S}^{rr} = \frac{l_0}{U_0\mu_0}S^{rr},\ \mu_0 = \frac{\overline{\mu_P}}{\mu_C},\ E_0 = \frac{\overline{E_P^{'}}}{E_C^{'}},\ D_0 = \frac{\overline{D_P}}{D_C},\ \ \rho_0 = \frac{\overline{\rho_P}}{\rho_C},\ c_0 = \frac{\overline{c_P}}{c_C}.
\end{gathered}
\tag{6.24}
$$

In the above definitions, $\overline{W}$ is axial velocity, $\bar{r}$ is radial coordinate, $\bar{z}$ axial directional co-ordinate, $\bar{t}$ is time, $\overline{R}$ is the radius, $\bar{p}$ is the pressure, Br the Brinkman number, Pe is Peclet number, Re is the Reynolds number, Gr is the local thermal Grashof number, Pr is the Prandtl number, U_0 is the average velocity of the blood, T_w represent the wall temperature, σ is nanoparticles concentration function, T_m represent the thermodynamic temperature, μ_0 is viscosity ratio among the plasma and core regions, ρ_0 is ratio of density in core and plasma regions, E is chemical reaction parameter, k_0 is ratio of thermal conductivity in core and plasma regions, Sc is Schmidt parameter and β is heat source or sink parameter.

When the constraints were lifted, the Simplified after removing bars Eqs. (6.6)-(6.15) are:

Core region:

$$\delta\left(\frac{\partial}{\partial r}(r+R_c)U_C\right)+R_c\frac{\partial W_C}{\partial z}=0, \tag{6.25}$$

$$\begin{aligned}\operatorname{Re}\delta\varepsilon^2\frac{1}{\rho_0}\left(\frac{\partial U_C}{\partial t}+\delta\varepsilon U_C\frac{\partial U_C}{\partial r}+\varepsilon\frac{R_c}{r+R_c}W_C\frac{\partial U_C}{\partial z}-\frac{\varepsilon}{\delta}\frac{U_C^2}{r+R_c}\right)=-\frac{\partial p}{\partial r}\\ +\varepsilon^2\left(\frac{1}{(r+R_c)^2}\frac{\partial}{\partial r}\left((r+R_c)S^{rr}\right)\right)+\varepsilon^2\left(\frac{R_c}{r+R_c}\right)\frac{\partial S^{rz}}{\partial z}-\frac{\varepsilon^2 S^{zz}}{r+R_c},\end{aligned} \tag{6.26}$$

$$\begin{aligned}\operatorname{Re}\frac{1}{\rho_0}\frac{\partial W_C}{\partial t}+\operatorname{Re}\frac{1}{\rho_0}\left(\delta\varepsilon\frac{\partial W_C}{\partial r}+\varepsilon\frac{R_c}{r+R_c}W_C\frac{\partial W_C}{\partial z}+\delta\varepsilon\frac{U_C W_C}{r+R^c}\right)=-\left(\frac{R_c}{r+R_c}\right)\frac{\partial p}{\partial z}\\ +\frac{1}{(r+R_c)^2}\frac{\partial}{\partial r}\left((r+R_c)^2 S^{rz}\right)+\varepsilon^2\left(\frac{R_c}{r+R_c}\right)\frac{\partial S^{zz}}{\partial z}+\frac{1}{\rho_0}Gr_T\theta_C+\frac{1}{\rho_0}Br\sigma_C,\end{aligned} \tag{6.27}$$

$$\frac{Pe}{\rho_0 c_0}\left(\frac{\partial\theta_C}{\partial t}+\delta\varepsilon\frac{\partial\theta_C}{\partial r}+\varepsilon\frac{R_c}{r+R_c}W_C\frac{\partial\theta_C}{\partial z}\right)=\frac{\partial^2\theta_C}{\partial r^2}+\frac{1}{r+R_c}\frac{\partial\theta_C}{\partial r}+\varepsilon^2\left(\frac{R_c}{r+R_c}\right)^2\frac{\partial^2\theta_C}{\partial z^2}+\frac{\theta_0(e_0)^2}{(T_1-T_w)}\frac{k_{0f}}{k_{Pf}}, \tag{6.28}$$

$$\operatorname{Re}\left(\frac{\partial\sigma_C}{\partial t}+\delta\varepsilon\frac{\partial\sigma_C}{\partial r}+\varepsilon W\frac{\partial\sigma_C}{\partial z}\right)=\frac{1}{D_0}\frac{1}{Sc}\left(\frac{\partial^2\sigma_C}{\partial r^2}+\frac{1}{r+R_c}\frac{\partial\sigma_C}{\partial r}+\varepsilon^2\left(\frac{R_c}{r+R_c}\right)^2\frac{\partial^2\sigma_C}{\partial z^2}\right)+\frac{E}{E_0}\sigma_C. \tag{6.29}$$

Plasma region:

$$\delta\left(\frac{\partial}{\partial r}(r+R_c)U_P\right)+R_c\frac{\partial W_P}{\partial z}=0, \tag{6.30}$$

$$\begin{aligned}\operatorname{Re}\delta\varepsilon^2\left(\frac{\partial U_P}{\partial t}+\delta\varepsilon U_P\frac{\partial U_P}{\partial r}+\varepsilon\frac{R_c}{r+R_c}W_P\frac{\partial U_P}{\partial z}-\delta\varepsilon\frac{U_P^2}{r+R_c}\right)=-\frac{\partial p}{\partial r}\\ +\frac{\mu_P}{\mu_0 l_0^{\,2}}\delta\frac{1}{(r+R_c)}\frac{\partial}{\partial r}\left((r+R_c)\frac{\partial U_P}{\partial r}\right)+\left(\frac{R_c}{r+R_c}\right)^2\frac{1}{\mu_0}\varepsilon^3\frac{\partial^2 W_P}{\partial z^2}-\frac{1}{\mu_0}\varepsilon\frac{W_P}{(r+R_c)^2}-\frac{2R_c}{(r+R_c)^2}\delta\varepsilon\frac{\partial U_P}{\partial z}\end{aligned} \tag{6.31}$$

$$\begin{aligned}\operatorname{Re}\frac{\partial W_P}{\partial t}+\operatorname{Re}\left(\delta\varepsilon\frac{\partial W_P}{\partial r}+\varepsilon\frac{R_c}{r+R_c}W_P\frac{\partial W_P}{\partial z}+\delta\varepsilon\frac{U_P W_P}{r+R^c}\right)=-\left(\frac{R_c}{r+R_c}\right)\frac{\partial p}{\partial z}\\ +\frac{1}{(r+R_c)}\frac{\partial}{\partial r}\left((r+R_c)\frac{\partial W_P}{\partial r}\right)+\left(\frac{R_c}{r+R_c}\right)^2\varepsilon^2\frac{\partial^2 W_P}{\partial z^2}-\frac{W_P}{(r+R_c)^2}\\ -\frac{2R_c}{(r+R_c)^2}\varepsilon\frac{\partial W_P}{\partial z}+Gr_T\theta_P+Br\sigma_P,\end{aligned} \tag{6.32}$$

$$\mathrm{P}e\left(\frac{\partial \theta_P}{\partial t}+\delta\varepsilon\frac{\partial \theta_P}{\partial r}+\varepsilon\frac{R_c}{r+R_c}W_P\frac{\partial \theta_P}{\partial z}\right)=\frac{\partial^2 \theta_P}{\partial r^2}+\frac{1}{r+R_c}\frac{\partial \theta_P}{\partial r}+\varepsilon^2\left(\frac{R_c}{r+R_c}\right)^2\frac{\partial^2 \theta_P}{\partial z^2}+\frac{\theta_0\left(e_0\right)^2}{\left(T_1-T_w\right)k_{Pf}}, \tag{6.33}$$

$$\mathrm{Re}\left(\frac{\partial \sigma_P}{\partial t}+\delta\varepsilon\frac{\partial \sigma_P}{\partial r}+\varepsilon W\frac{\partial \sigma_P}{\partial z}\right)=\frac{1}{Sc}\left(\frac{\partial^2 \sigma_P}{\partial r^2}+\frac{1}{r+R_c}\frac{\partial \sigma_P}{\partial r}+\varepsilon^2\left(\frac{R_c}{r+R_c}\right)^2\frac{\partial^2 \sigma_P}{\partial z^2}\right)+E\sigma_P. \tag{6.34}$$

We utilize two assumptions based on mild stenosis in the accompanying analysis: $\varepsilon\left(=\frac{e_0}{l_0}\right)=O(1)$ and $\delta\left(=\frac{\delta^*}{e_0}\right)\ll 1$ i.e. The first requirement is that the stenotic region be no longer than the channel's radius. The second requirement is that the track length's elevation be smaller than the channel radius.

equation (6.25) to (6.34) is here's a reduction of the following:

Core region:

$$\frac{\partial p}{\partial r}=0, \tag{6.35}$$

$$\begin{aligned}\mathrm{Re}\frac{1}{\rho_0}\frac{\partial W_C}{\partial t}&=-\left(\frac{R_c}{r+R_c}\right)\frac{\partial p}{\partial z}+\frac{1}{\rho_0}Gr_T\theta_C+\frac{1}{\rho_0}Br\sigma_C\\&+\frac{1}{\left(r+R_c\right)^2}\frac{\partial}{\partial r}\left(\left(r+R_c\right)^2\left(\mu\left(\frac{\partial W_C}{\partial r}-\frac{W_C}{r+R^c}\right)^{n-1}+\tau\left(\frac{\partial W_C}{\partial r}-\frac{W_C}{r+R^c}\right)^{-\frac{1}{2}}\right)\left(\frac{\partial W_C}{\partial r}-\frac{W_C}{r+R^c}\right)\right),\end{aligned} \tag{6.36}$$

$$\frac{\mathrm{P}ek_0}{\rho_0 c_0}\frac{\partial \theta_C}{\partial t}=\frac{\partial^2 \theta_C}{\partial r^2}+\frac{1}{r+R_c}\frac{\partial \theta_C}{\partial r}+k_0\beta, \tag{6.37}$$

$$\mathrm{Re}\frac{\partial \sigma_C}{\partial t}=\frac{1}{D_0}\frac{1}{Sc}\left(\frac{\partial^2 \sigma_C}{\partial r^2}+\frac{1}{r+R_c}\frac{\partial \sigma_C}{\partial r}\right)+\frac{E}{E_0}\sigma_C. \tag{6.38}$$

Plasma region:

$$\frac{\partial p}{\partial r}=0, \tag{6.39}$$

$$\mathrm{Re}\frac{\partial W_P}{\partial t}=-\left(\frac{R_c}{r+R_c}\right)\frac{\partial p}{\partial z}+\frac{1}{\left(r+R_c\right)}\frac{\partial}{\partial r}\left(\left(r+R_c\right)\frac{\partial W_P}{\partial r}\right)-\frac{W_P}{\left(r+R_c\right)^2}+Gr_T\theta_P+Br\sigma_P, \tag{6.40}$$

$$\mathrm{P}e\frac{\partial\theta_P}{\partial t}=\frac{\partial^2\theta_P}{\partial r^2}+\frac{1}{r+R_c}\frac{\partial\theta_P}{\partial r}+\beta, \tag{6.41}$$

$$\mathrm{Re}\frac{\partial\sigma_P}{\partial t}=\frac{1}{Sc}\left(\frac{\partial^2\sigma_P}{\partial r^2}+\frac{1}{r+R_c}\frac{\partial\sigma_P}{\partial r}\right)+E\sigma_P. \tag{6.42}$$

The equation for the Pulsatile Pressure gradient:

$$-\frac{\partial p}{\partial z}=A_0+A_1\cos\left(2\pi\omega_p t\right),\qquad\qquad t>0. \tag{6.43}$$

Equation (6.43), A_0 denotes the mean pressure gradient, and A_1 which represents the amplitude of the pulsatile component, which may be found by solving for it.

$$-\frac{\partial p}{\partial z}=B_1\left(1+c\cos\left(c_1 t\right)\right), \tag{6.44}$$

Where

$$c_1=\frac{2\pi\omega_p e_0}{U_0},\quad c=\frac{A_1}{A_0},\quad B_1=\frac{A_0e_0^2}{\mu_0U_0}. \tag{6.45}$$

In Equation (6.36) and (6.40) using the term $-\partial p/\partial z$ we get:

$$\mathrm{Re}\frac{1}{\rho_0}\frac{\partial W_C}{\partial t}=\left(\frac{R_c}{r+R_c}\right)B_1\left(1+c\cos\left(c_1t\right)\right)+\frac{1}{\rho_0}Gr_T\theta_C+\frac{1}{\rho_0}Br\sigma_C$$
$$+\frac{1}{\left(r+R_c\right)^2}\frac{\partial}{\partial r}\left(\left(r+R_c\right)^2\left(\mu\left(\frac{\partial W_C}{\partial r}-\frac{W_C}{r+R^c}\right)^{n-1}+\tau\left(\frac{\partial W_C}{\partial r}-\frac{W_C}{r+R^c}\right)^{-\frac{1}{2}}\right)\left(\frac{\partial W_C}{\partial r}-\frac{W_C}{r+R^c}\right)\right), \tag{6.46}$$

$$\mathrm{Re}\frac{\partial W_P}{\partial t}=\left(\frac{R_c}{r+R_c}\right)B_1\left(1+c\cos\left(c_1t\right)\right)+\frac{1}{\left(r+R_c\right)}\frac{\partial}{\partial r}\left(\left(r+R_c\right)\frac{\partial W_P}{\partial r}\right)-\frac{W_P}{\left(r+R_c\right)^2}+Gr_T\theta_P+Br\sigma_P, \tag{6.47}$$

Eqs. (6.23) have the following set of constraints and beginning conditions imposed on them:

$$\begin{cases} W_P = 0,\ \theta_P = 1,\ \sigma_P = 1 & at \quad r = R(z), \\ W_P = W_C,\ \theta_P = \theta_C,\ \sigma_P = \sigma_C & at \quad r = R_1(z), \\ \dfrac{\partial \theta_C}{\partial r} = \dfrac{\partial \theta_P}{\partial r},\ \dfrac{\partial \sigma_C}{\partial r} = \dfrac{\partial \sigma_P}{\partial r} & at \quad r = R_1(z), \\ \dfrac{\partial W_C}{\partial r} = 0,\ \dfrac{\partial \theta_C}{\partial r} = 0,\ \dfrac{\partial \sigma_C}{\partial r} = 0 & at \quad r = 0. \end{cases} \tag{6.48}$$

Wall shear stress is a crucial flow component to assess in the study of stenosed arterial blood flow, since physical stress causes vascular tissue in the artery to change histologically and morphologically. The shear stress at the core-plasma contact wall is determined as

$$\tau = \left(\frac{\partial W_C}{\partial r} \right)_{R_1}, \tag{6.49}$$

Shear stress at the arteries outside the wall is calculated as

$$\tau' = \frac{1}{\mu_0} \left(\frac{\partial W_P}{\partial r} \right)_{R_0}, \tag{6.50}$$

where the ratio of viscosity between the core and plasma regions is denoted by μ_0.

The blood flow in the artery's total volumetric flow rate is computed as

$$Q = \int_{-R}^{R} W dr. \tag{6.51}$$

For pulsed flow, the longitudinal impedance is expressed as the pressure gradient's phase relationship with the flow rate. This impedance connects the forces that are acting on blood that are connected to the local gradient of pressure as a function of blood flow as a result of the pulsed flow mechanism:

$$\Lambda = \frac{\left(\dfrac{\partial p}{\partial z} \right)}{Q}. \tag{6.52}$$

The simple equation for the dimensionalized geometry of an arterial segment is as follows:

$$R(z) = (1 + \tau z)\left[\beta - \frac{64}{10}\eta_1 \left(\frac{11}{32}(z-\sigma) - \frac{47}{48}(z-\sigma)^2 + (z-\sigma)^3 - \frac{1}{3}(z-\sigma)^4 \right) \right],$$

$$\sigma \le z \le \sigma + \frac{3}{2}, \ \ Outer\ wall,$$

(6.53)

$$R_1(z) = (-1+\tau z)\left[\beta - \frac{64}{10}\eta_1\left(\frac{11}{32}(z-\sigma) - \frac{47}{48}(z-\sigma)^2 + (z-\sigma)^3 - \frac{1}{3}(z-\sigma)^4\right)\right],$$

$$\sigma \le z \le \sigma + \frac{3}{2},\ \textit{Inner wall},$$

Where $\eta_1 = 4\delta,\ \delta = \frac{\delta^*}{e_0},\ \sigma = \frac{d}{l_0},\ \tau = \frac{\tau' l_0}{e_0}.$

6.2 Solution Methodology

The numerical method utilizes the explicit finite difference approach. By utilizing the algebraic transformation provided above in Eqs. (6.46) & (6.47) for core and plasma region respectively:

$$W_{Ci}^{k+1} = W_{Ci}^{k} + \left(\frac{R_c}{r+R_c}\right)\frac{\Delta t \rho_0}{\mathrm{Re}} B_1\left(1 + c\cos(c_1 t)\right)$$
$$+ \frac{1}{(r+R_c)^2}\frac{\partial}{\partial r}\left((r+R_c)^2\left(\mu\left((W_C)_r - \frac{W_{Ci}^k}{r+R^c}\right)^{n-1} + \tau\left((W_C)_r - \frac{W_{Ci}^k}{r+R^c}\right)^{-\frac{1}{2}}\right)\left((W_C)_r - \frac{W_{Ci}^k}{r+R^c}\right)\right)$$
$$+ \frac{1}{\rho_0} Gr_T \theta_{Ci}^k + \frac{1}{\rho_0} Br \sigma_{Ci}^k,$$

(6.57)

$$W_{Pi}^{k+1} = W_{Pi}^{k} + \frac{\Delta t}{\mathrm{Re}}\begin{Bmatrix} \left(\frac{R_c}{r+R_c}\right) B_1\left(1+c\cos(c_1 t)\right) + \frac{1}{(r+R_c)}\frac{\partial}{\partial r}\left((r+R_c)(W_P)_r\right) \\ -\frac{W_{Pi}^k}{(r+R_c)^2} + Gr_T\theta_{pi}^k + Br\sigma_{pi}^k \end{Bmatrix},$$

(6.58)

Eqs. (6.37) & (6.41) becomes,

$$\theta_{Ci}^{k+1} = \theta_{Ci}^{k} + \frac{\Delta t \rho_0 c_0}{\mathrm{Pe}\, k_0}\left\{(\theta_C)_{rr} + \frac{1}{r+R_c}(\theta_C)_r + k_0\beta\right\}, \tag{6.59}$$

$$\theta_{Pi}^{k+1} = \theta_{Pi}^{k} + \frac{\Delta t}{\mathrm{Pe}}\left\{(\theta_P)_{rr} + \frac{1}{r+R_c}(\theta_P)_r + \beta\right\}, \tag{6.60}$$

Eqs. (6.38) & (6.42) becomes

$$\sigma_{Ci}^{j+1}=\sigma_{Ci}^{j}+\frac{\Delta t}{\mathrm{Re}}\left\{\frac{1}{D_0}\frac{1}{Sc}\left(\left(\sigma_C\right)_{rr}+\frac{1}{r+R_c}\left(\sigma_C\right)_r\right)+\frac{E}{E_0}\sigma_{Ci}^{j}\right\}, \tag{6.61}$$

$$\sigma_{Pi}^{j+1}=\sigma_{Pi}^{j}+\frac{\Delta t}{\mathrm{Re}}\left\{\frac{1}{Sc}\left(\left(\sigma_P\right)_{rr}+\frac{1}{r+R_c}\left(\sigma_P\right)_r\right)+E\sigma_{Pi}^{j}\right\}. \tag{6.62}$$

The numerical boundary and initial condition have been defined as follows:

$$\begin{cases} W_{Pi}^{1}=0,\ \theta_{Pi}^{1}=1,\ \sigma_{Pi}^{1}=1 & at\quad r=R(z), \\ W_{P1}^{k}=W_{C1}^{k},\ \theta_{P1}^{k}=\theta_{C1}^{k},\ \sigma_{P1}^{j}=\sigma_{C1}^{j} & at\quad r=R_1(z), \\ \left(\theta_C\right)_r=\left(\theta_P\right)_r,\ \left(\sigma_C\right)_r=\left(\sigma_P\right)_r & at\quad r=R_1(z), \\ \left(W_C\right)_r=0,\ \left(\theta_C\right)_r=0,\ \left(\sigma_C\right)_r=0 & at\quad r=0. \end{cases} \tag{6.63}$$

6.3 Discussion of Result

The sections that follow analyse the outcomes of the numerical results in considerable depth. The programming code is developed in MATLAB. To solve the partial differential equation, a set of preset integers is chosen. $\mathrm{P}e=1.87,\ \mathrm{Re}=1,\ B_1=1.41,\ E=0.5,\ \beta=0.1,\ k_0=0.8,\ c_0=1,\ Sc=1,\ \mu_0=1.2,\ \ n=0.95.$ It has been demonstrated that the mentioned data is strongly linked to conditions in the bloodstream, which is a real-world manifestation.

Demonstrates the outcomes of the two-layered fluid model's axial velocity profile, which is defined by the Newtonian fluid in the plasma area and the Herschel–Bulkley fluid in the core region. The velocity profile is shown to grow in both the single phase and two phase areas. The profiles in this region are determined to be linear since the periphery region is minimal. Nonetheless, the curves become parabolic in the core area. It's interesting to note that growing peripheral layer causes the velocity profile in the core region to rise.

Fig. (6.2) shows the graph of curvature (R_c). At larger curvatures (R_c) the velocity profile increases because the artery becomes straight, as shown in Fig. (6.2). Fig. (6.3) shows the graph of Reynold number (Re) is decreasing in the single phase and two phase the effects are clearer in the core region. Fig. (6.4) Blood's dimensionless axial velocity, calculated for various power law parameter values using the Herschel–Bulkley model's constitutive equation (n) shows the velocity profile of the shear thickening effect is increased by increasing the value of (n). The Grashof number (Gr), This dimensionless parameter is a ratio of the buoyancy to the viscous force that is operating on the plasma, and it is responsible for the growth of core areas. By increasing the Grashof number (Gr), The viscous forces become less powerful, and as a result, the shear thinning forces grow more powerful. These effects are revealed by the velocity profile. Fig. (6.5). The velocity distribution in a stenotic blood artery for different Brinkman number (Br) levels is shown in Fig. (6.6) the hypothesis that increasing (Br) levels raise blood temperature along the arterial axis is tested both for core and plasma region in singal and two phase. Also, since the flow at the interface is continuous according to the boundary condition, the angular velocity of the plasma fluid is directly affected by the reduced red blood cell velocity.

Fig. (6.7) shows the graph of curvature (R_c). The effects of curvature are increasing in core and plasma region as the dilation occurs in the single phase and is better in two phases. Fig. (6.8) demonstrates that the temperature profile shows an increasing function of the heat source or sink parameter (β). When the Peclet number is varied, the temperature profile of the blood flow shifts in a variety of ways (Pe), as seen in Fig. (6.9). As the Peclet number increases, the graphic shows that the temperature profile in the core and plasma regions decreases where singal phase (S.P) and two phase (T.P) are written in graphs.

The concentration profiles for the core and plasma areas show a reduction when the Reynold number (Re) and Schmidt number (Sc) decrease, respectively, as shown in Figures (6.10) and (6.11), which are part of the current computational work. For certain values of the Reynold number and Schmidt number, the concentration profile fall from the arterial wall and the interface region towards the middle of the artery and beyond.

Fig. (6.12) certain values of the chemical reaction parameter (E) the concentration profile rises from the arterial wall and the interface region towards the middle of the artery and beyond. This tendency is depicted in the concentration profile because, as the chemical reaction parameter (E) values increase, the molecular diffusivity decreases, hence reducing the species concentration.

Assuming the pulsatile, non-Newtonian Herschel–Bulkley model of blood flow for core and Newtonian blood flow plasma areas has allowed for accurate estimation of flow wall shear stress, total flow rate, and resistance, which are necessary for having an understanding of the two-phase flow dynamics of blood as it travels through a stretch of a stenosed artery. Fig (6.13), (6.14) & (6.15) provides the default values of the parameters that are used to visually examine the model's efficiency.

Figure (6.13) displays the wall shear stress graph as a function of the curvature (R_c) in the core and plasma regions. The graph increases as the curvature increases. The graph in Fig. (6.14) shows how the blood flow rate increases as the sink parameter (β) between the core and plasma region increases. Fig (6.15) shows the graph of curvature Figure (6.15) displays the resistance profiles sink parameter (β) graph, which decreases as the sink parameter decrease in the resistance profile which decreases with sink parameter (β).

6.4 Concluding Remarks

A mathematical model consisting of two layers has been created to simulate pulsatile blood flowing through an artery that is formed like a W and has been stenosed. While the model assumes Newtonian behavior in the plasma region, it takes into account the non-Newtonian Herschel-Bulkley character of the blood flow in the core region so that it may accurately represent the blood flow. Through the application of the finite difference approach, the numerical solution was brought about. Whenever there is an increase in the thickness of the peripheral plasma layer, the blood flow's velocity, temperature, and concentration profile all drop.

- Raising the chemical reaction parameter (E) causes a decline in the concentration profile.
- Rising molecule diffusivity directly dampens the flow's concentration profile, causing this to occur.
- The study reveals that Peclet number (Pe) and Schmidt's number (Sc) both function to lower blood flow concentration and temperature, respectively.
- The temperature results are more symmetrical in two-phase flow when considering curvature(R_c).
- It is discovered that when the plasma layer increases, the flow rate increases with sink parameter (β).
- As the stenosis height grows, so does the power of the vortices in the overlapping stenotic zone.
- The divergent tapering artery is the most resistant to flow and has the greatest heat. The taper angle plays a significant role in determining flow parameters. Always consider the taper angle in the process.

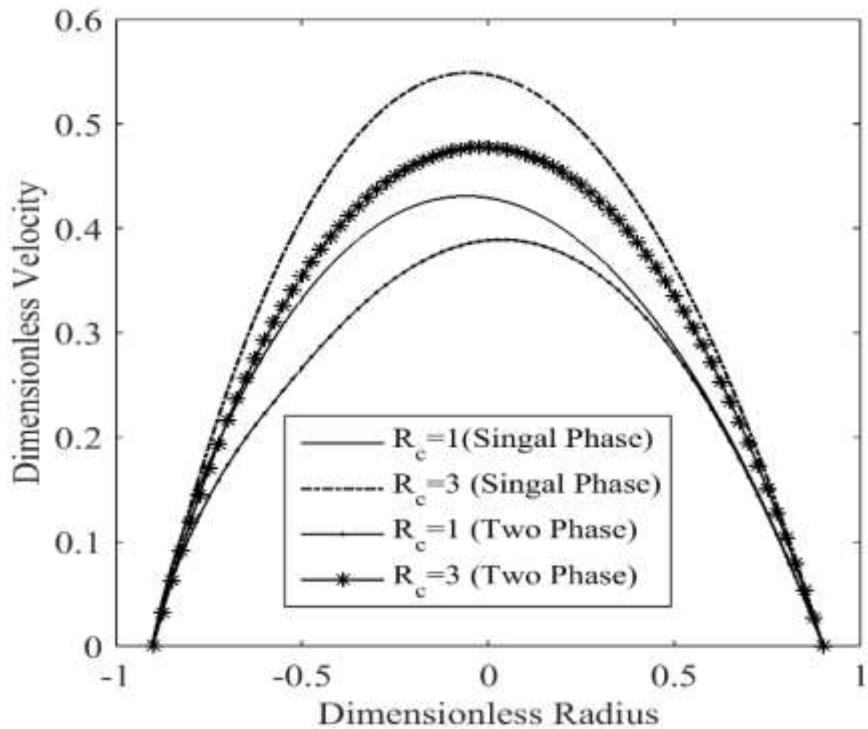

Figure 6.2

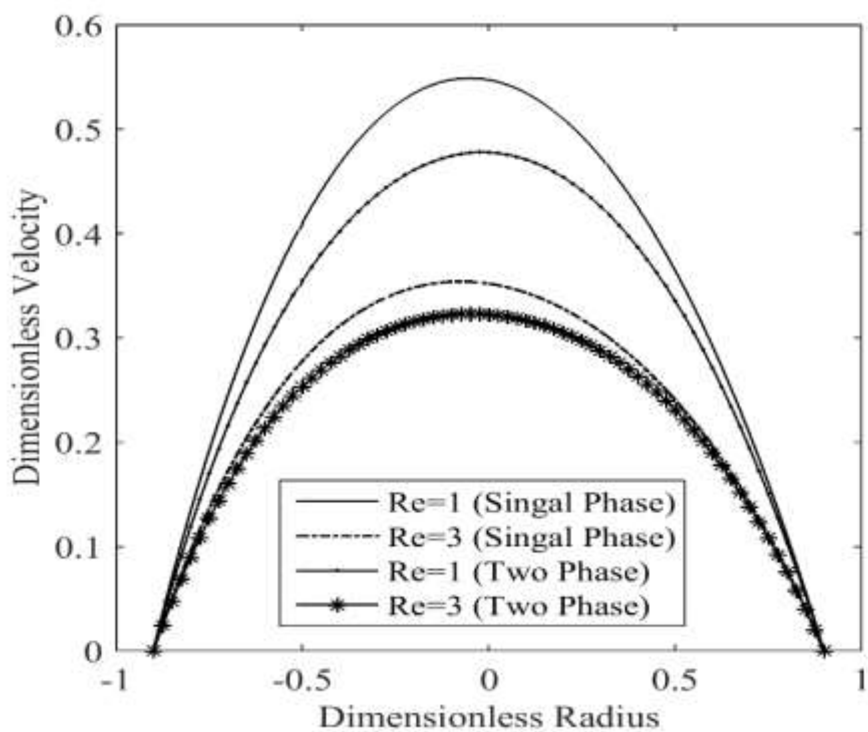

Figure 6.3

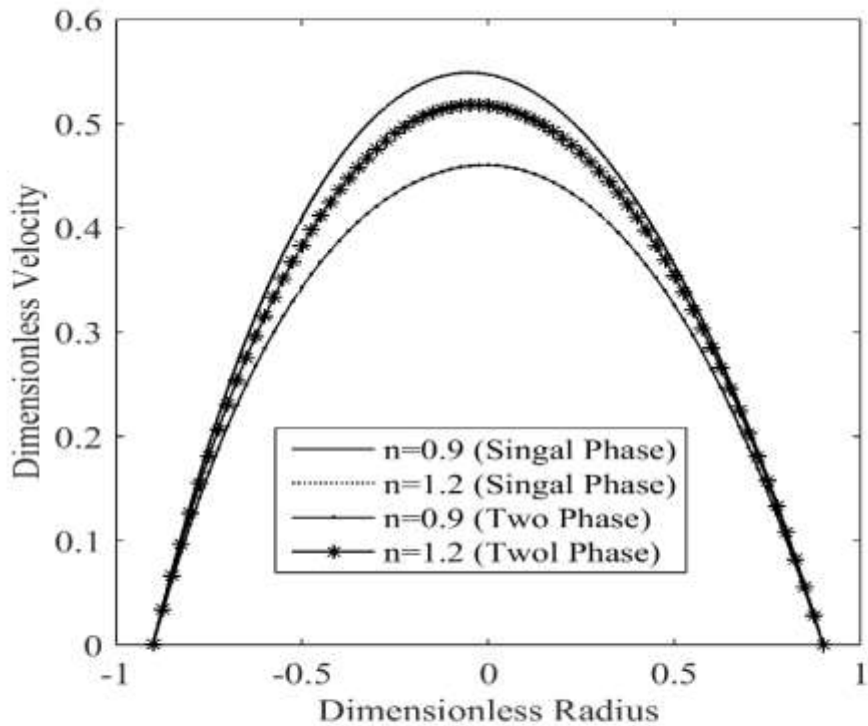

Figure 6.4

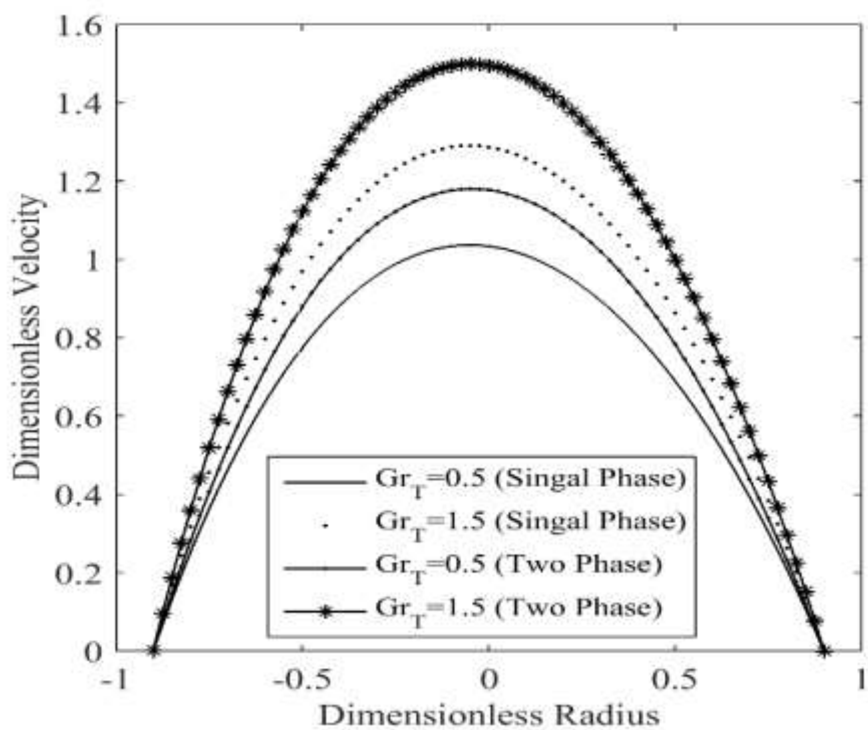

Figure 6.5

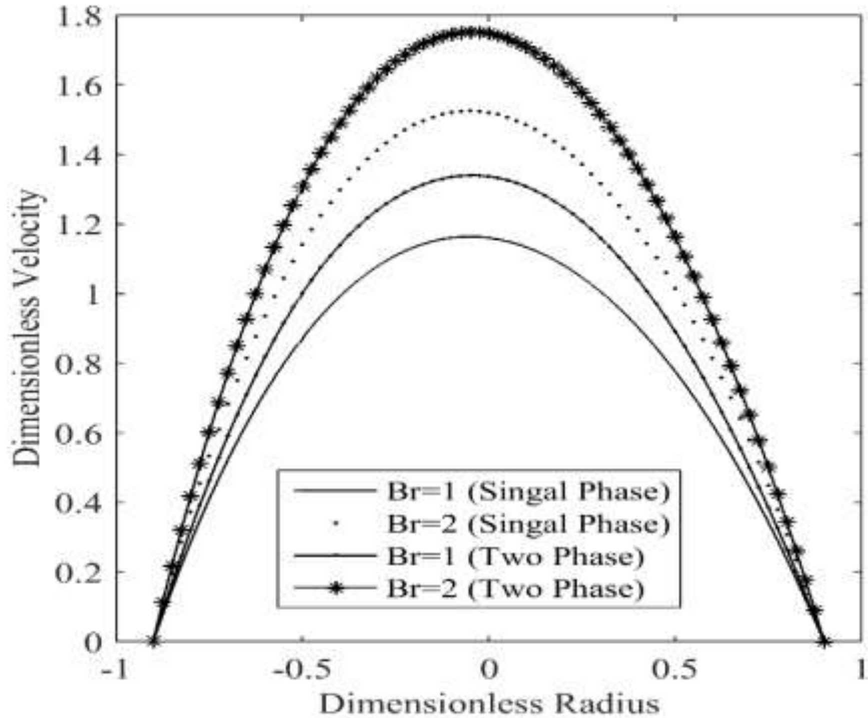

Figure 6.6

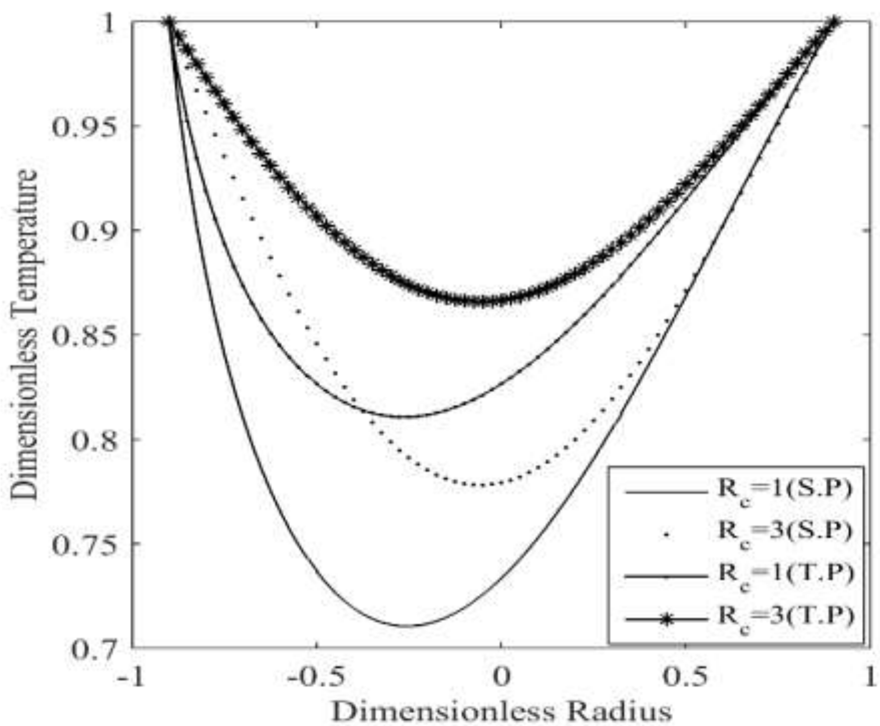

Figure 6.7

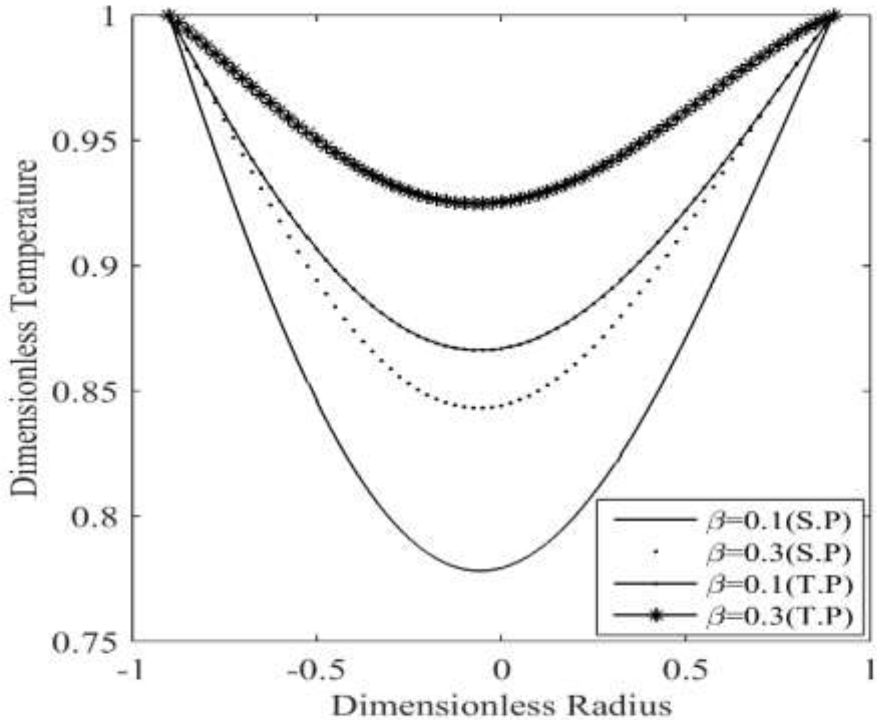

Figure 6.8

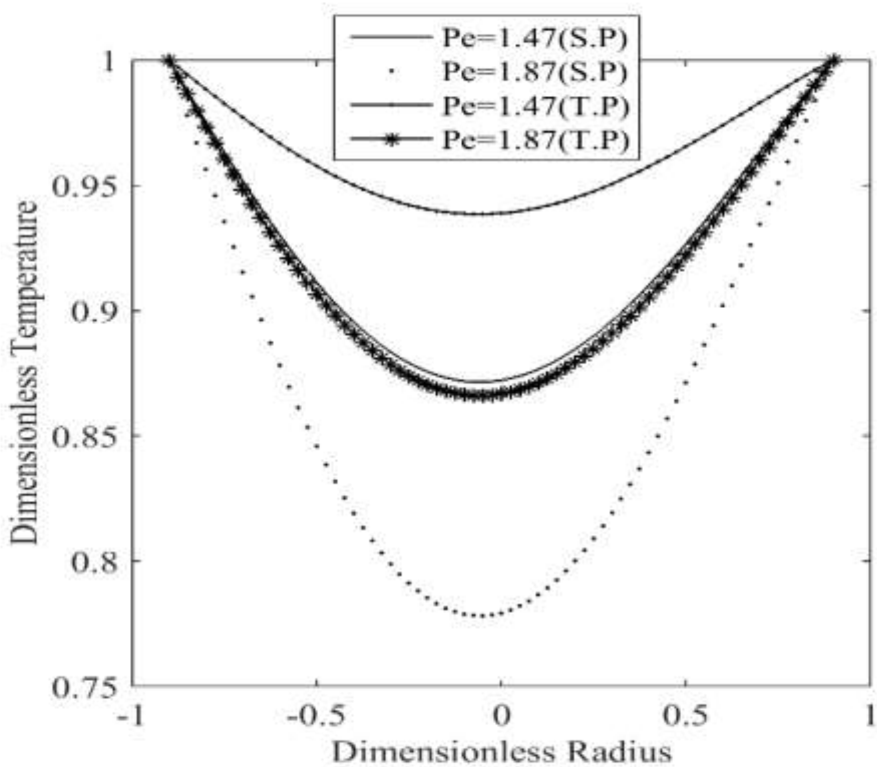

Figure 6.9

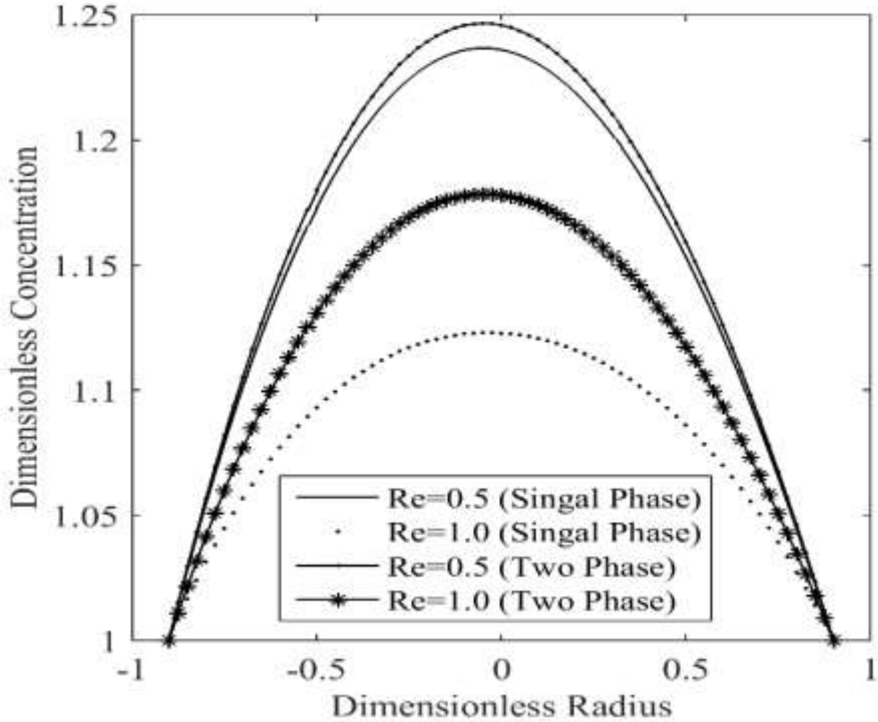

Figure 6.10

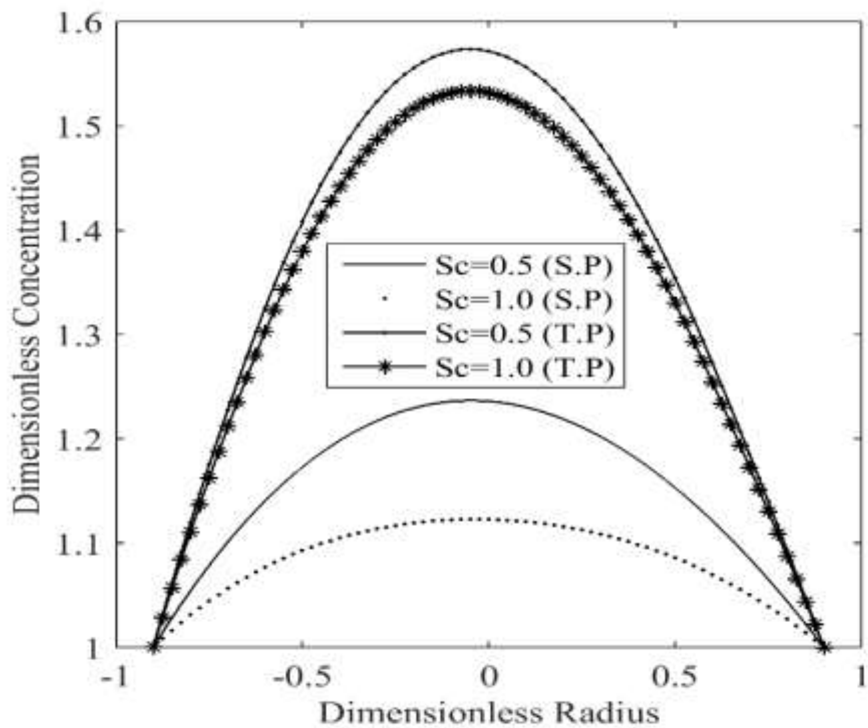

Figure 6.11

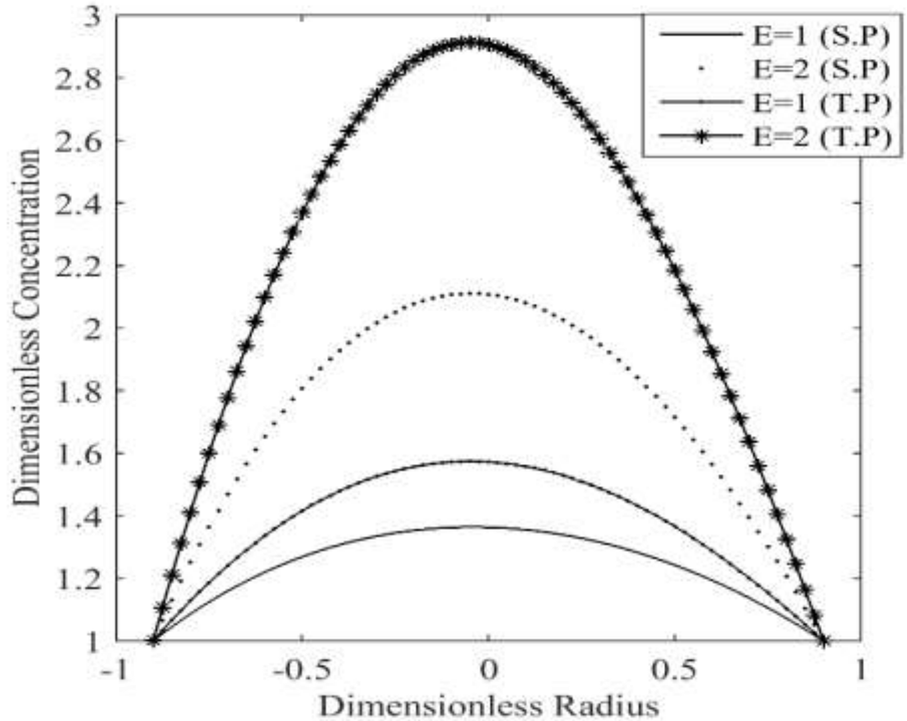

Figure 6.12

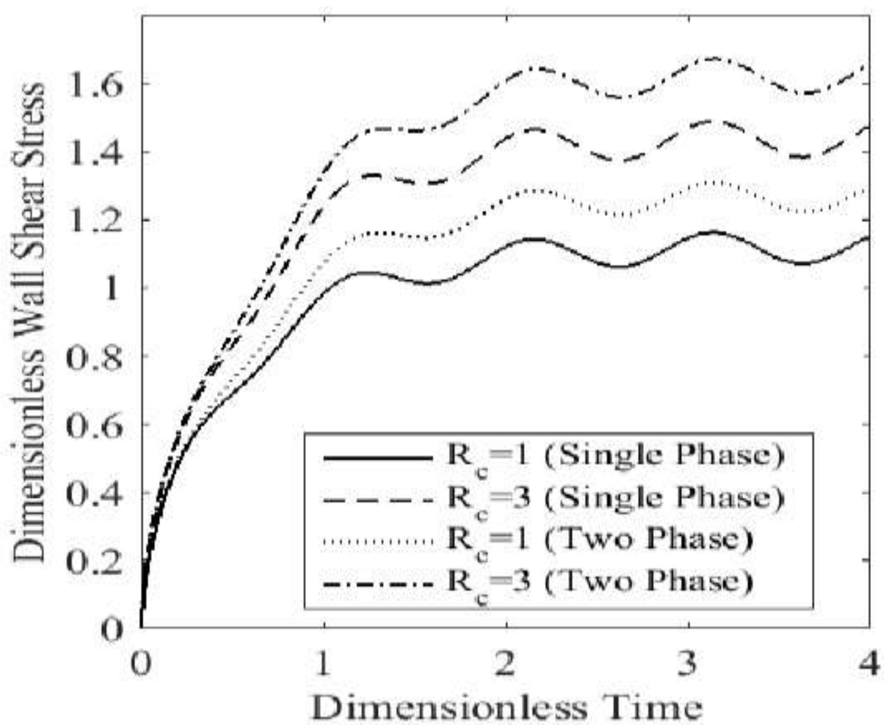

Figure 6.13

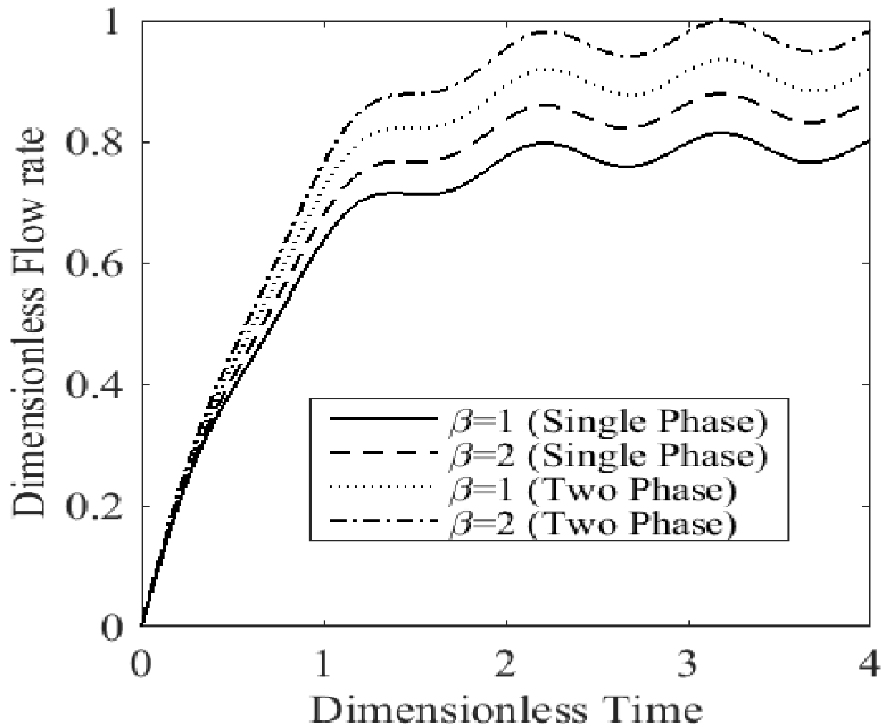

Figure 6.14

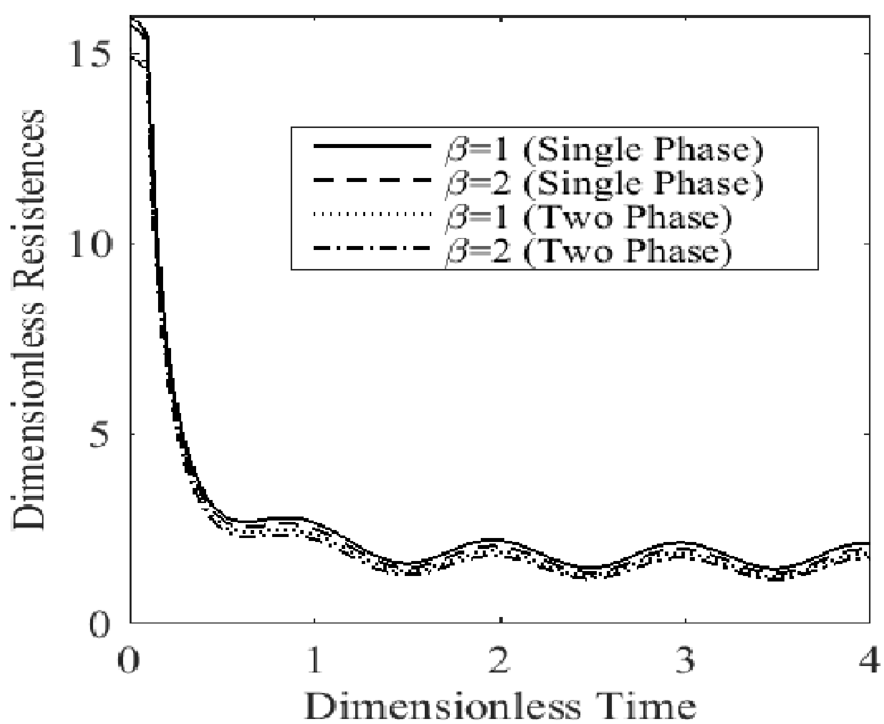

Figure 6.15

References

Abbas, M. A., Bai, Y., Bhatti, M., & Rashidi, M. (2016). Three dimensional peristaltic flow of hyperbolic tangent fluid in non-uniform channel having flexible walls. *Alexandria Engineering Journal*, *55*(1), 653-662.

Abbas, Z., Iftikhar, B., Shabbir, M., Alghamdi, M., & Iqbal, J. (2020). Numerical treatment of slip velocity and catheterization on the gravity flow of non-Newtonian fluid model through a uniform blood vessel. *Physica Scripta*, *95*(5), 055006.

Abbas, Z., Shabbir, M., & Ali, N. (2017). Analysis of rheological properties of Herschel-Bulkley fluid for pulsating flow of blood in ω-shaped stenosed artery. *AIP Advances*, *7*(10).

Abbasian, M., Shams, M., Valizadeh, Z., Moshfegh, A., Javadzadegan, A., & Cheng, S. (2020). Effects of different non-Newtonian models on unsteady blood flow hemodynamics in patient-specific arterial models with in-vivo validation. *Computer Methods and Programs in Biomedicine*, *186*, 105185.

Chakravarty, S. (1987). Effects of stenosis on the flow-behaviour of blood in an artery. *International journal of engineering science* **25**(8): 1003-1016.

Abdelsalam, S. I., Mekheimer, K. S., & Zaher, A. (2020). Alterations in blood stream by electroosmotic forces of hybrid nanofluid through diseased artery: aneurysmal/stenosed segment. *Chinese Journal of Physics*, *67*, 314-329.

Ahmed, A., & Nadeem, S. (2017). Effects of magnetohydrodynamics and hybrid nanoparticles on a micropolar fluid with 6-types of stenosis. *Results in physics*, *7*, 4130-4139.

Akram, J., Akbar, N. S., & Tripathi, D. (2022). Analysis of electroosmotic flow of silver-water nanofluid regulated by peristalsis using two different approaches for nanofluid. *Journal of Computational Science*, *62*, 101696.

Ali, N., Javid, K., Sajid, M., & Anwar Bég, O. (2016). Numerical simulation of peristaltic flow of a biorheological fluid with shear-dependent viscosity in a curved channel. *Computer methods in biomechanics and biomedical engineering*, *19*(6), 614-627.

Ali, N., Zaman, A., Sajid, M., Nieto, J., & Torres, A. (2015). Unsteady non-Newtonian blood flow through a tapered overlapping stenosed catheterized vessel. *Mathematical biosciences*, *269*, 94-103.

Azuma, T., & Fukushima, T. (1976). Flow patterns in stenotic blood vessel models. *Biorheology*, *13*(6), 337-355.

Berntsson, F., Ghosh, A., Kozlov, V., & Nazarov, S. (2018). A one dimensional model of blood flow through a curvilinear artery. *Applied Mathematical Modelling*, *63*, 633-643.

Burton, A. (1966). Introductory text, Physiology and Biophysics of the Circulation. *Year Book Medical Publisher, Chicago, IL*.

Caballero, A., & Laín, S. (2015). Numerical simulation of non-Newtonian blood flow dynamics in human thoracic aorta. *Computer methods in biomechanics and biomedical engineering*, *18*(11), 1200-1216.

Chakravarty, S. (1987). Effects of stenosis on the flow-behaviour of blood in an artery. *International journal of engineering science* **25**(8): 1003-1016.

Chakravarty, S., et al. (1996). Effect of body acceleration on unsteady flow of blood past a time-dependent arterial stenosis. *Mathematical and computer modelling* **24**(2): 57-74.

Chakravarty, S. and P. K. Mandal (2005). Effect of surface irregularities on unsteady pulsatile flow in a compliant artery. *International journal of non-linear mechanics* **40**(10): 1268-1281.

Cho, Y. I. and K. R. Kensey (1991). Effects of the non-Newtonian viscosity of blood on flows in a diseased arterial vessel. Part 1: Steady flows. *Biorheology* **28**(3-4): 241-262.

Choi, S. U., & Eastman, J. A. (1995). *Enhancing thermal conductivity of fluids with nanoparticles*.

Choudhari, R., Mebarek-Oudina, F., Öztop, H. F., Vaidya, H., & Prasad, K. V. (2022). Electro-osmosis modulated peristaltic flow of non-Newtonian liquid via a microchannel and variable liquid properties. *Indian Journal of Physics*, *96*(13), 3853-3866.

Chow, J., & Soda, K. (1973). Laminar flow and blood oxygenation in channels with boundary irregularities.

Doffin, J., & Chagneau, F. (1981). Oscillating flow between a clot model and a stenosis. *Journal of biomechanics*, *14*(3), 143-148.

El-Shahed, M. (2003). Pulsatile flow of blood through a stenosed porous medium under periodic body acceleration. *Applied Mathematics and Computation*, *138*(2-3), 479-488.

Eldesoky, I. M. (2012). Slip effects on the unsteady MHD pulsatile blood flow through porous medium in an artery under the effect of body acceleration. *International Journal of Mathematics and Mathematical Sciences* .

Fahim, M., Sajid, M., Ali, N., & Sadiq, M. (2022). Unsteady nonisothermal tangent hyperbolic fluid flow in a stenosed blood vessel with pulsatile pressure gradient and body acceleration. *The European Physical Journal Plus*, *137*(7), 847.

Fahraeus, R., & Lindqvist, T. (1931). The viscosity of the blood in narrow capillary tubes. *American Journal of Physiology-Legacy Content*, *96*(3), 562-568.

Forrester, J. H., & Young, D. F. (1970). Flow through a converging-diverging tube and its implications in occlusive vascular disease—I: Theoretical development. *Journal of biomechanics*, *3*(3), 297-305.

Frolov, S., Sindeev, S., Liepsch, D., Balasso, A., Arnold, P., Kirschke, J., Prothmann, S., & Potlov, A. Y. (2018). Newtonian and non-Newtonian blood flow at a 90∘-bifurcation of the cerebral artery: a comparative study of fluid viscosity models. *Journal of Mechanics in Medicine and Biology*, *18*(05), 1850043.

Gijsen, F., Allanic, E., Van De Vosse, F., & Janssen, J. (1999). The influence of the non-Newtonian properties of blood on the flow in large arteries: unsteady flow in a 90 curved tube. *Journal of biomechanics*, *32*(7), 705-713.

Gudekote, M., Choudhari, R., Vaidya, H., & Prasad, K. V. (2018). Peristaltic flow of Herschel-Bulkley fluid in an elastic tube with slip at porous walls. *Journal of Advanced Research in Fluid Mechanics and Thermal Sciences*, *52*(1), 63-75.

Hernandez, T. (1983). Alligator metabolism studies on chemical reactions in vivo. *Comparative biochemistry and physiology Part B: Comparative biochemistry*, *74*(1), 1-175.

Hong, H., et al. (2017). Characteristics of pulsatile flows in curved stenosed channels. *PloS one* **12**(10): e0186300.

Iasiello, M., Vafai, K., Andreozzi, A., & Bianco, N. (2017). Analysis of non-Newtonian effects within an aorta-iliac bifurcation region. *Journal of biomechanics*, *64*, 153-163.

Ikbal, M. A., et al. (2009). Unsteady response of non-Newtonian blood flow through a stenosed artery in magnetic field. *Journal of Computational and Applied Mathematics* **230**(1): 243-259.

Irgens, F. (2014). *Rheology and non-newtonian fluids* (Vol. 190). Springer.

Jyothi, S., Reddy, M. S., & Gangavathi, P. (2016). Hyperbolic tangent fluid flow through a porous medium in an inclined channel with peristalsis. *Int J Adv Sci Res Manag*, *1*(4), 113-121.

Karimipour, A., et al. (2020). Simulation of blood flow into the popliteal artery to explain the effect of peripheral arterial disease: Investigation the conditions and effects of different foot states during the daily activity of the patient. *Computer methods and programs in biomedicine* **195**: 105638.

Ku, D. N. (1997). Blood flow in arteries. *Annual review of fluid mechanics*, *29*(1), 399-434.

Kumawat, C., Sharma, B., & Mekheimer, K. (2021). Mathematical analysis of two-phase blood flow through a stenosed curved artery with hematocrit and temperature dependent viscosity. *Physica Scripta*, *96*(12), 125277.

Lee, J.-S., & Fung, Y.-C. (1970). Flow in locally constricted tubes at low Reynolds numbers.

MacDonald, D. (1979). On steady flow through modelled vascular stenoses. *Journal of biomechanics*, *12*(1), 13-20.

Manchi, R., & Ponalagusamy, R. (2022). Pulsatile flow of EMHD micropolar hybrid nanofluid in a porous bifurcated artery with an overlapping stenosis in the presence of body acceleration and joule heating. *Brazilian Journal of Physics*, *52*(2), 52.

Mandal, D., et al. (2010). A numerical model study of steady flow through bell-shaped stenoses with and without asymmetry. *International Journal of Experimental and Computational Biomechanics* **1**(3): 306-331.

Mandal, P. K. (2005). An unsteady analysis of non-Newtonian blood flow through tapered arteries with a stenosis. *International journal of non-linear mechanics*, *40*(1), 151-164.

Mandal, P. K., Chakravarty, S., Mandal, A., & Amin, N. (2007). Effect of body acceleration on unsteady pulsatile flow of non-Newtonian fluid through a stenosed artery. *Applied Mathematics and Computation*, *189*(1), 766-779.

Mathur, P. and S. Jain (2013). Mathematical modeling of non-Newtonian blood flow through artery in the presence of stenosis. *Advances in Applied Mathematical Biosciences* **4**(1): 1.

Medvedev, A., & Fomin, V. (2011). Two-phase blood-flow model in large and small vessels. Doklady Physics,

Mekheimer, K. S., & El Kot, M. (2012). Mathematical modelling of unsteady flow of a Sisko fluid through an anisotropically tapered elastic arteries with time-variant overlapping stenosis. *Applied Mathematical Modelling*, *36*(11), 5393-5407.

Melcher, J. R., & Woodson, H. H. (1968). Electromechanical dynamics. *Part I: Discrete Systems; John Wiley & Sons, Inc.: Hoboken, NJ, USA*.

Mirza, I. A., Abdulhameed, M., Vieru, D., & Shafie, S. (2016). Transient electro-magneto-hydrodynamic two-phase blood flow and thermal transport through a capillary vessel. *Computer Methods and Programs in Biomedicine*, *137*, 149-166.

Misra, J., & Sahu, B. (1988). Flow through blood vessels under the action of a periodic acceleration field: A mathematical analysis. *Computers & Mathematics with Applications*, *16*(12), 993-1016.

Misra, J., Sinha, A., & Shit, G. (2008). Theoretical analysis of blood flow through an arterial segment having multiple stenoses. *Journal of Mechanics in Medicine and Biology*, *8*(02), 265-279.

Moradicheghamahi, J., Sadeghiseraji, J., & Jahangiri, M. (2019). Numerical solution of the Pulsatile, non-Newtonian and turbulent blood flow in a patient specific elastic carotid artery. *International Journal of Mechanical Sciences*, *150*, 393-403.

Moayeri, M. and G. Zendehbudi (2003). Effects of elastic property of the wall on flow characteristics through arterial stenoses. *Journal of biomechanics* **36**(4): 525-535.

Morgan, B. E., & Young, D. F. (1974). An intergral method for the analysis of flow in arterial stenoses. *Bulletin of Mathematical Biology, 36,* 39-53.

Mwanthi, V., et al. (2017). "Velocity profiles of unsteady blood flow through an inclined circular tube with magnetic field."

Nadeem, S., & Ijaz, S. (2016). Theoretical analysis of shear thinning hyperbolic tangent fluid model for blood flow in curved artery with stenosis. *Journal of Applied Fluid Mechanics, 9*(5), 2217-2227.

Nadeem, S. and S. Ijaz (2015). Theoretical analysis of metallic nanoparticles on blood flow through stenosed artery with permeable walls. *Physics Letters A* **379**(6): 542-554.

Niimi, H., et al. (1984). Structure of blood flow through a curved vessel with an aneurysm. *Biorheology* **21**(4): 603-615.

Noreen, S., Waheed, S., & Hussanan, A. (2019). Peristaltic motion of MHD nanofluid in an asymmetric micro-channel with Joule heating, wall flexibility and different zeta potential. *Boundary Value Problems*, *2019*, 1-23.

O'callaghan, S., Walsh, M., & McGloughlin, T. (2006). Numerical modelling of Newtonian and non-Newtonian representation of blood in a distal end-to-side vascular bypass graft anastomosis. *Medical engineering & physics, 28*(1), 70-74.

Perktold, K., Peter, R., & Resch, M. (1989). Pulsatile non-Newtonian blood flow simulation through a bifurcation with an aneurysm. *Biorheology*, *26*(6), 1011-1030.

Ponalagusamy, R., & Priyadharshini, S. (2018). Numerical investigation on two-fluid model (micropolar-Newtonian) for pulsatile flow of blood in a tapered arterial stenosis with radially variable magnetic field and core fluid viscosity. *Computational and Applied Mathematics*, *37*, 719-743.

Ponalagusamy, R., & Tamil Selvi, R. (2015). Influence of magnetic field and heat transfer on two-phase fluid model for oscillatory blood flow in an arterial stenosis. *Meccanica*, *50*, 927-943.

Rahma, A. G., et al. (2022). Blood flow CFD simulation on a cerebral artery of a stroke patient. *SN Applied Sciences* **4**(10): 1-12.

Rashid, M., et al. (2020). Effects of induced magnetic field for peristaltic flow of Williamson fluid in a curved channel. *Physica A: Statistical Mechanics and its Applications* **553**: 123979.

Rajashekhar, C., Manjunatha, G., Prasad, K., Divya, B., & Vaidya, H. (2018). Peristaltic transport of two-layered blood flow using Herschel–Bulkley Model. *Cogent Engineering*, *5*(1), 1495592.

Ram, D., Bhandari, D., Sharma, K., & Tripathi, D. (2023). Progression of blood-borne viruses through bloodstream: A comparative mathematical study. *Computer Methods and Programs in Biomedicine*, *232*, 107425.

Roy, M., Sikarwar, B. S., Bhandwal, M., & Ranjan, P. (2017). Modelling of blood flow in stenosed arteries. *Procedia computer science*, *115*, 821-830.

Sankar, D. (2011). Two-phase non-linear model for blood flow in asymmetric and axisymmetric stenosed arteries. *International journal of non-linear mechanics*, *46*(1), 296-305.

Sankar, D., & Lee, U. (2009). Mathematical modeling of pulsatile flow of non-Newtonian fluid in stenosed arteries. *Communications in Nonlinear Science and Numerical Simulation*, *14*(7), 2971-2981.

Sanyal, D. and N. Maji (1999). Unsteady blood flow through an indented tube with atherosclerosis. *Indian Journal of Pure & Applied Mathematics* **30**(10): 951-959.

Sharzehee, M., et al. (2018). Fluid-structure interaction modeling of aneurysmal arteries under steady-state and pulsatile blood flow: a stability analysis. *Computer methods in biomechanics and biomedical engineering* **21**(3): 219-231.

Singh, B., et al. (2010). Blood flow through an artery having radially non-summetric mild stenosis. *Appl. Math. Sci* **4**(22): 1065-1072.

Shabbir, M. S., Abbas, Z., & Ali, N. (2022). Numerical study of heat and mass transfer on the pulsatile flow of blood under atherosclerotic condition. *International Journal of Nonlinear Sciences and Numerical Simulation*(0).

Shabbir, M. S., Ali, N., & Abbas, Z. (2023). Impact of unsteadiness on the non-Newtonian flow of blood in a vascular tube with stenosis and aneurysm: analytical solution. *Waves in Random and Complex Media*, 1-15.

Sharma, B., Kumawat, C., & Makinde, O. (2022). Hemodynamical analysis of MHD two phase blood flow through a curved permeable artery having variable viscosity with heat and mass transfer. *Biomechanics and Modeling in Mechanobiology*, *21*(3), 797-825.

Sharma, B. K., Poonam, & Chamkha, A. J. (2022). Effects of heat transfer, body acceleration and hybrid nanoparticles (Au–Al2O3) on MHD blood flow through a curved artery with stenosis and aneurysm using hematocrit-dependent viscosity. *Waves in Random and Complex Media*, 1-31.

Sharma, K. (2022). FHD flow and heat transfer over a porous rotating disk accounting for Coriolis force along with viscous dissipation and thermal radiation. *Heat Transfer*, *51*(5), 4377-4392.

Sharma, K., Vijay, N., Bhardwaj, D., & Jindal, R. (2023). Flow of water conveying Fe3O4 and Mn–ZnFe2O4 nanoparticles over a rotating disk: Significance of thermophoresis and Brownian motion. *Journal of Magnetism and Magnetic Materials*, *574*, 170710.

Sharma, M., & Gaur, R. (2017). Effect of variable viscosity on chemically reacting magneto-blood flow with heat and mass transfer. *Global Journal of Pure and Applied Mathematics*, *13*(3), 26-35.

Sood, T., et al. (2018). Effect of pulse rate variation on blood flow through axisymmetric and asymmetric stenotic artery models. *Mathematical biosciences* **298**: 1-18.

Soulis, J. V., Giannoglou, G. D., Chatzizisis, Y. S., Seralidou, K. V., Parcharidis, G. E., & Louridas, G. E. (2008). Non-Newtonian models for molecular viscosity and wall shear stress in a 3D reconstructed human left coronary artery. *Medical engineering & physics*, *30*(1), 9-19.

Sriyab, S. (2014). Mathematical analysis of non-Newtonian blood flow in stenosis narrow arteries. *Computational and mathematical methods in medicine* .

Tandon, P. and U. Rana (1995). A new model for blood flow through an artery with axisymmetric stenosis. *International journal of bio-medical computing* **38**(3): 257-267.

Thomas, B. and K. Sumam (2016). Blood flow in human arterial system-A review. *Procedia Technology* **24**: 339-346.

Tzirtzilakis, E. (2005). A mathematical model for blood flow in magnetic field. *Physics of fluids* **17**(7): 077103.

Tripathi, B., & Sharma, B. K. (2018). Influence of heat and mass transfer on MHD two-phase blood flow with radiation. *AIP Conference Proceedings*.

Tu, C., & Deville, M. (1996). Pulsatile flow of non-Newtonian fluids through arterial stenoses. *Journal of biomechanics*, *29*(7), 899-908.

Usha, R., & Prema, K. (1999). Pulsatile flow of particle-fluid suspension model of blood under periodic body acceleration. *Zeitschrift für angewandte Mathematik und Physik ZAMP*, *50*(2), 175-192.

Verma, S., & Srivastava, A. (2014). Analytical study of a two-phase model for steady flow of blood in a circular tube. *IJERA*, *12*, 1-10.

Venkateswarlu, K. and J. A. Rao (2004). Numerical solution of unsteady blood flow through an indented tube with atherosclerosis.

Wang, C. and J. Bassingthwaighte (2003). Blood flow in small curved tubes. *J. Biomech. Eng.* **125**(6): 910-913.

Wagner, V., Dullaart, A., Bock, A.-K., & Zweck, A. (2006). The emerging nanomedicine landscape. *Nature biotechnology*, *24*(10), 1211-1217.

Xu, Z., Chen, N., Shadden, S. C., Marsden, J. E., Kamocka, M. M., Rosen, E. D., & Alber, M. (2009). Study of blood flow impact on growth of thrombi using a multiscale model. *Soft Matter*, *5*(4), 769-779.

Yilmaz, F., & Gundogdu, M. Y. (2008). A critical review on blood flow in large arteries; relevance to blood rheology, viscosity models, and physiologic conditions. *Korea-Australia Rheology Journal*, *20*(4), 197-211.

Yongchareon, W., & Young, D. F. (1979). Initiation of turbulence in models of arterial stenoses. *Journal of biomechanics*, *12*(3), 185-196.

Young, D. F., et al. (1977). Hemodynamics of arterial stenoses at elevated flow rates. *Circulation Research* **41**(1): 99-107.

Young, D. F. and F. Y. Tsai (1973). Flow characteristics in models of arterial stenoses—I. Steady flow. *Journal of biomechanics* **6**(4): 395-410.

Young, D. (1968). Effect of a time-dependent stenosis on flow through a tube.

Zaman, A., & Ali, N. (2016). Effects of peripheral layer thickness on pulsatile flow of Herschel–Bulkley fluid through a stenotic artery. *Canadian Journal of Physics*, *94*(9), 920-928.

Zaman, A., Ali, N., & Kousar, N. (2018). Nanoparticles (Cu, TiO2, Al2O3) analysis on unsteady blood flow through an artery with a combination of stenosis and aneurysm. *Computers & Mathematics with Applications*, *76*(9), 2179-2191.

Zaman, A., Ali, N., & Sajid, M. (2016). Slip effects on unsteady non-Newtonian blood flow through an inclined catheterized overlapping stenotic artery. *AIP Advances*, *6*(1).

Zaman, A., & Khan, A. A. (2021). Time dependent non-Newtonian nano-fluid (blood) flow in w-shape stenosed channel; with curvature effects. *Mathematics and Computers in Simulation*, *181*, 82-97.

Zaman, A., Khan, A. A., & Kousar, N. (2023). Simulation of magneto-hydrodynamics effects on cross fluid (blood) model with entropy generations in multiple stenosed (aneurysm) curved channel. *Chinese Journal of Physics*, *85*, 616-628.

Zaman, A., et al. (2018). Effects of nanoparticles (Cu (Copper), Silver (Ag)) and slip on unsteady blood flow through a curved stenosed channel with aneurysm. *Thermal Science and Engineering Progress* **5**: 482-491.

Zaman, A., et al. (2019). Effects of nanoparticles (Cu, TiO2, Al2O3) on unsteady blood flow through a curved overlapping stenosed channel. *Mathematics and Computers in Simulation* **156**: 279-293.

Zaman, A., et al. (2021). Simulations of unsteady blood flow through curved stenosed channel with effects of entropy generations and magneto-hydrodynamics. *International Communications in Heat and Mass Transfer* **127**: 105569.